Title

Direct Charm Reconstruction in Association with W Bosons at $\sqrt{s}$ = 13 TeV in the ATLAS Detector

Author

Ottino, Gregory James

Publication Date

2023

Peer reviewed|Thesis/dissertation

Direct Charm Reconstruction in Association with W Bosons at $\sqrt{s} = 13\,\text{TeV}$ in the ATLAS Detector

by

Gregory James Ottino

A dissertation submitted in partial satisfaction of the

requirements for the degree of

Doctor of Philosophy

in

Physics

in the

Graduate Division

of the

University of California, Berkeley

Committee in charge:

Professor Marjorie D. Shapiro, Chair
Professor Barbara Jacak
Professor Karl Van Bibber

Fall 2023

Direct Charm Reconstruction in Association with W Bosons at $\sqrt{s} = 13\,\text{TeV}$ in the ATLAS Detector

Abstract

Direct Charm Reconstruction in Association with W Bosons at $\sqrt{s} = 13\,\text{TeV}$ in the ATLAS Detector

by

Gregory James Ottino

Doctor of Philosophy in Physics

University of California, Berkeley

Professor Marjorie D. Shapiro, Chair

The production of a W boson in association with a single charm quark is studied using $140\,\text{fb}^{-1}$ of $\sqrt{s} = 13\,\text{TeV}$ proton–proton collision data collected with the ATLAS detector at the Large Hadron Collider. The charm quark is tagged by the presence of a charmed hadron, reconstructed with a secondary-vertex fit. The W boson is reconstructed from the decay to either an electron or a muon and the missing transverse momentum present in the event. The $W + D^{(*)}$ process is sensitive to the strange quark PDF, and can be combined with other measurements to improve uncertainties and central values of global PDF fits. Charmed mesons are reconstructed in the decay channels $D^+ \to K^-\pi^+\pi^+$, $D^{*+} \to D^0\pi^+ \to (K^-\pi^+)\pi^+$, $D^+ \to \phi\pi \to (KK)\pi$, and $D_s \to \phi\pi \to (KK)\pi$ and the charge conjugate decays in the fiducial regions where $p_\text{T}(e,\mu) > 30\,\text{GeV}$, $|\eta(e,\mu)| < 2.5$, $p_\text{T}(D^{(*)}) > 8\,\text{GeV}$, and $|\eta(D^{(*)})| < 2.2$. The integrated and normalized differential cross-sections as a function of the pseudorapidity of the lepton from the W boson decay, and of the transverse momentum of the charmed hadron, are extracted for the $D^+ \to K\pi\pi$ and $D^* \to D^0\pi \to K\pi\pi$ decay modes. The total fiducial cross section is measured for the $D_s \to \phi\pi \to (KK)\pi$ and $D^+ \to \phi\pi \to (KK)\pi$ decay modes. All observables are extracted from the data using a profile likelihood fit. The measured total fiducial cross-sections for the $D^+ \to K\pi\pi$ and $D^* \to D^0\pi \to K\pi\pi$ modes are $\sigma_\text{fid}^{\text{OS}-\text{SS}}(W^-{+}D^+) = 50.2 \pm 0.2\,(\text{stat.})\,^{+2.4}_{-2.3}\,(\text{syst.})\,\text{pb}$, $\sigma_\text{fid}^{\text{OS}-\text{SS}}(W^+{+}D^-) = 48.5 \pm 0.2\,(\text{stat.})\,^{+2.3}_{-2.2}\,(\text{syst.})\,\text{pb}$, $\sigma_\text{fid}^{\text{OS}-\text{SS}}(W^-{+}D^{*+}) = 51.1 \pm 0.4\,(\text{stat.})\,^{+1.9}_{-1.8}\,(\text{syst.})\,\text{pb}$, and $\sigma_\text{fid}^{\text{OS}-\text{SS}}(W^+{+}D^{*-}) = 50.0 \pm 0.4\,(\text{stat.})\,^{+1.9}_{-1.8}\,(\text{syst.})\,\text{pb}$. These differential and total cross section results are compared with the predictions of next-to-leading-order quantum chromodynamics calculations performed using state-of-the-art parton distribution functions. Additionally, the ratio of charm to anti-charm production cross-sections is studied to probe the s-$\bar{s}$ quark asymmetry. The ratio is found to be $R_c^\pm = 0.971 \pm 0.006\,(\text{stat.}) \pm 0.011\,(\text{syst.})$. The ratio and cross-section measurements are consistent with the predictions obtained with parton distribution function sets that have a symmetric s-$\bar{s}$ sea, indicating that any s-$\bar{s}$ asymmetry in the Bjorken-x region relevant for this measurement is small. For the $D_s \to \phi\pi \to (KK)\pi$ and

$D^+ \to \phi\pi \to (KK)\pi$ analysis, the observables that are measured are the inclusive cross section in both charges for the $W+D_s$ process, the ratio of the cross sections with respect to the charge, and the ratio of the D_s to the D^+ process. The measured values are $\sigma_{\rm fid}^{\rm OS-SS}(W^-+D_s^+) = 17.8\pm0.4\,({\rm stat.})\,^{+1.8}_{-1.6}\,({\rm syst.})\,{\rm pb}$, $\sigma_{\rm fid}^{\rm OS-SS}(W^++D_s^-) = 15.8\pm0.4\,({\rm stat.})\,^{+1.5}_{-1.4}\,({\rm syst.})\,{\rm pb}$, $R_c^{\pm}(D_s) = 0.885 \pm 0.029\,({\rm stat.})^{+0.059}_{-0.057}\,({\rm syst.})$, and $R_{D^+/D_s} = 2.93 \pm 0.06({\rm stat.}) \pm 0.24({\rm sys.})$. These result are consistent with the differential $W + D^+$ analysis within 1.5 standard deviations, and are at a lower precision due to lower data and MC simulation statistics and increased systematic uncertainties related to background modeling.

To every would be scientist denied the opportunity to explore the universe due to circumstance and injustice, may we build a better world for you.

≪*Nunca llegáremos a ninguna parte -se lamentaba ante Úrsula-. Aquí nos hemos de pudrir en vida sin recibir los beneficios de la ciencia.*≫
- Gabriel García Márquez

Contents

List of Figures

List of Tables

Acknowledgments

I would like to thank, before anyone else, my parents for their endless love and support, without which I would be neither at the end of this thesis nor the person I am today. Thanks to my brothers, whose efforts to develop my character are matched only by their unflagging faith in me.

I want to express my heartfelt gratitude to Marjorie, who has always been the mentor I've needed throughout my Ph.D. and has cared about my personal well being as much as my scientific accomplishments. Thank you to Timon and Karol for all of your hardware expertise, patience with my questions, and humor at my many, many mistakes. Thanks to my ATLAS colleagues at LBL and further afield for the wisdom and guidance that made this work possible, especially Heather for her mentorship. A special thanks to Miha, the postdoc every grad student would dream to work with. I want to acknowledge all my LBL peers, Jennet, Cesar, Patrick, Neha, and Ryan for leading the way and walking the path with me.

I want to show gratitude to all of my coworkers and friends, especially those fellow union members who helped me believe in and achieve, in our own small way, a better world for grad student workers, postdocs, and researchers. Sam for bringing me into this mess, Max and Vikram for our years in the trenches, Val, Garrett, Kavitha, Connor, Burhan, and countless other UAW members I am lucky to call friends who organized, and were organized by, me. Thanks to Jackie for every meal, conversation, and copy editing this document, I couldn't have done it without you.

Most importantly, thank you Ness. If one person can take credit for everything I am proud of, it's you. I love you.

Chapter 1

Introduction: the Standard Model

This thesis describes studies related to measurements of a W boson produced with a D meson using the ATLAS detector at the Large Hadron Collider (LHC). This process is predicted by the Standard Model of particle physics, and provides an important test of the strong sector. Due to the large data set collected by the ATLAS experiment in Run 2, the W boson with associated D meson process is not limited by statistical uncertainties, but instead by systematic uncertainties related to the calibrations of the detector and modeling of the underlying theoretical processes. This thesis describes the precision measurement of the cross section of the W boson with associated D meson process. This result can then be compared to modern theoretical calculations that serves to validate the Standard Model prediction. Beyond this validation of the Standard Model theory, this measurement seeks to contribute to global understanding of the the structure of the proton.

The first chapter provides a general overview of the Standard Model of particle physics, hadron collider physics, and parton distribution functions. The second chapter gives a more detailed overview of the phenomenology of W boson with associated charm quark or D meson measurements. Chapter three discusses the Large Hadron Collider generally, and the ATLAS experiment specifically. The fourth chapter addresses the data and simulation that are used in the measurement. The reconstruction of relevant physics objects is discussed in Chapter five. Chapter six covers the explicit charm meson reconstruction that is employed in the analysis; the event selection that targets $W + D^{(*)}$ events is discussed as well. Chapter seven discusses the data-driven estimation of the QCD multijet background. The full profile likelihood fit, which is how the signal is extracted from the data, is described in Chapter 8. The systematic uncertainties in the profile likelihood fit are addressed in Chapter nine. Chapter ten discusses the results from the differential $W + D^{(*)}$ cross section analysis. Chapter eleven, describes the results related to the measurement of the production cross section of the $W + D_s$ final state. The final chapter provides the conclusion.

1.1 The Standard Model of Particle Physics

The Standard Model (SM) of particle physics is a quantum field theory that describes all known fundamental particles and the forces governing their interactions. As a theory, the Standard Model has been enormously successful at predicting the discovery of new particles by experiments across many orders of magnitude of energy scales. The known fundamental particles are broadly separated into two categories: fermions, which are the matter particles, and bosons, which carry the fundamental forces. The three forces described by the SM are, in descending order of strength, the Strong force, the Electromagnetic force, and the Weak force. The fourth fundamental force, gravity, is 29 orders of magnitude weaker than the Weak force, and not described by the Standard Model [1]. The particle content of the Standard Model can be seen in Figure 1.1.

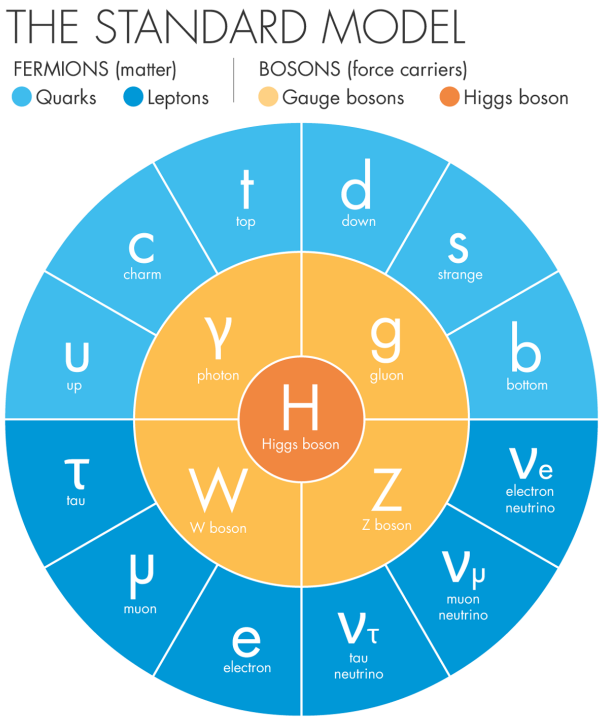

Figure 1.1: The particle content of the Standard Model [2].

The Standard Model began in 1961 with the Glashow-Weinberg-Salam model that unified the Electromagentic and Weak forces and made use of the Higgs mechanism to explain the spontaneous symmetry breaking in the model [3][4][5]. Further experimental and theoretical developments throughout the 1960's led in 1971 to the inclusion of the Strong force by Gross and Wilczek, and the form of model LaGrangian was then largely complete[6]. On the experimental front, the following decades saw the discovery of the W at CERN [7] [8] and top

quark [9] [10] at Fermilab. The final SM particle, the Higgs boson, was discovered in 2012 by the Compact Muon Solenoid (CMS) [11] and the A Toroidal LHC Apparatus (ATLAS) [12] experiments.

While there are observed phenomena in fundamental physics, such as dark matter, dark energy, and gravity, that are not explained by the SM, it has been remarkably successful in regions where it does make predictions. In particular, high-energy collider experiments show astounding agreement between theory and experiment. In Figure 1.2, agreement between SM theory and experiment is shown across multiple orders of magnitude for a variety of processes, as measured by the ATLAS experiment. Summary results like these underscore the theoretical and experimental success of the SM as a framework for understanding particle physics at the highest energy scales which are accessible in collider laboratory environments.

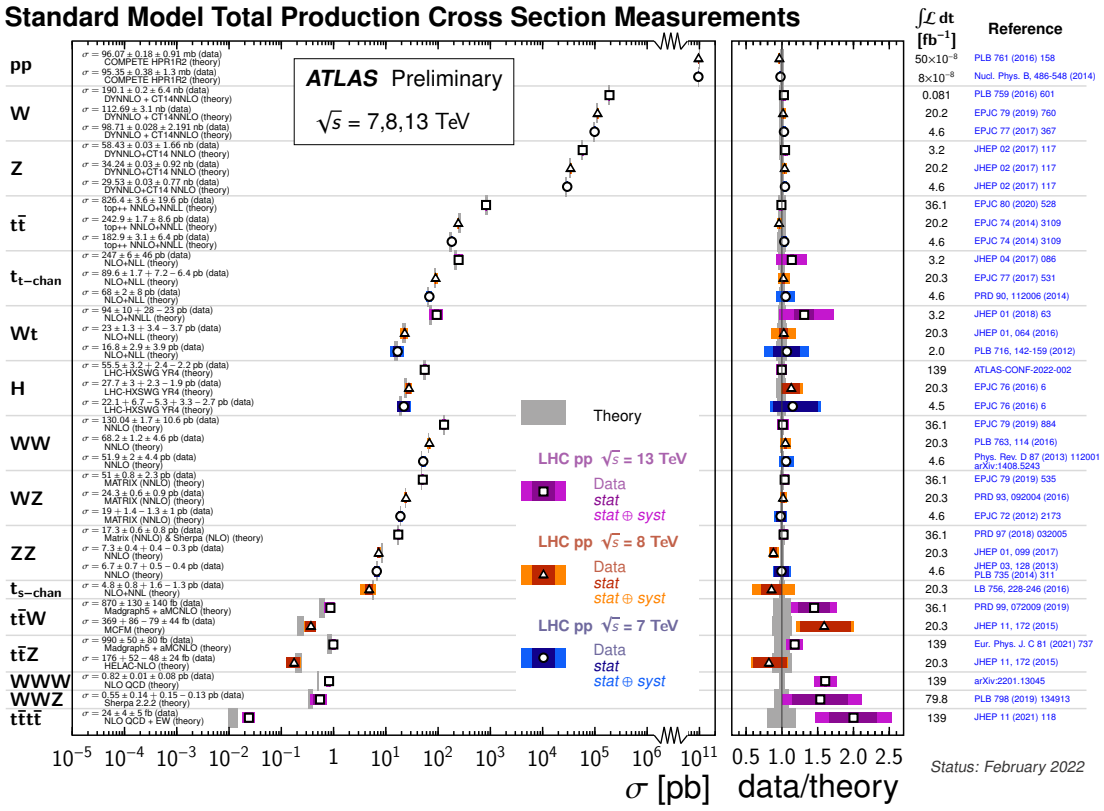

Figure 1.2: Summary of measured SM results from the ALTAS collaboration, corrected for branching fractions. The ratio of experimental results with respect to theory is shown in the right panel [13].

1.2 Hadron Collider Physics and QCD

Hadron collider experiments measure fundamental processes in particle physics and serve as both to test the SM and to investigate into physics beyond the Standard Model. The operating principle of a hadron collider is to accelerate hadrons (in this thesis protons), which are composite particles of quarks and gluons, to high energies in order to probe physics at the center-of-mass energy, denoted by $\sqrt{s}$. This is given by the relativistic equation in the lab frame for two protons of the same energy and equal and opposite momentum:

$$\sqrt{s} = \sqrt{(E_p + E_p)^2 - (\vec{p_1} \cdot \vec{p_2})^2} = 2E_p. \tag{1.1}$$

As hadrons are composite objects, the relevant energy scale of any collision is usually set by the highest momentum transfer (hardest) interaction, governed by Quantum Chromodynamics (QCD) or by Electroweak (EW) interactions. Using perturbation theory, computations of observables are performed in expansions around a small coupling parameter, which guarantees that the infinite series used to calculate observable quantities sum to a finite result, and can be approximated by summing a smaller number of terms at each order of the coupling parameter. Looking to QCD, terms that are quadratic in the strong coupling, α_s, are called Leading Order (LO), while subsequent higher order terms are indicated with the prefix "Next to", e.g. Next to Leading Order for $\mathcal{O}(\alpha_s^4)$ (NLO), Next to Next to Leading Order for $\mathcal{O}(\alpha_s^6)$ (NNLO) etc. The guarantee that these infinite series will converge, for a small coupling parameter, is known as renormalizability. The process of computing an observable in a renormalized gauge field theory requires the introduction of an arbitrary scale, known as the renormalization scale, μ_R [14]. The square of this scale, for comparisons to experiment, is usually set to near the momentum transfer of the interaction, Q^2. Note that the finite series approximation incurs a theoretical uncertainty in the sum of the constituent series terms; at infinite order, changing the renormalization scale does not change the sum of the series. This uncertainty is included in experimental results.

A general feature of Quantum Field Theories known as the "running" of the coupling, modulates the value of the coupling in different energy regimes. This complicates theoretical calculations of experimentally measurable quantities in regimes where the coupling is large. QCD is a non-Abelian, SU(3) color gauge theory that gives the strong force carrier, the gluon, a strong charge [14]. The self-charge of the gluon, number of quark flavors, and number of colors, increase the strength of the strong interaction between two color-charged particles when the energy scale is small. Thus for QCD, observables in high energy regimes, $Q^2 >> 1\,\text{GeV}$, can be estimated perturbatively and in those regimes the theory is renomalizable. In lower energy regimes, the strong coupling is large, and QCD becomes non-perturbative, which makes first principle calculations intractable, requiring parameterized models with input from experiments. This dichotomy introduces another arbitrary scale into QCD calculations, the factorization scale μ_F, which is set to be $\mu_F^2 \approx \mathcal{O}(Q^2)$. The running of strong coupling explains two important features of QCD, confinement and asymptotic freedom. Confinement is the phenomenon that all observed strongly coupled particles are only seen in bound states

that are colorless, and bare quarks are never observed. Asymptotic freedom is the weakening of the strong coupling at high energies that crucially allows for perturbative QCD calculations.

1.2.1 Parton Distribution Functions

Hadron collider experiments exploit the composite nature of the proton to probe fundamental physics. As opposed to lepton colliders which use point-like particles, that are governed only by the EW matrix element, hadron colliders convolve the QCD or EW matrix element with the structure of the colliding protons. This protonic structure is described by Parton Distribution Functions (PDFs).

The composite nature of the proton was first observed definitively at SLAC in 1969 by colliding electrons into proton and neutron rich targets, in a process known as deep inelastic scattering (DIS) [15]. The strong deviations of the observed scattering curves from the elastic scattering expectation, see Figure 1.3, indicated that the proton does not have a point-like structure. Initially, this structure was parameterized by empirical form factors, but as the theory of QCD further developed, the point-like constituents of the proton were instead associated with the quarks; the form factors were then related to structure functions that accounted for the distributions of the quarks inside of the protons. At energies that probe the point-like proton constituents, DIS can be conceptualized at LO as a single photon exchange of the impinging electron and one of the charged point-like constituents in the proton. The form factors are generically functions of the momentum transfer Q^2 and Bjorken x, which is Lorentz-invariant defined as $x = \frac{Q^2}{2p_p \cdot q}$ where q is the four momentum of the virtual photon exchanged and p_p is the four momentum of the nuclear target. These functions are denoted as $F_1(x, Q^2)$ and $F_2(x, Q^2)$ which describe the magnetic and electric structure of the proton in the DIS regime. Two key observed features of deep inelastic scattering, scaling and the Callan-Gross relation, confirm its relation to the quark model. Scaling refers to the sole dependence of the structure functions on the x variable, $F(x, Q^2) = F(x)$, which indicates that the proton constituents are point-like. The Callan-Gross relation relates the electric and magnetic components of the structure functions, $F_2(x) = 2xF_1(x)$, which is characteristic of a substructure composed of spin 1/2 particles. Furthermore, once the PDFs are generalized beyond the DIS regime, the variable x can be understood to represent the fraction of the proton's momentum carried by the struck quark.

Once PDFs are measured, it is possible to then apply them to a hadron collider environment. The physical observable in hadron collider experiments is often a cross section, σ_{obs}. This quantity generically contains a high-energy interaction with high Q^2, known as the hard scatter, that is calculable in perturbative QCD or as an Electroweak (EW) process, and non-perturbative components related to the proton PDFs and other non-perturbative QCD effects. Separate from the hard scatter interaction is the underlying event, which describes the low-energy hadronic activity from protonic constituents that do not participate in the hard scatter. The ability to theoretically calculate these high- and low-energy interactions separately facilitates comparison to experimental determinations of the cross section. In this process, called "colinear factorization," the perturbative piece can then be computed

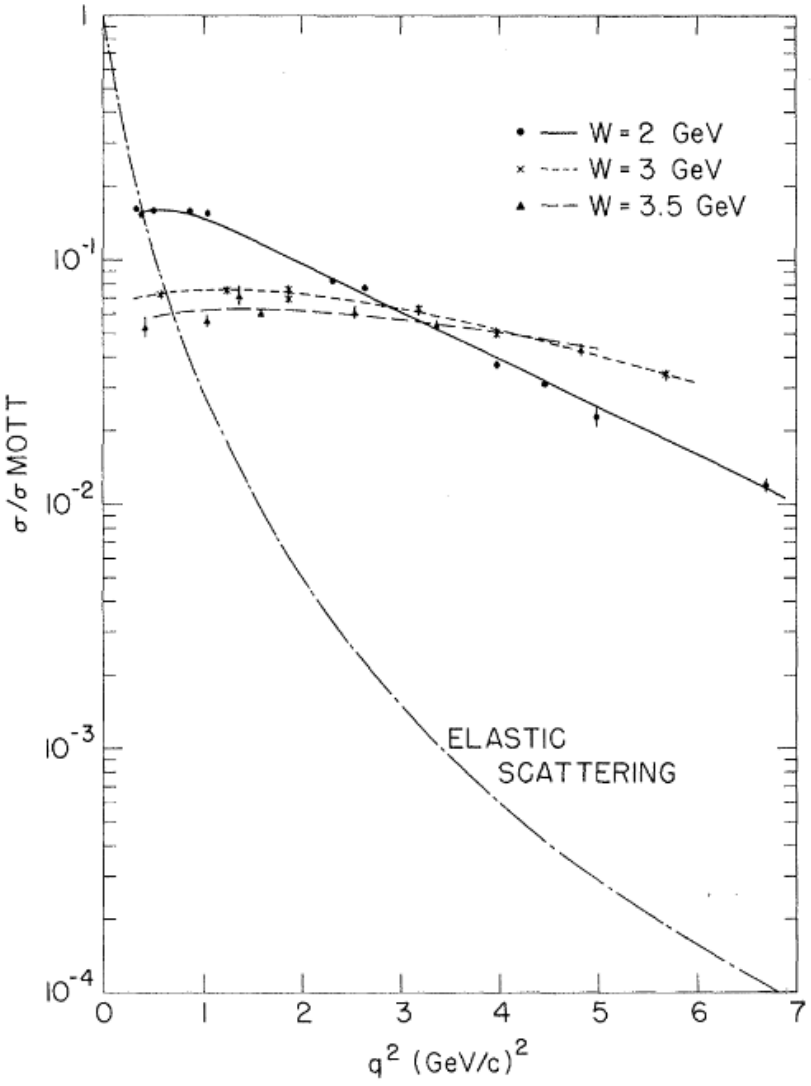

Figure 1.3: Scattering curves from DIS experiments at SLAC spanning various momentum transfers [15] are shown and compared to an elastic scattering curve. The notable deviation from the elastic prediction established definitively the composite nature of the proton.

directly and the PDF can be estimated from data-driven methods. This can be shown as the following relation:

$$\sigma_{obs} = \int dx_1 dx_2 \sigma_{HS} F_1(x, Q^2) F_2(x, Q^2) \tag{1.2}$$

Thus, beyond their intrinsic interest as objects of study in QCD, knowledge of the PDFs is fundamental to understanding results from hadron collider experiments.

PDFs are determined from a global fit to data drawn from a range of experimental inputs [16] [17]. The largest set of experimental inputs come from DIS results, including those made at HERA, as well as hadron collider results from the Tevatron and the LHC. Illustrative examples from the a modern PDF set, MSHT20, for two values of Q^2 can be seen in Figure 1.4. The proton's structure here becomes particularly clear given the presence of the valence u and d quarks, and the high fraction of gluons at low values of x. For the presence of heavy quarks, in particular b quarks, two schemes can be used. The four-flavor scheme allows b quarks to be produced only via gluon splitting from the initial state, while the five-flavor scheme allows for the presence of a massless b quark to be included in the proton constituents. Of particular interest in this thesis is the fraction of strange and anti-strange quarks in the proton PDF; refer to Section 2.1 for more detail.

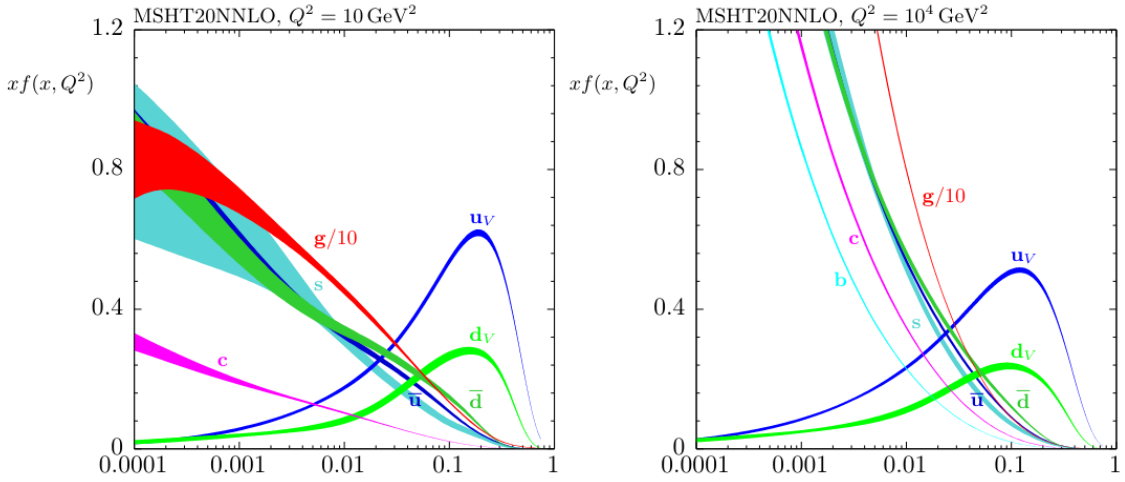

Figure 1.4: PDFs for two values of Q^2, as a function of Bjorken-x from the MSHT20 PDF set [17]. The distributions are shown with 68% uncertainty confidence bands.

1.2.2 Perturbative and Non-Perturbative QCD Interactions

Once the initial conditions of a QCD interaction are calculated via an understanding of the hard scatter interaction and the PDFs modeling the initial state, further modeling is required for the QCD that leads to an observable final state. The first stage in this process is known

as parton showering, which perturbative describe the radiation of gluons and pair production of quarks from the strongly charged particles in the final state. Parton showering models are based on perturbative QCD calculations and tuned to correspond with experimental data. To ensure that calculations of the hard scattering interaction are consistent with the parton showering, matching and merging schemes are deployed [18] to ensure that full accuracy of the NLO calculation from the hard scatter is retained, as well as keeping the same order of accuracy (e.g. NLO) used in the hard scatter for the parton shower resummation.

Due to asymptotic freedom and confinement, the parton shower must eventually resolve into color singlet hadrons, in a process known as hadronization. For sufficiently high energy initial state quarks and gluons, this process results in the formation of hadronic jets, which are collimated groups of hadrons with momentum largely in one direction. Empirical models of hadronization include the string model and the cluster model [19]. A diagram of these two models can be seen in Figure 1.5. The former uses one dimensional color flux tubes of high energy density that are then broken into hadrons from the intense color field in the string. The cluster model splits gluons into $q\bar{q}$ pairs, which are then formed into color singlet clusters that decay isotropically into hadrons.

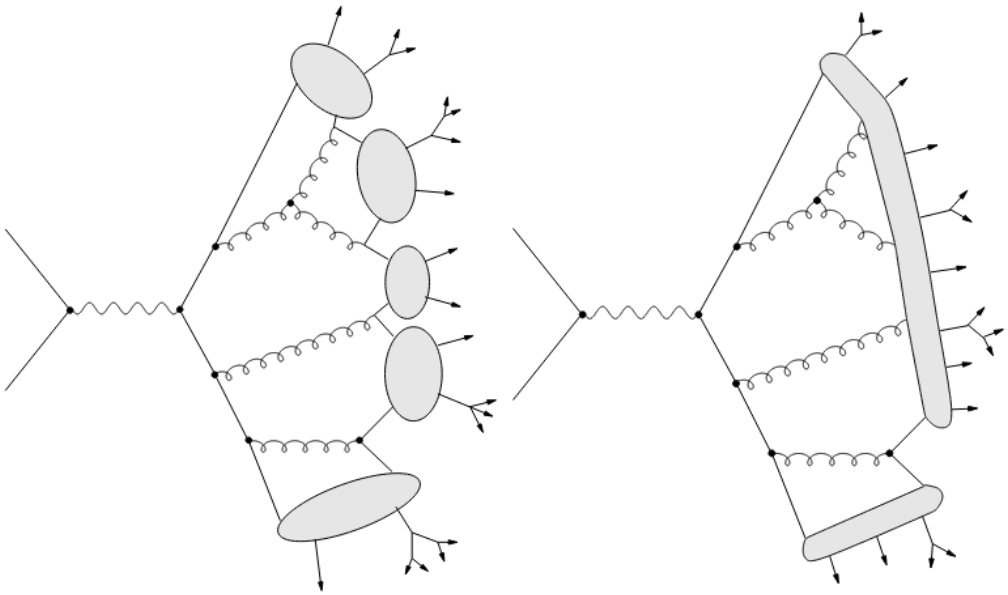

Figure 1.5: Cluster (left) and string (right) models of hadronization [19].

1.3 Electroweak Theory and the Higgs Mechanism

Within the Standard Model, the Electromagnetic and Weak forces are unified into one Electoweak sector under the symmetry $SU(2)_L \times U(1)_Y$. As was shown by the Glashow-Weinberg-Salam model, the EW Lagrangian can be written as the sum of a kinetic and potential term,

$$\mathcal{L} = |\mathcal{D}_\mu \phi|^2 + V(\phi) \tag{1.3}$$

where $\mathcal{D}_\mu$ is the covariant derivative, and ϕ is a doublet under the $SU_L(2)$ group that is symmetric under gauge transformations. To ensure the kinetic term is invariant under the same gauge transformation as ϕ, the covariant derivative takes the form,

$$\mathcal{D}_\mu = \partial_\mu - i\frac{g'}{2}B_{mu} - i\frac{g}{2}W^j_{mu}\sigma^j \tag{1.4}$$

where B is the field associated with the hypercharge Y, W^j is the field associated with $SU(2)_L$, and σ_j are the standard Pauli matrices. With appropriate substitutions, the Langrangian can be rewritten as

$$\mathcal{L} = |\partial_\mu \phi|^2 + \frac{g^2 + g'^2}{2} Z_\mu Z^\mu |\phi|^2 + \frac{g^2}{2} W^-_\mu W^{\mu +} |\phi|^2 + V(\phi) \tag{1.5}$$

which contains the kinetic term, the standard W and Z bosons as well as the potential term.

The EW potential term is where the Higgs boson enters the SM. The potential can be written as,

$$V(\phi) = -\mu^2 |\phi|^2 + \frac{\lambda}{2}|\phi|^4. \tag{1.6}$$

When the parameter $\mu^2 > 0$, the potential has a local minimum at $\sqrt{\frac{\mu^2}{\lambda}}$. The scalar doublet ϕ can be written as a small perturbation around this minimum which manifests as the physical Higgs boson. Further analysis of the EW Lagrangian shows that the W and Z boson masses arise from their interaction with the Higgs field. Additionally, the Higgs field interaction with the fermions leads to a kinetic term giving rise to the fermion masses.

Chapter 2

Phenomenology of $W + D$ Production

The structure of the proton is described by its Parton Distribution Function, introduced in Section 1.2.1. Modern PDF sets are composed of a variety of measurements included in a global fit, and the uncertainty for different constituents of the proton depends on which measurements are included in those fits. The fraction of strange quarks inside of the proton, as well as the relative contribution of s vs. $\bar{s}$, are quantities that are less constrained than for the other light quarks, and are sensitive to constraint by target measurement of initial state strange quarks in the proton. This chapter gives an overview of strange PDF sensitive measurements, with a particular focus on measurements that are in tension, and hadron collider results.

2.1 Strangeness in the Proton

The nature of the strange quark's interactions enables several types of measurements to be used as direct probes of its contribution to the total PDF [20][21][22][23]. This direct probe is necessary due to the larger uncertainties on the strange PDF than that of the other light quarks. Due to the non-perturbative nature of PDFs, it is not possible at the present time to definitively answer questions about protonic strangeness from first principles. There are two quantities in particular, that have various theoretical arguments for their values, but are ultimately experimental questions. First, the expectation that the strange and anti-strange contributions ought to be symmetric, and second, the expected ratio of the strangeness to the other light flavors in the proton, parameterized as $R_s = (s + \bar{s})/(\bar{u} + \bar{d})$. If the s, u, and d quark masses are neglected, they behave under a, distinct from QCD, SU(3) symmetry. The proton contains three "valence" quarks, two up and one down, that are always present, in addition to "sea" quarks that are created from gluon splitting into $q\bar{q}$ pairs inside of the proton. If the uds SU(3) symmetry was perfect, the expectation would be that the three light quarks would be present in equal measure, excepting the valence quarks. The expected symmetry of $s\bar{s}$ in the proton has a expectation that it should always be near zero, since the conditions of producing a the quark or antiquark should naively be identical. For the

expectation of production of the *uds* quarks, mass effects should fully explain how much strangeness ought to be seen in the proton, relative to up and down quarks. Note the antiup and antidown quarks are used for the comparison in order neglect the effects from the valence quarks. Ultimately, neither of the simple symmetry arguments fully explain the observed experimental results. In particular, neutrino nucleon scattering results indicate that protonic strangeness is largely suppressed at low x, with $R_s \approx 0.5$ for $Q = 1.6$ and $x = 0.023$, whereas hadron collider results show strangeness as somewhat less suppressed. These two categories of measurements are discussed below.

One direct probe of protonic strangeness is to look for muon neutrinos interacting with a fixed target nucleon, producing a muon and a charm hadron that decays semileptonically to a final state containing a muon,

$$\nu_\mu + N \to \mu^- + c + X \to \mu^- + \mu^+ + \nu_\mu + X \tag{2.1}$$

This process leaves a distinctive dimuon signature that has a relatively low background. Experiments searching for this signature count these events using muon neutrino beams that come from beamline experiments at CERN [24][25] and Fermilab [26][27]. A diagram of the process of interest can be seen in Figure 2.1. These experiments are able to directly probe the strange sea, and some of them probe the asymmetries between the strange quark and its charge conjugate. Early results [26] limited by uncertainties did not observe significant differences in the $s - \bar{s}$ sea, but later results from the NuTeV [27] collaboration measured an asymmetry of $\alpha = 0.02$ at a significance of 1.6σ. With respect to the suppression of the strange quark, the NOMAD experiment [25] shows results that indicate a suppression, integrated over x at $Q^2 = 20\,\mathrm{GeV}^2$ of $\kappa_s = 0.591 \pm 0.019$ While this result is difficult to compare directly to LHC results due to differing values of Q^2, discussed in Section 2.1.1, the integrated results are inconsistent with unsuppressed strangeness at low x.

2.1.1 Protonic Strangeness at the LHC

The other major source of protonic strangeness measurements comes from the ATLAS and CMS experiments. The measurements of interest are of two types, generic W and Z produced in combination with hadronic jets ($V+$jets) [21][28][23][29], and the specific process of looking at W with associated charm quarks [30][31][32]. The first of these processes probes the strange PDF via ratios of production of W and Z that are sensitive to the strange sea. In order to assess that impact, the results from ATLAS or CMS are combined with DIS results from HERA, and a PDF fit is performed. While CMS did not combine its precision $V+$jets measurements with DIS results to estimate the protonic strangeness, results and interpretations from ATLAS in 2016 [21], 2020 [22], and 2021 [23] sought to extract these contributions. A plot of R_s from the early ATLAS results [22] can be seen in Figure 2.2, showing unsuppressed strangeness at low x, and suppressed strangeness at high x. These results, ATLASepWZ16(20), had large uncertainties at high x, while the inclusion of $V+$jets, ATLASepWZVjet20, removes that possibility from the PDF fit, requiring suppressed

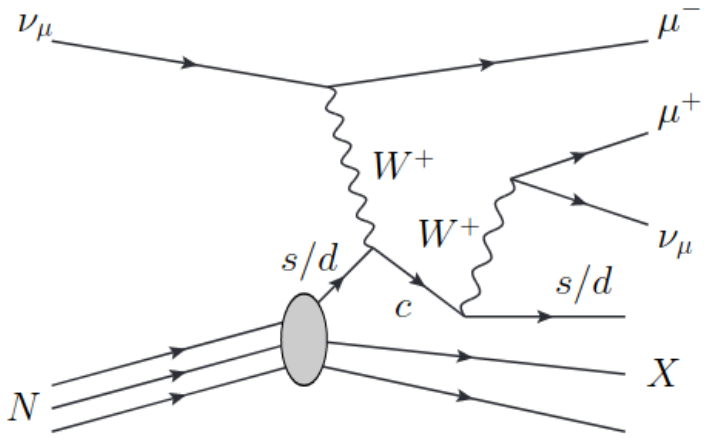

Figure 2.1: Feynman diagram of dimuon production in muon neutrino-nucleon scattering experiments [25].

strangeness in that x region. The most recent results, ATLASpdf21, [23], incorporating further data sets in the fit, and correlating relevant uncertainties between the data sets, further suppresses strangeness at low x values. Results at $Q^2 = 1.9\,\mathrm{GeV}^2$ can be seen in Figure 2.3 and comparison to various PDF sets for $x = 0.023$ and $Q^2 = 1.9\,\mathrm{GeV}^2$ can be seen in Figure 2.4.

In contrast to the ATLASepWZVjet20 results, other combinations of measurements not produced directly by ATLAS or CMS, but including ATLAS and CMS data, have shown that strangeness is more suppressed in the low x region. A combination [20] including the ATLAS and CMS W and Z measurements, ATLAS and CMS c+jets measurements, and NOMAD neutrino results extracts a combined fit of the strange sea to determine its suppression. These results do not include the most up-to-date ATLASpdf21 results in the combination. This combination showed a less suppressed strange sea at $x = 0.023$ and PDFs computed at $Q^2 = 1.9\,\mathrm{GeV}^2$, as can be seen in Figure 2.5. While these are not computed at exactly the scale of the comparable ATLAS results, the ratios of PDFs evolve sufficiently slowly such that there is a slight disagreement in the central value of the suppression of the strange quark near this scale, although it is contained with slightly greater than 1σ of the uncertainty bands. The more measurements from ATLASpdf21 show a better agreement with this combination, indicating a convergence of results from various sources towards strangeness that is strongly suppressed at high x and mildly suppressed at low x.

The final category of measurement that can effectively probe strangeness in the proton is $g + s \to W + c$ production. These events provide a direct probe of the strange sea, analogous to the $\nu_\mu + N \to 2\mu + \nu_\mu + c + X$. The LO diagrams for this process are shown in Figure 2.6, where it can be seen that an antistrange (or its charge conjugate) in the initial state leads to the presence of anticharm in the final state. This signal has only one irreducible background

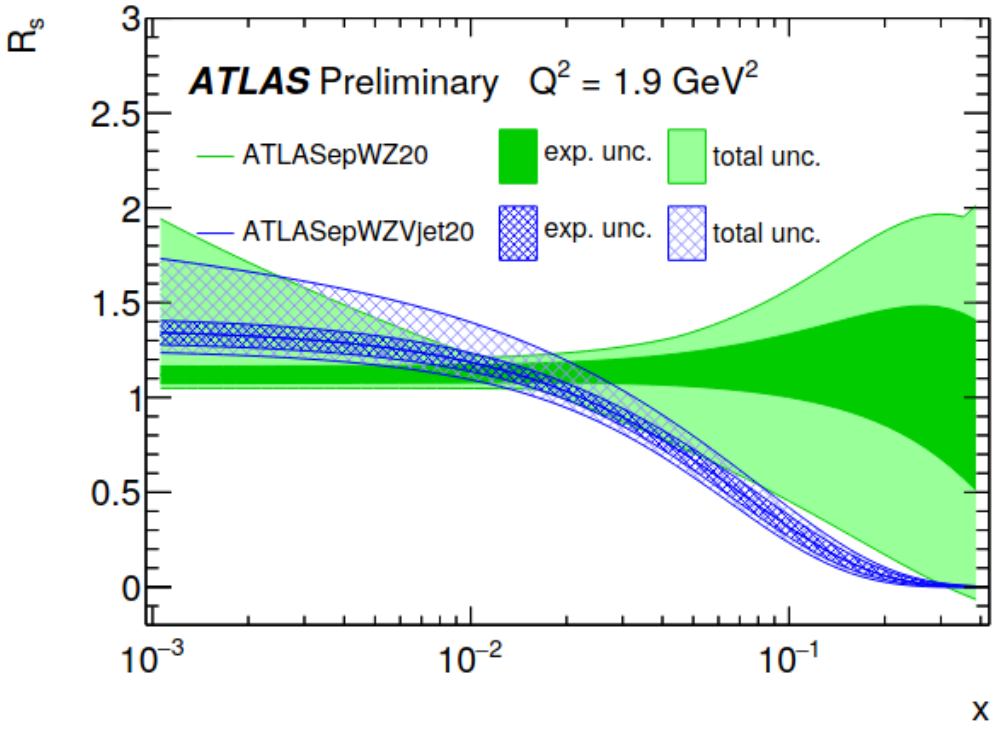

Figure 2.2: R_s vs. x for the ATLASepWZVjet20 and ATLASepWZ20 PDF sets. In particular, the reduced uncertainty in the fit rule out the unsuppressed strangeness at high x.

at LO, namely the Cabibbo-suppressed $g + d \to W + c$, but this is well understood through the contribution to the total production from the CKM matrix element $|V_{cd}|$. In this final state, the strange quark initial state is approximately 90% of the $W + c$ production [33], whereas the down initial state is the remaining 10%. The presence of valence down quarks in the proton breaks the symmetry between the charges of the W boson at the level of near 1%. The NLO contributions to this signal include the one loop corrections to $g + s \to W + c$, as well as $g + g \to s + W + c$, $g + s \to q + W + c$, and $q + q' \to sWc$. The other CKM matrix angle contribution, $|V_{bc}|$, is negligible.

The $W + c$ production at hadron colliders can be measured with two statistically independent methods of identifying the charm quark, with charm quark tagging or with charm hadron reconstruction. Charm quark tagging [34], is the process of identifying jets which originate from charm quarks, exploiting the properties of heavy flavor quarks. More detail on flavor tagging in ATLAS is described in Section 5.6. The second method seeks to directly identify charmed hadrons, and use those reconstructed hadrons to identify the presence of charm quarks.

$W + c$ measurements utilizing charm tagging have been made by CMS [32] and ATLAS

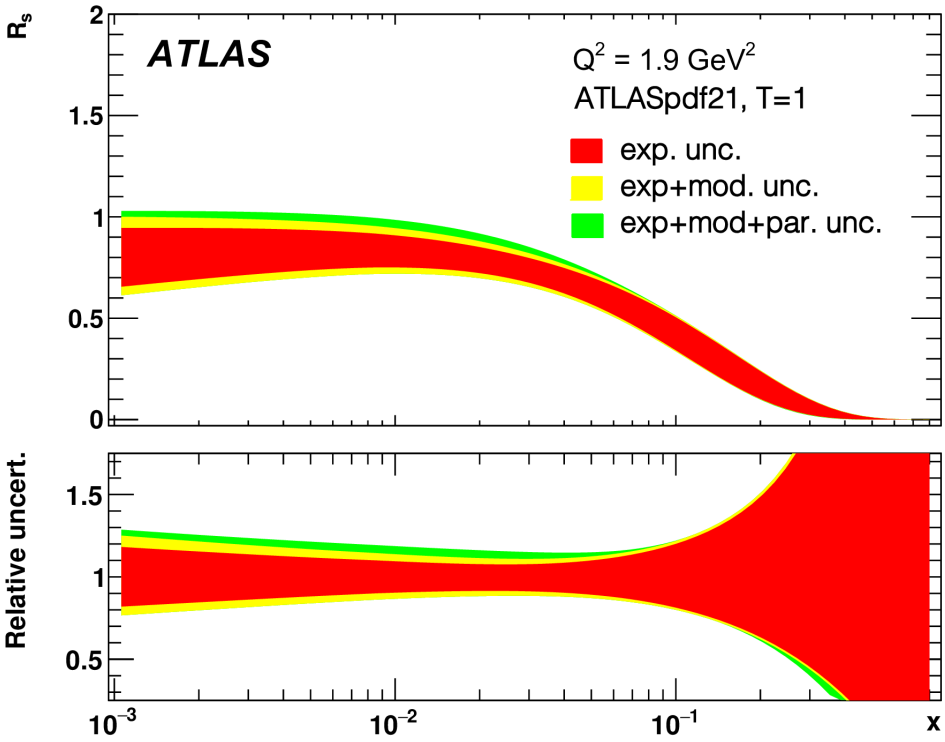

Figure 2.3: R_s vs. x for the ATLASpdf21, with associated relative uncertainty. These results show a slight suppression at low x, which is more in line with other combinations [23].

[30]. These results are not generally directly applied to computations of quantities related to the strange PDF, nor are they used in combination results [20] due to the fact that the correction from the hadronic jet to charm quark has significant uncertainties.

$W + c$ measurements using direct charm meson reconstruction ($W + D^{(*)}$) have been made at CMS [35] [31] and, as a central topic of this thesis, ATLAS [36] [37][1]. For this class of results, its impact on the protonic strangeness is discussed in Section 2.2.

Understanding both the strange asymmetry in the proton and the ratio of strange to light quarks is a dynamic area of research still being improved by measurements at the LHC. Modern combinations are beginning to converge towards fully suppressed strangeness at high x, and less suppressed strangeness at low x. For measurements made in the LHC era, using a larger combination of data-sets from sources that are sensitive to the strange PDF leads to a convergence of R_s distributions. Beyond answering questions on the central value of R_s, improved uncertainty modeling for the strange quark will reduce uncertainties for other measurements that are particularly sensitive to PDFs, including the W mass [38] and potential future measurements of the Higgs boson [39].

[1]Results in this thesis overlap with the referenced paper

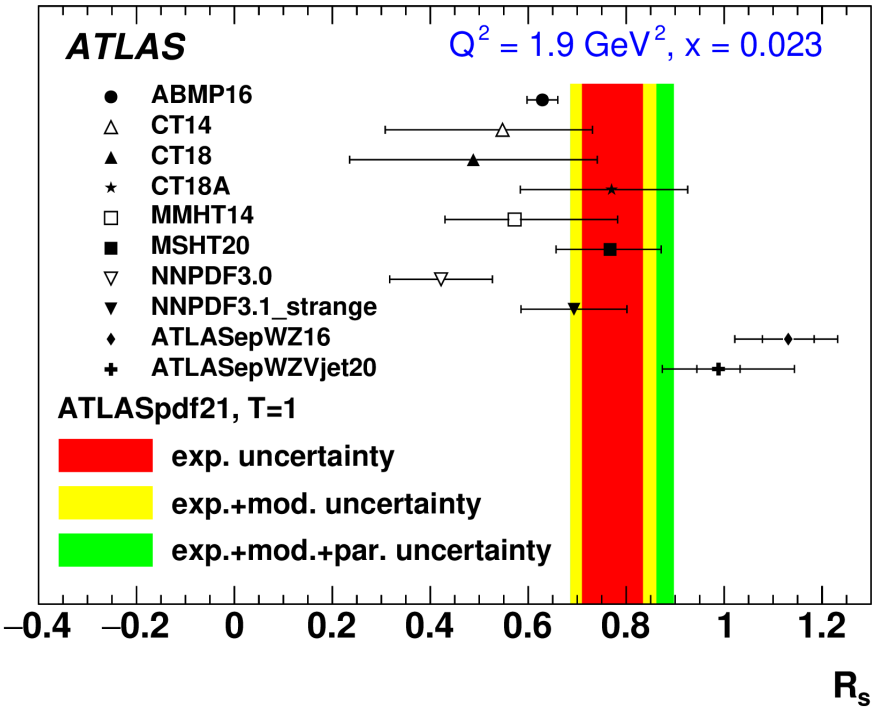

Figure 2.4: R_s at $x = 0.023$ and $Q^2 = 1.9\,\mathrm{GeV}^2$, showing a central value of 0.8. This result is consistent with the most up-to-date PDF sets, CT18A, MSHT20 and NNPDF3.1_strange, which include the ATLAS W and Z data sets [23].

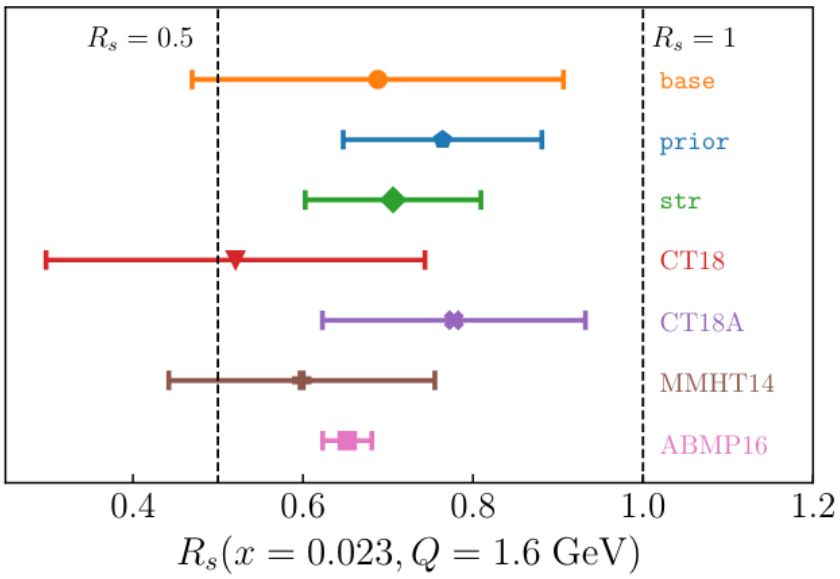

Figure 2.5: Combination from [20], showing values of R_s at $x = 0.023$ and $Q = 1.6\,\text{GeV}$ `base` , `prior`, and `str` show fits from the analysis, while the CT18, CT18A, MMHT14, and ABMP16 show the same quantity for their respective PDF set.

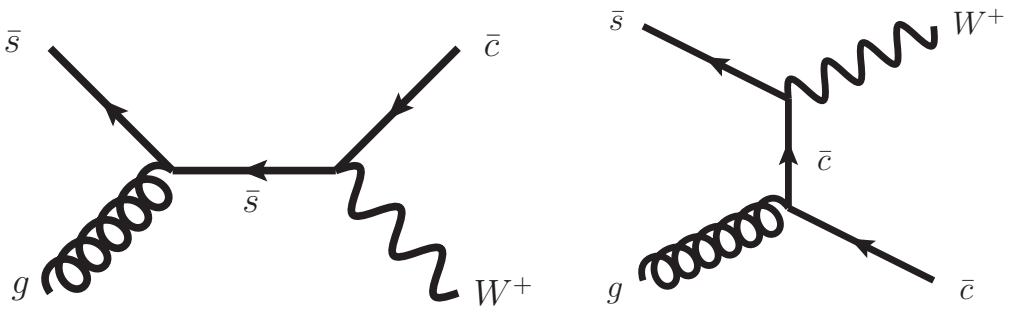

Figure 2.6: The leading order diagrams for $W^+ + \bar{c}$ production in the s and t channels.

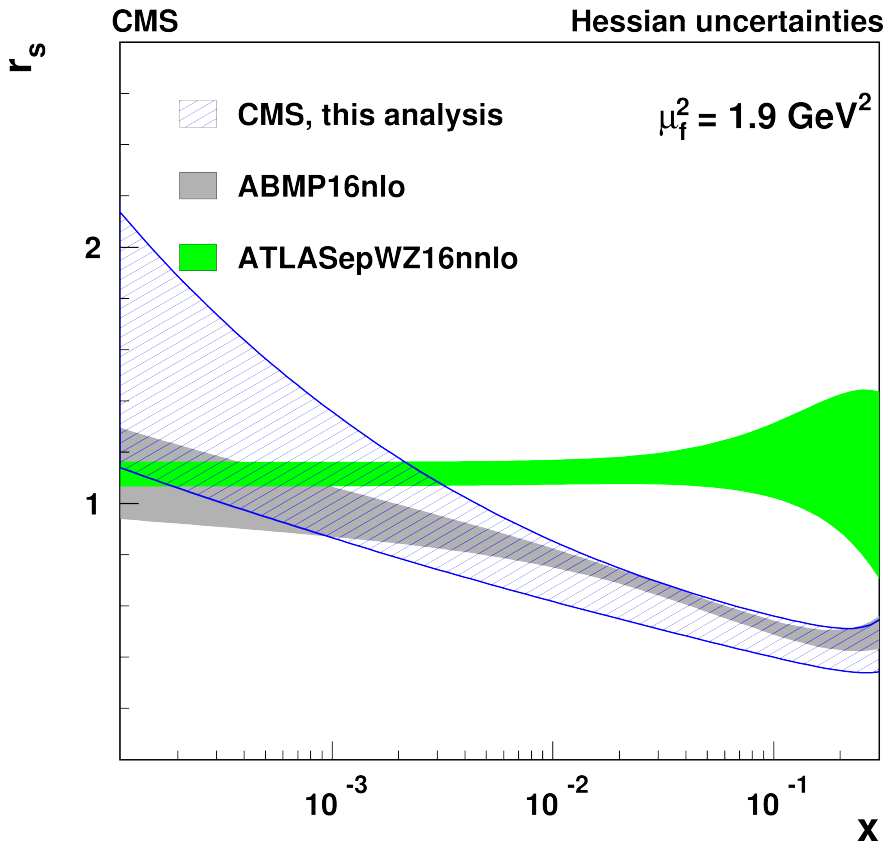

Figure 2.7: CMS $W + D^*$ results showing the impact of the analysis with strangeness suppression at high x and unsuppressed strangeness at low x. These results are a combination with other results at the scale of $Q^2 = 1.9\,\mathrm{GeV}^2$ [31].

2.2 $W + D^{(*)}$ Production

$W + D^{(*)}$ measurements have the potential to improve understanding of the strange quark PDF. They were first proposed in the 1990s [40, 41] and first observed at the Tevatron [9]. Direct extraction of the strange PDF in the $W + D$ is complicated by the effect of the hadronizing charm quark that must be inferred from the reconstructed $D^{(*)}$. The ATLAS results presented in this thesis do not interpolate from the measured $W + D^{(*)}$ cross section to the $W + c$ cross section of interest, due to the lack of an appropriate NLO or NNLO calculation that includes the fragmentation function with which to make comparisons.

The CMS results measure the impact of the $W + D^*$ on the strange PDF by targeting a charm quark that hadronizes to a D^* meson and then decays to a particular decay mode, $D^* \to D^0\pi \to (K\pi)\pi$. When combined with DIS results, the CMS analysis found that R_s was suppressed at high x, consistent with other updated results, and unsuppressed at low x, which is inconsistent with other updated results, see Figure 2.7. Note in Figure 2.7 the tension at high values of x between CMS and ATLAS is removed when more recent ATLAS results are included. The low x region has a large uncertainty, and differences in the strategy of unfolding the particle to the parton level make it difficult to directly compare with ATLAS results.

An important development in the theoretical study of $W+c$ production is the publication of the first NNLO calculation [42] of the process. This calculation includes an off-shell treatment of the W and is performed in a five flavor scheme using the flavored k_T algorithm [43] and neglecting c-quark finite mass effects. At present, non-diagonal CKM matrix elements are included only for the LO diagrams. Such NNLO calculations should ultimately allow for the incorporation of $W + c$ measurements into NNLO PDF fits. However, before this is possible, $W + c$-jet measurements must be unfolded to the flavored k_T scheme. Alternatively, in the case of $W + D^{(*)}$ measurements, the charm fragmentation function could be incorporated into theory predictions using methods pioneered in Ref. [44]. In the absence of directly incorporating the charm fragmentation into the calculation, experimental results cannot be directly compared the theory predictions.

There are existing NLO calculations using the MadGraph5_aMC@NLO [45] framework that are better suited for comparison to experimental results. These NLO plus parton shower calculations use multiple modern PDFs and provide a theoretical prediction that is able to be compared to measurements of the $W + D$ process. In the case of MadGraph5_aMC@NLO, such comparisons can be made using either NLO or NNLO PDF sets as input. To account for uncertainties related to the parton showering matching and merging, an additional calculation using the Powhel event generator make predictions for $W + D^{(*)}$ production at NLO in the Powheg NLO plus parton shower matching framework. These calculations include finite charm-quark mass in the hard-scattering matrix elements, treatment of the W as off-shell, and include non-diagonal CKM matrix effects [46]. Powhel calculations are possible only for NLO PDF sets. Theoretical work in this direction is ongoing, with expectations that improvements in the calculations will help connect $W + D^{(*)}$ results to modern PDF fits.

In this thesis, events in which the W decays to an electron or a muon (and the associated neutrino) are studied and the presence of the charm quark is detected through explicit charm hadron reconstruction. Events in which the W decays to τ are treated as background and the term lepton will be used to refer to electrons and muons collectively. The production of three different charm hadrons, D^+, D^*, and D_s, collectively referred to as $D^{(*)}$, including their charge conjugates, are studied using the following decay modes:

- $D^+ \to K\pi\pi$
- $D^{*+} \to D^0\pi \to K\pi\pi$
- $D_s \to \phi\pi \to (KK)\pi$
- $D^+ \to \phi\pi \to (KK)\pi$

The $W + D^{(*)}$ signal events can be measured through a statistical fit to the reconstructed D meson mass distribution, where the $D^{(*)}$ are reconstructed by using final states with charged particles that leave a reconstructed trajectory (track, see Section 5.1). Charm and bottom hadrons, collectively known as heavy flavor, have properties which allow their decay to be separated from the primary vertex in a pp collision. In particular, weakly decaying, heavy flavor hadrons [14] are long lived in the ATLAS detector, with a lifetime of $c\tau \approx 100$ to $300\,\mu$m. Thus, charm hadron decays can be reconstructed as a secondary vertex (SV), measurably separated from the primary pp vertex (PV). Additionally, charm hadron decays tend to be isolated, where a true $D^{(*)}$ decay accounts for the majority of energy in some radius around its momentum vector.

In addition to displaced vertices and isolation, charm hadron decays in the selected modes have distinguishing topological features that allow them to be effectively reconstructed. The D^+ hadron is the longest lived weakly decaying charm, and is more likely to be reconstructed as its vertices are further displaced from the PV. When it decays to three charged particles with a sufficiently high branching ratio, $D^+ \to K\pi\pi$ occurs in $\approx 10\%$ of D^+ mesons, this mode can be easily identified by its peaking mass distribution. The $D^{*+} \to D^0\pi \to K\pi\pi$ mode exploits the narrow mass difference between the D^* and D^0 modes. The $D^0\pi \to (K\pi)\pi$ can be reconstructed as a SV, while the D^* can be associated with it by incorporating an additional charged particle as a soft pion, constrained by the narrow mass difference to have a small momentum in the D^* rest frame. Thus by measuring the difference between the D^* and D^0 masses, the signal is cleanly separated from backgrounds. Lastly, for both the $D_s \to \phi\pi \to (KK)\pi$ and $D^+ \to \phi\pi \to (KK)\pi$ decays, the presence of an intermediate ϕ meson with a narrow mass peak allows for additional separation power. Since the D_s and D^+ in this mode have the same final state, both signals can be extracted simultaneously.

The main backgrounds for the $W + D^{(*)}$ process are W in conjunction with one or more hadronic jets, $W+$jets, and production of pairs of top quarks, $t\bar{t}$. For $W+$jets, only about 10% of events contain a charm quark in the final state. The remaining 90% of events contribute to the what is known as the "combinatorial background," whereby a false $D^{(*)}$ vertex is

reconstructed through an incorrect combination of charge particle tracks. This combinatorial background is due to the lack of explicit Particle Identification in the ATLAS detector, and thus the species of each decay product must be hypothesized, e.g. in the $D^+ \to K\pi\pi$ decay for three charged particles, the oppositely charged particle is assigned the kaon mass. In addition to the combinatorial background, background events originate from $W+$jets that contain a charm quark, including charm from gluon splitting produced in association with a W boson, the production of other species of $D^{(*)}$ hadrons in association with W bosons, and other $W + D^{(*)}$ decay modes. For $t\bar{t}$ events, the background originates from a semileptonic top decay, in association with either a bottom hadron cascading to a charm hadron, or a $W \to cs$ decay. There are several other smaller backgrounds, originating from Z production and diboson production, which are subdominant.

A key feature of utilizing $W + D^{(*)}$ production to probe $W + c$ relates to the reconstruction of the charm quark at the level of the hard scatter. As shown in Figure 2.6, at LO in $W + c$ production, the W boson and the charm quark always have opposite sign, i.e. either $W^+ + \bar{c}$ or $W^- + c$. For those diagrams where one of the initial state partons is an s-(anti-)quark, this charge correlation remains at NLO and NNLO [42]. However, many of the backgrounds have a similar number of events with the W boson having the opposite charge of the $D^{(*)}$ (OS) or the two particles having the same sign charge (SS), whereas the signal is always in the OS category. In particular, gluon splitting always produces an oppositely charged pair of charm quarks, and $t\bar{t}$ events where the charm originates from a bottom quark is statistically equally likely to originate from the antibottom, in both cases leading to equal contributions of OS and SS events. This is exploited in $W + D^{(*)}$ measurements by performing the signal extraction separately in the OS and SS channel, and taking the difference between the two (OS-SS) as the signal region. This serves to extrapolate the background estimation from the SS region into the OS region. There are several backgrounds that are expected to have residual components after OS-SS subtraction. $W + D^{(*)}$ events, where the D meson is partially reconstructed (or of a different species or decay mode) leads to events that are preferentially OS. In addition, $t\bar{t}$ decays include a final state where one W from top decays to a lepton, and the other W from top decays to a charm and strange pair. These decays are shown at leading order in Figure 2.8, where the OS correlation between the two W, and hence the charm and lepton, can be seen.

This thesis presents results from the most recent ATLAS $W + D^{(*)}$ measurement in two $D^{(*)}$ decay channels, $D^+ \to K\pi\pi$ and $D^* \to D^0\pi \to (K\pi)\pi$, as well as ongoing studies to measure additional $D^{(*)}$ decay channels, $D_s \to \phi\pi \to (KK)\pi$ and $D^+ \to \phi\pi \to (KK)\pi$. These analyses aim to improve PDF fits by incorporating $W + D^{(*)}$ measurements into global combinations. This requires as an input NNLO calculations of $W + c$ that include the effect of hadronization to the $D^{(*)}$ level. Measurements of the $W + D^+$ and $W + D^*$ cross sections presented here have been published in Ref. [37]. Measurements of the $W + D_s$ cross section are as yet unpublished.

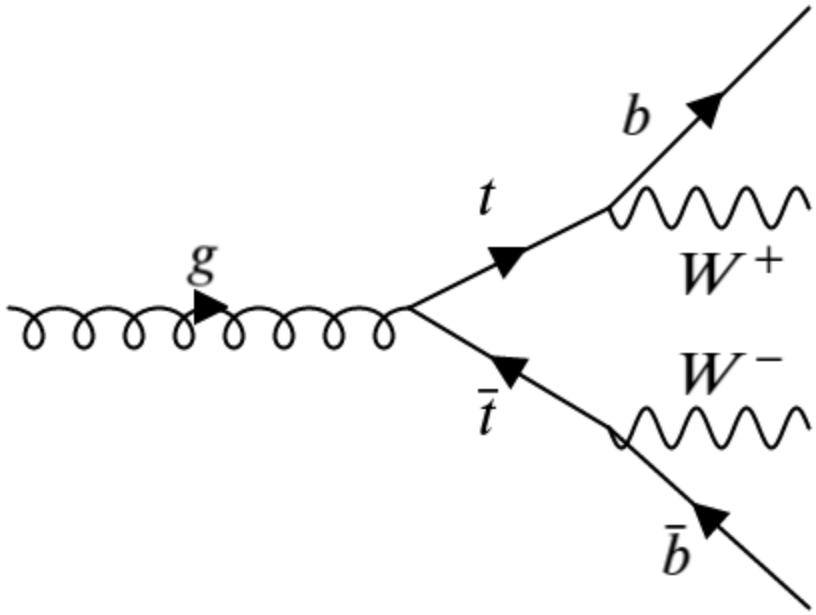

Figure 2.8: $t\bar{t}$ decay from gluon splitting. This process occurs as a background in the $W + c$ process as it can produce both a lepton from a W decay and charm quark from a B hadron cascade decay or from a $W \to cs$.

2.3 Weakly Decaying Charm Production Fractions

The rate of fragmentation of any particular open charm hadron (hadrons with a single charm quark) are related to one another via unitarity. These rates are known as production fractions. Predictions for the cross sections of $W + D$ production to a given D species depend on these production fractions. The modern theoretical and experimental framework for determination of the charm production fractions [47] combines measurements from a variety of sources, typically e^+e^- and $e^{\pm}p$ collision results, under the assumption that such measured relative rates are universal. A summary plot of such measurements is shown in Figure 2.9, where the results can be seen under the unitarity constraint that the sum of the production cross section for all weakly decaying open charm is $S = 1$. While there are multiple charm baryons, only the Λ_c is has been measured to high precision in multiple experiments, and the other baryonic states are assumed to be produced according to their relative production for equivalent light states when not measured directly.

Monte Carlo simulation does not always reproduce the world average results and exhibits disagreement from one simulation to another. Ensuring that Monte Carlo generators are properly weighted when handling open charm is crucial to producing accurate results, and in this thesis is discussed in detail in Section 8.2.

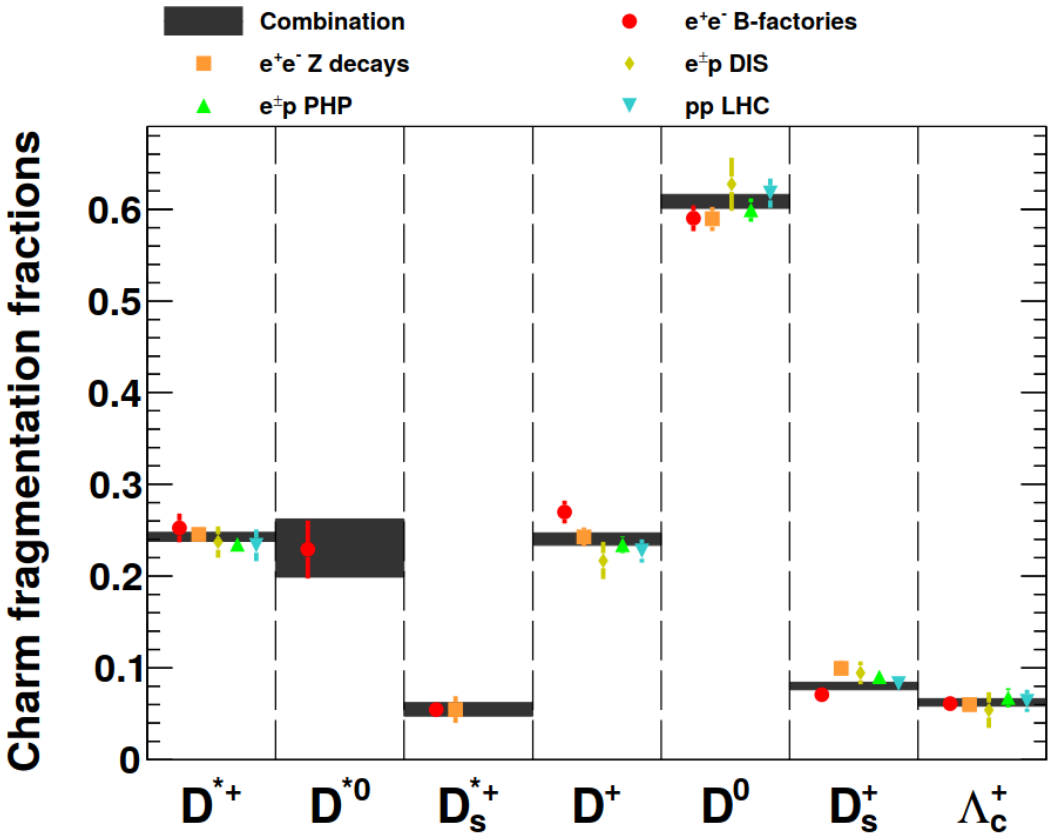

Figure 2.9: World average charm production fractions [47]

Beyond the world average, recent results from the ALICE collaboration [48] indicate that production fraction universality may not apply to hadron collider environments. In particular, as seen in Figure 2.10, ALICE suggests that charm baryon production may be enhanced at hadron colliders. These results indicate that there may be different hadronization mechanisms present in pp collisions, due to QCD effects in the hadron rich environment. The tension in these results motivates investigating whether charm production fractions can be systematically measured in ATLAS. The results from ongoing studies in this area are presented in Section 11.

This thesis presents results from both $W + D^+$ and $W + D^*$ differential cross section measurements (denoted as $W + D^{(*)}$ differential), as well as ongoing studies into $W + D^{(*)}$ in the $D_s \to \phi\pi \to (KK)\pi$ and $D^+ \to \phi\pi \to (KK)\pi$ decay channels (collectively denoted as $W + D_s$ inclusive). While these analyses share some commonalities, the differences are noted where appropriate. The goal of the differential $W + D^{(*)}$ analysis, beyond the precision cross section measurement is to ultimately be combined with theoretical predictions at the NNLO level, and integrate into global PDF fits. The $W + D^{(*)}$ results in the $D_s \to \phi\pi \to (KK)\pi$ and

$D^+ \to \phi\pi \to (KK)\pi$ channels will begin the process of a production fraction measurement at ATLAS, as well providing useful input to Monte Carlo generators including the ratio of D^+ to D_s in ATLAS which can improve simulation and have an impact on identifying hadronic jets containing charm hadrons.

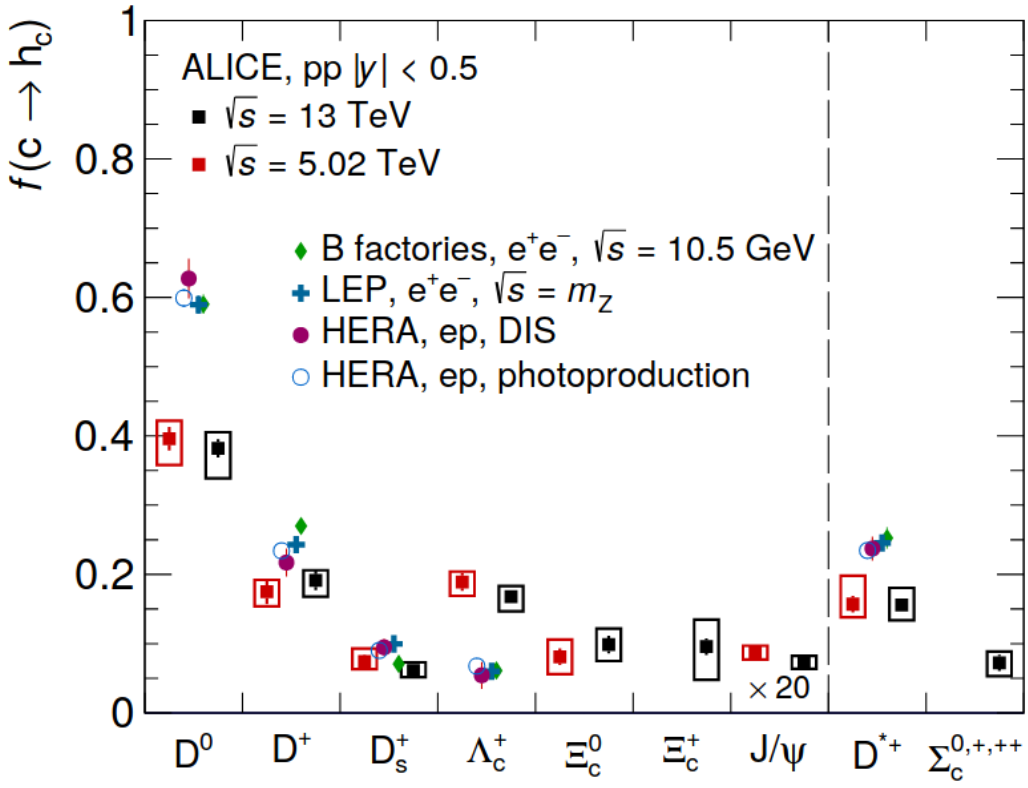

Figure 2.10: Alice charm production fractions compared to other experimental results [48]. These results show significant discrepancies from results that come from electron-proton and electron-positron experiments. These results indicate that there may be modification to the production fractions related to hadronic effects that need to be characterized by more hadron collider measurements.

Chapter 3

The LHC and the ATLAS Experiment

In the late 20th and early 21st centuries, the field of high energy particle physics has transitioned from small, single institution efforts, into massive global collaborations. No single project more embodies this global scale of physics than the Large Hadron Collider (LHC) and its associated experiments. The LHC involves participation from nearly 40 nations, cost nearly 5 billion dollars, and built multiple detectors with precision placement at the millimeter level, with components covering tens of meters in scale. This section describes both the LHC in general, as well as a particular focus on the ATLAS detector.

3.1 The Large Hadron Collider

The LHC is a 27 km circumference ring located at the *Organisation Européenne pour la Recherche Nucléaire* (CERN) site outside of Geneva, Switzerland [49] [50]. The technical design report for the LHC was released in 1994 [49] and first collisions were recorded in 2009 at $\sqrt{s} = 7\,\text{TeV}$. LHC Run 1 began with these collisions and ran through 2012. The second LHC run, and the origin of the data analyzed in this document, began in 2015 and lasted through 2018 at $\sqrt{s} = 13\,\text{TeV}$. LHC Run 3 began in 2022, and will continue for several years at $\sqrt{s} = 13.6\,\text{TeV}$.

The LHC consists of several stages in order to achieve the highest energy protons. The process begins with hydrogen gas, which has the electrons stripped away via an electric field, prior to the initial acceleration. The first accelerator stage is the Linear Accelerator 2 (LINAC2), which uses a series of RF cavities to achieve an energy of 50 GeV. As a consequence of the RF cavities, the protons change from a continuous gas into discrete groupings known as "bunches." The bunches further pass into the Synchrotron Booster (BOOSTER), Proton Synchrotron (PS), and Super Proton Synchrotron (SPS) which accelerates the protons to 1.4 GeV, 25 GeV, and 450 GeV respectively. The final stage is the LHC itself, which achieves the highest collision energies of 13 TeV in Run 2. A schematic diagram of the full complex is shown in Figure 3.1.

The LHC itself is composed of two basic sections, the first of which are straight RF

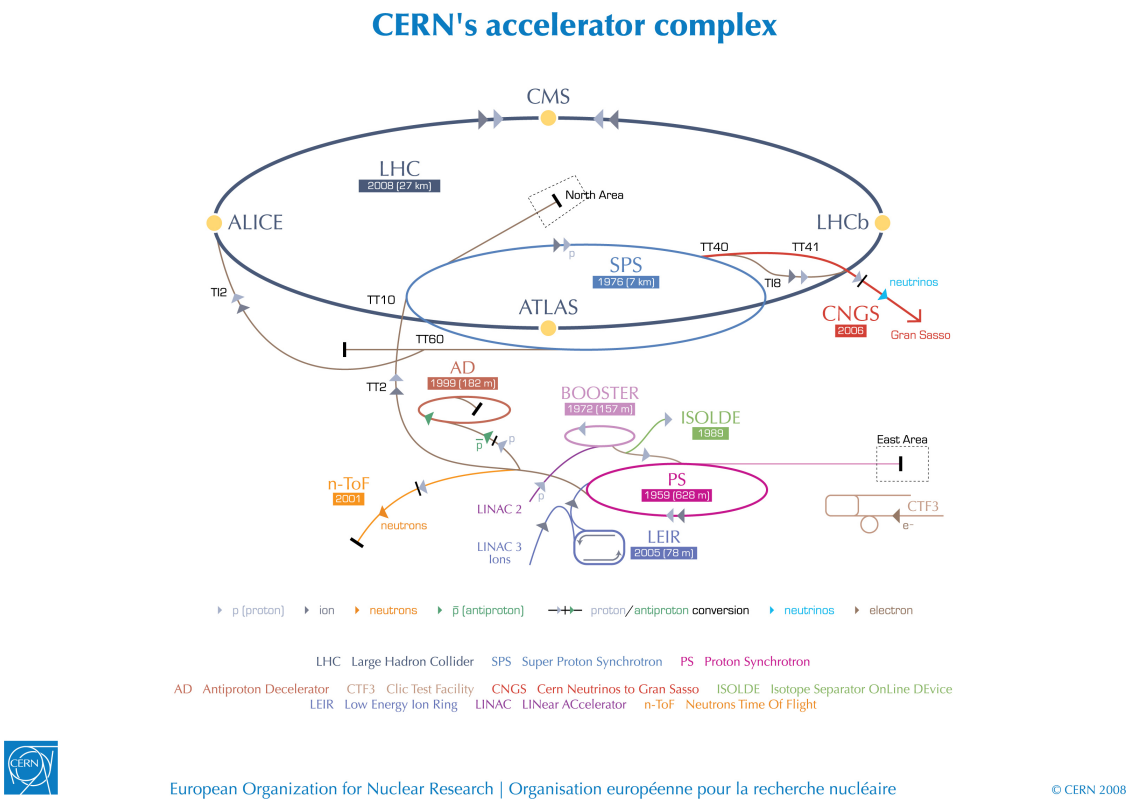

Figure 3.1: Schematic cartoon of the LHC accelerator complex showing the various stages of the collider as well as the sites of major experiments [51]

cavities for accelerating the protons to their final energies. The second sections are made of dipole magnets for bending and directing the bunches, and quadripole magnets which are used to focus the beam at the appropriate interaction points. The two general purpose LHC experiments, ATLAS and CMS, are situated opposite each other on the LHC ring, at the sites of maximum bunch intensity.

3.1.1 Luminosity

For particle physics experiments, the critical parameter provided by the collider, beyond the center of mass energy, is the luminosity. Instantaneous luminosity, $\mathcal{L}$, is the parameter that connects experimental interaction rates $\frac{dN}{dt}$, which can be measured, with cross sections, σ:

$$\frac{dN}{dt} = \sigma\mathcal{L} \tag{3.1}$$

Instantaneous luminosity can be computed from the machine parameters and can be measured using dedicated experimental setups. To compute $\mathcal{L}$ for beam experiments, it is necessary to

integrate over the expected time-dependent densities of interacting bunches [52]. In the case of Gaussian densities in all three dimensions and identical bunches, the integration simplifies significantly, and the instantaneously luminosity, considering all bunches, becomes:

$$\mathcal{L} = \frac{n_p^2 n_b f}{4\pi\sigma_x\sigma_y}. \tag{3.2}$$

The relevant parameters are number of protons in the bunches (n_p), the number of bunches (n_b), the frequency of bunch crossings (f), and the transverse width of the Gaussian distributions of protons in the bunches, ($\sigma_{x(y)}$).

While the simplistic models of luminosity give a first order understanding of the interactions in the collider, there are second order effects that arise due to corrections to the model. Two of the most significant effects are displaced beams with a crossing angle, and the hourglass effect [52]. The former is caused by beams that do not lie on the same longitudinal axis crossing at a small angle, which can be computed with a small correction to the double Guassian bunch model. The hourglass effect is due to the physical shape of the bunches, which are not uncorrelated in the transverse and longitudinal directions, but are instead denser near the interaction point.A β function describes the correlated densities and its shape is determined by a parameter β^* that characterizes this effect, and an example is shown in Figure 3.2 These effects are accounted for in luminosity calculations by analytical corrections and numerical solutions to the relevant integral over proton densities.

Luminosity at hadron colliders is measured either absolutely on an infrequent basis or relatively on a frequent basis. Absolute measurements of luminosity for the ATLAS detector are performed using a technique known as the van der Meer scan [53]. To perform the scan, experimental conditions are modified to run with fewer bunches to reduce parasitic effects from incoming and outgoing bunches, approximately zero crossing angle to reduce beam beam effects, and an increased β^* to shrink and control the size of the luminous region which reduces vertexing uncertainties. With these conditions, the one beam is moved in steps across the other which allows for the transverse profile in the x and y directions, σ_x and σ_y, to be determined via changes in the measured interaction rate. The interaction rate is measured with the LUCID2 Cerenkov detector [54].

Relative luminosity measurements are combined with the absolute measurements in order assess luminosity during the entire run period. Relatively luminosity measurements utilize both the LUCID detector, and a technique track counting. The track counting algorithm uses the mean number of reconstructed charge particle tracks, averaged over a luminosity block, in order to estimate the visible interaction rate. Measurements of luminosity over the entire run period use primarily a combination of the LUCID2 detector measurements, which are corrected for the high luminosity physics running conditions with the track counting algorithm.

The ultimate quantity of interest related to luminosity is the time integrated luminosity or simply integrated luminosity, $\mathcal{L}_{int}$. This number is reported in units of fb^{-1}, and is a direct measurement of the total data available for physics analysis. The final measured luminosity for the ATLAS experiment Run 2 was $(140.1 \pm 1.2)\,\text{fb}^{-1}$ [53].

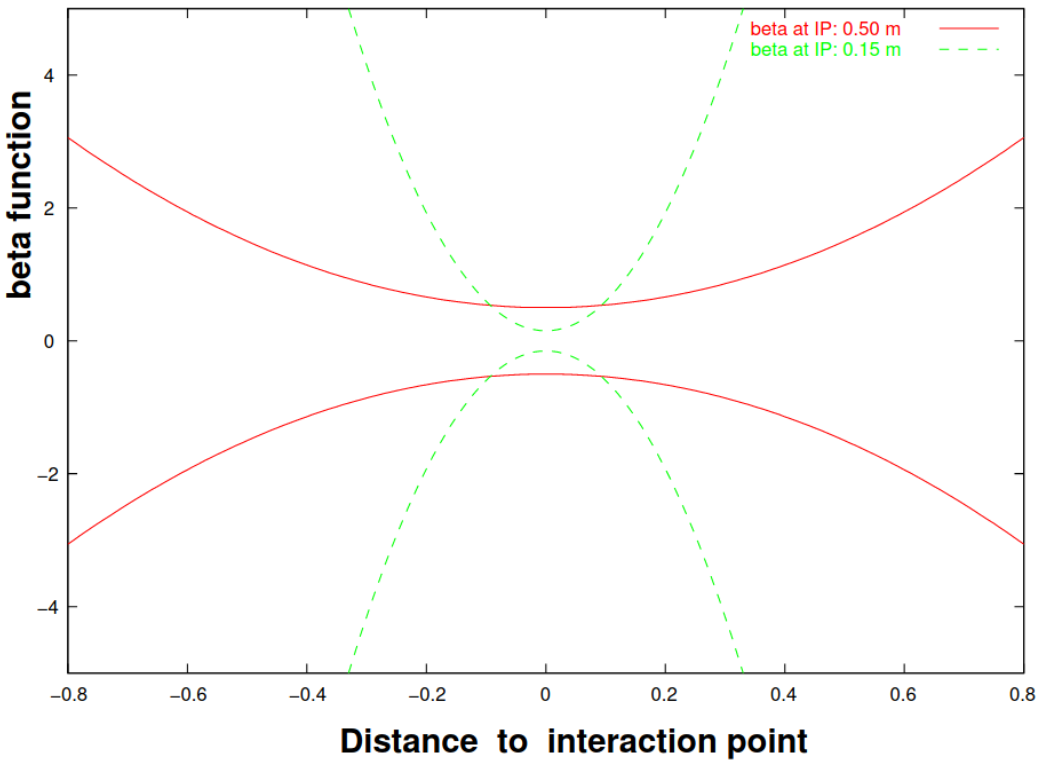

Figure 3.2: Illustrations for different values of β^* demonstrating dependence of the beam density on longitudinal position [52]

3.2 The ATLAS Detector

The ATLAS detector, located at point 1 on the collider ring in Meyrin, Switzerland, is one of two general physics detectors in operation at the LHC. It is the largest detector to date of any accelerator experiment; it is cylindrically shaped with a diameter of 26 m and a length along the beam axis of 46 m. The detector has a coverage in solid angle of nearly 4π, is hermetic, and consists of layers of sub-detectors extending over three orders of magnitude from 33.25 mm to the full length of 44 m. A schematic cartoon of the detector is shown in Figure 3.3, highlighting the scale and various detector subsystems.

ATLAS uses a right-handed coordinate system, with the global origin at the interaction point of the beams, the x-axis pointing towards the center of the LHC ring, the y axis pointing up, and the z axis along the beam line. As is generally the case in hadron collider detectors, a more natural coordinate system is defined for particle interactions that accommodates the physics of the collisions and the cylindrical shape of the machine. ATLAS is azimuthally symmetric about the beam line, and therefore the transverse plane is parameterized by the transverse radial distances r and the angle with respect to the positive x-axis ϕ. These

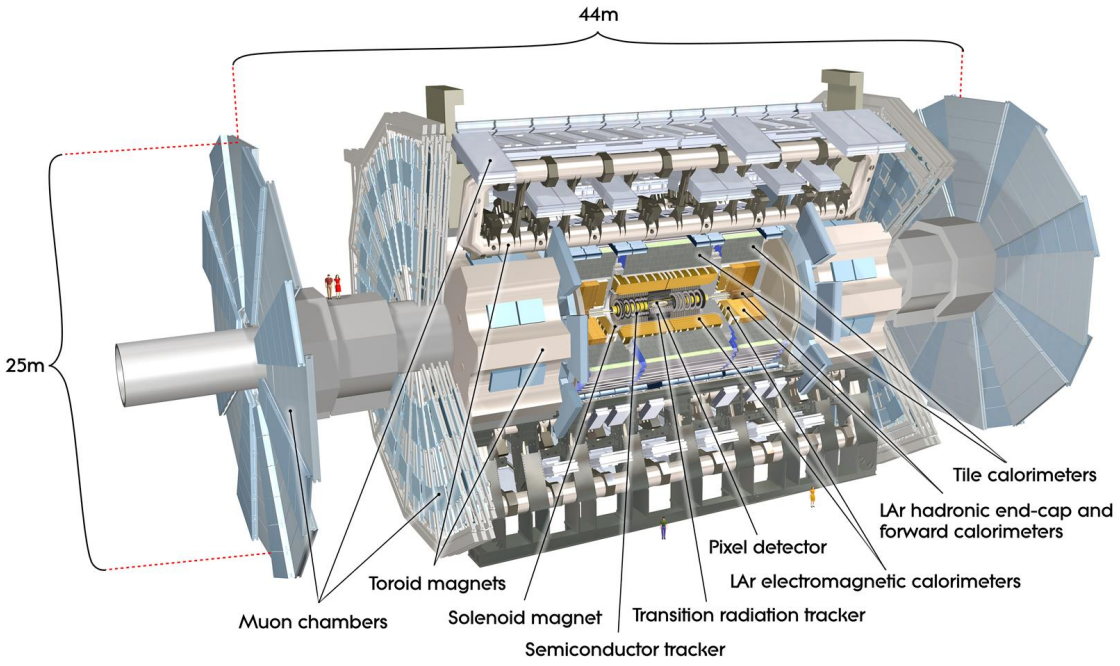

Figure 3.3: Diagram of the ATLAS detector [55]

transverse coordinates are reflected in the physics measurements frequently made by the detector; the momentum in the transverse plane is recorded as $p_T = \sqrt{p_x^2 + p_y^2}$, along with the angle ϕ. In the longitudinal direction, the relevant coordinate for particles is the pseudo rapidity, η, defined as:

$$\eta = -\log\left(\frac{\theta}{2}\right), \tag{3.3}$$

where θ is the angle with respect to the z-axis. Pseudorapidity is preferred to using θ directly due to its approximation of rapidity, y. Rapidity differences are Lorentz invariant quantities in the longitudinal direction, and pseudorapidity for a given particle becomes rapidity in the limit where $m \to 0$. Thus, p_{T}, η, and ϕ, along with mass or energy, provide a complete description of the kinematics of a given particle as a four vector. A diagram of η for various values can be seen in Figure 3.4.

The following sections describe in greater detail the various subsystems of the ATLAS detector. The sub-detectors can be broken up into three main categories: the inner detector for charged particle tracking, the calorimeters for measuring energy of electromagnetic and hadronic particles, and the muon spectrometer.

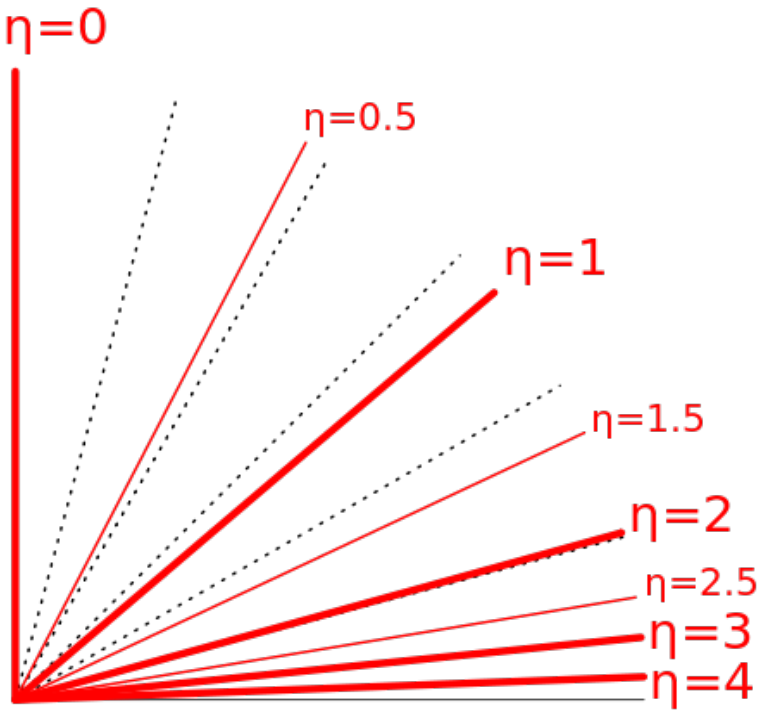

Figure 3.4: Pseudorapidity for different values in a polar cutaway [56].

3.2.1 Inner Detector

The ATLAS Inner Detector (ID) [57] [58] consists of four major components, from innermost to outermost, the Insertable B-Layer (IBL), the Pixel detector, the SemiConductor Tracker (SCT), and the Transition Radiation Tracker (TRT). Each of these detectors were installed at the commissioning of ATLAS, with the exception of the IBL which began physics operation in 2015. The ID provides precision measurement of charged particle tracks by detecting the interaction of particles with the detector material, reconstructing particle trajectories. The ID is inside of a 2 T magnetic field, oriented along the beam axis, which bends the charged particles, such that their momentum can be determined from their reconstructed trajectories. The subsystems have two distinct geometric configurations, the barrel components which form cylindrical shells around the interaction region, and the end caps, which are disks orthogonal to the beam pipe. The full ID layout is seen in Figure 3.5.

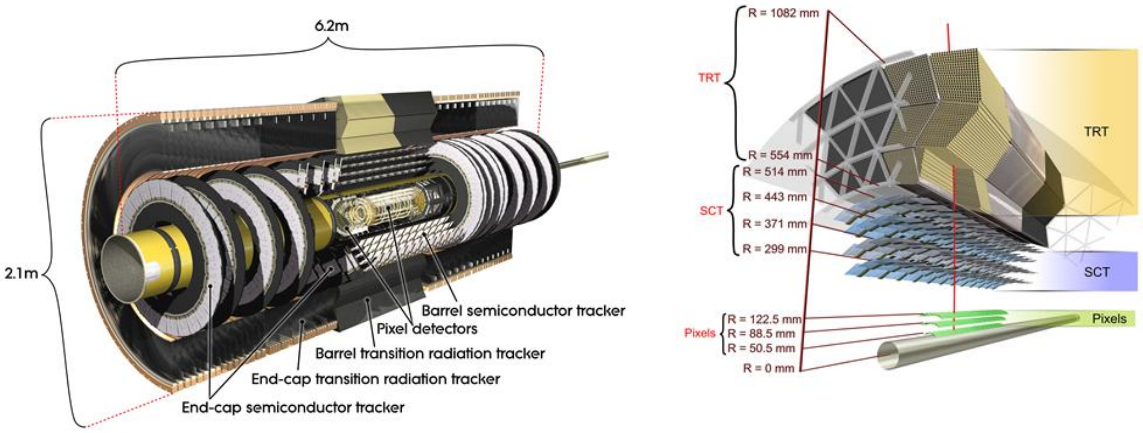

(a) (b)

Figure 3.5: Cartoon diagrams of the ATLAS ID [59]. (a) shows a cutaway of the ID detector, (b) shows the scale of the various subcomponents. Note this figure predates the IBL, located at 33.25 mm, and hence it is not seen in the image.

Pixel Detector

The innermost layers of the ID are the IBL and the Pixel detectors. Both of these detectors use silicon pixels to measure the deposition of ionization energy in the active material, and the series of multiple layers of pixels enable the reconstruction of particle trajectories. The IBL [60] was installed during the Long Shutdown 1, between ATLAS Run 1 and Run 2, and functions as an additional layer of pixel detector closest to the beam pipe. The IBL sits at a radial distances of $r = 33.25\,\text{mm}$ from the interaction point. The additional layer of tracking was added prior to Run 2 to satisfy the increased need for precision vertexing precipitated by the increase in instantaneous luminosity from Run 1. In particular, for the purpose of identifying secondary vertices from B-hadron decays (b-tagging), precision vertexing is key to separate signal from background. Tests of the IBL showed 4x improvement in the rejection of light jets with respect to Run 1, at a standard 70% working point [61]; see Section 5.6 for a more thorough discussion. Additionally, given the increased proximity of the IBL to the interaction region, new technology was developed in order to tolerate the higher radiation environment. The final installed detector consists of approximately 12 million individual pixel readout channels.

The Pixel detector is a cylindrical geometry with 3 layers in the barrel region and 5 layers on each endcap [62] [58]. The detector is designed for coverage out to $\eta < |2.5|$, with impact parameter resolution of $\approx 15\,\mu\text{m}$, and primary vertex reconstruction of charged tracks with a Gaussian width of $\sigma(z) < 1\,\text{mm}$. These design capabilities highlight the purposes of the pixel detector, which are charged particle track reconstruction, identification of secondary

vertices for b-tagging, and identification of the primary vertex in environments with multiple collisions per bunch crossing, also known as pileup (PU).The Pixel detector barrel sits at a radial distance of $r = 50.5\,\text{mm}$ to $120.5\,\text{mm}$ and covers up to $z = 400.5\,\text{mm}$ in the longitudinal direction. The Pixel endcap has a radius of $r = 88.8\,\text{mm}$ to $149.6\,\text{mm}$ and lies at $z = 495\,\text{mm}$ to $650\,\text{mm}$. The detector has 67 million readout channels in the barrel region, and about 13 million total in the endcaps.

SemiConductor Tracker

Similar to the IBL and Pixel detector, the SCT [63] [58] relies on silicon layers to record the deposition of ionization energy in layers traversed by charged particles. The SCT consists of 4 layers in the barrel region, and 9 layers in each endcap region. In the barrel, silicon strip detector modules are created by wire bonding two, $12\,\text{cm}$ strips back-to-back, such that one layer is perpendicular to the beam line, and the other is offset $40\,\text{mrad}$. This offset allows spatial resolution in both the longitudinal and transverse directions. The endcap modules are constructed similarly. The endcap sensors grow in width in the radial direction to account for the increase in surface area needed for full coverage. The SCT barrel sits at a radial distance of $r = 299\,\text{mm}$ to $514\,\text{mm}$ and covers up to $z = 749\,\text{mm}$ in the longitudinal direction. The SCT endcap has a radius of $r = 275\,\text{mm}$ to $560\,\text{mm}$ and lies at $z = 810\,\text{mm}$ to $2797\,\text{mm}$. The detector has 67 million readout channels in the barrel region, and about 13 million total in the endcaps.

Transition Radiation Tracker

The TRT uses substantially different technology for track reconstruction than the IBL, Pixels, and SCT. It consists of straw drift tubes filled with xenon gas and a cathode wire [64] [58]. This detector extends in the barrel region out to $\eta < |0.7|$ with the straws oriented parallel to the beam line. In the endcap region, the straws extend radially from the z-axis. Each straw is $4\,\text{mm}$ in diameter provides a space point resolution of $130\,\mu\text{m}$, significantly less than the silicon detectors, and yields no measurement in the longitudinal direction. However, the strengths of the TRT are its large number of measured space points and its relatively large lever arm, which improves the resolution of momentum measurements. Additionally, the TRT measures transition radiation from photons, which can be a useful discriminator between photons and neutral pions.

3.2.2 Calorimeters

The ATLAS calorimeter system is composed of two subsystems: one measures the energy of electromagnetic showers, photons and electrons, and the other is optimized to measure the energy of hadronic particles [65] [66] [67] [68] [58]. As hadrons travel further in material than electrons and photons, the hadronic calorimeter (HCAL) is located at a larger radius than the electromagnetic calorimeter (ECAL). The technologies used in each of the detection

regions are optimized for precision as well as radiation hardness, the latter of which is critical to maintaining optimal performance over the lifetime of the detector. Schematic diagrams of the calorimeters can be seen in Figure 3.6.

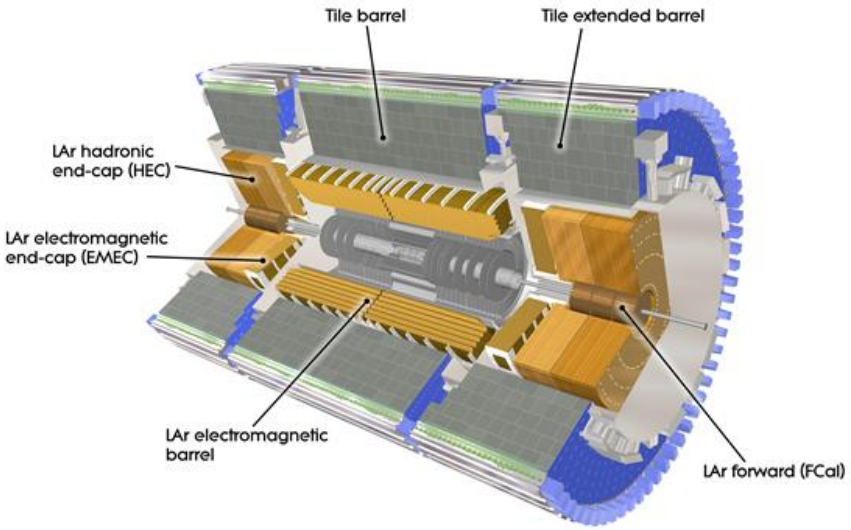

Figure 3.6: Diagram of the ATLAS calorimeter [69]

Electromagnetic Calorimeter

The ECAL is a sampling calorimeter [67] [68] that uses liquid argon as the active material and lead as the absorber. To cover the full region in ϕ, the active material and absorber are layered on top of each other in an accordion structure. The detector extends from $r = 1.5\,\text{m}$ to 1.7 m which is approximately 24 radiation lengths in the central region of the detector. In the barrel region, the ECAL is broken into three segments in the $\eta - \phi$ plane, with the granularity of each layer decreasing with increasing radius. The detector is also less granular in high pseudorapidity regions, for $|\eta > 1.4|$. The fine granularity region in the layer of the detector closest to the interaction point is crucial for the identification of neutral pions, which decay to collimated pairs of photons, and general photon vertices, which cannot be recovered with the tracking detector alone. A diagram of the barrel component of the ECAL can be seen in Figure 3.7.

In the endcap, the ECAL is composed of two concentric wheels, in the transverse plane, extending radially from $r = 302\,\text{mm}$ to 2077 mm and longitudinally from $z = 3.7\,\text{m} - 4.2\,\text{m}$. The endcap is designed such that the folds in the alternating layers of the detector vary with the radius, providing uniform coverage in the polar angle. While the extent of the ECAL covers a large range in solid angle, the region known as the crack, $1.37 < |\eta| < 1.52$, has

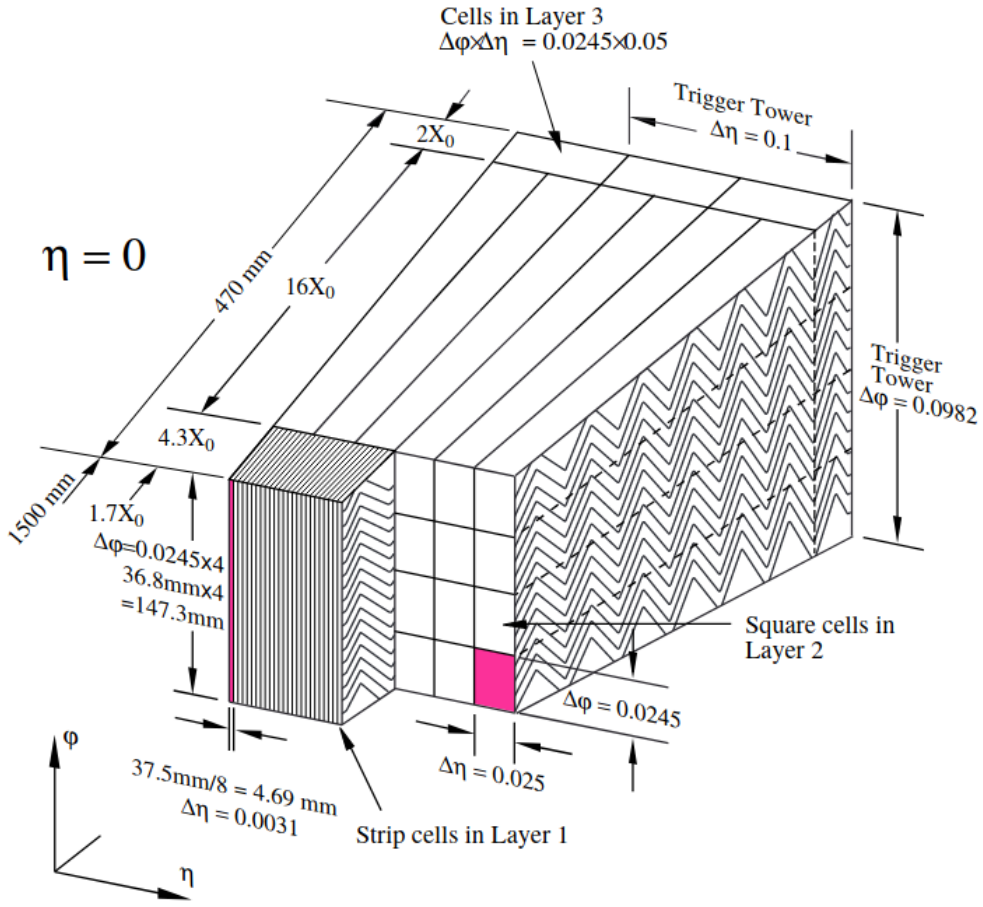

Figure 3.7: Barrel region of the ATLAS Electromagnetic Calorimeter [58]. Clearly seen here are the various segments of decreasing granularity, and the scale of the ECAL, both in SI units as well as radiation lengths.

candidates vetoed, due to large amounts of material between this part of the detector and the interaction region.

Hadronic Calorimeter

The hadronic calorimeter uses distinct technologies in the central, endcap, and very forward regions, due to the large differences in particle flux requiring different levels of radiation hardness. These calorimeters are designed to stop the vast majority of the remaining particles resulting from collisions, in particular hadrons which pass through the preceding layers of the detector. Muons pass through the calorimetry layers to the muon spectrometer.

In the barrel, the hadronic Tile Calorimeter [65] [66] utilizes steel as an absorber and plastic scintillating tiles as the active material. This detector is broken up into two pieces, each with 64 modules, with a radial symmetry. The Tile Barrel extends from $r = 2.280\,\text{m}$ to $3.875\,\text{m}$ and $z = 0\,\text{m} - 2.82\,\text{m}$. The Tile Extended Barrel encompasses the same radial distance as the Tile Barrel and longitudinally covers $z = 3.2\,\text{m} - 6.1\,\text{m}$. The layout of the Tile Calorimeter is oriented such that the geometry is centered around the interaction point at the center of the detector. To fully contain hadronic jets, the extent of this detector covers 9.7 nuclear interaction lengths. Readout from the Tile Calorimeter uses wavelength shifting fibers connected to photomultiplier tubes (PMTs) located at the outer radius of the detector.

The Hadronic Endcap Calorimeters (HECs) [67] [68] utilize similar technology to the ECAL, using copper instead of lead as the absorber. The HEC consists of 4 sampling layers at various points in z, extending from $z = 4.26\,\text{m} - 6.21\,\text{m}$ and having a radial coverage of $r = 475\,\text{mm}$ to $2.03\,\text{m}$. This detector extends the η coverage up to $\eta < 3.1$, and is 10 nuclear interaction lengths thick.

The final calorimeter is the Forward Calorimeter (FCAL), with a coverage in pseudorapidity from the HCAL out to $|\eta| < 4.9$. The FCAL has three layers, using liquid argon for the active material, one layer of copper absorber upstream, and two layers of tungsten absorber downstream. The first tungsten layer is designed for forward electromagnetic particles, while the latter two layers are for hadronic particles [58]. The forward region of the calorimeter, highlighting the various sub-components of the calorimeter system, is shown in Figure 3.8.

3.2.3 Muon Spectrometer

The ATLAS Muon Spectrometer (MS) is the portion of the detector designed to identify and measure the momentum of muons [58][70][71], which pass through the calorimeter system without significant interaction. The muon subsystem is the outermost layer of the ATLAS detector, and it utilizes 3 strong toroidal magnets, one in the barrel and one in each end cap, that produces a field which deflects charged particles in the longitudinal direction. A cartoon diagram shows the sub-detector in Figure 3.9. The muon spectrometer has two main components, the Monitored Drift Tubes (MDT) and the Cathode Strip Chambers (CSC). Additionally, there is a dedicated muon trigger system with faster readout.

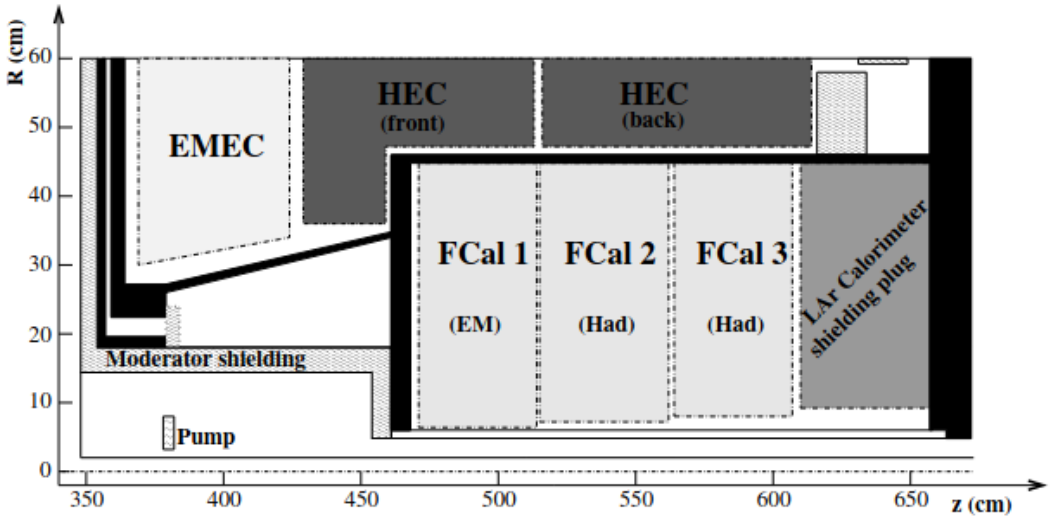

Figure 3.8: Forward region of the calorimeters in ATLAS [58]. Structural components, particularly the cryostat, that are not active pieces of the detector, are shown in black.

Monitored Drift Tubes

The MDT system provides the highest precision measurement of muons in ATLAS in the central region, out to approximately $|\eta| = 2$. It consists of 30 mm diameter aluminum wires, with a central cathode wire, and filled with argon gas. In the barrel region, the MDT consists of three layers at $r = 5\,\text{m}$, 7.5 m, and 10 m. The tubes are oriented in the ϕ direction, which makes the plane of the detector perpendicular to the bending direction of particles in the toroidal field. The barrel detector is broken into 16 sections with respect to the azimuthal angle. In the endcap region, there are 4 layers of MDTs. These are configured as wheels to accommodate the magnets and supports in the detector. As in the barrel region, the tubes run in the ϕ direction and are arranged into sixteen subsections. A longitudinal cutaway of the muon system is shown in Figure 3.10, highlighting that the MDTs provide the bulk of coverage for muons in ATLAS.

Cathode Strip Chambers

The CSCs are used in the forward region where the high flux necessitates a detector that can tolerate high occupancy. These detectors cover from $\eta = 2 - 2.7$ in pseudorapidity. CSCs use multiwire proportional chambers that measure ionization cascades from an anode to a cathode wire. Similar to the MDTs, the CSCs are oriented along the ϕ direction, and segmented into 8 sections, located at a longitudinal distance of $z = 7\,\text{m}$.

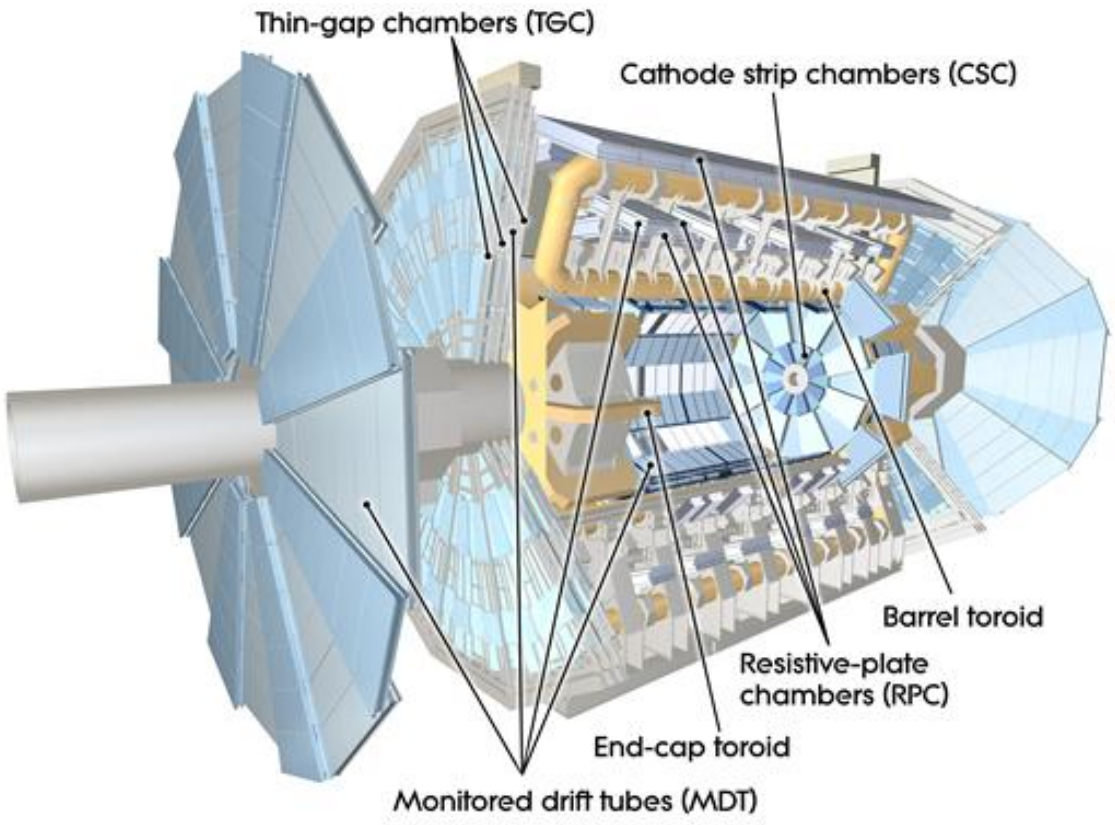

Figure 3.9: Diagram of the muon subsystem in ATLAS [72].

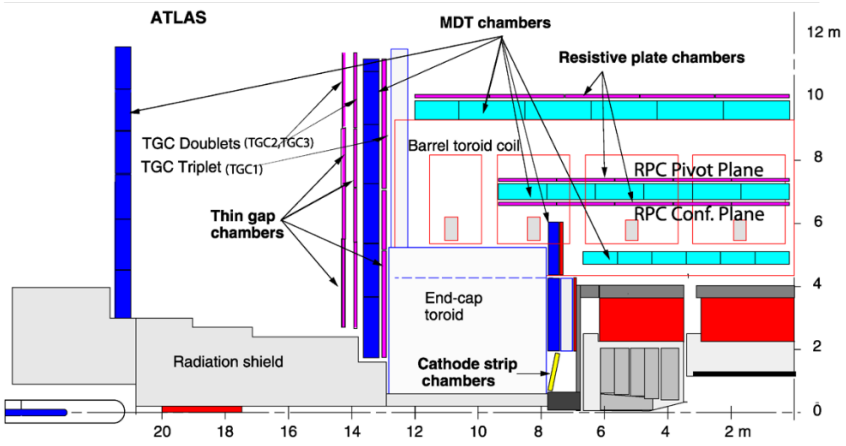

Figure 3.10: Longitudinal, schematic view of the muon subsystem in ATLAS [58].

Muon Trigger System

The MS contains, in addition to its primary detectors, two systems used primarily for coarse-grained and fast readout that can be used to trigger data collection in the presence of an energetic muon. These two detectors are the Resistive Plate Chambers (RPCs) and the Thin Gap Chambers (TGCs).

In the barrel, RPCs are arranged parallel to the MDTs, providing triggering coverage out to $|\eta| = 1.05$. The RPCs use two plates made of resistive phenolic-melaminic plastic laminate, and are filled with $C_2H_2F_4$ / Iso $- C_4H_{10}$ / SF_6 (94.7/5/0.3) gas. Due to the E-field between the plates, passing muons induce charge avalanches that are read out via capacitive coupling to strips at the end of the detectors. There are three radial distances of RPC, such that the two of smaller radius can trigger on lower p_T muons, $p_T = 6 - 9\,\text{GeV}$, and the larger lever arm of the outermost layer triggers on high p_T muons $p_T = 9 - 35\,\text{GeV}$.

In the endcap, the TGCs use a multiwire proportional chamber technology with a larger spacing between the wires than the CSC. The TGC provides a complementary trigger to the RPCs, and spans from $|\eta| = 1.05 - 2.4$.

3.2.4 Triggering and Data Acquisition

The ATLAS experiment sees colliding bunches at a rate of 40 MHz, with event sizes $\mathcal{O}(1\,\text{MB})$. This leads to a baseline data accumulation rate of 10 TB/s, such that reading every event to disk is impossible. In order to accommodate the high rate of data taking, various triggers are employed to quickly discriminate events of and prioritize those when reading out the full detector chain. The cumulative effect of the triggers brings the final event readout frequency down about 4 orders of magnitude, to $< 1\,\text{kHz}$ [73]. The ATLAS trigger is separated into two components, the Level 1 (L1) trigger implemented at a hardware level, and the High Level Trigger (HLT) implemented in software. The triggers serve as a coarse event reconstruction, and once the triggering objects are assembled by the L1 and HLT triggers, they are compared against a list of conditions, known in ATLAS as a Trigger Menu, to determine if the entire event should be read to disk. A schematic of the ATLAS Trigger and Data Acquisition system (TDAQ), can be seen in Figure 3.11.

Level 1 Trigger

The L1 trigger operates using the Calorimeter and MS trigger detectors and custom electronics for lower resolution and faster readout. The L1 Calo trigger routes calibrated trigger-level signals to two processors, the Cluster Processor (CP) and the Jet/Energy-sum Processor (JEP). The CP identifies energy clusters in the calorimeter that pass trigger criteria as photon, electron, and tau candidates. The JEP system identifies jet candidates and makes a preliminary assessment of the missing energy in the detector. See Section 5.7 for more details on the full reconstruction of this missing energy.

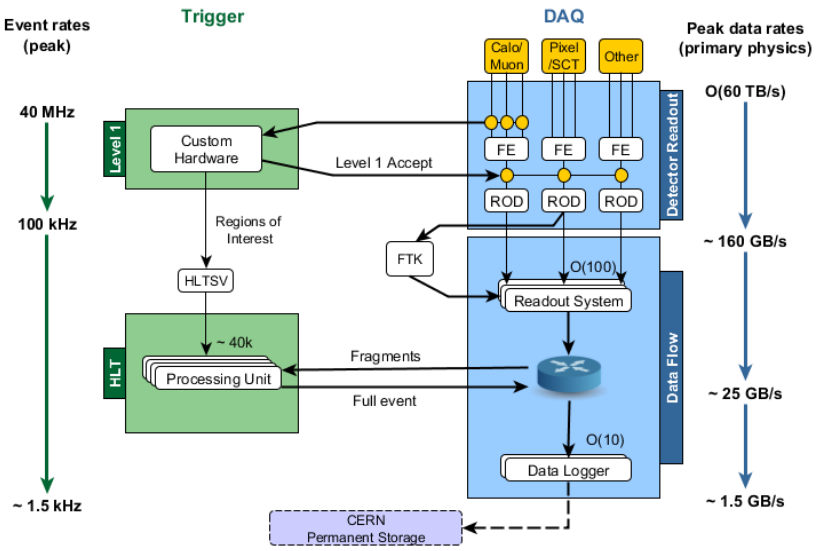

Figure 3.11: Schematic of the ATLAS Trigger and Data Acquisition system [74]. In particular, this diagram shows the interaction of the Triggers in ATLAS with the data readout system and the event rate and bandwidth after various stages.

In the MS, the L1 Muon trigger uses the RPCs and TGC to identify muon candidates that deviate from infinite momentum. In order to veto muons that do not originate from the interaction region, coincidence is required for the inner and outer TGC stations and the TGC and Tile Calorimeter.

The signals from the L1 trigger are then routed to a Central Trigger Processor (CTP), which can select events by looking at quantities such as total energy in the event or multiplicity of objects exceeding a certain threshold. For example, the studies in this thesis focus on events containing a single high p_{T} electron or muon as a trigger. The L1 trigger reduces the event rate from 40 MHz to 100 kHz. The contribution to the total L1 trigger rate from the various subsystems is shown in Figure 3.12. In particular, it can be seen that the trigger rate is approximately $\frac{1}{4}$ single leptons, but because trigger conditions overlap, the overall trigger rate is smaller than the sum of each component.

High Level Trigger

The HLT is the software-based trigger system in ATLAS that reduces the data rate from $\mathcal{O}(100\,\mathrm{kHz})$ to $\mathcal{O}(1\,\mathrm{kHz})$. It utilizes Regions of Interest (ROIs) from the L1 trigger to perform a dedicated online reconstruction which is closely related to the final offline reconstruction, and frequently utilizes the same software. The quantities on which the HLT triggers are

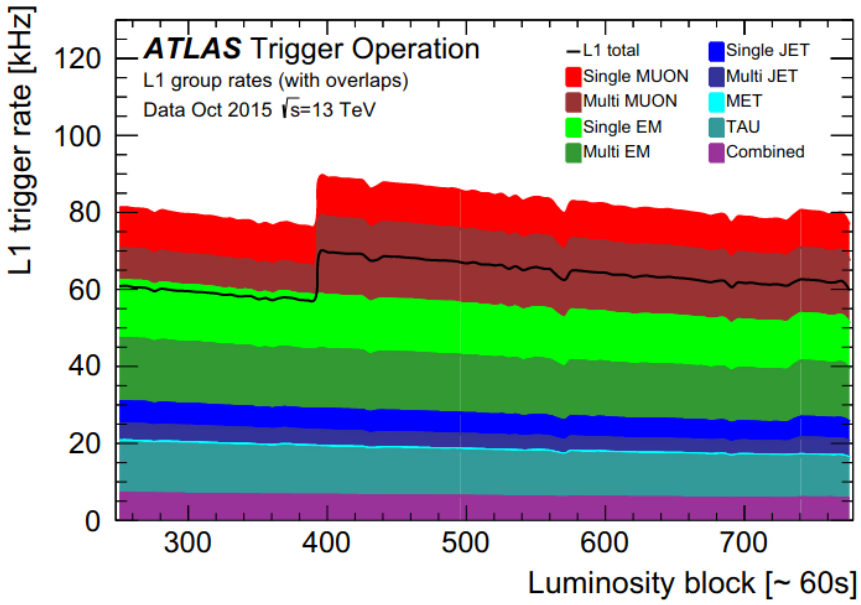

Figure 3.12: L1 Trigger rate in 2015 at the beginning of ATLAS Run2 [75]. The x-axis shows luminosity blocks, which are periods of time corresponding to approximately one second.

similar to those of the L1 trigger, utilizing the full detector readout. Figure 3.13 illustrates the various components of the HLT rate in early 2015; comparing this to Figure 3.12, the relative decline in the contribution from certain trigger sources, for example Multi-Muon, can be seen. Additionally, the HLT introduces additional triggers related to B-hadrons that are not present at L1.

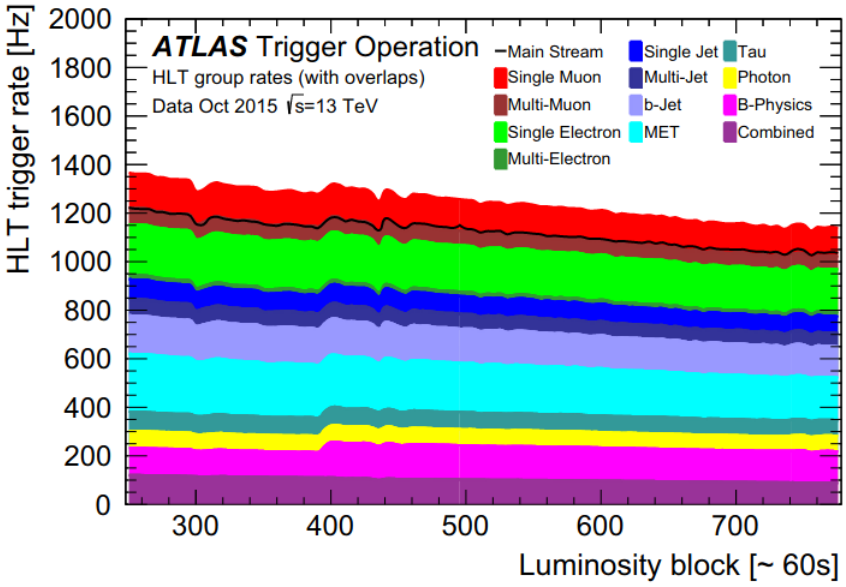

Figure 3.13: HLT rate in 2015 at the beginning of ATLAS Run2 [75]. The x-axis shows luminosity blocks, which are periods of time corresponding to approximately one second.

Chapter 4

$W + D^{(*)}$ Data and Monte Carlo Samples

This Chapter describes the triggers, the data, and Monte Carlo simulation samples that are used in the various ATLAS $W + D^{(*)}$ analyses.

4.1 ATLAS Run 2 Data Set

The data in this thesis were collected by the ATLAS experiment during Run 2, which lasted from 2015 until 2018. The full Run 2 integrated luminosity amounts to $\mathcal{L}_{\text{int}} \approx 141\,\text{fb}^{-1}$. The uncertainty in the integrated luminosity is 1.2% [53], which was obtained using the LUCID-2 detector [76] for the primary luminosity measurements. The absolute luminosity scale was determined using van der Meer scans during dedicated running periods in each year and extrapolated to physics data-taking using complementary measurements from several luminosity-sensitive detectors. This is described in more generality in Section 3.1.1.

The data collected by the ATLAS detector are divided into luminosity blocks. All events in a single luminosity block have approximately constant instantaneous luminosity and the same data-taking conditions. Luminosity blocks are typically about a minute long. Only the luminosity blocks where the LHC had stable beams and all ATLAS sub-detectors were operating well are used. The average number of additional pp interactions per bunch crossing (pileup) in the Run 2 data set is 33.7 [77] and Table 4.1 shows the breakdown for the pileup for each year. The accumulation of data by year is seen in Figure 4.1.

The analyses in this thesis use single lepton (electron and muon) triggers, which are the standard triggers in ATLAS for identifying events containing a single W boson [79]. These triggers require that events pass at least one electron trigger for the electron channel, or at least one muon trigger for the muon channel. The electron trigger is split into a low, medium, and high p_{T} trigger which require increasingly loose selection of the online likelihood-based identification variable. In addition to the identification variable, the low p_{T} trigger has additional requirements of a track-based isolation variable, requiring the electron to contain

Table 4.1: The run periods used in the analysis. The year in which the data were collected, the integrated luminosity, and the average pileup are shown.

Year	Integrated luminosity [fb^{-1}]	Mean number of pp interactions per crossing
2015	3.24	13.4
2016	33.40	25.1
2017	44.63	37.8
2018	58.79	36.1
All years	140.07	33.7

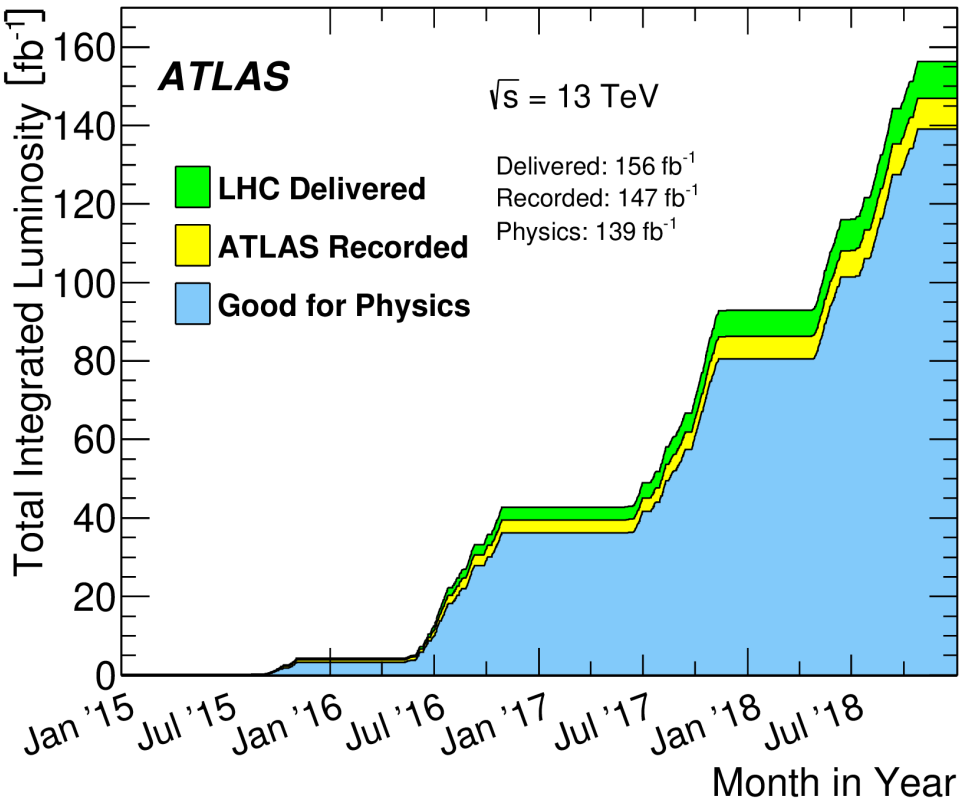

Figure 4.1: Accumulation of luminosity in the ATLAS experiment by year [78]. This plot shows the three categorizations of data in the experiment, delivered luminosity, recorded luminosity, and luminosity that is good for physics analyses.

more than 90% of the scalar sum of track momentum in a cone of $\Delta R < 0.2$, which decreases in size with increasing electron p_{T}. The muon trigger is composed of a low p_{T} trigger and a high p_{T} trigger. The former has an additional isolation requirement, while the high p_{T} trigger has no such requirement.

4.2 Monte Carlo Simulation Samples

Monte Carlo (MC) simulations are used to model the signal and all backgrounds except multijet. Samples produced with various MC generators are processed using a full detector simulation [80] based on GEANT4 [81] and then reconstructed using the same algorithms as the data. The effect of multiple interactions in the same and neighboring bunch crossings (pileup) is modeled by overlaying each simulated hard-scattering event with inelastic pp events generated with PYTHIA 8.186 [82] using the NNPDF2.3LO set of PDFs [83] and a set of tuned parameters called the A3 tune [84]. The MC events are weighted to reproduce the distribution of the average number of interactions per bunch crossing ($\langle\mu\rangle$) observed in the data, scaled up by a factor of 1.03 ± 0.04 to improve agreement between data and simulation in the visible inelastic pp cross section [85]. A reweighting procedure is applied to all MC samples to correct the charmed hadron production fractions to the world-average values [86, 87]. The change in the individual charmed meson production fractions is as large as 20%, depending on the MC configuration. An overview of all signal and background processes and the generators used to model them is given in Table 4.2, and further information about the relevant generators' configurations is provided below. Processes with more than one jet, known as multi-leg processes, can have different numbers of jets in each event. To improve the accuracy of calculations, samples with different jet multiplicities are often merged. In such multi-leg samples, the QCD accuracy for each jet multiplicity is specified in the table.

4.2.1 Background $V+$jets samples

Three generator configurations are used to model inclusive vector boson (W or Z) plus jet production. These samples are used to estimate the $W + D^{(*)}$ backgrounds and the corresponding experimental and theory systematic uncertainties.

Sherpa: The nominal MC generator used for this analysis is SHERPA 2.2.11 [88]. NLO-accurate matrix elements (ME) for up to two partons, and LO-accurate matrix elements for between three and five partons, are calculated in the five-flavor scheme using the Comix [89] and OPENLOOPS [90–92] libraries. The b- and c-quarks are treated as massless at matrix-element level and massive in the parton shower. The Hessian NNPDF3.0NNLO PDF set [93] is used. The default SHERPA parton shower [94] based on Catani–Seymour dipole factorization and the cluster hadronization model [95] is used. The samples are generated using a dedicated set of tuned parameters developed by the SHERPA authors and use the NNPDF3.0NNLO set. The NLO matrix elements for a given jet multiplicity are matched to the parton shower (PS) using a color-exact variant of the MC@NLO algorithm [96]. Different jet multiplicities are

Table 4.2: The generator configurations used to simulate the signal and background processes. The acronyms ME, PS, and UE stand for matrix element, parton shower, and underlying event, respectively. The column "HF decay" specifies which software package is used to model the heavy-flavor decays of bottom and charmed hadrons. For multi-leg samples where different jet multiplicities are merged, the QCD accuracy for each jet multiplicity is specified.

Process	ME generator	QCD accuracy	ME PDF	PS generator	UE tune	HF decay
$W+$jets (background modeling)						
$W+$jets	Sherpa 2.2.11	0–2j@NLO+3–5j@LO	NNPDF3.0nnlo	Sherpa	Default	Sherpa
$W+$jets	aMC@NLO (CKKW-L)	0–4j@LO	NNPDF3.0nlo	Pythia 8	A14	EvtGen
$W+$jets	aMC@NLO (FxFx)	0–3j@NLO	NNPDF3.1nnlo_luxqed	Pythia 8	A14	EvtGen
$W + D^{(*)}$ (signal modeling and theory predictions)						
$W + D^{(*)}$	Sherpa 2.2.11	0–1j@NLO+2j@LO	NNPDF3.0nnlo	Sherpa	Default	EvtGen
$W + D^{(*)}$	aMC@NLO (NLO)	NLO	NNPDF3.0nnlo	Pythia 8	A14	EvtGen
$W + D^{(*)}$	aMC@NLO (FxFx)	0–3j@NLO	NNPDF3.1nnlo_luxqed	Pythia 8	A14	EvtGen
Backgrounds						
$Z+$jets	Sherpa 2.2.11	0–2j@NLO+3–5j@LO	NNPDF3.0nnlo	Sherpa	Default	Sherpa
$t\bar{t}$	Powheg Box v2	NLO	NNPDF3.0nlo	Pythia 8	A14	EvtGen
Single-t, Wt	Powheg Box v2	NLO	NNPDF3.0nlo	Pythia 8	A14	EvtGen
Single-t, t-channel	Powheg Box v2	NLO	NNPDF3.0nlo	Pythia 8	A14	EvtGen
Single-t, s-channel	Powheg Box v2	NLO	NNPDF3.0nlo	Pythia 8	A14	EvtGen
$t\bar{t}V$	aMC@NLO	NLO	NNPDF3.0nlo	Pythia 8	A14	EvtGen
Diboson fully leptonic	Sherpa 2.2.2	0–1j@NLO+2–3j@LO	NNPDF3.0nnlo	Sherpa	Default	Sherpa
Diboson hadronic	Sherpa 2.2.1	0–1j@NLO+2–3j@LO	NNPDF3.0nnlo	Sherpa	Default	Sherpa
Diboson fully leptonic	Sherpa 2.2.11	0–1j@NLO+2–3j@LO	NNPDF3.0nnlo	Sherpa	Default	Sherpa
Diboson hadronic	Sherpa 2.2.12	0–1j@NLO+2–3j@LO	NNPDF3.0nnlo	Sherpa	Default	Sherpa
Special						
Single Particle Gun $D^{(*)}$ meson	ATLAS ParticleGun	—	—	—	EvtGen	

then merged into an inclusive sample using an improved CKKW matching procedure [97, 98] which is extended to NLO accuracy using the MEPS@NLO prescription [99]. The merging scale Q_{cut} is set to 20 GeV.

Uncertainties from missing higher orders in Sherpa samples are evaluated [100] using seven variations of the QCD renormalization (μ_{r}) and factorization (μ_{f}) scales in the matrix elements by factors of 0.5 and 2, avoiding variations in opposite directions. The strong coupling constant α_{s} is varied by ± 0.001 to assess the effect of its uncertainty. Additional details of the use of these samples are available in Ref. [101].

MadGraph5_aMC@NLO (CKKW-L): $V+$jets production is simulated with LO-accurate matrix elements for up to four partons with MadGraph5_aMC@NLO 2.2.2 [45]. The matrix-element calculation is interfaced with Pythia 8.186 for the modeling of the parton shower, hadronization and underlying event. To remove overlap between the matrix element and the parton shower, the CKKW-L merging procedure [102, 103] is applied with a merging scale of $Q_{\text{cut}} = 30$ GeV and a jet-clustering radius parameter of 0.2. In order to better model the region of large jet p_{T}, the strong coupling α_{s} is evaluated at the scale of each splitting to determine the weight. The matrix-element calculation is performed with the NNPDF3.0nlo PDF set [93] with $\alpha_{\text{s}} = 0.118$. The calculation is done in the five-flavor

scheme with massless b- and c-quarks. Cross sections are calculated using a diagonal CKM matrix. Heavy-quark masses are reinstated in the PYTHIA 8 shower. The values of μ_r and μ_f are set to one half of the transverse mass of all final-state partons and leptons. The A14 tune [104] of PYTHIA 8 is used with the NNPDF2.3LO PDF set with $\alpha_s = 0.13$. The decays of bottom and charmed hadrons are performed by EVTGEN 1.7.0 [105].

MadGraph5_aMC@NLO (FxFx): The MADGRAPH5_AMC@NLO 2.6.5 program [45] is used to generate weak bosons with up to three additional partons in the final state at NLO accuracy. The scales μ_r and μ_f are set to one half of the transverse mass of all final-state partons and leptons. Cross sections are calculated using a diagonal CKM matrix. The showering and subsequent hadronization are performed using PYTHIA 8.240 with the A14 tune and the NNPDF2.3LO PDF set with $\alpha_s = 0.13$. The different jet multiplicities are merged using the FXFX NLO matrix-element and parton-shower merging prescription [106]. PYTHIA 8.186 is used to model the parton shower, hadronization and underlying event.

The calculation uses a five-flavor scheme with massless b- and c-quarks at the matrix-element level, and massive quarks in the PYTHIA 8 shower. At the event-generation level, the jet transverse momentum is required to be at least 10 GeV, with no restriction on the absolute value of the jet pseudorapidity. The PDF set used for event generation is NNPDF3.1NNLO_luxqed. The merging scale is set to $Q_{cut} = 20$ GeV. Scale variations where μ_r and μ_f are varied independently by a factor of 2 or 0.5 in the matrix element are included as generator event weights. The decays of bottom and charmed hadrons are performed by EVTGEN 1.7.0.

4.2.2 Signal $W + D^{(*)}$ Samples

Only about 2% of the events in the inclusive W+jets samples pass the $W + D^{(*)}$ fiducial requirements. This, coupled with the branching ratios of 9.2% (2.5%) to the D^+ (D^{*+}) decay mode of interest, means that even very large W+jets samples provide statistically inadequate measurements of the $W + D^{(*)}$ fiducial efficiency. Filtered signal samples are therefore used to enhance the statistical precision. The generated events are filtered to require the presence of a single lepton with $p_T > 15$ GeV and $|\eta| < 2.7$ and either a D^{*+} or a D^+ meson with $p_T > 7$ GeV and $|\eta| < 2.3$. EVTGEN 1.7.0 is used to force all D^0 mesons to decay through the mode $D^0 \to K^-\pi^+$ and all D^+ mesons to decay through the mode $D^+ \to K^-\pi^+\pi^+$ (plus charge conjugates). EVTGEN describes this three-body D^+ decay using a Dalitz plot amplitude that includes contributions from the $\overline{K}^{*0}(892)$, $\overline{K}^{*0}(1430)$, $\overline{K}^{*0}(1680)$ and $\kappa(800)$ resonances, as measured by CLEO-c [107].

These samples are used for signal modeling, for calculating the detector response matrix and fiducial efficiencies with small statistical uncertainties, and for determining the $W + D^{(*)}$ signal mass distribution used in the statistical analysis described in Section 8. The AMC@NLO+PY8 (NLO) simulation described below is also used to calculate the theory predictions with the up-to-date PDF sets in Section 10. Three such filtered samples are used:

Sherpa 2.2.11 $W + D^{(*)}$: To reduce the per-event CPU time for the generation of the

$W + D^{(*)}$ signal MC simulated data, SHERPA 2.2.11 is configured to have lower perturbative accuracy than for the inclusive $V+$jets samples described above. Events are generated with NLO-accurate matrix elements for up to one jet, and LO-accurate matrix elements for two partons, in the five-flavor scheme. Other SHERPA parameters are set to the same values as for the baseline inclusive samples and uncertainties are evaluated using the same variations in QCD scale and α_s as for the baseline. The production cross section for this configuration differs from that of the inclusive sample by ∼2%. The two configurations show no significant differences in kinematic distributions associated with the $D^{(*)}$ meson or W boson.

aMC@NLO+Py8 (NLO) $W + D^{(*)}$**:** MADGRAPH5_AMC@NLO 2.9.3 is used to generate the $W+c$-jet process at NLO accuracy. A finite charm quark mass of $m_c = 1.55\,\text{GeV}$ is used to regularize the cross section, and a full CKM matrix is used to calculate the hard-scattering amplitudes. The values of μ_r and μ_f are set to half of the transverse mass of all final-state partons and leptons. The PDF set used for event generation is NNPDF3.0NNLO with $\alpha_s = 0.118$. The matrix-element calculation is interfaced with PYTHIA 8.244 for the modeling of the parton shower, hadronization, and underlying event and the A14 tune is employed. Scale variations where μ_r and μ_f are varied independently by a factor of 2 or 0.5 in the matrix element are included as generator event weights.

aMC@NLO+Py8 (FxFx) $W + D^{(*)}$**:** Events are generated using the same PYTHIA 8 configuration as used for the inclusive AMC@NLO+PY8 (FxFx) sample, but with the event-level filtering and configuration described above.

4.2.3 Top quark pair production background samples

The production of $t\bar{t}$ events is modeled using the POWHEG BOX v2 [108–111] generator. This generator's matrix elements at NLO in the strong coupling constant α_s with the NNPDF3.0NLO PDF and the h_{damp} parameter[1] set to $1.5\,m_{\text{top}}$ [112]. The functional form of μ_r and μ_f is set to the default scale $\sqrt{m_{\text{top}}^2 + p_T^2}$ where p_T is the transverse momentum of the top quark obtained using the underlying Born kinematics. Top quarks are decayed at LO using MADSPIN [113, 114] to preserve all spin correlations. The events are interfaced with PYTHIA 8.230 for the parton shower and hadronization, using the A14 tune and the NNPDF2.3LO PDF set. The decays of bottom and charmed hadrons are simulated using EVTGEN 1.6.0.

The NLO $t\bar{t}$ inclusive production cross section is corrected to the theory prediction at NNLO in QCD including the resummation of next-to-next-to-leading logarithmic (NNLL) soft-gluon terms calculated using TOP++ 2.0 [115–121].

POWHEG+HERWIG 7.04 and MADGRAPH5_AMC@NLO+PYTHIA 8 $t\bar{t}$ samples are used to estimate the systematic uncertainty incurred by the choice of MC model. The details of these estimations are provided below.

[1]The h_{damp} parameter controls the transverse momentum p_T of the first additional emission beyond the leading-order Feynman diagram in the parton shower and therefore regulates the high-p_T emission against which the $t\bar{t}$ system recoils.

$t\bar{t}$ POWHEG+HERWIG 7.04: The systematic uncertainty associated with using a different parton shower and hadronization model is evaluated by comparing the nominal $t\bar{t}$ sample with another event sample. The latter sample is produced with the POWHEG BOX v2 generator using the NNPDF3.0NLO parton distribution function. These non $t\bar{t}$ samples are interfaced with HERWIG 7.04 [122, 123], using the H7UE set of tuned parameters [123] and the MMHT2014LO PDF set [124]. The decays of bottom and charmed hadrons are simulated using EVTGEN 1.6.0 [105].

$t\bar{t}$ MADGRAPH5_AMC@NLO+PYTHIA 8: The uncertainty in the matching of NLO matrix elements to the parton shower is assessed by comparing the POWHEG sample with events generated with MADGRAPH5_AMC@NLO 2.6.0 interfaced with PYTHIA 8.230. The MADGRAPH5_AMC@NLO calculation used the NNPDF3.0NLO set of PDFs and PYTHIA 8 used the A14 tune and the NNPDF2.3LO set of PDFs. The decays of bottom and charmed hadrons are simulated using EVTGEN 1.6.0.

4.2.4 Wt-channel single-top background samples

Single-top Wt associated production is modeled using the POWHEG BOX v2 generator which provides matrix elements at NLO in the strong coupling constant α_s in the five-flavor scheme with the NNPDF3.0NLO parton distribution function set. The functional form of μ_r and μ_f is set to the default scale $\sqrt{m_{top}^2 + p_T^2}$. The diagram removal scheme [125] is employed to handle the interference with $t\bar{t}$ production [112]. Top quarks are decayed at LO using MADSPIN to preserve all spin correlations. The events are interfaced with PYTHIA 8.230 using the A14 tune and the NNPDF2.3LO PDF set. The decays of bottom and charmed hadrons are simulated using EVTGEN 1.6.0. The inclusive cross section is corrected to the theory prediction calculated at NLO in QCD with NNLL soft gluon corrections [126, 127].

4.2.5 t-channel and s-channel single-top background samples

Single-top t-channel (s-channel) production is modeled using the POWHEG BOX v2 generator at NLO in QCD using the four-flavor (five-flavor) scheme and the corresponding NNPDF3.0NLO set of PDFs. The events are interfaced with PYTHIA 8.230 using the A14 tune and the NNPDF2.3LO set of PDFs.

The uncertainty due to initial-state radiation (ISR) is estimated by simultaneously varying the h_{damp} parameter and μ_r and μ_f, and choosing the VAR3C up and down variants of the A14 tune as described in Ref. [128]. The impact of final-state radiation (FSR) is evaluated by halving and doubling the renormalization scale for emissions from the parton shower.

4.2.6 $t\bar{t} + V$ background samples

The production of $t\bar{t}V$ events, where V denotes either W, Z, or $\ell^+\ell^-$ produced through Z/γ interference, is modeled using the MADGRAPH5_AMC@NLO 2.3.3 [45] generator at

NLO with the NNPDF3.0NLO parton distribution function. The events are interfaced with PYTHIA 8.210 using the A14 tune and the NNPDF2.3LO PDF set. The uncertainty due to ISR is estimated by comparing the nominal $t\bar{t}V$ sample with two additional samples, which have the same settings as the nominal one, but with the VAR3 up or down variation of the A14 tune.

4.2.7 Diboson background samples

For the $W + D^{(*)}$ analysis, samples of diboson final states (VV) are simulated with the SHERPA 2.2.1 or 2.2.2 [88] generator depending on the process (see Table 4.2), including off-shell effects and Higgs boson contributions, where appropriate. For the $W + D_s$ analysis, samples of diboson final states are simulated with SHERPA 2.2.11 or 2.2.12 generator, depending on the process Fully leptonic final states and semileptonic final states, where one boson decays leptonically and the other hadronically, are generated using matrix elements at NLO accuracy in QCD for up to one additional parton and at LO accuracy for up to three additional parton emissions. Samples for the gluon-loop-induced processes $gg \to VV$ are generated using LO-accurate matrix elements for up to one additional parton emission for both the cases of fully leptonic and semileptonic final states. The matrix-element calculations are matched and merged with the SHERPA parton shower based on Catani–Seymour dipole factorization using the MEPS@NLO prescription. The virtual QCD corrections are provided by the OPENLOOPS library. The NNPDF3.0NNLO set of PDFs is used along with the dedicated set of tuned parton-shower parameters developed by the SHERPA authors.

Matrix element to parton shower matching [96] is employed for different jet multiplicities, which are then merged into an inclusive sample using an improved CKKW matching procedure which is extended to NLO accuracy using the MEPS@NLO prescription. These simulations are NLO-accurate for up to one additional parton and LO-accurate for up to three additional partons. The virtual QCD correction for matrix elements at NLO accuracy is provided by the OPENLOOPS library. The calculation is performed in the G_μ scheme [129], ensuring an optimal description of pure EW interactions at the EW scale.

4.2.8 Single Particle Gun Sample

A special sample for evaluating tracking related uncertainties were generated as a Single Particle Gun (SPG) sample. These samples consist of custom generated single $D^{(*)}$'s that decay into the final states that are reconstructed in the $W + D^{(*)}$ analysis, in particular the $D^+ \to K\pi\pi$ and $D^* \to D^0\pi \to K\pi\pi$ (see Section 6.1 for more details on these states). These samples are generated with the ATLAS `ParticleGun` generator and decayed with EVTGEN using the standard decay tables. ParticleGun provides methods to generate particles of a specified PDG ID where the distribution of p_{T} and η for the generated particles are drawn from histograms that come from the SHERPA 2.2.11 W+jets sample. The samples discussed here drew events with p_{T} between 5 GeV and 150 GeV based on a histogram with 0.75 GeV bins in p_{T} and with $-2.2 < \eta < 2.2$ in bins of size 0.06.

Chapter 5

Object Reconstruction

In the ATLAS experiment, particles and physics objects are reconstructed based on their interaction with various sub-components of the detector. A cartoon overview of particle reconstruction can be seen in Figure 5.1.

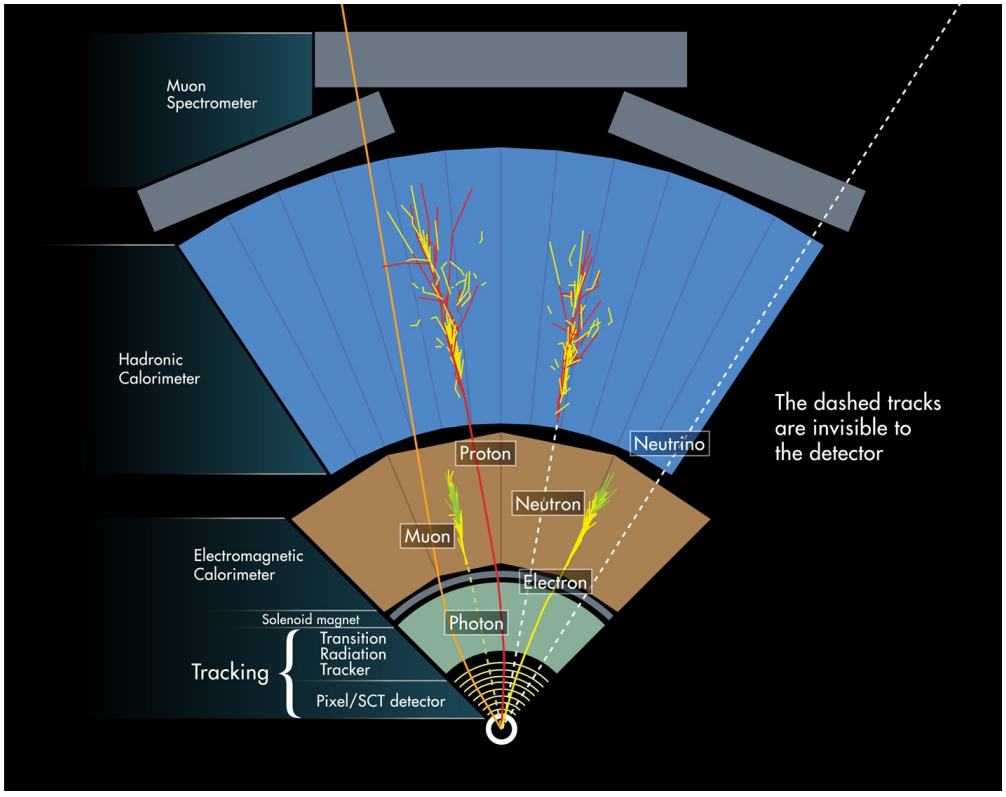

Figure 5.1: Transverse cross section of the reconstruction of particles in the ATLAS detector [130]. The operational principles of the sub-systems are given in Section 3.

For the $W + D^{(*)}$ analyses the reconstruction requirements can be factorized by examining the W and $D^{(*)}$ candidates separately. First, the W is reconstructed through a combination of a reconstructed lepton, and the missing transverse momentum ($E_{\mathrm{T}}^{\mathrm{miss}}$), which acts as a proxy for the momentum of the neutrino which passes through the detector with negligible interactions. The $D^{(*)}$ candidates are reconstructed using charged particle tracks are associated with its decay products. Additionally, jets are reconstructed for the purpose of overlap removal and flavor tagged jets are used for the categorization of backgrounds, in particular $t\bar{t}$. This Chapter outlines the reconstruction of the physics objects relevant to the work presented in this thesis. For a full account of systematic uncertainties in the $W + D^{(*)}$ analysis, including those related to physics object reconstruction, see Section 9. While the definition of physics objects is largely unchanged between the $W + D^{+}$ results related to [37] and the $D_s \to \phi\pi \to (KK)\pi$ and $D^{+} \to \phi\pi \to (KK)\pi$ studies, the differences are noted where appropriate.

5.1 Track Selection

Due to the magnetic field present in the detector, charged particles in ATLAS follow a helical trajectory whose curvature is inversely proportional to the particle momentum. The trajectories of these particles are measured by the ATLAS ID (see Section 3.2.1) by measuring the intersection of the particles with the layers of the tracking detector using a Kalman filtering algorithm [131][132]. These trajectories are parameterized by five *track parameters*: $(d_0, z_0, \phi_0, \theta, q/p)$, where d_0 is the transverse impact parameter, z_0 is the longitudinal impact parameter, ϕ_0 and θ are defined as the azimuthal and the polar angle of the track at its perigee, and q/p defines the orientation and the curvature of the helical trajectory. In the latter, q corresponds to the electric charge and p corresponds to the momentum. A graphical presentation of these five parameters is presented in Figure 5.2. Tracks also determine the primary vertex (PV) in the analysis; the reconstructed vertex with the highest sum of track p_{T} is used as the PV.

Tracks are also used in the electron and muon reconstruction, and have to be associated with the primary vertex, using constraints on the transverse impact parameter significance and on the longitudinal impact parameter. The transverse impact parameter is evaluated with respect to the beamline ($r = 0$) and it is required to be $|d_0/\sigma(d_0)| < 3.0$ for muons and $|d_0/\sigma(d_0)| < 5.0$ for electrons. The longitudinal parameter is defined as the longitudinal position of the track along the beamline at the point where d_0 is calculated and is corrected by the reconstructed position of the primary vertex. It is required to have $|\Delta z_0^{\mathrm{BL}} \sin\theta| < 0.5\,\mathrm{mm}$, where θ is the polar angle of the track and $\Delta z_0^{\mathrm{BL}} = z_0^{\mathrm{BL}} + \mathrm{BS}_z - \mathrm{PV}_z$, BS_z being the z-coordinate of the beam-spot and PV_z being the z-coordinate of the primary vertex. The transverse impact parameter cut is less restrictive for electrons than muons because the bremsstrahlung process of the former in material interactions generally increases the impact significance.

Inner Detector tracks with $p_{\mathrm{T}} > 500\,\mathrm{MeV}$ and $|\eta| < 2.5$ are used in the secondary vertex fit as part of the $D^{(*)}$ reconstruction, described in Section 6.1. Depending on the charm meson

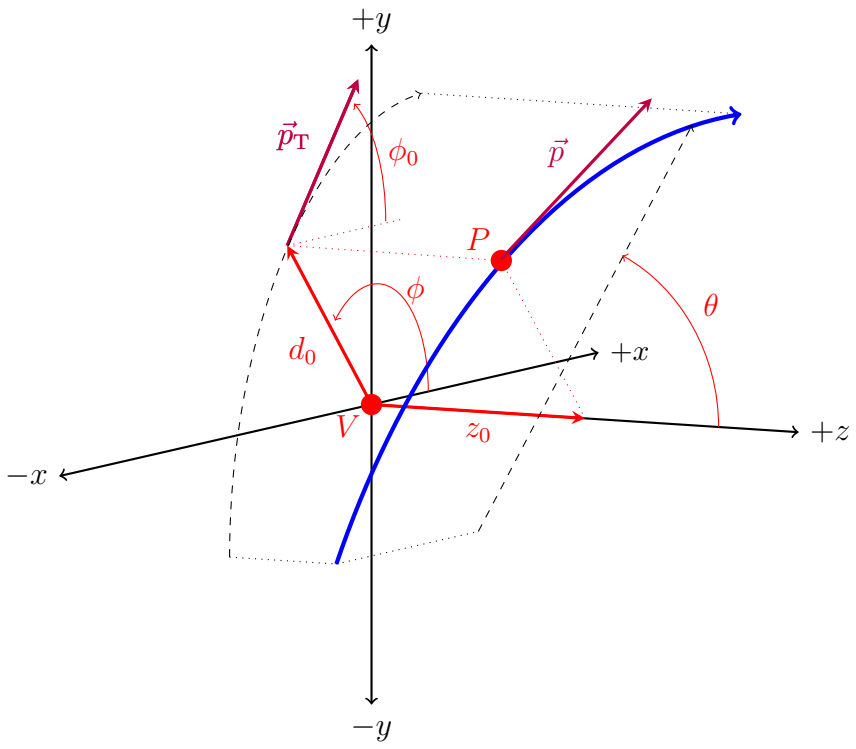

Figure 5.2: Graphical view of the defining track parameters $(d_0, z_0, \phi_0, \theta, q/p)$ at the perigee.

and the decay mode, the track p_{T} cut ranges from 500 to 800 MeV balancing the acceptance with contamination from combinatorial candidates. A cut of $|z_0 \sin\theta| < 5\,\mathrm{mm}$ with respect to the primary vertex along the beamline is applied. The Loose track requirements for track quality is applied to all tracks used in the analysis; these requirements are summarized in Table 5.1. Relevant cuts used in tracking refer to which layers have or have not been hit, and if particular silicon modules have shared hits. Holes are defined as layers of silicon which do not record a hit for the track in question, and are utilized as a cut for the silicon as a whole or the Pixel subsystem alone. The silicon hits (holes) are the sum of pixel detector and the SCT detector hits (holes). Shared modules occur when hits in the silicon are included in one or more reconstructed track, and a module is considered shared if it has one shared hit in the pixel, or two shared hits in the SCT. More details on the track selection for ATLAS Run 2 are available in Ref. [133].

Although `Loose` tracks are used in this analysis, the alternative of `TightPrimary` tracks was considered. The tighter track selection reduces the tracking efficiency by $5-7\%$ for track $p_{\mathrm{T}} > 20\,\mathrm{GeV}$. This effect is illustrated in Figure 5.3, which shows track reconstruction efficiency in a $D^{(*)}$ SPG sample for the `Loose` working point and `Loose` plus each additional `TightPrimary` track cut individually. The figure shows that the source of the inefficiency for `TightPrimary` tracks is the requirement that the track have hits in one of the two innermost

Table 5.1: `TrackParticle` object selection criteria.

Track quality selection (official)	`Loose`	`TightPrimary`
p_{T}	$> 500\,\mathrm{MeV}$	$> 500\,\mathrm{MeV}$
$\lvert\eta\rvert$	< 2.5	< 2.5
Number of Hits in Silicon ($\lvert\eta\rvert < 1.65$)	$N_{\mathtt{Si}} \geq 7$	$N_{\mathtt{Si}} \geq 9$
Number of Hits in Silicon ($\lvert\eta\rvert > 1.65$)	$N_{\mathtt{Si}} \geq 7$	$N_{\mathtt{Si}} \geq 11$
Number of Shared Modules	$N^{\mathtt{sh}}_{\mathtt{mod}} \leq 1$	$N^{\mathtt{sh}}_{\mathtt{mod}} \leq 1$
Number of Holes in Silicon	$N^{\mathtt{hole}}_{\mathtt{Si}} \leq 2$	$N^{\mathtt{hole}}_{\mathtt{Si}} \leq 2$
Number of Holes in Pixels	$N^{\mathtt{hole}}_{\mathtt{Pix}} \leq 1$	$N^{\mathtt{hole}}_{\mathtt{Pix}} \leq 0$
Number of Hits in Innermost layers	N/A	$N_{IBL} + N_{B-layer} > 0$

layers of the silicon tracker, the IBL and B-layer. While `TightPrimary` tracks have a lower rate of fake tracks, the reduction in fakes does not compensate for the loss of efficiency, motivating the selection of loose tracks.

5.2 Lepton Categories

Three different categories of leptons are used in the analysis: `baseline`, `loose`, and `tight` leptons. The categories are inclusive, i.e. `baseline` includes all leptons and `loose` includes `tight` leptons. The `baseline` leptons are required to have $p_{\mathrm{T}} > 20\,\mathrm{GeV}$, while `loose` and `tight` leptons are required to have $p_{\mathrm{T}} > 30\,\mathrm{GeV}$. The `tight` leptons are required to meet additional isolation requirements.

The `baseline` objects are used in the $E_{\mathrm{T}}^{\mathrm{miss}}$ calculation and the object overlap removal procedure. `Anti-tight` leptons are used for the multijet background estimation, see Section 7, and are required to pass the `loose` requirements, but fail the `tight` requirements. The `tight` leptons for the definition of the signal region (SR). More details in the where the categories are used can be found in Section 7.

5.3 Electron Selection

Electron candidates are reconstructed from an isolated energy deposit in the electromagnetic calorimeter matched to a track in the inner detector as described in Ref. [134]. All electrons are required to pass the `Tight` likelihood-based working point, described in Ref. [134]. Electrons are required to be in the fiducial region of pseudorapidity within $|\eta| < 2.47$, excluding the calorimeter crack region between $1.37 < |\eta| < 1.52$. `Tight` electrons are required to be isolated, as described in Ref. [134]. The isolation is a combination of track-based and calorimeter-based isolation, with both utilizing the same basic principle. For the track-based method, the electron candidate's track defines the central axis of a cone in ΔR. The sum

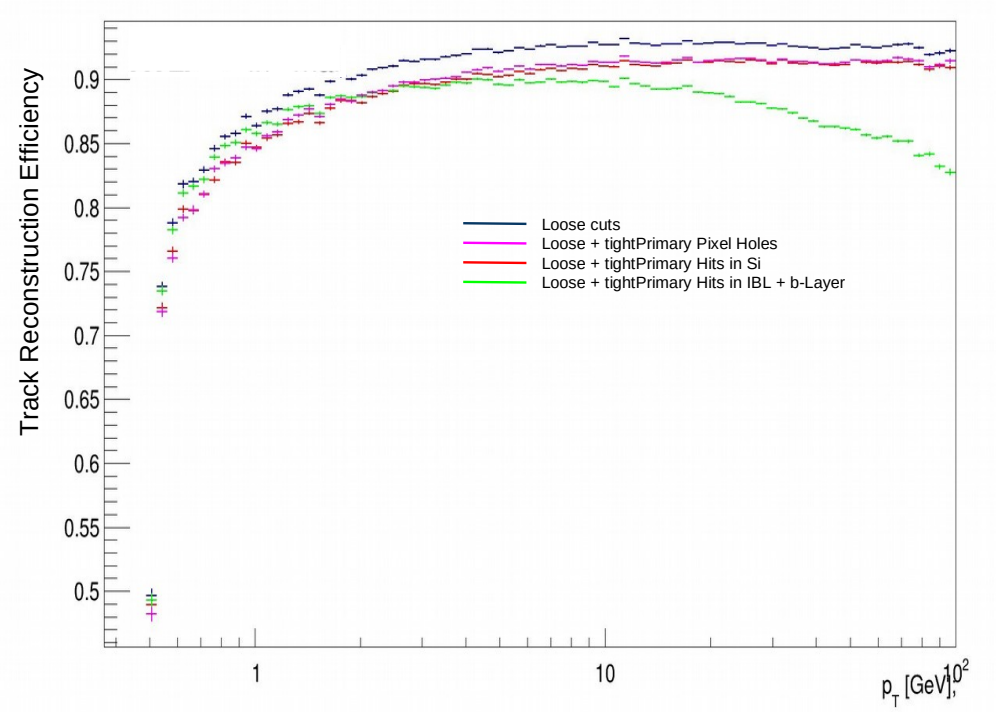

Figure 5.3: Track reconstruction efficiency for the SPG sample with forced $D^+ \to K\pi\pi$ decays with a flat p_{T} distribution. Starting from the `Loose` cuts, `TightPrimary` cuts are added sequentially to identify the cause of the declining track reconstruction efficiency.

of the momenta of all tracks in that cone, excluding the electron candidate track, is then required to fall below a certain value which is the isolation criteria. For calorimeter isolation, a cluster of energy in the EM Cal is used as the candidate electron, and the sum is performed on all calorimeter clusters around the candidate, again excluding the candidate itself. The isolation criteria used for the $W + D^{(*)}$ differential analysis and the $W + D_s$ inclusive analysis differ slightly in the tracking isolation cone size, and both are summarized in Table 5.2.

Typical electron reconstruction efficiencies are shown in Figure 5.4, taken from Ref. [135], for several combinations of identification and isolation working points. The efficiencies are measured using prompt electrons from the $Z \to ee$ decay. The working point most similar to the one used in the analysis is denoted as 'Tight + Fix' and marked with red triangles.

5.4 Muon Selection

Muon candidates are reconstructed in the region $|\eta|$ <2.5 by matching tracks in the muon spectrometer with those in the inner detector. The *global refit* algorithm [136] is used to combine the information from the ID and MS subdetectors. Muons are identified with `Tight`

Table 5.2: Electron isolation criteria, defined for both analyses in this thesis. The relevant quantities for isolation are the cone size (expressed as a limit on ΔR) and the fraction of momentum or energy in that cone (expressed as $\Sigma_{tracks} p_{\mathrm{T}}$ and topoETcone respectively) that cannot exceed the momentum or energy of the candidate itself. The only difference between the two analyses is in the cone size for track-based isolation.

Isolation Criteria	$W + D^{(*)}$ differential	$W + D_s$ inclusive
Track Iso Cone	$\Delta R < 0.2$	$\Delta R < 0.3$
Track Iso Criteria	$\Sigma_{tracks} p_{\mathrm{T}} / p_{\mathrm{T}}(\mathrm{el}) < 0.06$	$\Sigma_{tracks} p_{\mathrm{T}} / p_{\mathrm{T}}(el) < 0.06$
Calo Iso Cone	$\Delta R < 0.2$	$\Delta R < 0.2$
Calo Iso Criteria	$\mathrm{topoETcone}/p_{\mathrm{T}}(\mathrm{el}) < 0.06$	$\mathrm{topoETcone}/p_{\mathrm{T}}(el) < 0.06$

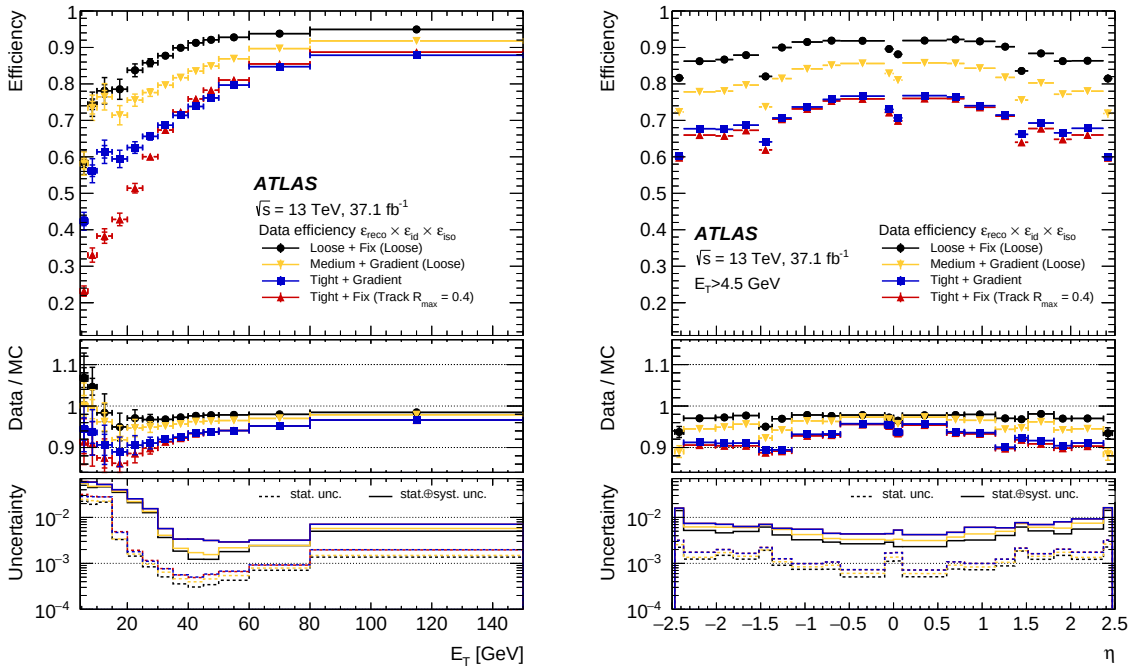

(a) (b)

Figure 5.4: The product of reconstruction, identification, and isolation efficiencies for data from a $Z \to ee$ sample as a function of electron p_{T} (a) and η for $p_{\mathrm{T}} > 4.5\,\mathrm{GeV}$ (b), for several combinations of working points Ref. [135]. The inner uncertainties are statistical while the total uncertainties include both the statistical and systematic components. The lower panels show data-to-simulation ratios as well as the relative statistical and total uncertainties (statistical and systematic added in quadrature) applicable to both the data efficiencies and correction factors.

quality criteria [137], characterized by the number of hits in the inner detector and in the muon spectrometer subsystems.

The `tight` muons are required to be isolated, based on a combination of the track-based and particle-flow-based [138] isolation. The particle-flow algorithm is further explained in Section 5.5. The track-based isolation is defined as the scalar sum of the transverse momenta of the ID tracks associated with the primary vertex in a cone of ΔR around the muon, excluding the muon track itself. The cone is defined as $\Delta R = \min(10\,\text{GeV}/(p_{\text{T}}(\mu)[\text{GeV}]), 0.3)$ and the corresponding track-based isolation variable is denoted as ptvarcone30.

The particle-flow isolation variable [137] is constructed as the sum of the transverse energy of neutral particle-flow objects in a cone of size $\Delta R = 0.2$ around the muon, labelled as neflowisol20. The transverse energy is corrected for the contribution from the energy deposit of the muon itself, for pileup effects, and is weighted by a factor $w = 0.4$. The weighting factor is optimized to maximize the rejection of heavy flavour hadron decays in the desired range of prompt muon efficiencies. Finally, the muon isolation criteria is defined as $(\text{ptvarcone30\_TightTTVA\_pt500} + 0.4\text{neflowisol20})/p_{\text{T}} < 0.045$.

Typical efficiencies for this isolation working point for prompt muons from the $Z \to \mu\mu$ process are shown in Figure 5.5.

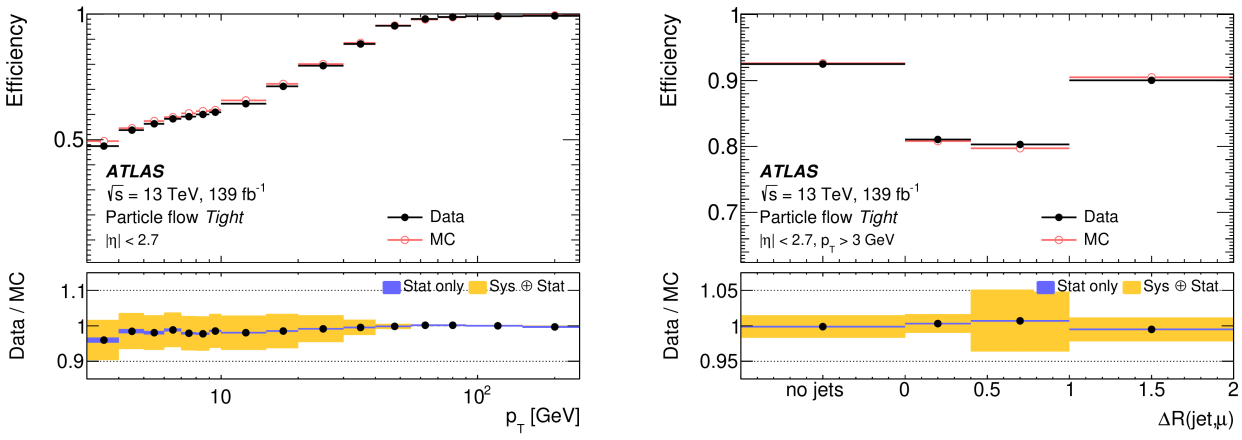

(a) (b)

Figure 5.5: Muon isolation efficiency measured in $Z \to \mu\mu$ events for the `PflowTight_VarRad` criteria, as a function of p_{T} (a) and $\Delta R\mu, jet$ for muons with $p_{\text{T}} > 30\,\text{GeV}$ (b). The error bars on the efficiencies indicate the statistical uncertainty. The panel at the bottom shows the ratio of the measured to predicted efficiencies, with statistical and systematic uncertainties. Taken from Ref. [137].

5.5 Jet Selection

Jets are reconstructed using the particle-flow jet reconstruction algorithm. In order to make theoretical comparisons with experimental results, jet finding algorithms are required to be Infrared and Collinear safe (IRC), satisfying two conditions. First, the jet finding algorithm must not be impacted by the contribution of low p_{T} (soft) objects, known as infrared safety. Second, the jet finding cannot be impacted by splitting the highest p_{T} components into two collinear components. The algorithm takes as an input the energy of the charged tracks (reconstructed by ID) minus the calorimeter energy in overlapping regions, in addition to energy of all particles via the deposition of energy in the calorimeter. The energy after subtraction is then passed to the IRC safe, anti-k_t [139] jet-reconstruction algorithm with a distance parameter $R = 0.4$. The jets are required to have $p_{\mathrm{T}} > 20\,\mathrm{GeV}$ and $|\eta| < 5.0$.

The jet energy scale (JES) calibration restores the jet energy to that of jets reconstructed at the particle level, as described in Ref. [140]. Calibration includes five separate steps: p_{T}-density-based pileup correction, residual pileup correction, absolute MC-based calibration, global sequential-calibration, and residual in-situ calibration. Pileup corrections remove the excess energy due to the additional bunch crossings. The absolute JES calibration corrects the jets so that it matches the energy of the underlying truth jet and is derived using dijet MC events. The global sequential-calibration is designed to improve the jet p_{T} resolution and reduce the corresponding uncertainties. The *in-situ* calibration is applied to correct for the remaining differences between the data and MC simulation.

5.6 Jet Flavor Tagging

Jets with $|\eta| < 2.5$ and $p_{\mathrm{T}} > 20\,\mathrm{GeV}$ can be identified as originating from bottom quarks through the reconstruction of secondary vertices and tracks with large impact parameter from the decay of b-hadrons. For this purpose, a multivariate discriminant DL1 tagger [141, 142] that uses displaced tracks, secondary vertices and decay topologies is used. The chosen working point has 70% efficiency for identifying b-jets in a simulated $t\bar{t}$ sample and the measured rejection factor (the inverse misidentification efficiency) for c-jets (light-jets) is about 11 (600) [143]. The b-jets are defined according to the presence of b-hadrons with $p_{\mathrm{T}} > 5\,\mathrm{GeV}$ within a cone of size $\Delta R = 0.3$ around the jet axis. If a b-hadron is not found and a c-hadron is found, then the jet is labeled a c-jet. Light-jets are all the remaining unclassified jets. The b-tagging efficiency and rejections can be seen in Figure 5.6.

As the b-tagging algorithms rely on the same information used in the $D^{(*)}$ meson secondary vertex fits, a dedicated overlap removal procedure is used. All b-jets are required to be geometrically separately from reconstructed $D^{(*)}$ mesons by applying the following requirement: $\Delta R(b-\mathrm{jet}, D^{(*)}) < 0.4$. Without such an overlap removal procedure, approximately 50% of the signal $W + D^{(*)}$ events would have one b-jet overlapping with the explicitly reconstructed $D^{(*)}$ meson. These b-jet can either be mis-tagged c-jets or b-jets that have a charm hadron in the cascade. The overlap removal requirement significantly increased the sensitivity of

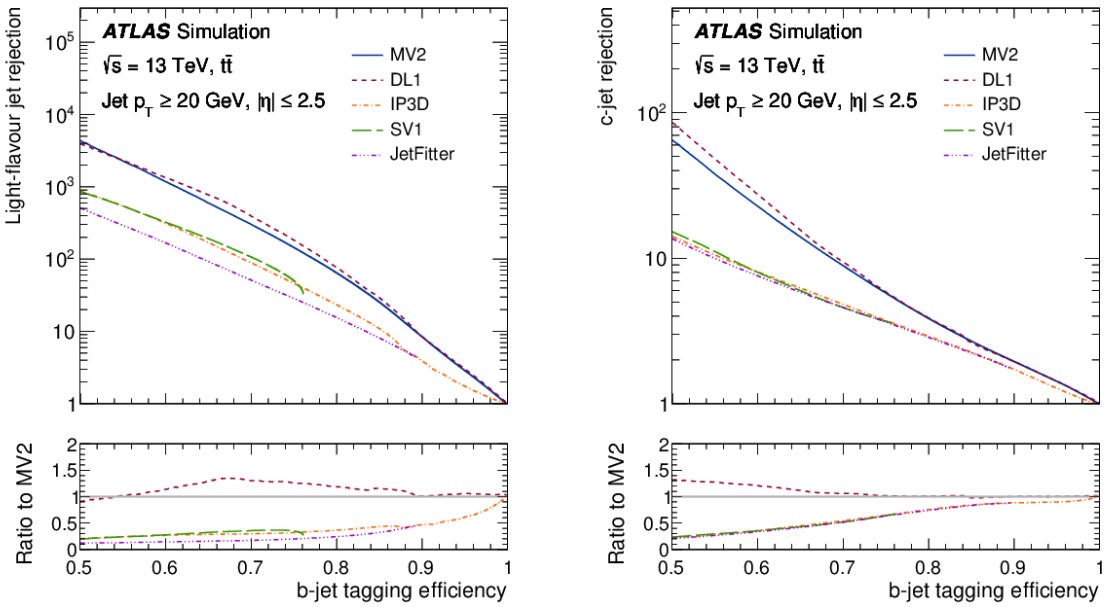

(a) (b)

Figure 5.6: ATLAS b-tagging efficiencies with a variety of algorithms that are used to identify b-jets. The algorithms fall into two categories, deterministic algorithms that identify jets with large impact parameters or secondary vertices, or multivariate machine learning algorithms. The inputs to the algorithms are particle and jet level quantities in all cases, as well as the output of the deterministic algorithms that are input to the machine learning based algorithms. MV2 is a multivariate BDT based algorithm and DL1 is a deep neural net based algorithm. IP3D deterministically identifies jets with large impact parameters. SV1 and JetFitter deterministically identify secondary (and tertiary in the case of JetFitter) vertices. The machine learning based algorithms have similar performance with respect to each other that is superior to the deterministic algorithms.

the analysis by achieving better separation between the signal and the $t\bar{t}$ background and eliminated a large flavor tagging uncertainty. In the following, throughout this thesis, the term b-jet will refer to b-jets after applying overlap removal with $D^{(*)}$ meson candidates.

5.7 $E_{\mathrm{T}}^{\mathrm{miss}}$ Reconstruction

The missing transverse momentum ($E_{\mathrm{T}}^{\mathrm{miss}}$) in the events is calculated as the sum of negative vectors of the selected high-p_{T} calibrated objects (electrons, muons, jets), and of the soft-event contribution which is reconstructed from tracks or calorimeter cell clusters not associated with the calibrated objects [144]. The calibrated objects are also called 'hard objects'. The `baseline` electron and muon candidates are used in the $E_{\mathrm{T}}^{\mathrm{miss}}$ calculation. The pileup degrades the resolution of the calorimeter-based measurement of missing transverse momentum, therefore a track-based measurement of the soft objects is used [144]. A restriction is placed on jets at large η, requiring a cut of $p_{\mathrm{T}} > 30\,\mathrm{GeV}$.

Chapter 6

Charm Meson Reconstruction and Event Selection

Events for both the $W + D^{(*)}$ differential and $W + D_s$ inclusive measurements require the reconstruction of a W candidate, via lepton and $E_{\mathrm{T}}^{\mathrm{miss}}$ requirements, and a $D^{(*)}$, reconstructed from charged particle tracks. This section describes first the reconstruction of $D^{(*)}$ candidates in the various decay modes used in the analysis, then describes the full event selection.

6.1 Charm Meson Reconstruction

This analysis uses a c-tagging strategy that relies on explicitly reconstructed charm mesons in fully charged, hadronic decay modes. The use of modes containing neutral hadrons or leptons is therefore excluded as each $D^{(*)}$ decay product must generate a track in the detector. Additionally, each $D^{(*)}$ decay mode must be targeted and reconstructed individually to ensure that an accurate estimation of the cross section times branching ratio is available for the Monte Carlo prediction. This method of c-tagging is less efficient than c-jet tagging, due to the acceptance being reduced by a factor of the product of the reconstruction efficiency, the production fraction of the $D^{(*)}$ species, the decay mode branching ratio. However, the diminished background and clean $D^{(*)}$ mass peak are exploited in the fit to compensate for this reduction in efficiency by providing higher purity.

Four charm meson decay channels are studied, two in each analysis. For the $W + D^{(*)}$ differential analysis, $D^+ \to K\pi\pi$ and $D^* \to D^0\pi \to (K\pi)\pi$ are reconstructed. The $D^* \to D^0\pi \to (K\pi)\pi$ mode is a cascade decay that involves the intermediate and long lived D^0 decaying from a reconstructed secondary vertex, while the full D^* is reconstructed by including an additional pion, denoted as the soft pion due to its low momentum from phase space restrictions in the D^* rest frame. For the $W + D_s$ inclusive analysis, $D_s \to \phi\pi \to (KK)\pi$ and $D^+ \to \phi\pi \to (KK)\pi$ are reconstructed identically so they can be fit simultaneously and are referred to as the $\phi\pi \to (KK)\pi$ modes. These modes were selected based on charged track multiplicity, kinematic features that allowed signal to background discrimination, and a

sufficiently high branching ratio.

This section describes the common features of the various $D^{(*)}$ mesons used to build the reconstructed candidate mesons and the selections applied to those candidates to enhance the signal. Details specific to each mode are described in their respective subsections. The charm meson reconstruction is based on the method used in the 7 TeV $W + D$ analysis [30].

As the ATLAS experiment lacks explicit hadronic particle identification, $D^{(*)}$ candidates are reconstructed by combining tracks that are assigned a pion or kaon mass hypothesis. Tracks corresponding to the leptons used for the W boson candidates are excluded. For both the $D^+ \to K\pi\pi$ and $D^* \to D^0\pi \to (K\pi)\pi$ modes, the particle species are determined by the track charges: the two tracks with the same charge are assigned the pion mass, and the opposite sign track is assigned the kaon mass. For the $\phi\pi \to (KK)\pi$ modes, the kaons tracks are assigned by taking two oppositely charged tracks with a mass close to the ϕ mass and the remaining track is assigned the pion mass; this process is described in more detail in Section 6.1.3. A vertex fit is performed on the tracks, using the VKalVrt package [145], which yields a $D^{(*)}$ meson candidate. In the case of the $D^* \to D^0\pi$ mode, the vertex fit is performed on the long-lived D^0, which is then combined with a prompt track to account for the additional soft pion. The $D^{(*)}$ selections values were optimized using MC signal and data templates for the background. The background data templates use the "side-band" method, that generates templates from regions in the data where no signal is expected, and interpolates into the signal region.

The $D^+ \to K\pi\pi$ and $\phi\pi \to (KK)\pi$ (D^0 from the $D^* \to D^0\pi \to (K\pi)\pi$) modes are reconstructed using three (two) tracks with $p_{\mathrm{T}} > 800\,\mathrm{MeV}(600\,\mathrm{MeV})$, required to be within a cone of $\Delta R < 0.6$, and having total charge $= \pm 1(0)$. The tracks are fit to determine a secondary vertex (SV), and the fit is required to have $\chi^2 < 8.0, 10.0, 6.0$ for the $D^+ \to K\pi\pi$, $D^* \to D^0\pi$, and $\phi\pi \to (KK)\pi$ modes, respectively. All candidates place a requirement on the $\sigma_{3\mathrm{D}}$, which is defined as the 3D impact parameter divided by the uncertainty of that measurement. The $D^{(*)}$ candidate is required to have $\sigma_{3\mathrm{D}} < 4.0$ to reduce the contribution from pileup for the $D^+ \to K\pi\pi$ and $D^* \to D^0\pi \to (K\pi)\pi$ modes and $\sigma_{3\mathrm{D}} < 6.0$ for the $\phi\pi \to (KK)\pi$ modes.

The finite lifetime of the D^+, D^0 (associated with each D^*), and D_s candidates — $c\tau = 311.8\,\mu\mathrm{m}$, $122.9\,\mu\mathrm{m}$, and $151.2\,\mu\mathrm{m}$ respectively [14] — is exploited through a requirement on the distance between the primary and second vertex projected on to the direction of flight, L_{xy}. We require $L_{xy} > 1.1\,\mathrm{mm}$ for $D^+ \to K\pi\pi$ candidates with $p_{\mathrm{T}} < 40\,\mathrm{GeV}$, $L_{xy} > 2.5\,\mathrm{mm}$ for $D^+ \to K\pi\pi$ candidates with $p_{\mathrm{T}} > 40\,\mathrm{GeV}$, $L_{xy} > 0.0\,\mathrm{mm}$ for D^0 candidates, and $L_{xy} > 0.5\,\mathrm{mm}$ for D_s and D^+ candidates in the $\phi\pi \to (KK)\pi$ channels to reduce the combinatorial background. The impact parameter is required to satisfy $d_0 < 1.0\,\mathrm{mm}$. A sketch of the SV fit with the definitions of the L_{xy} and d_0 variables is shown in Figure 6.1.

The $D^{(*)}$ candidates are required to be isolated by summing the momentum of tracks within a cone with $\Delta R < 0.4$. The momentum of the tracks within the cone are required to be less than the p_{T} of the $D^{(*)}$ for the $D^+ \to K\pi\pi$ and $D^* \to D^0\pi \to (K\pi)\pi$ modes, while the $\phi\pi \to (KK)\pi$ candidates require the $D^{(*)}$ to have twice the momentum of the tracks in the cone. Background from semi-leptonic B decays is reduced by requiring $\Delta R(D^{(*)}, l) > 0.3$.

Finally, the $D^{(*)}$ candidates are required to have $8\,\text{GeV} < p_{\text{T}} < 150\,\text{GeV}$ and $|\eta| < 2.2$. The p_{T} fiducial cuts ensure that $D^{(*)}$ candidates can be accurately reconstructed. The η cut is applied to avoid the edge of the ID where the amount of the detector material rapidly increases and causes a drop in the reconstruction efficiency and a degradation of the resolution.

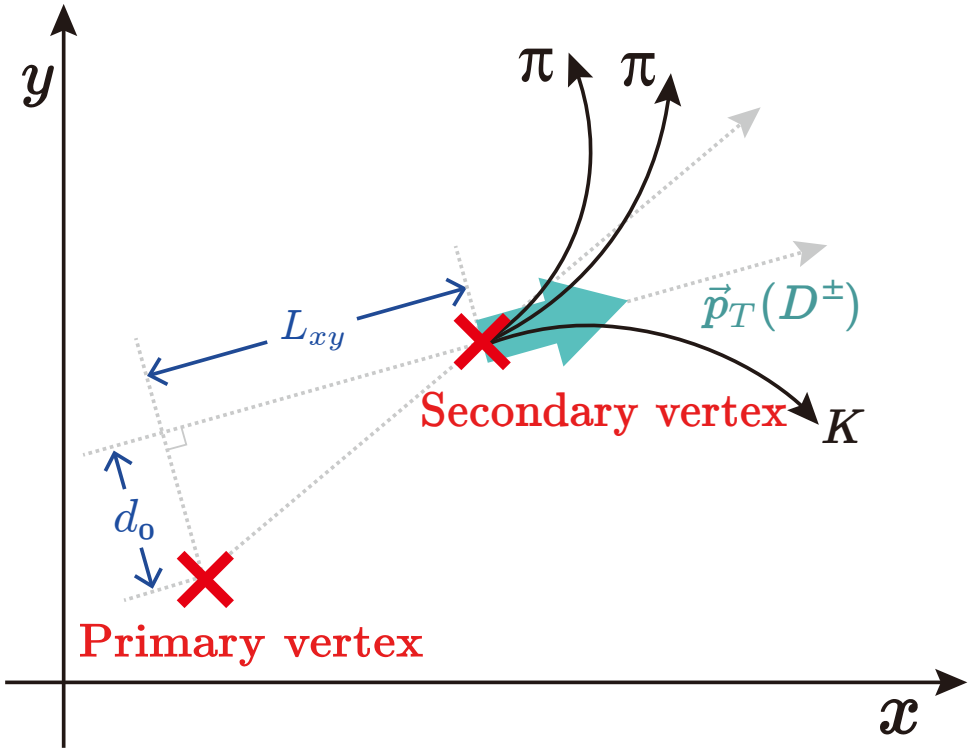

Figure 6.1: A schematic of the SV fit of the $D^+ \to K\pi\pi$ decay, along with the definitions of L_{xy} and d_0 variables used in the $D^{(*)}$ meson reconstruction as explained in the text.

6.1.1 D^+ Meson Specific Reconstruction

There are certain features unique to the $D^+ \to K\pi\pi$ decay that allow for further signal and background separation. The angle between the kaon track in the rest frame of the D^+ candidate and the line of flight of the D^+ candidate in the center-of-mass frame, $cos\theta^*(K)$, is required to be greater than -0.8. Kinematic requirements are applied to D^+ ensure orthogonality from other $D^{(*)}$ decays with similar final states. The contamination of $D^{*+} \to D^0\pi \to K\pi\pi$, which has identical final state content as the $D^+ \to K\pi\pi$ mode, is reduced by requiring $\Delta m = m(K\pi\pi) - m(K\pi) > 160\,\text{MeV}$. Background due to the $\phi\pi \to (KK)\pi$ modes with one of the kaons misidentified as a pion, is removed by requiring the mass of

each pair of oppositely charged particles with the kaon mass hypothesis to be $m(K^+K^-) > |m_\phi^{PDG} - 8\,\text{MeV}|$. Due to the D^+ having the longest lifetime of the weakly decaying open charm, its transverse flight length, is required to satisfy $L_{xy} > 1.1\,\text{mm}$ for candidates with $p_\text{T} < 40\,\text{GeV}$ and $L_{xy} > 2.5\,\text{mm}$ for candidates with $p_\text{T} > 40\,\text{GeV}$. The full selection requirements for D^+ are summarized in Table 6.1.

Table 6.1: D^+ object selection criteria.

D^+ cut	Cut value
N_tracks at SV	3
SV charge	± 1
SV probability	$\chi^2 < 8$
Track p_T	$p_\text{T} > 800\,\text{MeV}$
Track angular separation	$\Delta R < 0.6$
Flight Length ($p_\text{T}(D^+) < 40\,\text{GeV}$)	$L_{xy} > 1.1\,\text{mm}$
Flight Length ($p_\text{T}(D^+) > 40\,\text{GeV}$)	$L_{xy} > 2.5\,\text{mm}$
SV impact parameter	$d_0 < 1\,\text{mm}$
SV 3D impact significance	$\sigma_\text{3D} < 4.0$
Combinatorial background rejection	$cos\theta^*(K) > -0.8$
Isolation	$\Sigma p_\text{T}{}^{\Delta R<0.4}_\text{tracks}/p_\text{T}$ (D)< 1.0
$D_s \to \pi\phi$ rejection	$m(K^+K^-) > \lvert m_\phi^{PDG} - 8\rvert$ MeV
D^* background rejection	$m(KK\pi) - m(K\pi) > 160\,\text{MeV}$
QCD background rejection	$\Delta R(l, D^+) > 0.3$
Fiducial Region	D^+ $p_\text{T} > 8\,\text{GeV}$, $\lvert\eta\rvert < 2.2$

6.1.2 D^* Meson Specific Reconstruction

The $D^* \to D^0\pi \to (K\pi)\pi$ mode exploits the small mass difference between the D^* and D^0 mesons. This small difference restricts the phase space of the associated prompt pion, which has low momentum and hence is referred to as the soft pion. The discriminating variable used in the fit is the mass difference of the D^* and D^0, ($\Delta m(D^*, D^0)$). The D^* decays promptly therefore the secondary vertex is that of the D^0 meson. Due to its relatively shorter lifetime and the reduction in the background provided by the $\Delta m(D^*, D^0)$ requirement, the D^0 is subjected to a transverse flight length cut of $L_{xy} > 0.0$.

The soft pion track is required to have $p_\text{T} > 500\,\text{MeV}$, and an impact parameter of $|d_0| < 1.0\,\text{mm}$. Additionally, the angular separation between the soft pion and the D^0 must be small, $\Delta R(\pi_\text{soft}, D^0) < 0.3$. The mass of the D^0 candidate must be within 40 MeV of the PDG world average value of the D^0 mass, 1864 MeV [14]. The D^* selection requirements are summarized in Table 6.2.

Table 6.2: $D^* \to D^0\pi$ objects selection criteria.

$D^* \to D^0\pi$ cut	Cut value $D^0 \to K\pi$
N_{tracks} at SV	2
SV charge	0
SV probability	$\chi^2 < 10.0$
SV Track p_{T}	$p_{\text{T}} > 600\,\text{MeV}$
Track angular separation	$\Delta R < 0.6$
Flight Length	$L_{xy} > 0\,\text{mm}$
SV 3D impact significance	$\sigma_{\text{3D}} < 4.0$
Isolation	$\Sigma p_{\text{T}}{}^{\Delta R<0.4}_{\text{tracks}}/p_{\text{T}}\ (D^*) < 1.0$
SV impact parameter	$\lvert d_0\rvert < 1\,\text{mm}$
D^0 mass	$\lvert m_{K\pi} - m^{\text{PDG}}_{D^0}\rvert < 40\,\text{MeV}$
$\pi_{\text{soft}} p_{\text{T}}$	$p_{\text{T}} > 500\,\text{MeV}$
π_{soft} angular separation	$\Delta R(\pi_{\text{soft}}, D^0) < 0.3$
$\pi_{\text{soft}} d_0$	$\lvert d_0\rvert < 1\,\text{mm}$
QCD background rejection	$\Delta R(l, D^*) > 0.3$
Phase Space	$D^*\ p_{\text{T}} > 8\,\text{GeV}$, $\lvert\eta\rvert < 2.2$

6.1.3 D_s Meson Specific Reconstruction

The $D_s \to \phi\pi \to (KK)\pi$ decay, and associated $D^+ \to \phi\pi \to (KK)\pi$ decay, leverage the intermediate decay of ϕ mesons and are reconstructed simultaneously. ϕ mesons have a narrow width of $\Gamma = 4.2\,\text{MeV}$ which is used to separate both the true D_s and D^+ candidates from the backgrounds. The two $D^{(*)}$ species in the $\phi\pi \to (KK)\pi$ decay modes are separated only by the mass of the parent particle. Thus, identical reconstruction on $D^{(*)}$ candidates in this mode will reconstruct the peaks of both D_s and D^+, allowing the modes to be analyzed simultaneously.

The angle between the pion track in the rest frame of the D_s or D^+ candidate and the line of flight of the candidate in the center-of-mass frame, $cos\theta^*(\pi)$, is required to be less than 0.8. Kinematic requirements are applied to D^+ ensure orthogonality from other $D^{(*)}$ decays with similar final states. The contamination of $D^{*+} \to D^0\pi \to K\pi\pi$, which has identical final state content as the $D^+ \to K\pi\pi$ mode, is reduced by requiring $\Delta m = m(K\pi\pi) - m(K\pi) > 160\,\text{MeV}$. To take advantage of the ϕ decay, the oppositely charged kaon tracks are required to have a mass of each pair of oppositely charged particles with $m(K^+K^-) < |m^{PDG}_{\phi} - 8\,\text{MeV}|$.

Table 6.3: D_s object selection criteria.

D_s cut	Cut value
N_{tracks} at SV	3
SV charge	± 1
SV probability	$\chi^2 < 6$
Track p_{T}	$p_{\text{T}} > 800$ MeV
Track angular separation	$\Delta R < 0.6$
Flight Length	$L_{xy} > 0.5$ mm
SV impact parameter	$d_0 < 1$ mm
SV 3D impact significance	$\sigma_{\text{3D}} < 6.0$
Combinatorial background rejection	$cos\theta^*(\pi) < 0.8$
Isolation	$p_{\text{T}}(D)$ / $\Sigma p_{\text{T}}^{\Delta R<0.4}_{\text{tracks}} < 0.5$
$D^{\pm} \to K\pi\pi$ rejection	$m(K^+K^-) < \lvert m_{\phi}^{PDG} - 8\rvert MeV\rvert$
QCD background rejection	$\Delta R(l, D^+) > 0.3$
Phase Space	D^+ $p_{\text{T}} > 5$ GeV, $\lvert\eta\rvert < 2.2$

6.2 Event Selection

Events for the analysis are selected through requirements on leptons, $E_{\text{T}}^{\text{miss}}$, jets and $D^{(*)}$ mesons satisfying the criteria defined in Section 5 and Section 6.1. The events must also pass single-lepton triggers as discussed in Section 4.1. Reconstruction of W bosons is based on their leptonic decays to either an electron ($W \to e\nu$) or a muon ($W \to \mu\nu$). The lepton is measured in the detector and the presence of a neutrino is inferred from $E_{\text{T}}^{\text{miss}}$. Events are required to have exactly one `tight` lepton with $p_{\text{T}} > 30\,\text{GeV}$ and $|\eta| < 2.5$. Events with additional `loose` leptons are rejected. To reduce the multijet background and enhance the W boson signal purity, additional requirements are imposed: $E_{\text{T}}^{\text{miss}} > 30\,\text{GeV}$ and $m_{\text{T}} > 60\,\text{GeV}$, where the W boson transverse mass (m_{T}) [146] is defined as $\sqrt{2p_{\text{T}}(\text{lep})E_{\text{T}}^{\text{miss}}(1-\cos(\Delta\phi))}$ and $\Delta\phi$ is the azimuthal separation between the lepton and the missing transverse momentum. Additional regions are constructed for the data-driven modeling of the multijet background, as described in Section 7. Candidate $D^{(*)}$ mesons are reconstructed using a secondary-vertex fit as described in Section 6.1. Any number of $D^{(*)}$ meson candidates satisfying these criteria are permitted, which accounts for the production of multiple mesons in a single event.

Events selected in this way are used to extract the $W + D^{(*)}$ observables with a profile likelihood fit described in Section 8. Furthermore, the selected events are categorized according to the b-jet multiplicity to separate the $W + D^{(*)}$ signal process from the $t\bar{t}$ background with events containing $t \to bW \to c + X$ decays. The ID tracks associated with the reconstructed $D^{(*)}$ candidates are often also associated with a jet mis-tagged as a b-jet. To avoid categorizing these $W + D^{(*)}$ signal events as events with one or more b-jets, the b-jets are required to be

geometrically separated from a reconstructed $D^{(*)}$ meson by satisfying $\Delta R(b\text{-jet}, D^{(*)}) > 0.4$. Events with exactly zero such b-tagged jets are classified as the $W + D^{(*)}$ signal region (SR). Events with one or more b-tagged jets comprise the Top control region (CR). In this way, about 80% of the $t\bar{t}$ background events are in the Top CR and about 99% of $W + D^{(*)}$ signal events remain in the $W + D^{(*)}$ SR, effectively reducing the amount of $t\bar{t}$ background. Collectively, the $W + D^{(*)}$ SR and Top CR are called the "fit regions". These requirements are summarized in Table 6.4(a).

Table 6.4: Tables summarizing the event selection in the analysis: (a) fit regions used in the statistical analysis, (b) the "truth" fiducial selection. The $W + D^{(*)}$ signal is defined by performing the OS-SS subtraction as described in the text.

(a)

Detector-level selection		
Requirement	$W + D^{(*)}$ SR	Top CR
$N(b\text{-jet})$	0	≥ 1
$E_{\mathrm{T}}^{\mathrm{miss}}$	$> 30\,\mathrm{GeV}$	
m_{T}	$> 60\,\mathrm{GeV}$	
Lepton p_{T}	$> 30\,\mathrm{GeV}$	
Lepton $\lvert\eta\rvert$	< 2.5	
$N(D^{(*)})$	≥ 1	
$D^{(*)}$ p_{T}	$> 8\,\mathrm{GeV}$ and $< 150\,\mathrm{GeV}$	
$D^{(*)}$ $\lvert\eta\rvert$	< 2.2	

(b)

Truth fiducial selection	
Requirement	$W + D^{(*)}$
$N(b\text{-jet})$	—
$E_{\mathrm{T}}^{\mathrm{miss}}$	—
m_{T}	—
Lepton p_{T}	$> 30\,\mathrm{GeV}$
Lepton $\lvert\eta\rvert$	< 2.5
$N(D^{(*)})$	≥ 1
$D^{(*)}$ p_{T}	$> 8\,\mathrm{GeV}$
$D^{(*)}$ $\lvert\eta\rvert$	< 2.2

The analysis exploits the charge correlation of the W boson and the charm quark to enhance the signal and reduce the backgrounds. The signal has a W boson and a $D^{(*)}$ meson of opposite charge, while most backgrounds are symmetric in charge. Therefore, the signal is extracted by measuring the difference between the numbers of opposite-sign (OS) and same-sign (SS) $W + D^{(*)}$ candidates, which is referred to as OS–SS. While the signal-to-background ratio is about unity in the OS region, the OS–SS $W + D^{(*)}$ signal is an order of magnitude larger than the remaining background after the subtraction.

The $W + D^{(*)}$ measurement is unfolded to a "truth" fiducial region defined at MC particle level to have exactly one "truth" lepton with $p_{\mathrm{T}}(\ell) > 30\,\mathrm{GeV}$ and $|\eta(\ell)| < 2.5$. The lepton must originate from a W boson decay, with τ decays excluded. Lepton momenta are calculated using "dressed" leptons, where the four-momenta of photons radiated from the final-state leptons within a cone of $\Delta R = 0.1$ around the lepton are added to the four-momenta of leptons. Truth $D^{(*)}$ mesons are selected by requiring $p_{\mathrm{T}}(D^{(*)}) > 8\,\mathrm{GeV}$ and $|\eta(D^{(*)})| < 2.2$. The OS–SS subtraction is also applied to the truth fiducial events. This removes any charge-symmetric processes, which are expected to originate mostly from gluon splitting in the

final state. The $E_{\mathrm{T}}^{\mathrm{miss}}$ and m_{T} requirements and b-jet veto are not included in the fiducial selection. The truth fiducial selection is summarized in Table 6.4(b). The fiducial efficiency is defined as the fraction of $W + D^{(*)}$ signal events from the truth fiducial region that pass the detector-level reconstruction and requirements in Table 6.4(a). In the unfolding for the differential $W + D^{(*)}$ analysis, events where the reconstructed objects pass the event selection but the truth objects fail the truth fiducial requirements are treated as fakes; cases where the reconstructed objects fail the reconstruction fiducial selection but the truth objects pass the truth selection are treated as inefficiencies.

6.3 Charm Meson Truth Matching

Charm mesons that are reconstructed in the $W + D^{(*)}$ analysis are targeted for particular species, however it is possible for charm mesons from other species or decay modes to pass all selection requirements. Therefore, to ensure that the signal can clearly be separated from backgrounds in MC simulation, a procedure is used on the $W+$jets sample to categorize signal and background such that systematic uncertainties can be consistently applied and particles are scaled correctly in the fit used to extract the number of signal events.

$D^{(*)}$ candidates are categorized using a truth matching procedure, which relies on the probability that the constituent tracks of the candidate originate from the $D^{(*)}$ decay daughter particles. This probability is the fraction of reconstructed hits on a track that originate from a particular truth particle to the total reconstructed hits from the layers of the ID on a track; each hit is weighted according to which subdetector it interacts with, as disscussed in Ref. [147]. Tracks with a truth match probability greater than 50% are considered to be matched to the corresponding truth particle. $D^{(*)}$ meson candidates are sorted into categories once their tracks have been truth matched. These categories are summarized in Table 6.5.

The origin of each track with a valid truth link is determined by tracing the simulation history of the MC truth daughter particle to determine if it originates from a $D^{(*)}$ meson decay. If all tracks are truth-matched, originate from the correct charmed hadron species, and are the correct particles for the decay mode, the reconstructed $D^{(*)}$ meson is labelled as $W + D^{(*)}$. If all tracks are truth matched, but they either originate from a different charmed hadron species or from a different decay mode, the reconstructed $D^{(*)}$ meson is labelled as $W + c^{\mathrm{matched}}$. This would include, for example, a D_s being incorrectly reconstructed as a D^+. Matched charm background of the $W + c^{\mathrm{matched}}$ category are assumed to scale with the signal, as the signal is the most precise measurement of the presence of charm. It is necessary in the $W + D_s$ likelihood fit to separate the $W + c^{\mathrm{matched}}$ generic background from the specific $W + D^{+\,\mathrm{matched}}$ background, as the later is assumed to scale with the measurement of D^+, not with the measurement of the D_s.

If at least one but not all tracks are truth matched to a charm hadron, the reconstructed $D^{(*)}$ meson is labelled as $W + c^{\mathrm{mis-matched}}$. Lastly, if none of the tracks are matched to a particle originating from a charm particle, the candidate is labeled $W+$jets. This includes the

combinatorial background originating either from the additional activity in the hard-scatter event, underlying event, or additional pp collisions (pileup).

Events may contain multiple truth level $D^{(*)}$'s, such as results from gluon splitting to $c\bar{c}$, and therefore have multiple truth classified objects that enter into the pre-fit signal or background templates. The object level matching is critical for the unfolding procedure that is used in the fit. In order to correctly capture the truth and reconstructed p_{T} spectrum of the $W + D^{+}$, all candidates in an event must enter into the pre-fit distributions.

Table 6.5: $D^{(*)}$ meson candidate truth matching categories, whether tracks are matched to an object, and from which object the associated truth particles descended. The table identifies the number of tracks from each category that are truth matched to a $D^{(*)}$ and whether those tracks are all from the targeted signal decay mode.

Truth Category	Tracks Matched to a $D^{(*)}$ meson	Decay Mode Match
$W + D^{(*)}$	all	Yes
$W + c^{\mathrm{matched}}$	all	No
$W + c^{\mathrm{mis-matched}}$	> 0 but not all	N/A
$W+$jets	0	N/A

Chapter 7

Multijet Background Estimation

The multijet process is a particularly difficult source of background to model in the $W + D^{(*)}$ $W + D^{(*)}$ SR when a non-prompt or fake lepton is selected instead of the lepton from the W boson. These non-prompt leptons are due to a semi-leptonic heavy flavor decay. The fake leptons are created when a jet or final state radiation electromagnetic interaction is incorrectly reconstructed as a lepton, most commonly for electrons. MC simulations predicting these processes generally have large theoretical uncertainties. Furthermore, a prohibitively large sample of MC events would be required to overcome the low probability of a fake lepton passing the reconstruction criteria. Instead, a data-driven method, called the Matrix Method, is used. Due to statistical limitations, the Matrix Method is only estimated for the $D^+ \to K\pi\pi$ and $D^* \to D^0\pi \to K\pi\pi$ modes; the $\phi\pi \to (KK)\pi$ modes use the estimation from the $D^+ \to K\pi\pi$ channel, as the topology of the decays are similar, but the D^+ mode has much higher statistical power.

7.1 The Matrix Method

The Matrix Method is based on the fact that fake and non-prompt leptons are less likely to be well isolated than real leptons. Collectively, fake and non-prompt leptons are called 'fake' leptons and denoted with 'F'. Prompt leptons originating from hard-scatter decays (e.g. W or Z) are called 'real' and denoted with 'R'. Two sets of lepton working points are defined to exploit the difference in isolation: `tight` leptons are equivalent to those in the signal region and require isolation, and `loose` leptons are equivalent to `tight` leptons with the isolation requirement inverted, see Table 7.1. Leptons passing the `loose` criteria are denoted with the symbol 'L' and leptons passing the `tight` criteria are denoted with 'T', which are dominated by signal leptons. The `tight` leptons are used in the $W + D^{(*)}$ SR definition, and they are a subset of `loose` leptons. An orthogonal working point is also defined by requiring the lepton to pass the `loose` selection and fail the `tight`. They are called the anti-`tight` leptons (!T), and are dominated by fake/non-prompt leptons. The anti-`tight` leptons are used to create orthogonal regions to the $W + D^{(*)}$ fit SRs, where all event selection is the same except the

anti-`tight` lepton working point is used instead. The multijet background is then estimated in a data-driven way by extrapolating the fake/non-prompt leptons from the anti-`tight` to the `tight` region, using the Matrix Method, described in the following paragraph.

The number of events in the $W + D^{(*)}$ fit SR is denoted with N_T and the number of events in the corresponding anti-`tight` region is given by $N_{!T}$. Real and fake lepton efficiencies are defined as the probability of a `loose` lepton passing the `tight` criteria: (r) corresponds to real leptons and (f) corresponds to fake leptons. The number of real (fake) leptons passing the `loose` selection criteria in the $W + D^{(*)}$ SR is denoted with N_R (N_F). By definition, the number of fake leptons in the $W + D^{(*)}$ SR is given by $N_T^{\text{fake}} = fN_F$. In order to measure this in a data-driven way, N_F needs to be expressed with the measurable quantities N_T and $N_{!T}$. The relation between N_T, $N_{!T}$, N_R, and N_F is given by the matrix in Eq. 7.1.

$$\begin{pmatrix} N_T \\ N_{!T} \end{pmatrix} = \begin{pmatrix} r & f \\ 1-r & 1-f \end{pmatrix} \begin{pmatrix} N_R \\ N_F \end{pmatrix}, \tag{7.1}$$

By inverting the matrix, the number of events with real and fake leptons (N_R and N_F) can be expressed with the real and fake efficiencies, r and f, and the number of `tight` and anti-`tight` leptons. The inverted matrix is shown in Eq. 7.2:

$$\begin{pmatrix} N_R \\ N_F \end{pmatrix} = \frac{1}{r-f} \begin{pmatrix} 1-f & -f \\ r-1 & r \end{pmatrix} \begin{pmatrix} N_T \\ N_{!T} \end{pmatrix} \tag{7.2}$$

Using this, N_T^{fake} can now be expressed using only the measurable quantities:

$$N_T^{\text{fake}} = \frac{f}{r-f}\left((r-1)N_T + rN_{!T}\right). \tag{7.3}$$

Eq. 7.3 provides a data-driven way of estimating the number of events caused by a fake lepton by measuring the number of events, both N_T and $N_{!T}$, in the SR. Moreover, a dedicated measurement of the lepton fake and real efficiencies is also needed, as discussed further in Section 7.2. The matrix in Eq. 7.1 becomes singular when f approaches r, so the lepton working points have been defined in a way to separate the two as much as possible.

The real and fake efficiencies, r and f, are sensitive to the choice of trigger, therefore special care is taken to address the 2015 data, which had a separate trigger configuration from 2016-2018 that included isolation, and therefore changed the definitions of the lepton regions. The 2015 data lacked sufficient statistical power for an independent calculation of r and f, and thus instead the efficiencies are calculated for 2016-2018 data and are applied to 2015 data. As the 2015 triggers differ, a conservative uncertainty was assigned to the multijet background, which is addressed in Section 7.2.3. All real and fake efficiencies that follow are computed for 2016-2018 data only.

Table 7.1: Regions in the $W + D^{(*)}$ analysis including the signal region and control regions used to estimate the contribution from fake leptons.

	Fake lepton eff. measurement		Fit regions	
Requirement	1-tag Fake CR	0-tag Fake CR	$t\bar{t}$ CR	$W + D^{(*)}$ SR
N(b-jet)	≥ 1	0	≥ 1	0
$E_{\mathrm{T}}^{\mathrm{miss}}$	$< 30\,\mathrm{GeV}$		$\geq 30\,\mathrm{GeV}$	
m_{T}	$< 40\,\mathrm{GeV}$		$\geq 60\,\mathrm{GeV}$	
Lepton selection	`tight` and anti-`tight` (fake eff. measurement)		`tight` (anti-`tight` to estimate multijet)	
Lepton p_{T}	$> 30\,\mathrm{GeV}$			
Lepton $\lvert\eta\rvert$	< 2.5			
N($D^{(*)}$)	≥ 1			
$D^{(*)}$ p_{T}	$> 8\,\mathrm{GeV}$			
$D^{(*)}$ $\lvert\eta\rvert$	< 2.2			

7.2 Real and Fake Efficiency Determination for the $W + D^{(*)}$ Selection

The real and fake efficiencies, r and f, that serve as inputs to the matrix method are determined from a combination of data and MC. These efficiencies are defined as the fraction of `loose` leptons that pass the `tight` criteria, and are calculated in the signal region or a fake control region for r and f respectively. These regions, and a comparison to the signal region, is shown in Table 7.1.

The r and f used for the $W + D^{(*)}$ selection are calculated by requiring at least one $D^{(*)}$ meson to be present in the regions used for the efficiency determination, to better reflect the fit SR. The inclusion of this requirement is intended to better reflect the fit to the SR.

7.2.1 Real Efficiency Determination for the $W + D^{(*)}$ Selection

Real efficiencies are determined using MC in the signal region. The SR kinematic cuts, selecting the W boson and at least one $D^{(*)}$ meson, are required for the events. In addition, leptons are required to be truth-matched to ensure that only real leptons are selected. Real efficiencies are determined separately for events with zero b-tagged jets and events with one or more b-tagged jets.

Events are split into two categories based on whether the lepton corresponding to the W boson selection is `tight` or anti-`tight`. MC samples are normalized to the predicted cross

sections. The real efficiencies corresponding to the $W + D^{(*)}$ selection are determined as the ratio of the number of events in the `tight` selection to the number of events in the `loose` (anti-`tight` + `tight`) selection:

$$r = N_T/(N_T + N_{!T})$$

where r is the real efficiency. The real efficiency most strongly depends on the lepton kinematics (e.g. isolation/ID/trigger efficiencies) so it is expressed in bins of lepton p_{T} and $|\eta|$ along with the b-jet classification.

Real efficiencies are calculated for multiple MC samples to assess the effect of process-dependencies and generator effects on the real efficiencies. The samples used for the real efficiency determination are SHERPA 2.2.11 $W+$jets, LO MADGRAPH $W+$jets and $t\bar{t}$.

No differences exceeding 0.5% - 1.5% are observed between the 0-tag and 1-tag selections, for SHERPA $W+$jets, MADGRAPH $W+$jets and $t\bar{t}$ MC samples, or for D^+ vs D^*. Thus SHERPA $W+$jets and the $t\bar{t}$ efficiencies are averaged, to further reduce statistical uncertainties. Real efficiencies are shown in Figure 7.1 for the electron channel. Four η bins are defined; two in the barrel region and two in the end-cap. Real efficiencies for the muon channel are presented in Figure 7.2. Three η bins are defined for muons. In general, real efficiencies are very close to 1.0, indicating that the chance of prompt `loose` leptons failing the `tight` criteria and passing the anti-`tight` selection is very low. This is desired in view of the matrix method.

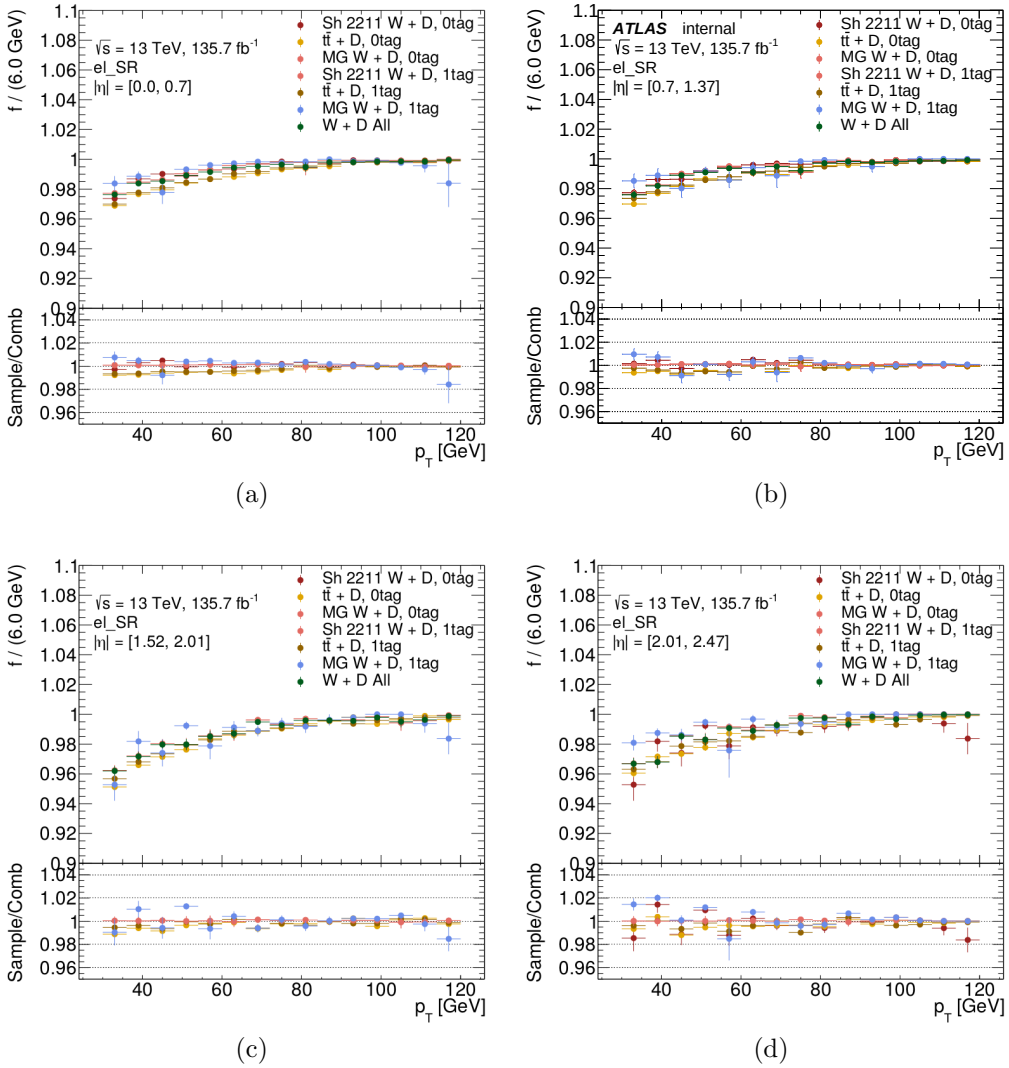

Figure 7.1: Real efficiencies for the electron channel in the categories that are used to estimate the fake rate, and the efficiency weighted average. These categories are the real rates estimated from the SHERPA 2.2.11 sample, the $t\bar{t}$ sample, the LO MADGRAPH sample in both the 0-tag and 1-tag channel. Plots are shown in bins of electron p_{T} separately for each η bin: (a) $0.0 \geq |\eta| < 0.7$, (b) $0.7 \geq |\eta| < 1.37$, (c) $1.52 \geq |\eta| < 2.01$, and (d) $2.01 \geq |\eta| \leq 2.47$. The error bars on each point are the statistical uncertainties in the real efficiencies.

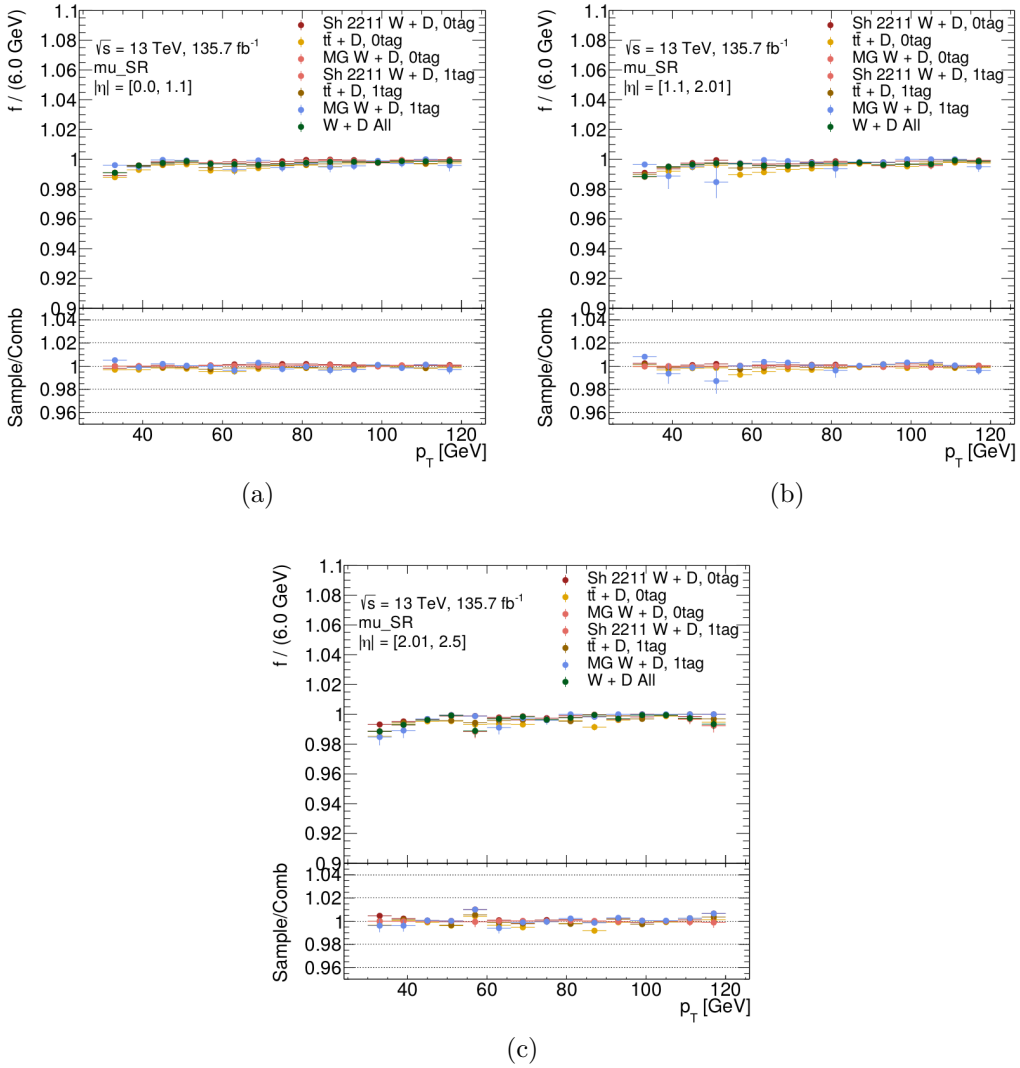

Figure 7.2: Real efficiencies for the muon channel. These categories are the real rates estimated from the SHERPA 2.2.11 sample, the $t\bar{t}$ sample, the LO MADGRAPH sample in both the 0-tag and 1-tag channel and the weighted combination of each of them. The muon real efficiencies are show as a function of p_{T} separately for each η bin: (a) $0.0 \geq |\eta| < 1.1$, (b) $1.1 \geq |\eta| < 2.01$, and (c) $2.01 \geq |\eta| < 2.5$. The error bands are the statistical uncertainties in the real efficiencies.

7.2.2 Fake Efficiency Determination for the $W + D^{(*)}$ Selection

Similar to real efficiencies, fake efficiencies are determined in bins of p_{T}, η and b-jet multiplicity to account for the corresponding dependencies in lepton isolation efficiencies and effects due to different amount and type of traversed material in the path of the lepton. In addition, it was observed that the fake efficiencies are different in the $W + D^{+}$ and $W + D^{*}$ selection, so they cannot be combined as they are in the case of the real efficiencies.

A pure sample of fake leptons is needed to measure the fake efficiency, MC samples cannot be directly used to create this sample because the processes leading to fake leptons are relatively rare and difficult to model accurately. A preferred strategy is to perform a selection in the data that maximally rejects prompt leptons and is orthogonal to all regions used in the final statistical analysis. Any residual contribution from prompt leptons is then subtracted using truth-matched MC samples. Because the estimation of these efficiencies requires this prompt subtraction, systematic uncertainties that affect the yield and shape of the prompt MC are included when estimating the fake rate. These systematics include QCD scale, MET control region, and MC generator and are described in more detail in Section 7.2.3. The region where the fake efficiency is calculated is called the Fake CR and is defined by inverting the $E_{\mathrm{T}}^{\mathrm{miss}}$ cut and restricting the m_{T} used for the $W+$jets selection while applying all the other $W + D^{(*)}$ SR cuts, as also indicated in Table 7.1:

- $m_{\mathrm{T}} < 40\,\mathrm{GeV}$
- $E_{\mathrm{T}}^{\mathrm{miss}} < 30\,\mathrm{GeV}$

To mimic the environment of leptons in the signal region selection, at least one $D^{(*)}$ meson is required to be present in the event.

Nominally, the Sherpa $W+$jets MC sample is used for the subtraction. Inclusively, the fraction of fake leptons after the MC subtraction is between 25% and 80% in the `tight` electron channel, between 15% and 60% in the `tight` muon channel, depending on lepton p_{T}. The fraction of fake or non-prompt leptons is always very high in the anti-`tight` regions (i.e. above 90%). The fake efficiencies corresponding to the $W + D^{(*)}$ selection are then determined as the ratio of the number of fake leptons in the `tight` selection to the number of events in the anti-`tight` selection:

$$f = N_T/(N_T + N_{!T})$$

where f is the fake efficiency.

For both muons and electrons, η bins are defined identical to the real efficiency estimation (see Section 7.2.1). The lepton p_{T} bin widths vary from 5 GeV to 20 GeV for the leptons in both the D^{+} and D^{*} in the 0-tag region. The electron efficiency is parameterized up to 120 GeV, with the last bin including overflow, for D^{+} and D^{*} because both channels suffer from statistical limitations at higher values of lepton p_{T}. Because fake muons are very rare at higher energies, parameterization could be implemented only up to 55 GeV in the 0-tag

region, with higher values of lepton p_{T} contained in the overflow bin. The bin size and upper limit of the efficiency were chosen due to trigger configurations and limited statistics at high lepton p_{T}. In the 1-tag regions only two p_{T} bins were used in the electron channel from 30 GeV - 80 GeV and only one p_{T} bin was used in the muon channel due to the very low statistics. The last p_{T} bin includes all leptons with higher energies in all cases.

Fake efficiencies for the D^+ electron channel are shown in Figure 7.3 for 0-tag. The fake efficiency plots for D^* are shown for 0-tag in Figure 7.4. These efficiencies are quite high in the CR, with generally low dependence on QCD variations or choice of MC sample. Structure is observed in the fake efficiencies around p_{T} equal to 60 GeV. This corresponds to the trigger requirement outlined in Section 4.1.

Fake efficiencies for the D^+ muon channel are shown in Figure 7.5 for 0-tag. The fake efficiency plots for D^* are shown for 0-tag in Figure 7.6. The efficiencies for muons are smaller than for electrons, which is expected given that the only source of "fake" muons is from non-prompt heavy flavor decays, whereas electrons have multiple sources. Additionally, the high p_{T} trigger is visible when the trigger becomes fully efficient around 55 GeV.

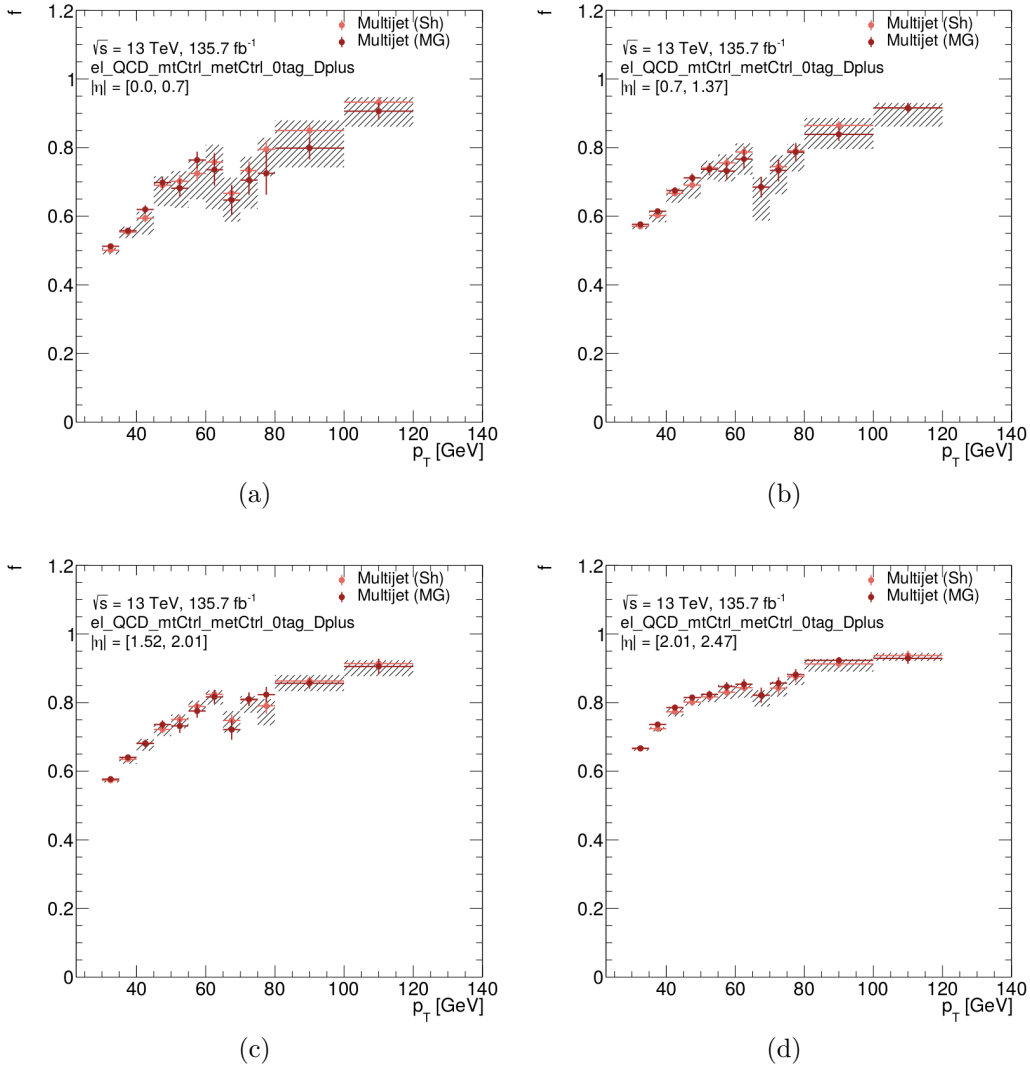

Figure 7.3: Fake efficiencies for the $W + D^+$ electron channel in the 0-tag selection for the SHERPA (Sh) and MADGRAPH (MG) W+jets samples. Plots are shown in bins of electron p_{T} separately for each η bin: (a) $0.0 \geq |\eta| < 0.7$, (b) $0.7 \geq |\eta| < 1.37$, (c) $1.52 \geq |\eta| < 2.01$, and (d) $2.01 \geq |\eta| \leq 2.47$. The error bars are the statistical uncertainty in the fake efficiency, while the hatched bands represent the QCD scale variations, implemented as described in Section 7.2.3.

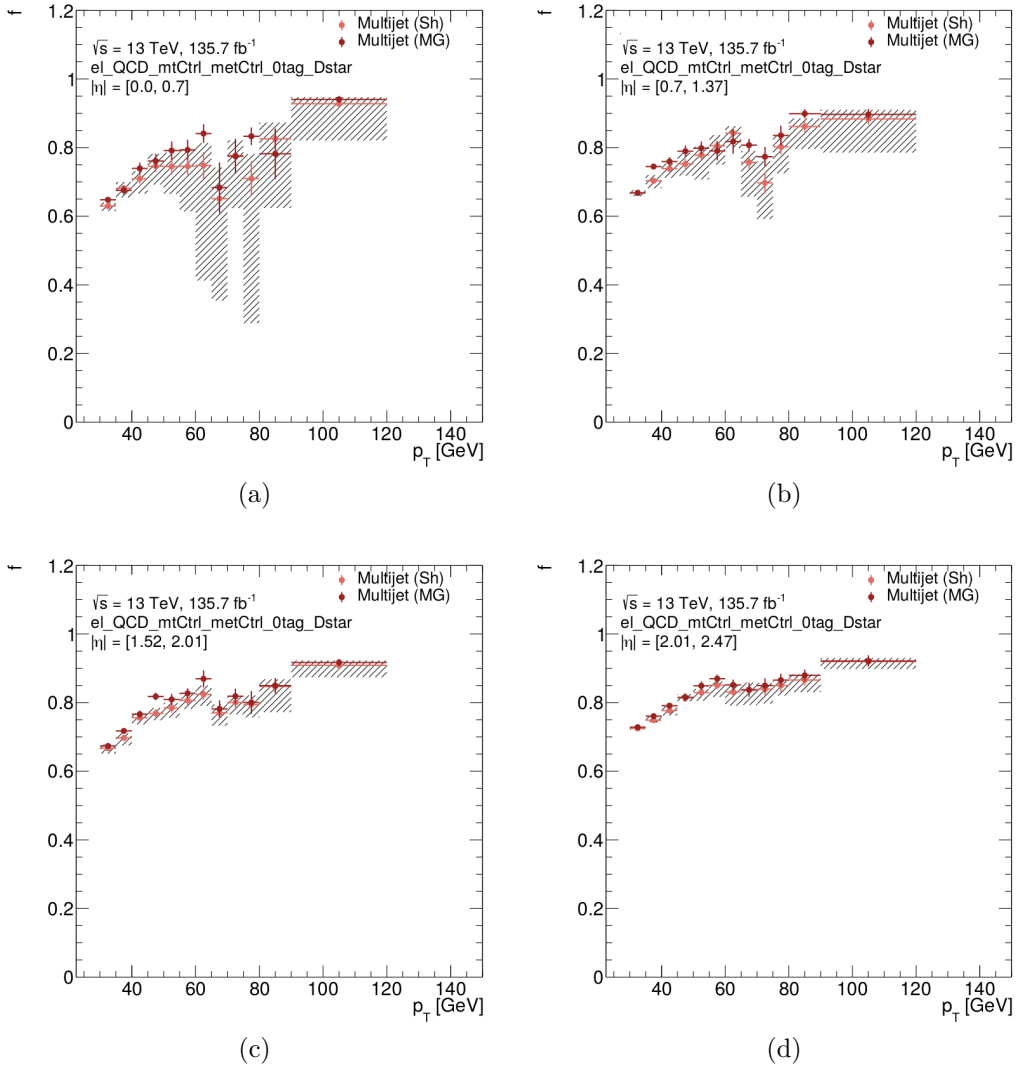

Figure 7.4: Fake efficiencies for the $W + D^*$ electron channel in the 0-tag selection for the SHERPA (Sh) and MADGRAPH (MG) W+jets samples. Plots are shown in bins of electron p_{T} separately for each η bin: (a) $0.0 \geq |\eta| < 0.7$, (b) $0.7 \geq |\eta| < 1.37$, (c) $1.52 \geq |\eta| < 2.01$, and (d) $2.01 \geq |\eta| \leq 2.47$. The error bars are the statistical uncertainty in the fake efficiency, while the hatched bands represent the QCD scale variations, implemented as described in Section 7.2.3.

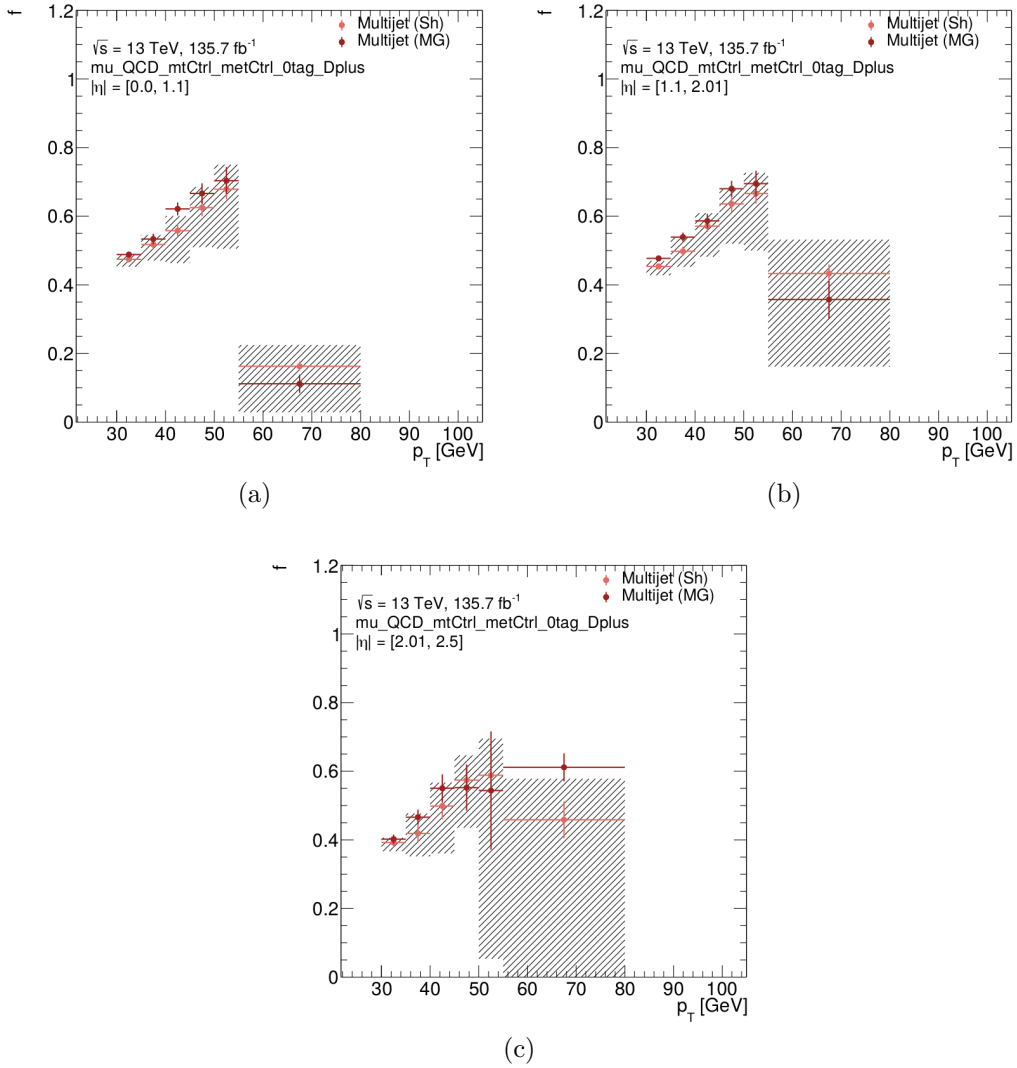

Figure 7.5: Fake efficiencies for the $W + D^+$ muon channel in the 0-tag selection for the SHERPA (Sh) and MADGRAPH (MG) W+jets samples. Plots are shown in bins of muon p_{T} separately for each η bin: (a) $0.0 \geq |\eta| < 1.1$, (b) $1.1 \geq |\eta| < 2.01$, and (c) $2.01 \geq |\eta| < 2.5$. The error bars are the statistical uncertainty in the fake efficiency, while the hatched bands represent the QCD scale variations, implemented as described in Section 7.2.3.

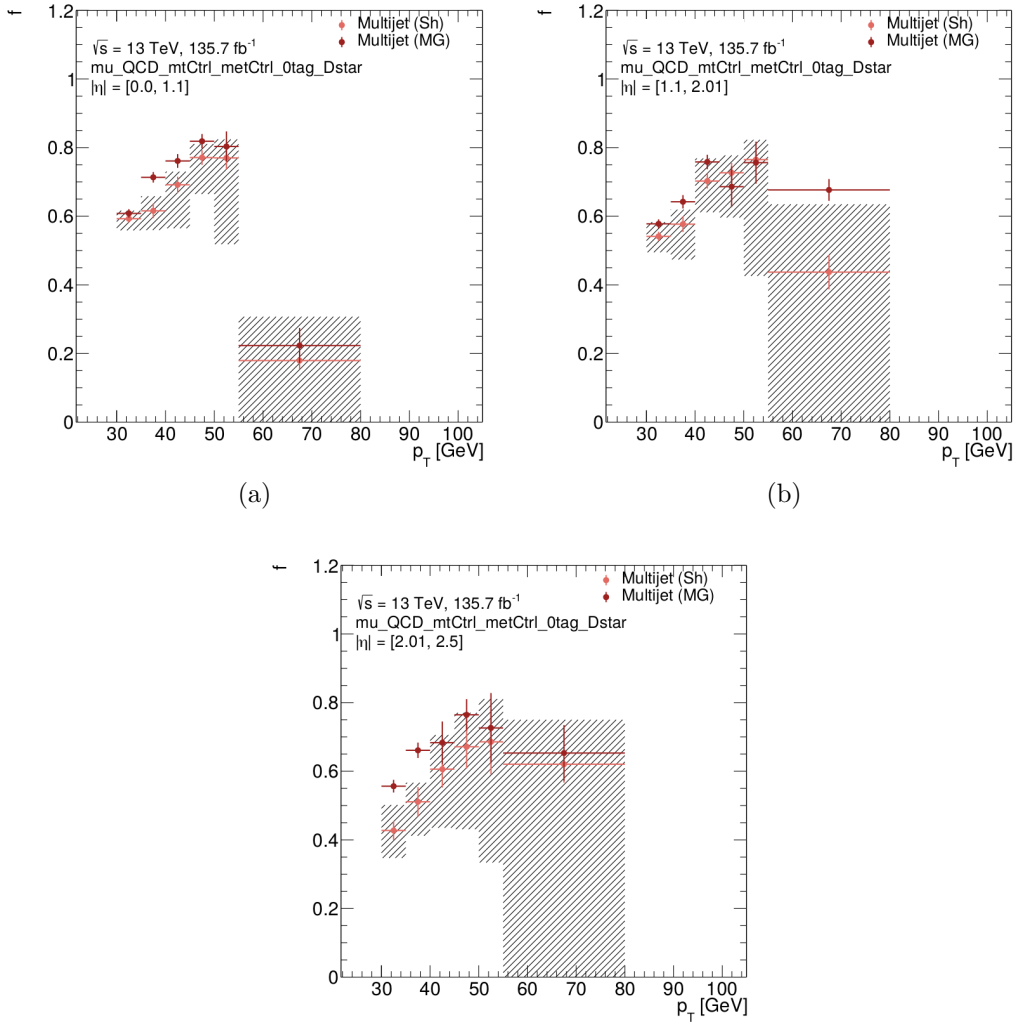

Figure 7.6: Fake efficiencies for the $W + D^*$ muon channel in the 0-tag selection for the SHERPA (Sh) and MADGRAPH (MG) W+jets samples. Plots are shown in bins of muon p_{T} separately for each η bin: (a) $0.0 \geq |\eta| < 1.1$, (b) $1.1 \geq |\eta| < 2.01$, and (c) $2.01 \geq |\eta| < 2.5$. The error bars are the statistical uncertainty in the fake efficiency, while the hatched bands represent the QCD scale variations, implemented as described in Section 7.2.3.

7.2.3 Systematic Uncertainties Associated with the Matrix Method for $W + D^{(*)}$

Systematic uncertainties related to the matrix method are estimated by using multiple MC samples in the real and fake efficiency determination. The statistical uncertainty is evaluated by considering the finite statistics of the data and MC samples used for the efficiency measurements.

The statistical uncertainty of the overall method is evaluated by varying all real and fake efficiencies up or down by one standard deviation and propagating this through the matrix method. The variation is performed independently for real and fake efficiencies, giving one variation for each. This estimation is conservative because in reality the bins of fake and real efficiencies are uncorrelated and should be varied separately. However, this would result in an unnecessarily large number of nuisance parameters in the fit. The uncertainty due to finite statistics is in most cases smaller than the other uncertainties.

Systematic uncertainties associated with the fake efficiency measurement are:

- Difference between MadGraph and Sherpa $W+$jets samples used to estimate the prompt contamination
- QCD scale variations in the Sherpa $W+$jets sample used to estimate the prompt contamination
- Variation of the $E_{\mathrm{T}}^{\mathrm{miss}}$ region used to estimate the fake efficiency

While the matrix method is primarily data driven, the use of prompt MC subtracted from data requires systematic variations, the impact of which is summarized in Table 7.2. In particular, the systematic variations in the normalization and shape of the $W+$jets MC has a non-negligible impact on estimated fake efficiency, from $1-2\%$ to 50% depending on the lepton species and the bin in p_{T} and η; refer to Figures 7.3–7.6. The MadGraph variation gives one NP using a two-point variation for the generator that is subtracted from the data in the fake control region. This systematic is symmetrized in the fit with respect to its impact on the multijet background yield.

The QCD variation is the combination of a set of five scale variations in the matrix element and parton shower. As the QCD scale can impact the size of the prompt contamination in the CR, varying the scale has an impact on the estimated fake efficiency. The uncertainty was determined bin-by-bin in the p_{T} and η parameterizations by choosing the maximum deviation, both up and down, in fake efficiency from all five scale variations. This results in an asymmetric up and down variation in yield and shape for the multijet estimate. The QCD scale variations that are selected are those found to have the largest impact on the prompt MC subtraction, while subleading α_{s} and PDF uncertainties are neglected.

The largest uncertainty on the fake efficiency estimation results from varying the MET region used to estimate the fake efficiency, and covers disagreement in the $E_{\mathrm{T}}^{\mathrm{miss}}$ modeling, as seen in Sect7.2.4. The nominal fake efficiency comes from the control region with $E_{\mathrm{T}}^{\mathrm{miss}} <$

30 GeV, as opposed to a more signal-like region with $E_{\mathrm{T}}^{\mathrm{miss}} > 30\,\mathrm{GeV}$. This choice was made for two reasons. First, this control region with lower $E_{\mathrm{T}}^{\mathrm{miss}}$ is consistent with the control region used to estimate the multijet background for the inclusive $W+$jets sample.The higher $E_{\mathrm{T}}^{\mathrm{miss}}$ control region showed significant mismodeling for the inclusive $W+$jets and thus for analysis consistency the same region is preferred for the $W+D^{+}$ multijet estimate. Secondly, the lower $E_{\mathrm{T}}^{\mathrm{miss}}$ control region has a larger fraction of fake leptons. Since there are more fake leptons in this control region, the relative size of other uncertainties to the multijet background is smaller, without losing any information since all systematics are included. This improves the behavior of the fit, by ensuring that systematic variations do not exceed 100%. This uncertainty is the largest systematic uncertainty for the multijet estimate, as summarized in Table 7.2, and varies from 50% for electrons to 70% for muons. These uncertainties are applied to the fit as nuisance parameters as described in Section 8.3.

Table 7.2: Fractional systematic uncertainties on the multijet background estimate resulting from the matrix method, for both $D^{(*)}$ species. All uncertainties are assessed simultaneously for the OS+SS region, with the SR requirements of $E_{\mathrm{T}}^{\mathrm{miss}} > 30\,\mathrm{GeV}$ and $m_{\mathrm{T}} > 60\,\mathrm{GeV}$. The presence of a $D^{(*)}$ is required and the lepton requirements are equivalent to the signal region.

Variation	D^{+} electron	D^{+} muon	D^{*} electron	D^{*} muon
Real Efficiency Statistical Variation	9.0%	8.0%	9.0%	18%
Fake Efficiency Statistical Variation	8.0%	9.0%	8.0%	13%
MadGraph Fake Efficiency Variation	1.0 %	2.0%	11%	41%
QCD Fake Efficiency Variation	9.0%	24%	12%	37%
MET CR Region Fake Efficiency Variation	46%	56%	52%	71%

The size of the systematic uncertainties varies based on each channel, but is approximately the same in both the OS and SS categories. For electrons, the total size of the systematic uncertainty is approximately 50%, added in quadrature. The dominant uncertainty is the choice of $E_{\mathrm{T}}^{\mathrm{miss}}$ region in the fake efficiency estimation. For muons, the total size of the systematic uncertainty is approximately 70%, added in quadrature. The dominant uncertainty is the choice of $E_{\mathrm{T}}^{\mathrm{miss}}$ region in the fake efficiency estimation.

7.2.4 Validation of the Matrix Method

Figure 7.7 demonstrates the extrapolation of the multijet background from the Fake CR to the $W + D^{(*)}$ SR. Without the OS–SS subtraction, most of the D mesons in the Top background originate from B meson decays. This background is larger in the D^{+} channel than in the D^{*} channel. For the D^{*}, because the slow pion in the reconstruction chain is required to be associated with the PV, charmed mesons produced in B meson decays often fail this requirement due to the sizable average lifetime of the B mesons. The central values of the fake-

lepton efficiencies are calculated in the $m_{\mathrm{T}} < 40\,\mathrm{GeV}$ region, but with the $E_{\mathrm{T}}^{\mathrm{miss}}$ requirement inverted ($E_{\mathrm{T}}^{\mathrm{miss}} < 30\,\mathrm{GeV}$). The figure instead shows the events with the $E_{\mathrm{T}}^{\mathrm{miss}} > 30\,\mathrm{GeV}$ requirement corresponding to the $W + D^{(*)}$ SR selection. The prediction disagrees with the data at low m_{T} due to an $E_{\mathrm{T}}^{\mathrm{miss}}$ dependence in the fake-lepton efficiencies that is not directly accounted for in the parameterization. A systematic uncertainty is introduced, as described above, by calculating the fake-lepton efficiencies with the $E_{\mathrm{T}}^{\mathrm{miss}} > 30\,\mathrm{GeV}$ requirement and taking the full difference between the two multijet predictions as the uncertainty. Since this is the largest systematic uncertainty in the multijet background, the data is almost exactly covered by the one-standard-deviation variation in this region. Furthermore, the multijet prediction and the uncertainties are extrapolated into the $W + D^{(*)}$ SR with the $m_{\mathrm{T}} > 60\,\mathrm{GeV}$ requirement. To validate the extrapolation, the prediction is evaluated in a validation region (VR) with an m_{T} requirement of $40\,\mathrm{GeV} < m_{\mathrm{T}} < 60\,\mathrm{GeV}$. Figure 7.7 shows that the prediction in the VR is in agreement with the data within the systematic uncertainties, indicating that the multijet background is appropriately modeled.

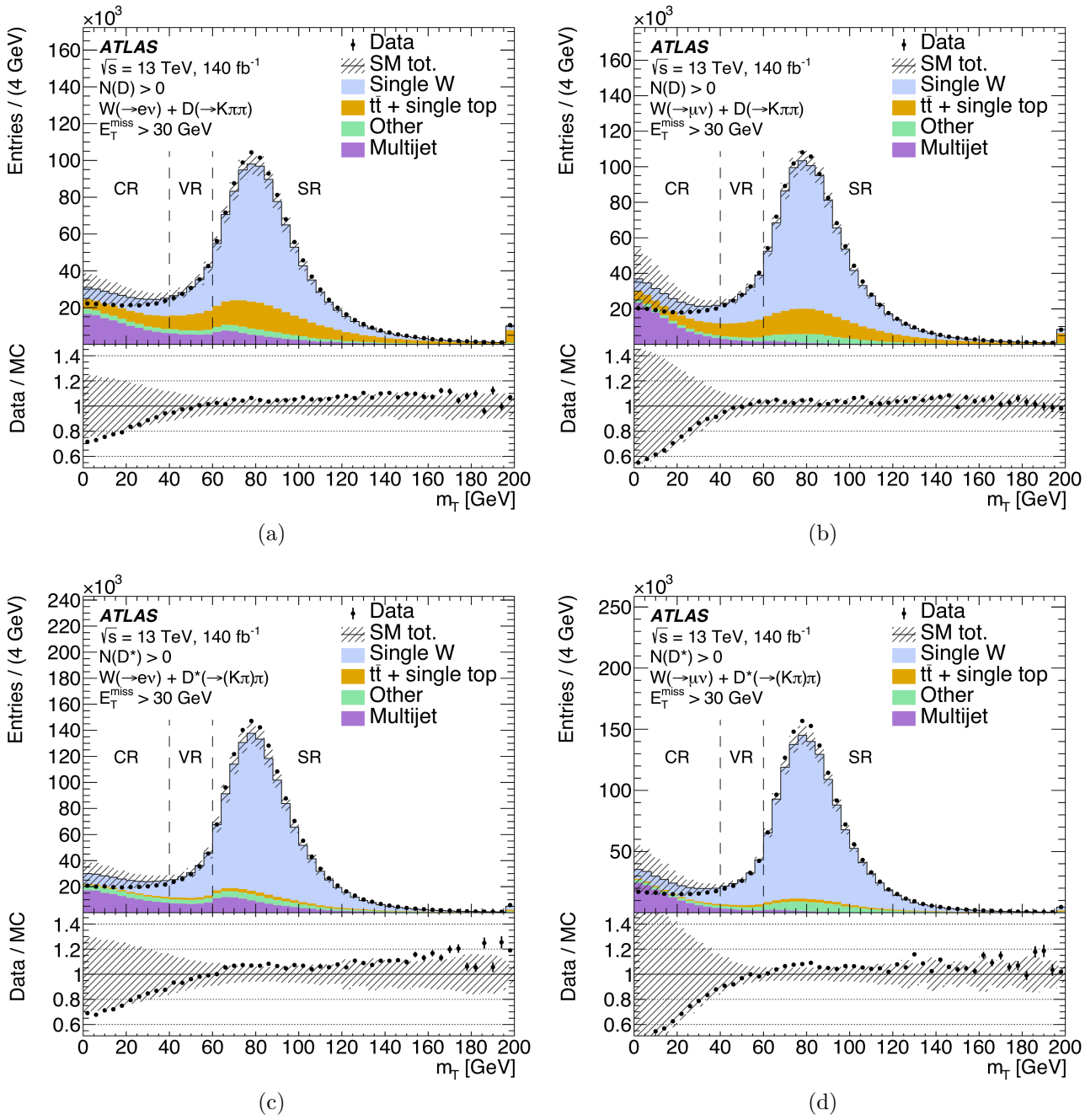

Figure 7.7: Modeling distributions of the m_{T} variable using the Matrix Method to estimate the multijet background. The distributions are (a) m_{T} in the D^{+} electron channel, (b) m_{T} in the D^{+} muon channel, (c) m_{T} in the D^{*+} electron channel, (d) m_{T} in the D^{*+} muon channel. The "SM Tot." line represents the sum of all signal and background samples and the corresponding hatched uncertainty band includes all Matrix Method systematic uncertainties, $E_{\mathrm{T}}^{\mathrm{miss}}$ systematic uncertainties, and QCD scale variations. The "Single W" component includes all contributions from Table 8.5. Dashed vertical lines indicate the m_{T} values defining the control, validation, and signal regions (CR, VR, and SR) as explained in the text. The last bin also includes the events with $m_{\mathrm{T}} > 200\,\mathrm{GeV}$.

Chapter 8

Profile Likelihood Fit

This Chapter describes the profile likelihood fit and its required inputs which extract the observables in both the $W + D^{(*)}$ differential cross section measurement and the $\phi\pi \to (KK)\pi$ inclusive measurements. A statistical fitting procedure based on the standard profile-likelihood formalism used in LHC experiments [148] [149] is employed to extract the observables from the data with corresponding uncertainties. The variable that is fit is the mass (or mass difference) of the $D^{(*)}$ candidate. The observables of interest are:

- absolute (or inclusive) fiducial cross sections: $\sigma(W^-+D^{(*)})$ and $\sigma(W^-+D^{(*)})$,
- the ratio of the inclusive cross section for a positively charged W to a negatively charged W: $R_c^{\pm}$,
- *differential cross sections for W^-+D^+ and $W^+ + D^-$. Two differential variables are considered, $p_{\mathrm{T}}(D^{(*)})$ and $|\eta(\ell)|$, each having 5 bins– 10 values in total,
- † the ratio of D^+ to D_s, in the same decay channel: R_{D^+/D_s}.

Note that items marked with * are only calculated in the differential analysis, and those marked with † are computed only in the inclusive $W + D_s$ analysis.

The profile likelihood fit can be performed either inclusively or with respect to a differential variable. The fit employs templates of the invariant mass distribution of the signal and background obtained from the simulation (or from data in the case of the multijet background) that result from explicitly reconstructing charm hadrons. The likelihood fit enables the estimation of background normalization and constraining of systematic uncertainties *in-situ* by extracting the information from the data in mass peak sidebands and control regions. It is a crucial ingredient in achieving percent-level precision in the $W + D^{(*)}$ differential cross section measurement and properly accounting for the systematic uncertainties in the $\phi\pi \to (KK)\pi$ measurements.

Section 8.1 explains the inputs that are needed to perform the fit for both differential $W + D^{(*)}$ and inclusive $\phi\pi \to (KK)\pi$ analyses including signal and background categories,

and Section 8.2 shows the pre-fit signal and background templates that are used in the profile likelihood fit. The formalism of the profile likelihood fit is given in Section 8.3.

8.1 Fit Inputs

The $W + D^{(*)}$ cross sections are extracted from profile likelihood fits to the candidate mass (for D^+ and D_s) or mass difference (for D^*) distributions. The likelihood functions are expressed in terms of the signal strength μ with respect to a baseline signal cross section (denoted the cross section prior), obtained from the SHERPA2.2.11 MC generator, as described in Section 4.2. Other inputs to the likelihood function are the fiducial efficiencies, the detector response matrices, and the signal and background fit templates.

Likelihood fits are performed differentially and simultaneously in bins of p_{T} $(D^{(*)})$ and $\eta(\mathrm{lep})$ for the differential $W + D^{(*)}$ analysis and inclusively in the $W + D_s$ inclusive analysis. The differential measurement is performed in bins of p_{T} $(D^{(*)})$ because it is a powerful observable for tuning MC modeling for vector boson plus heavy flavor production and discerning which MC configurations are consistent with the observed data. The bin edges of the five differential p_{T} $(D^{(*)})$ bins are given in Table 8.1. The last bin starts at 80 GeV and has no upper limit. The number of bins and bin edges were chosen such that the expected data statistical uncertainty is about 1 to 2% in the first four bins. The available MC statistics also play an important role in determining the bin size; up to a 1% statistical uncertainty is present in the diagonal elements of the detector response matrix, discussed in Section 8.1.3.

Differential $\eta(\mathrm{lep})$ distributions are sensitive to the s-quark PDF. The choice of the PDF set significantly impacts the shape of the pseudorapidity of the lepton, and thus an unfolded $\eta(\mathrm{lep})$ distribution can be used to improve future PDF fits. Similarly as in the p_{T} $(D^{(*)})$ fits, five bins are chosen in $\eta(\mathrm{lep})$ to allow for a percent-level precision. Furthermore, the absolute value of the pseudorapidity is used to further improve the statistics because there is no additional discriminating power in measuring the sign of the pseudorapidity. The $|\eta(\ell)|$ bin edges are given in Table 8.2.

Table 8.1: The differential p_{T} $(D^{(*)})$ bins used in the $W + D^{(*)}$ likelihood fit. The last p_{T} $(D^{(*)})$ bins has no upper limit.

Bin number	1	2	3	4	5
p_{T} $(D^{(*)})$ lower edge [GeV]	8	12	20	40	80
p_{T} $(D^{(*)})$ upper edge [GeV]	12	20	40	80	—

Table 8.2: The differential η(lep) bins used in the $W + D^{(*)}$ likelihood fit.

Bin number	1	2	3	4	5
$\|\eta(\ell)\|$ lower edge	0.0	0.5	1.0	1.5	2.0
$\|\eta(\ell)\|$ upper edge	0.5	1.0	1.5	2.0	2.5

8.1.1 Cross Section Prior

The baseline $\sigma(W + D^{(*)})^{\text{OS-SS}}$ cross sections for the fiducial $W + D^{(*)}$ selection used in the likelihood fits are derived using the SHERPA2.2.11 forced decay $W + D^{(*)}$ samples corrected to the world average production fractions by reweighting the simulated data, using the techniques developed in ATLAS for this purpose [87]. The absolute fiducial cross section priors are given in Table 8.3. These correspond to the OS-SS cross section in the fiducial region of lepton $p_{\text{T}} > 30\,\text{GeV}$ and $|\eta| < 2.5$ and charmed hadron $p_{\text{T}} > 8\,\text{GeV}$ and $|\eta| < 2.2$ with no additional requirements on the neutrino p_{T}. The $W + D^*$ cross sections are larger than the $W + D^+$ cross sections due to the application of production fraction weights only for D^+, D^0, D_s, and charm baryons. The reweighting procedure is only applied to weakly decaying D hadrons and does not properly bring the D^* fraction to the world average value. T his, however, has no impact on the fitted cross section since the result is independent of the size of the prior.

Table 8.3: The fiducial $\sigma(W + D^{(*)})^{\text{OS-SS}}$ cross section priors obtained with the SHERPA2.2.11 forced decay $W + D^{(*)}$ samples. Production fraction weights are applied as described in the text. The uncertainties given are the statistical uncertainties only.

Channel	$\sigma(W + D^+)^{\text{OS-SS}}$ [pb]		$\sigma(W + D^*)^{\text{OS-SS}}$ [pb]		$\sigma(W + D_s)^{\text{OS-SS}}$ [pb]	
e^-	44.648 $\pm$	0.051	50.800 $\pm$	0.065	13.844 $\pm$	0.050
e^+	44.218 $\pm$	0.057	50.880 $\pm$	0.069	14.088 $\pm$	0.054
μ^-	44.890 $\pm$	0.051	50.994 $\pm$	0.066	13.856 $\pm$	0.051
μ^+	44.330 $\pm$	0.055	51.107 $\pm$	0.070	14.104 $\pm$	0.054
Total	178.09 $\pm$	0.11	203.78 $\pm$	0.14	55.892 $\pm$	0.10

8.1.2 Fiducial Efficiencies

The fiducial efficiency ϵ_i^{fid} is defined as the fraction of $W + D^{(*)}$ events produced in the differential fiducial bin i, or as a single inclusive number, that also satisfy the signal region reconstruction criteria, which can be seen in Table 6.4(a). Truth matching described in Section 6.3 is used to select only the $D^+ \to K\pi\pi$, $D^* \to D^0\pi \to K\pi\pi$, $D_s \to \phi\pi \to (KK)\pi$, and $D^+ \to \phi\pi \to (KK)\pi$ candidates. The corresponding fiducial efficiencies for multiple $W+$jets and $W + D^{(*)}$ MC samples are shown in Figure 8.1 for the differential $W + D^{(*)}$ analysis and in Table 8.4 for the inclusive $W + D_s$ analysis.

Forced decay $W + D^{(*)}$ MC samples generally have smaller statistical uncertainties than the $W+$jets samples. The Sherpa2.2.11 forced decay $W + D^{(*)}$ sample is used for the nominal value and for deriving the theory systematic uncertainties.

Several uncertainties related to the fiducial efficiency are implemented as systematic uncertainties in the $W + D^{(*)}$ cross section fit. These are:

- Statistical uncertainty due to the finite number of generated MC events used to evaluate the fiducial efficiency,
- $W+$jets modeling uncertainty, defined as the difference in the fiducial efficiency between various $W + D^{(*)}$ samples obtained with different MC generators,
- $W+$jets theory uncertainties: QCD scale, PDF, and α_s uncertainties.

The statistical uncertainty is calculated as the binomial uncertainty in each lepton channel individually. This uncertainty is negligible in inclusive fits where no differential bins are used ($< 1\%$) and it becomes larger in the differential fits, where the efficiency needs to be calculated in the corresponding bins. The statistical uncertainty is discussed further in Section 8.1.3.

The modeling uncertainty is estimated by taking the maximum difference between the fiducial efficiencies calculated with NLO MadGraph, MadGraph5_aMC@NLO (FxFx), and Sherpa2.2.11 samples in each differential bin (the difference between blue (Sherpa2.2.11) and the maximum of red (NLO MadGraph) and green (MadGraph5_aMC@NLO (FxFx)) points in Figure 8.1). In general, MadGraph5_aMC@NLO (FxFX) and Sherpa2.2.11 are in better agreement with each other than with NLO MadGraph. The uncertainty has a shape dependence and can be up to 4% in size. This is one of the largest systematic uncertainties in the $W + D^{(*)}$ measurement. The difference originates from the different modeling of the W kinematics and subsequently from the correlation between W and $D^{(*)}$ kinematics in the $W + D^{(*)}$ selection. For example, a truth-only study of the W acceptance ($E_{\text{T}}^{\text{miss}} > 30\,\text{GeV}$ and $m_{\text{T}} > 60\,\text{GeV}$) as a function of $D^{(*)}$ p_{T} shows discrepancies at the same level. This uncertainty could be reduced by adding the $E_{\text{T}}^{\text{miss}}$ and m_{T} cuts in the truth fiducial selection (Table 6.4(b)), but that would bring complications in the fit related to the large non-fiducial signal due to the poor $E_{\text{T}}^{\text{miss}}$ resolution.

The $W + D^{(*)}$ theory uncertainties in the fiducial efficiency are calculated using the event weight variations in Sherpa2.2.11 samples using the LHAPDF prescription [150]. The PDF and α_s uncertainties are found to have a negligible effect. The QCD scale 7-point variations

and the corresponding envelope are shown in Figure 8.1. The size of the uncertainty is smaller than the modeling uncertainty and is at most 2%, depending on p_{T} ($D^{(*)}$). These effects are discussed in more detail in Section sec:uncertainties. No difference is expected in the fiducial efficiency between W^{-}+$D^{(*)}$ and W^{+}+$D^{(*)}$ selections, so for the purposes of unfolding the efficiencies are calculated inclusively to reduce the statistical uncertainties.

For the $W + D_s$ and $W + D^{+}$ simultaneous inclusive analysis, fiducial efficiencies (see Table 8.4) are computed as single numbers, in the absence of any differential bins. The efficiencies are computed for the nominal Sherpa2.2.11 sample, the MadGraph5_aMC@NLO (FxFx) variation, and the maximum difference obtained by from 7 QCD scale variations. The difference of the fiducial efficiencies between the D_s and D^{+} channels is largely due to the larger lifetime of the later. The MadGraph5_aMC@NLO (FxFx) variation is the largest difference, differing from the nominal efficiency by 5.2 - 5.6%, exceeding the statistical uncertainty.

Table 8.4: The fiducial efficiencies for the $D_s \to \phi\pi \to (KK)\pi$ and $D^{+} \to \phi\pi \to (KK)\pi$ decays in the W+D_s inclusive cross section analysis. The efficiencies are shown for Sherpa2.2.11, MadGraph5_aMC@NLO forced decay Monte Carlo samples, and QCD variations.

MC Sample	$W + D_s$	$W + D^{+}$
Sherpa 2.2.11	8.98 $\pm$0.01%	10.88 $\pm$0.01%
MadGraph5_aMC@NLO	8.51 $\pm$0.01%	10.27 $\pm$0.01%
Sherpa 2.2.11 QCD Variation	8.84 $\pm$0.01%	10.94 $\pm$0.01%

8.1.3 Detector Response Matrix

The detector response matrix r_{ij} is defined as the fraction of $W + D^{(*)}$ events produced in truth fiducial bin j that also satisfy the signal region reconstruction criteria in bin i. The first index (i) corresponds to the reconstructed observable and the second index (j) represents the corresponding truth observable. The sum over the first index is equivalent to the fiducial efficiency, i.e. $\sum_i r_{ij} = \epsilon_j$. Furthermore, the expected number of reconstructed events in bin i is given by Eq. 8.1:

$$N_i^{\mathrm{reco}} = \sum_j r_{ij} \cdot \sigma_j^{\mathrm{fid}} \cdot \mathscr{L} \cdot \mathrm{Br}_{D^{(*)}}, \tag{8.1}$$

where σ_j^{fid} is the fiducial cross section in the truth bin j and $\mathscr{L}$ is the integrated luminosity. The detector response matrix is used directly in the differential $\sigma(W + D^{(*)})^{\text{OS-SS}}$ cross section fit as described in Section 8.3. Note that for the inclusive fits, a detector response matrix

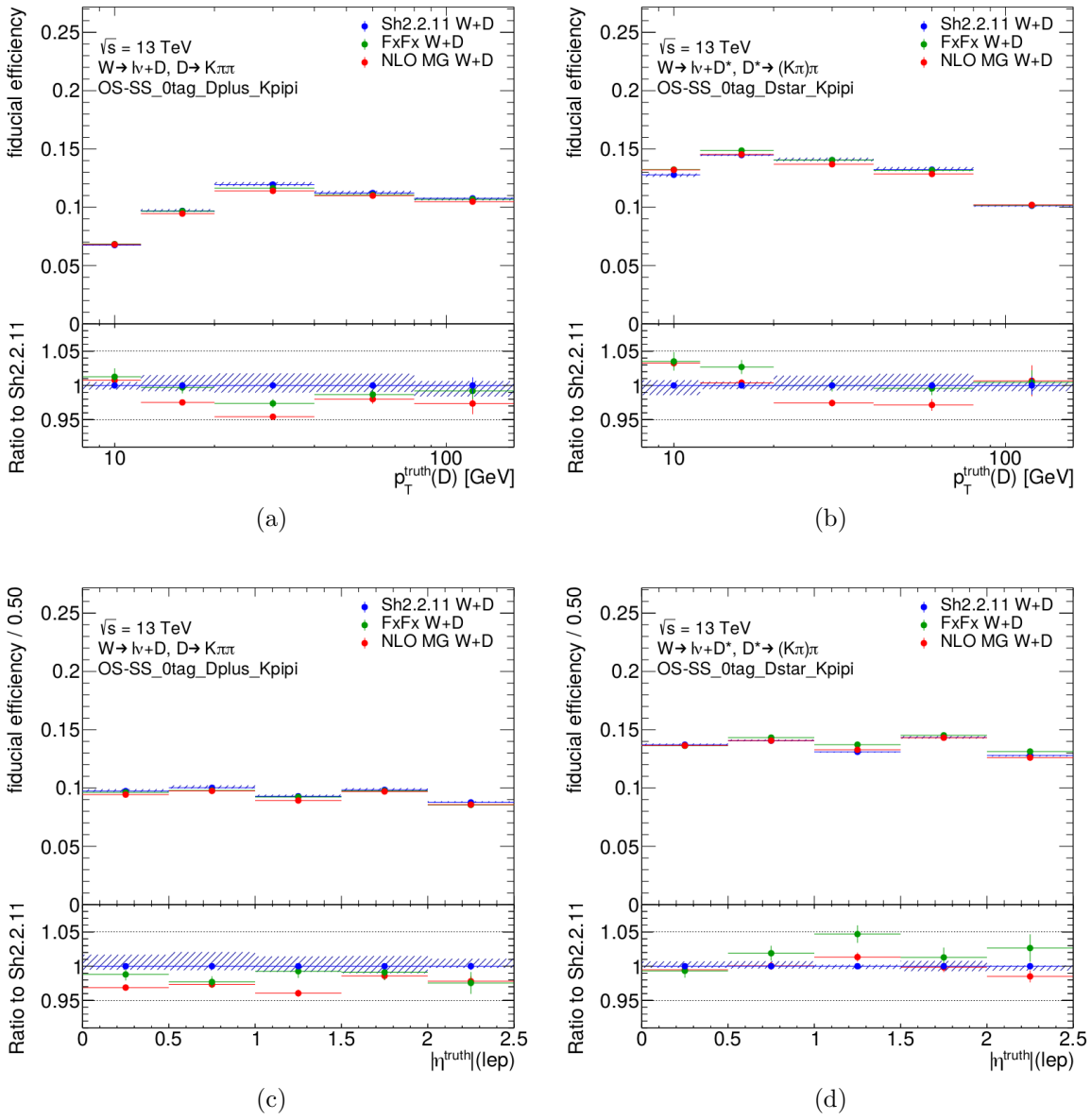

Figure 8.1: The $W + D^{(*)}$ fiducial efficiency in differential p_{T} ($D^{(*)}$) bins: (a) $W + D^{+}$, (b) $W + D^{*}$, and in differential $|\eta(\ell)|$ bins: (c) $W + D^{+}$, (d) $W + D^{*}$. The nominal values are calculated with the SHERPA2.2.11 forced decay $W + D^{(*)}$ samples. These are shown with blue markers and the hatched uncertainty band corresponds to the QCD scale uncertainty. The binomial statistical uncertainties are shown with the vertical error bars. The difference with respect to the other samples is used as a signal systematic uncertainty in the fit.

is not necessary as there are only one bin and thus migrations cannot occur. Therefore in expressions used to calculate the inclusive fit, the detector response matrix is simply unity.

$W + D^{(*)}$ detector response matrix is almost diagonal due to the excellentp_{T} ($D^{(*)}$) and η(lep) resolutions. The size of the off-diagonal entries is at most 1% of the size of the diagonal entries, and there are no events in the SHERPA2.2.11 $W + D^{(*)}$ sample that deviate from the diagonal by more than one element. The MC statistical uncertainty of each individual matrix entry is implemented as a separate nuisance parameter in the differential likelihood fit (see Section 8.3). In the individual W^{-}+$D^{(*)}$ and W^{+}+$D^{(*)}$ channels, the statistical uncertainty in the diagonal entries is below 1% at low p_{T} ($D^{(*)}$) and up to 2% in the last p_{T} ($D^{(*)}$) bin. The relative statistical uncertainty in the off-diagonal entries is up to 10%, but the impact of these uncertainties is low due to the small size of the off-diagonal entries.

8.2 Pre-fit Templates

The signal and background components used in the $W + D^{+}$, $W + D^{*}$, and $W + D_s$ fits are given in Table 8.5. Backgrounds from other events in the W+jets samples — $W + c^{\mathrm{matched}}$, $W + c^{\mathrm{mis-matched}}$, and W+jets — are described in Section 6.3. These backgrounds are separated into different components in the fit because they are affected by different systematic uncertainties:

- Charm hadron production fractions: the $W + c^{\mathrm{matched}}$ and $W + c^{\mathrm{mis-matched}}$ backgrounds are affected by production fraction reweighting systematics given in Section 9. These are relatively small 2 to 3% shape plus normalization uncertainties,
- $D^{(*)}$ branching ratio: a dedicated uncertainty for the $D^{(*)}$ branching ratios is implemented for the $W + c^{\mathrm{matched}}$ background in the $W + D^{+}$ channel. This is required due to the complicated nature of the constituent charm species that compose this background, which is eliminated by kinematic cuts in the D^{*}, and D_s reconstruction. This uncertainty is up to 20%, depending on the $D^{(*)}$ flavor and reconstructed mass range.

The category named 'Other' contains all events from Diboson and Z+jets processes. An additional 20% overall normalization uncertainty is added for this background separately for 0 and 1-tag with the name `OtherNorm_X-tag`. Processes containing top quarks ($t\bar{t}$, single-t, $t\bar{t}X$) are jointly represented by the 'Top' category, which is dominated by the $t\bar{t}$ process. Lastly, the multijet background is estimated with the Matrix Method.

Certain templates are marked as Loose Inclusive Selection (LIS). The LIS is a strategy designed to reduce bin-to-bin fluctuations in the background templates of the appropriate D meson mass (difference). LIS takes advantage of the fact that certain backgrounds originating from the W+jets MC sample, e.g. $W + c^{\mathrm{mis-matched}}$, have the same shape even when certain selection requirements are relaxed. In the case of the $W + D^{(*)}$ differential analysis, those relaxed selections are removing the W boson $E_{\mathrm{T}}^{\mathrm{miss}}$ and m_{T}; for the $W + D_s$

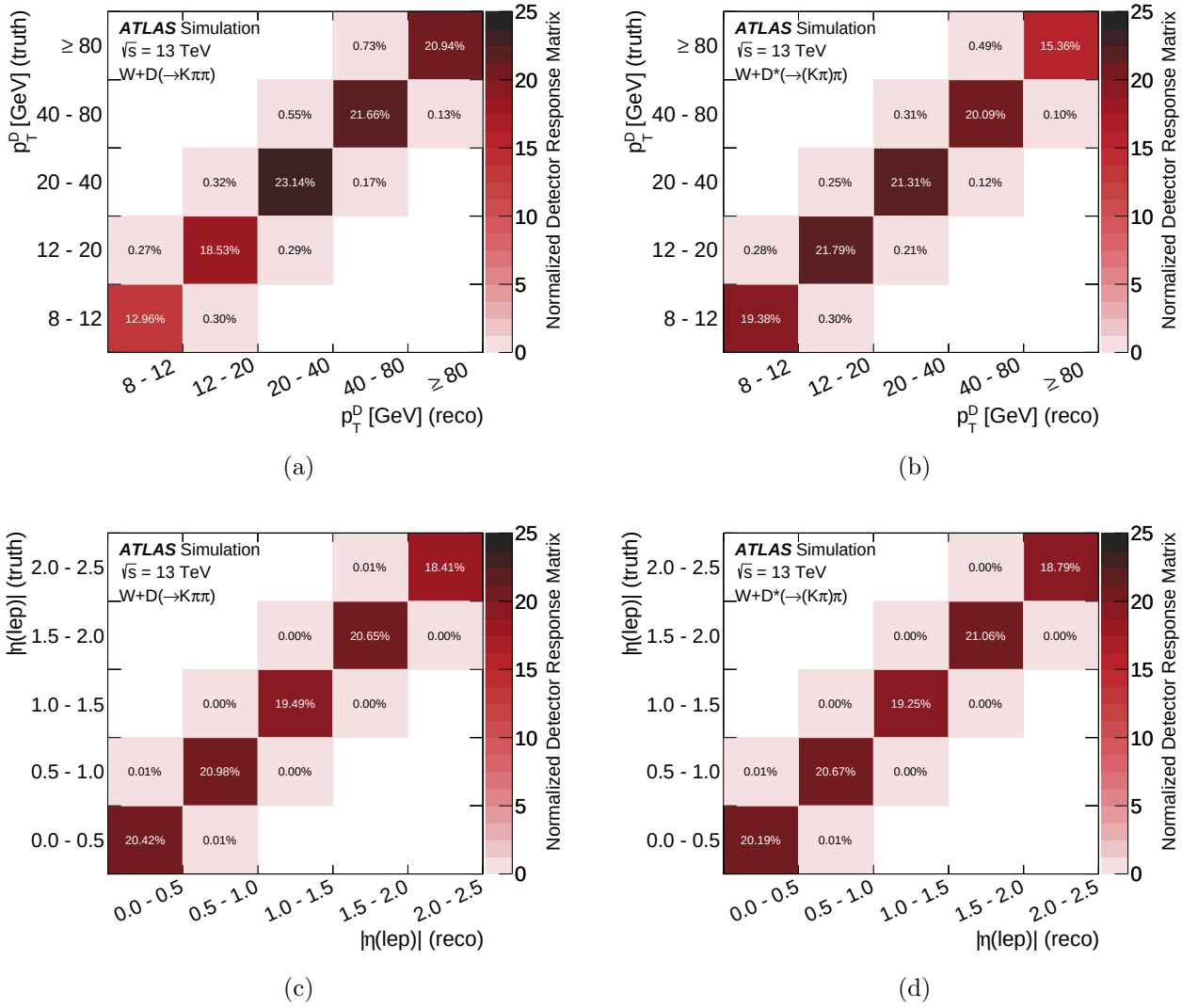

Figure 8.2: The $W + D^{(*)}$ normalized detector response matrix in differential p_{T} ($D^{(*)}$) bins: (a) $W + D^{+}$, (b) $W + D^{*}$, and in differential $|\eta(\ell)|$ bins: (c) $W + D^{+}$, (d) $W + D^{*}$. The detector response matrix is calculated with SHERPA2.2.11 $W + D^{(*)}$ samples. The values in the response matrix are given as a percentage and the quoted uncertainty is the relative binomial MC statistical uncertainty, also given as a percentage. The detector response matrices are normalized to unity such that the sum of all elements is 100%.

fit, that requirement is widening the mass window placed on the intermediate ϕ meson from $\pm 8\,\text{GeV}$ to $\pm 12\,\text{GeV}$ around the world average value of $m(\phi)$. The normalization of each background template is fixed to its value from the standard selection, while the shape and relative background uncertainties comes from the LIS selection. This process improves the stability of the likelihood fit.

The $W + D^{(*)}$ signal sample in the pre-fit templates is divided into five bins in p_{T} for each lepton charge and separately for OS and SS combinations of W and $D^{(*)}$. In all cases, a variable size binning is used in the 0-tag region. For D^+ the bin width is 0.25 GeV in the peak region, 0.50 GeV in the low mass tail, and 1.0 GeV in the high mass tail. For D^* the low mass region has 2.0 MeV bins, the peak region has 1.0 MeV bins and the width is increased to 7.5 MeV in the high mass tail. This binning keeps the good signal to background ratio in the peak region and reduces the number of bins as much as possible in the tails of the mass distributions.

Table 8.5: Breakdown of signal and background categories used in the $W + D^{(*)}$ fits. The 'Normalization', 'Shape', and 'Systematic' columns indicate the source used to calculate the corresponding property. 'LIS' refers to the Loose Inclusive Selection for each mode. D_s refers to both the D_s and D^+ decay modes in the $\phi\pi \to (KK)\pi$ mode. These methods are used to decrease the MC statistical uncertainties as described in the text.

Category	Normalization	Shape	Systematics
$W + D^+$ signal	Sherpa2.2.11	Sherpa2.2.11	Sherpa2.2.11
$W + D^*$ signal	Sherpa2.2.11	NLO MadGraph	Sherpa2.2.11
$W + D_s$ signal	Sherpa2.2.11	Sherpa2.2.11	Sherpa2.2.11
D^+ $W + c^{\text{matched}}$	LO MadGraph	LO MadGraph	Sherpa2.2.11
D^* $W + c^{\text{matched}}$	Sherpa2.2.11	Sherpa2.2.11	Sherpa2.2.11
D_s $W + c^{\text{matched}}$	Sherpa2.2.11	LIS Sherpa2.2.11	Sherpa2.2.11
D^+ $W + c^{\text{mis-matched}}$	Sherpa2.2.11	LIS Sherpa2.2.11	Sherpa2.2.11
D^* $W + c^{\text{mis-matched}}$	Sherpa2.2.11	LIS Sherpa2.2.11	Sherpa2.2.11
D_s $W + c^{\text{mis-matched}}$	Sherpa2.2.11	LIS Sherpa2.2.11	Sherpa2.2.11
D^+ $W+$jets	Sherpa2.2.11	LIS Sherpa2.2.11	Sherpa2.2.11
D^* $W+$jets	LO MadGraph	LIS LO MadGraph	Sherpa2.2.11
D_s $W+$jets	Sherpa2.2.11	LIS Sherpa2.2.11	Sherpa2.2.11
Top		Full Sim	
Other		Full Sim	
Multijet		Matrix Method	

Charm Hadron Production Reweighting

Charm hadron production fractions in all samples are reweighted to the world average values for weakly decaying charm species, using tools developed by the ATLAS collaboration for this analysis [87]The weights improve the pre-fit data-to-MC agreement by changing the signal and background normalizations and the shapes of the $W + D^{(*)}$ background templates via changing the relative contributions of each species. The related systematic uncertainties are described with three eigenvector variations that change the production fractions in a correlated fashion and keep the sum of the fractions equal to unity. The production fraction weights and the corresponding systematic uncertainties have no effect on the fitted signal yield because they do not affect the fiducial efficiency and because the signal originates from a single $D^{(*)}$ species in each channel. On the other hand, the normalization of the background templates may change up to 3%, depending on the $D^{(*)}$ species. These uncertainties enter the fit via the three nuisance parameters.

8.3 Profile Likelihood Fit

The fit strategy depends on a likelihood function which is defined as $\mathcal{L}$ in Eqs. 8.2–8.5. It is constructed as the product of Poisson probability terms for each bin of the input mass distributions based on the number of data events and the expected signal and background yields. The product over the yields in each $D^{(*)}$ mass bin is performed for each differential bin, either in bins of p_{T} ($D^{(*)}$) or $|\eta(\ell)|$ or inclusively for a single bin simultaneously for both $D^{(*)}$ species. The pre-fit distributions are shown in Section 8.2. To account for the impact of systematic uncertainties, they are included in the likelihood function as Guassian constrained nuisance parameters. Systematic uncertainties are correlated between all regions and samples (e.g. luminosity uncertainty), except for those that come from the finite size of the MC templates.

Events satisfying the signal region requirement (Table 6.4(a)) are split into events with 0, and 1-or-more b-tagged jets. As the $t\bar{t}$ background predominantly has one or more b-jets, the b-jet categorization allows the $t\bar{t}$ background to be estimated in situ from the 1-or-more b-jet region and extrapolated to the 0 b-jet region. Furthermore, it also improves the measurement precision by increasing the signal purity in the 0-tag region. The extrapolation of the $t\bar{t}$ normalization is done by performing a simultaneous fit to the 0-tag and 1-tag regions and by correlating the $t\bar{t}$ normalization factor between the two. The fits are done inclusively in lepton flavor for electrons and muons and simultaneously for the two charges, i.e. $W^{-}+D^{(*)}$ contains events with a reconstructed e^{-} or μ^{-} and $W^{+}+D^{(*)}$ contains a reconstructed e^{+} and μ^{+}.

A new fitting procedure exploiting the charge correlation between the W boson and the $D^{(*)}$ meson was developed to extract the OS-SS $\sigma(W^{-}+D^{(*)})$ cross section from the data. This is explained further with an example in Section 8.3. The signal $W + D^{(*)}$ events have a charge correlation between the W boson and the $D^{(*)}$ meson (only OS events), while

the backgrounds are largely the same in OS and SS (charge symmetric). Both OS and SS regions enter the likelihood function and a 'common floating component' is added in both of the regions. The additional component has one free parameter per invariant mass bin that is correlated between the corresponding OS and SS regions. Since the common floating component has free normalization and shape, it absorbs residual charge-symmetric processes and translates the maximization of separate OS and SS likelihoods into a maximization of the OS-SS likelihood.

The differential fits are performed separately for $W + D^+$ and $W + D^*$ channels and separately for the two differential variables. It is not possible to do a full two-dimensional fit in $p_{\mathrm{T}}(D^{(*)})$ and $|\eta(\ell)|$ due to the insufficient statistics both in the data and in the simulated samples. The inclusive fits in the $W + D_s$ analysis are performed simultaneously for both the $W + D_s$ and $W + D^+$ modes. Regions including both charges of the W are included in the fit at the same time so that we can also extract the cross section ratio $R_c^{\pm} = \sigma(W^+ + D^{(*)})/\sigma(W^- + D^{(*)})$. In total there are 24 regions in each differential fit with 20 Signal Regions and 4 Control Regions. SRs are in the 0-tag category and are split between the two W charges, into OS and SS events and into the five differential bins (i.e. $[W^-, W^+] \times [\mathrm{OS}, \mathrm{SS}] \times 5 = 20$ regions). The 1-tag CRs are split in the same way, but no differential bins are introduced since they are not needed to extract the $t\bar{t}$ normalization from the data. The regions used in the differential fit are summarized in Table 8.6. The inclusive fit is similar, but is performed for both $D^{(*)}$ species simultaneously leading to 4 SRs and 4 $t\bar{t}$ CRs (i.e. $[W^-, W^+] \times [\mathrm{OS}, \mathrm{SS}] = 4$). In addition to the charge cross section ratio $R_c^{\pm}$, fitting both D_s and D^+ simultaneously allows for the fitting of the ratio of D^+ to D_s production, R_{D^+/D_s}.

Table 8.6: A schematic of the Signal and Control Regions used in the differential fit.

b-tag	0-tag (SR)				1-tag (CR)			
W charge	W^-		W^+		W^-		W^+	
$D^{(*)}$ charge	OS	SS	OS	SS	OS	SS	OS	SS
Bin 1	0-tag W^- OS 1	0-tag W^- SS 1	0-tag W^+ OS 1	0-tag W^+ SS 1	1-tag W^- OS	1-tag W^- SS	1-tag W^+ OS	1-tag W^+ SS
Bin 2	0-tag W^- OS 2	0-tag W^- SS 2	0-tag W^+ OS 2	0-tag W^+ SS 2				
Bin 3	0-tag W^- OS 3	0-tag W^- SS 3	0-tag W^+ OS 3	0-tag W^+ SS 3				
Bin 4	0-tag W^- OS 4	0-tag W^- SS 4	0-tag W^+ OS 4	0-tag W^+ SS 4				
Bin 5	0-tag W^- OS 5	0-tag W^- SS 5	0-tag W^+ OS 5	0-tag W^+ SS 5				

The D^+ (D^*) invariant mass (mass difference) distribution is fitted in each region in Table 8.6. One signal sample and a corresponding signal normalization factor are defined for each truth bin of the differential distribution and for each W charge (10 in total). The signal samples are distributed among the reconstructed differential bins following the detector

response matrices (see Section 8.1.3). A likelihood equation describing this procedure is given in Eqs. 8.2–8.5:

$$\mathcal{L} = \prod_{\alpha} \Big(\prod_{i}^{\mathrm{W^-\,OS}} \mathcal{L}_i^{\alpha\,\mathrm{OS}} \times \prod_{i}^{\mathrm{W^-\,SS}} \mathcal{L}_i^{\alpha\,\mathrm{SS}} \times \prod_{i}^{\mathrm{W^+\,OS}} \mathcal{L}_i^{\alpha\,\mathrm{OS}} \times \prod_{i}^{\mathrm{W^+\,SS}} \mathcal{L}_i^{\alpha\,\mathrm{SS}} \Big) \times \mathcal{L}^{\mathrm{constraint}}, \tag{8.2}$$

$$\mathcal{L}_i^{\alpha\,\mathrm{OS}} = f\big(N_i^{\alpha} | \gamma_i^{\alpha} \cdot \big(\sum_{\beta} \left[\mu^{\beta} \cdot \sigma_{\mathrm{fid}}^{\beta} \cdot r^{\alpha\beta}(\vec{\theta}) \cdot \mathscr{P}_i^{\alpha\beta}(\vec{\theta})\right] \cdot \mathscr{L}(\theta_{\mathrm{lumi}}) \cdot \mathrm{Br}_{D^{(*)}} + \mathscr{B}_i^{\alpha}(\vec{\theta}, \mu_{\mathrm{Top}})\big) + \mathscr{S}_i^{\alpha}\big), \tag{8.3}$$

$$\mathcal{L}_i^{\alpha\,\mathrm{SS}} = f\big(N_i^{\alpha} | \gamma_i^{\alpha} \cdot \mathscr{B}_i^{\alpha}(\vec{\theta}, \mu_{\mathrm{Top}}) + \mathscr{S}_i^{\alpha}\big), \tag{8.4}$$

$$\mathcal{L}^{\mathrm{constraint}} = \prod_{t} g(\theta_0 | \theta_t, \Delta\theta_t) \times \prod_{i}^{\mathrm{allreco.bins}} f(N_i^{\mathrm{MC}} | \tau \cdot \gamma_i \cdot (S_i + B_i)), \tag{8.5}$$

where the Latin index i represents the bins of the $D^{(*)}$ mass distribution (either OS or SS) both in 0-tag and 1-tag regions and Greek indices α and β represent the differential reconstructed and truth bins respectively. Note in the inclusive fit, the Greek indices are simply 1, as there are no differential bins.

- N_i^{α} is the number of observed events in the mass bin i and reconstructed differential bin α,
- μ^{β} is the signal normalization factor for the truth differential bin β (one parameter per differential bin),
- $\sigma_{\mathrm{fid}}^{\beta}$ is the predicted fiducial cross section in the truth differential bin β (Section 8.1.1),
- $r^{\alpha\beta}(\vec{\theta})$ is the detector response matrix (Section 8.1.3),
- $\mathscr{P}_i^{\alpha\beta}(\vec{\theta})$ is mass shape distribution of the signal sample corresponding to the truth differential bin β in the reconstructed differential bin α
- $\mathscr{L}(\theta_{\mathrm{lumi}})$ is the integrated luminosity,
- $\mathrm{Br}_{D^{(*)}}$ is the branching ratio of either the D^+ or D^* decaying into $K\pi\pi$ (Ref. [14]),
- $\mathscr{B}_i^{\alpha}(\vec{\theta}, \mu_{\mathrm{Top}})$ is the total number of background events in the mass bin i and reconstructed differential bin α,
- μ_{Top} is the normalization factor for the $t\bar{t}$ background,
- $\mathscr{S}_i^{\alpha}$ is the common floating component in the mass bin i and reconstructed differential bin α.

The vector $\vec{\theta}$ represents all nuisance parameters corresponding to systematic uncertainties that are profiled in the fit (as discussed in Section 9). The corresponding Gaussian constraint is given with the $g(\theta_0|\theta_t, \Delta\theta_t)$ term. Moreover, γ_i are the Poisson-constrained parameters accounting for the MC statistical uncertainties in the invariant mass shapes of signal and background distributions. The parameter τ in the constraining term is the ratio of the effective integrated luminosities between MC and Data, N_i^{MC} is the 'raw' number of simulated signal and background events in bin i, and $S_i + B_i$ is the sum of the predicted number of signal and background events in bin i.

$W + D^{(*)}$ events failing the truth fiducial requirements laid out in Table 6.4(a) are included in the background, $\mathscr{B}_i^{\alpha}(\vec{\theta}, \mu_{\mathrm{Top}})$. These events are treated as background, and the normalization theory uncertainties associated with them are applied to their absolute event yield as opposed to only the fiducial efficiency as for the signal events (e.g. 10 to 20% as opposed to few percent). The constraint term $\mathcal{L}^{\mathrm{constraint}}$ describes the nuisance parameters $\vec{\theta}$ which are correlated across the reconstructed differential bins α. The only exception are the nuisance parameters representing the statistical uncertainty in the entries of the detector response matrix $r^{\alpha\beta}$.

The 10 parameters of interest in the differential fit are the μ^i parameters, which correspond to the unfolded differential cross sections. Correlations between the differential bins and event migrations between the bins are accounted for in the fit with the detector response matrix $r^{\alpha\beta}$. The normalization factors get constrained in the diagonal bins (e.g. μ^3 gets constrained in the reconstructed bin 3) and the resulting normalization is then applied to the off-diagonal signal samples in the neighboring reconstructed bins. This accounts for the event migrations between the differential bins and induces small correlations between the normalization factors. Because the fit takes into account migration between the differential bins, no additional unfolding steps are needed after the fit. Apart from profiling systematics, this approach is equivalent to unfolding with matrix inversion since no regularization is included. Since the off-diagonal elements are very small (1%), regularization is not necessary.

The 10 (4) normalization factors in Eq. 8.5 need to be combined appropriately to calculed the normalized differential (inclusive) cross sections and the $R_c^{\pm}$ (and R_{D^+/D_s}) parameter from the fit. This procedure is explained in Section 8.3.

The Common Floating Component $\mathscr{S}_i^{\mathrm{OS}\leftrightarrow\mathrm{SS}}$

The fit configuration with the common floating component is motivated by the fact that the absolute normalization and shape of any charge symmetric backgrounds (e.g. gluon splitting $W + c\bar{c}$) in OS and SS regions should not affect the fit results in the OS-SS region by construction.

The method used to extract the OS-SS $\sigma(W + D^{(*)})^{\mathrm{OS\text{-}SS}}$ cross section from a simultaneous fit to OS and SS is demonstrated in Figure 8.3 with the D^+ fit in the W^- channel. Only the p_{T} (D^+) bin 2 0-tag regions are shown for simplicity. The pre-fit OS, SS, and OS-SS distributions are shown in Figures 8.3(a)–8.3(c). Figure 8.3(d) is the post-fit OS distribution, Figure 8.3(e) corresponds to the post-fit SS distribution, and Figure 8.3(f) is the OS-SS

subtracted distribution. The plots show the post-fit values of the common floating component ($\mathscr{S}_i^{\mathrm{OS}\leftrightarrow\mathrm{SS}}$ in the likelihood equation in Eq. 8.2) with the gray histograms named 'Ch. Symm.' in the legend. By construction, this component is zero in OS-SS since it is bin-by-bin correlated between the two regions. The data to MC agreement in the post-fit OS-SS distribution is flat and compatible with unity within the uncertainty band. The common floating component is implemented with a bin-by-bin template. However, there is a technical limitation where these normalization factors cannot be negative. This is an issue for the case where the MC prediction is already very close to the data (or overshoots the data) and the common floating component would need to be negative. To overcome this, a negative offset is added in such bins as shown by the 'Offset' component in the legend.

The initial pre-fit values of the common floating component are arbitrary because they are free parameters in the fit not bound by any constraints. For technical purposes the initial values both in the OS and SS regions are set to the difference between the data and the MC prediction in the SS region (no differences in results were observed with other initial values). This ensures that the initial signal plus background predictions are positive and not too far away from the minimum, which could otherwise cause fit convergence issues.

Parameter Substitution for Normalized Differential Cross Section, $R_c^{\pm}$, and R_{D^+/D_s}

The differential cross sections extracted with the fit described in the previous section are the absolute cross sections. However, normalized differential cross sections are generally more powerful for comparing the observed data and the theory predictions. Since fully correlated systematic uncertainties like luminosity and branching ratios are removed by the normalization, they cancel in the normalized differential cross section. Instead of fitting for N absolute cross sections, where N is the number of differential bins, the fit is adjusted to fit for $N-1$ normalized cross sections and the total fiducial cross section. One of the differential cross sections then needs to be expressed with the other N parameters, otherwise the fit would have $N+1$ free parameters. By default, the last normalized differential cross section bin is chosen as shown in Eq. 8.6:

$$\begin{aligned}
&\mu^1 \to \mu^{\mathrm{tot.}} \times \mu^1_{\mathrm{rel}}, \\
&\mu^2 \to \mu^{\mathrm{tot.}} \times \mu^2_{\mathrm{rel}}, \\
&\cdots \\
&\mu^N \to \mu^{\mathrm{tot.}} \times \left[1 - \sum_{i=1}^{N-1} \left(\mu^i_{\mathrm{rel}} \times \frac{\sigma^i_{\mathrm{fid}}}{\sigma^{\mathrm{tot.}}_{\mathrm{fid}}}\right)\right] / \frac{\sigma^N_{\mathrm{fid}}}{\sigma^{\mathrm{tot.}}_{\mathrm{fid}}},
\end{aligned} \tag{8.6}$$

where σ^i_{fid} is the predicted fiducial cross section in the truth differential bin i, μ^i_{rel} are the normalization factors scaling the normalized differential cross sections, $\mu^{\mathrm{tot.}}$ is the total fiducial cross section, and $\sigma^{\mathrm{tot.}}_{\mathrm{fid}}$ is the predicted total fiducial cross section. This substitution is performed separately for both charges, $W^+ + D^{(*)}$ and $W^- + D^{(*)}$.

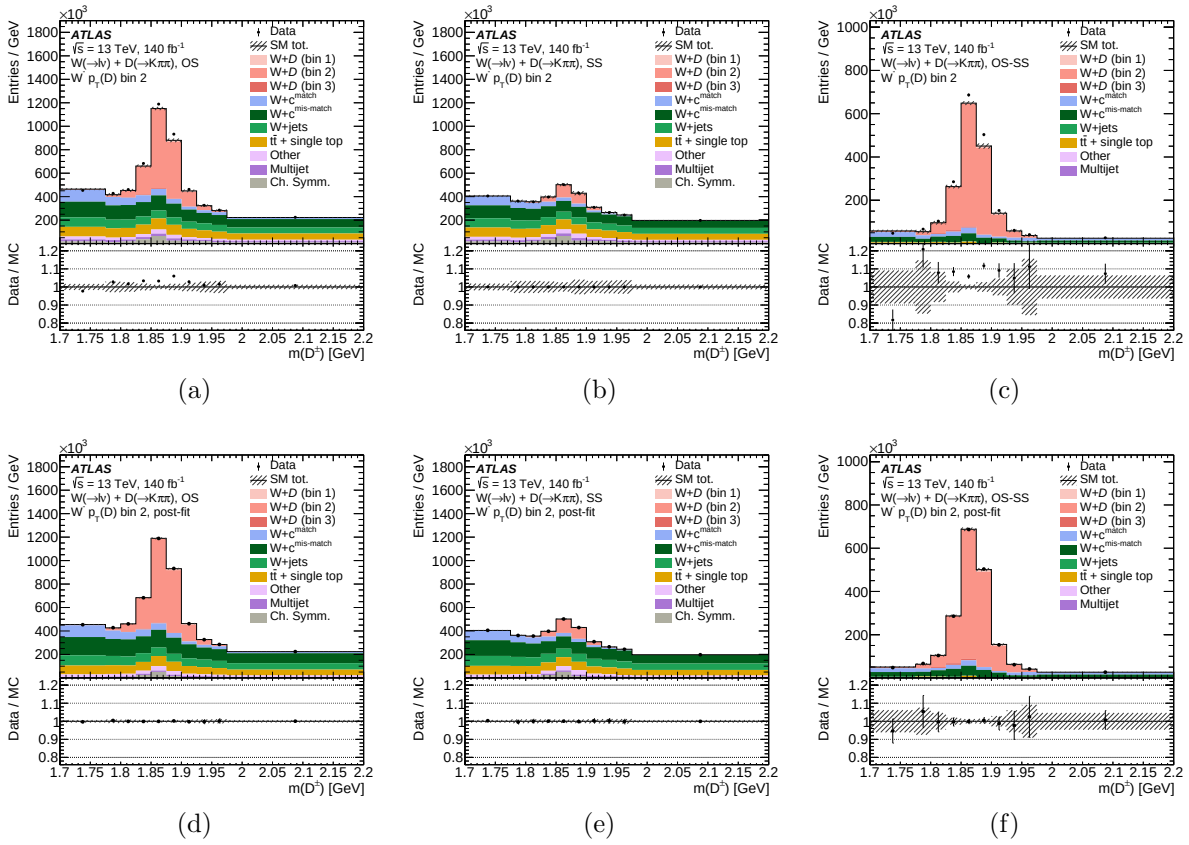

Figure 8.3: A demonstration of the OS-SS $W + D^{(*)}$ fitting strategy. Pre-fit $m(D^{(*)})$ distributions for the $W^- + D^+$ p_{T} $(D^{(*)})$ differential fit in bin 2: (a) OS $W + D^+$, (b) SS $W + D^+$, and (c) OS-SS $W + D^+$. The corresponding post-fit distributions: (d) OS $W + D^+$, (e) SS $W + D^+$, and (f) OS-SS $W + D^+$. The pre-fit uncertainty bands include MC statistical uncertainties only and the post-fit uncertainty bands include the total uncertainty extracted from the fit. The gray histograms represent the charge-symmetric common floating component.

A similar substitution is made for the $R_c^{\pm}$ parameter in both the differential and $W + D_s$ fits. The normalization factor for the $\sigma(W^+ + D^{(*)})$ total fiducial cross section is replaced by an expression as shown in Eq. 8.7:

$$\mu^{\text{tot.}}(W^+ + D^{(*)}) \to \frac{\sigma_{\text{fid}}^{\text{tot.}}(W^- + D^{(*)})}{\sigma_{\text{fid}}^{\text{tot.}}(W^+ + D^{(*)})} \times R_c^{\pm} \times \mu^{\text{tot.}}(W^- + D^{(*)}), \tag{8.7}$$

where $\sigma_{\text{fid}}^{\text{tot.}}(W^{\pm} + D^{(*)})$ are the cross section priors and $\mu^{\text{tot.}}(W^- + D^{(*)})$ is the normalization factor for the $W^- + D^{(*)}$ fiducial cross section. In the differential fit, the parameters after these substitutions are μ_{rel}^1, ..., μ_{rel}^{N-1} for both charges (8 parameters in total), $R_c^{\pm}$, and $\mu^{\text{tot.}}(W^- + D^{(*)})$. The rest of the observables are calculated from expressions in Eqs. 8.6 and 8.7 by propagating the uncertainties from the other parameters using the correlation matrix. These observables are μ_{rel}^N for both charges and $\mu^{\text{tot.}}(W^+ + D^{(*)})$. In the inclusive $W + D_s$ fit, the same procedure is used for the $W^+ + D_s^-$ as in Eq. 8.7.

For the $D^+ \to \phi\pi \to (KK)\pi$ in the $W + D_s$ fit, a similar expression is used to determine the D^+ cross section. The parameter substitution is performed in both the $W^+ + D^-$ and $W^- + D^+$ channels. For the $W^- + D_s^+$ channel, the cross section becomes:

$$\mu^{\text{tot.}}(W^- + D_s^+) \to \frac{\sigma_{\text{fid}}^{\text{tot.}}(W^- + D_s^+)}{\sigma_{\text{fid}}^{\text{tot.}}(W^- + D^+)} \times R_{D^+/D_s} \times \mu^{\text{tot.}}(W^- + D_s^+), \tag{8.8}$$

While there are four free parameters in the fit, this is constrained to three by the assumption that R_{D^+/D_s} is the same in the $W^+ + D_s^-$ and $W^- + D_s^+$ channel. With this assumption, the final expression for the $W^+ + D_s^-$ cross section becomes:

$$\mu^{\text{tot.}}(W^+ + D_s^-) \to \frac{\sigma_{\text{fid}}^{\text{tot.}}(W^- + D_s^+)}{\sigma_{\text{fid}}^{\text{tot.}}(W^+ + D^-)} \times R_c^{\pm} \times R_{D^+/D_s} \times \mu^{\text{tot.}}(W^- + D_s^+). \tag{8.9}$$

Chapter 9

Systematic Uncertainties

This Chapter describes the sources of systematic uncertainties that are present in the $W + D^{(*)}$ analyses. These uncertainties can be sorted into approximately three broad categories, experimental systematic uncertainties, theory systematic uncertainties, and other sources of uncertainty.

9.1 Systematic Categories

9.1.1 Experimental Uncertainties

Experimental uncertainties are defined as uncertainties associated with the MC modeling of the detector performance. These uncertainties are typically defined via number of nuisance parameters that characterize the uncertainties as a eigenset of variations to the quantities that characterize the performance. The uncertainties described this way include lepton and jet reconstruction, energy resolution, and energy scale, in lepton identification, isolation, and trigger efficiencies, in b-jet tagging efficiencies, and in the total integrated luminosity and pileup reweighting. These uncertainties affect the $W + D^{(*)}$ signal efficiency by altering the detector response matrix, yields of the background processes estimated with MC simulation, and the signal and background invariant mass templates used in the profile likelihood. These uncertainties are correlated between all samples and regions in the likelihood fit and are generally derived from auxiliary measurements performed centrally by the ATLAS collaboration, and are referenced in the appropriate section:

Charged Leptons

Electron and muon systematics are derived from data with large samples of $J/\psi \to \ell\ell$ and $Z \to \ell\ell$ events [134, 136] These systematic variations are based on reconstruction, isolation, identification, and trigger efficiencies, and the energy/momentum scale and resolution. Systematic variations of the MC efficiency corrections and energy/momentum calibrations

applied to MC samples are used to estimate the signal selection uncertainties. There are 8 NP for electrons and 13 for muons.

Jets and Missing Transverse Momentum

Although jets are not directly under study in the work presented in this thesis, uncertainties on jet quantities can indirectly modify the reconstructed $E_{\mathrm{T}}^{\mathrm{miss}}$ in the event and hence the selection efficiency of the $E_{\mathrm{T}}^{\mathrm{miss}}$ and m_{T} cuts. The two categories of jet systematics are the jet energy scale and energy resolution uncertainties. Systematic variations of the jet energy calibration are applied to MC samples to estimate signal selection uncertainties using the methodology described in [151]. In total, there are 20 independent jet energy scale variations and 8 independent jet energy resolution variations. These are marginal uncertainties in the analysis, and no individual jet uncertainty affects the signal selection efficiency by more than 1%. $E_{\mathrm{T}}^{\mathrm{miss}}$ enters more directly into the analysis, and the derivation of those systematic uncertainties follows the methodology described in [152]. Furthermore, a single nuisance parameter is included to model the uncertainty in the JVT selection efficiency.

Flavor Tagging

Samples of dileptonic $t\bar{t}$ events for b-jets and c-jets are used to understand the uncertainty in the calibration of the b-tagging efficiencies and mis-tag rates [141, 153]. For light flavor jets, a data sample a data sample is used that contains minimal heavy flavor jets [154]. Since the majority (>99%) of $W + D^{(*)}$ signal events have no additional b-tagged jets, these variations have a negligible impact on the signal efficiency. The largest impact of the variations is related to the top quark template, where it can have an impact of up to 10% on the relative yields in both the $W + D^{(*)}$ SR and Top CR.

Pileup and Luminosity

The uncertainty in the integrated luminosity is 0.83% [155], which is obtained using the LUCID-2 detector [76] for the primary luminosity measurements performed relatively during the data taking, and a dedicated Van der Meer scan to calibrate the measurement absolutely. MC samples are reweighted to have the distribution of pileup vertices match the pileup distribution measured in the Run 2 data. To account for the uncertainty in the pileup estimation, variations of the reweighting are applied to the MC samples. In addition to affecting the background yields, the pileup reweighting also has a small impact on the resolution of the reconstructed D^+ and D_s meson mass peaks and the $m(D^* - D^0)$ mass difference.

SV Reconstruction

Uncertainties in the secondary-vertex reconstruction efficiency arise from potential mismodeling of the amount and location of ID material, from the modeling of hadronic interactions

in GEANT4 and from possible differences between the impact parameter resolutions in data and MC events. These uncertainties are evaluated by generating large single-particle samples of D^+ and D^{*+} decays with the same p_{T} and η distributions as the baseline $W + D^{(*)}$ MC samples. These "single-particle gun" (SPG) samples (see Section 4.2.8 for details) are simulated multiple times with different simulation parameters, mirroring the procedure in [156]: passive material in the whole ID scaled up by 5%, passive material in the IBL scaled up by 10%, and passive material in the Pixel detector services scaled by 25%. In addition to the variations in the amount of detector material, a SPG sample where the physics model in the GEANT4 toolkit was changed to QGSP_BIC from FTFP_BERT [81] was generated.

The impact of the uncertainty in the ID material distribution is evaluated by comparing the efficiency obtained using the baseline simulation and that obtained using altered material distributions. For each variation the relative change in the $D^{(*)}$ reconstruction efficiency is parameterized as a function of $p_{\mathrm{T}}(D^{(*)})$ and $\eta(D^{(*)})$ separately for positive and negative charges of the mesons and separately for D^+ and D^{*+} mesons. The impact of changing the physics model was found to be negligible. The relative change in the reconstruction efficiency due to the increased amount of the ID material was found to vary by 1%–4%. The uncertainty is largest for low $p_{\mathrm{T}}(D^{(*)})$ and high $\eta(D^{(*)})$. Because $D^{(*)}$ candidates in the signal and in the $t\bar{t}$ background do not necessarily have the same $p_{\mathrm{T}}(D^{(*)})$ spectrum, their tracking efficiency NPs are treated as separate parameters to minimize the correlation between them. The $t\bar{t}$ background has large yields in the Top CR and could affect the shape of the $p_{\mathrm{T}}(D^{(*)})$ distribution via modifications from the tracking efficiency uncertainties. The measured cross-sections would change by up to 1.0% if the parameters were correlated, but this difference is covered by the associated systematic uncertainties.

The effect of the ID material variations on the shape of the D^+ invariant mass peak and the $m(D^* - D^0)$ mass difference is evaluated by fitting the mass distributions with a double-sided Crystal Ball function, with the modeling of the yield in the peak decoupled from the peak position. The width and position of the peak are characterized by the width and mean of the central Gaussian distribution, respectively. The shift in the position of the D^+ (D^{*+}) peak was found to be up to 0.2 MeV (0.05 MeV). The impact on the resolution of the peak was evaluated from the difference between the squares of the nominal width and the width obtained from each variation. The resolution was found to be smeared by up to 4.0 MeV (0.2 MeV) for the D^+ (D^{*+}) peak. The variations in the peak position and resolution are implemented in the likelihood fit as shape uncertainties; this additional freedom in the fit is necessary to achieve good agreement between the data and the fit model. These systematics are not applied in the $W + D_s$ analysis due to the decreased precision of the signal modeling with the lower data and simulation statistics with respect to the differential analysis.

An additional systematic uncertainty is applied to accommodate ID track impact-parameter resolution differences between simulation and data after the ID alignment is performed [157]. The difference is evaluated using minimum-bias data and the resulting uncertainty is extrapolated to higher p_{T} with muon tracks from Z boson decays [156]. The uncertainty is propagated to the $W + D^{(*)}$ measurement by generating D^+ and D^{*+} SPG

samples where the impact parameters of the ID tracks are smeared before performing the SV fit for the $D^{(*)}$ reconstruction. The relative change in the $D^{(*)}$ reconstruction efficiency was found to be up to 5% for high-p_{T} $D^{(*)}$ mesons and about 1.5% at low p_{T} (i.e. $p_{\mathrm{T}} < 40\,\mathrm{GeV}$). The systematic uncertainties in the $D^{(*)}$ meson reconstruction efficiency related to ID track impact-parameter resolution and ID material variations are among the largest systematic uncertainties in the analysis.

9.1.2 Theoretical Uncertainties

Many important theoretical inputs underlie the templates that are used in the profile likelihood fit. These inputs have uncertainties that are related to the physics modeling of signal and background processes, and are parameterized by varying the MC simulation that is used to determine the fiducial efficiencies and background templates. Additionally, there are uncertainties related to the choice of PDF, the QCD scale, the strong coupling α_{s}, and Electroweak corrections that are accounted for by varying the relevant theoretical quantities to extract the difference with respect to the nominal case. There are also uncertainties related to the charm hadronization model that must be accounted for in the fits.

Signal Modeling

The signal modeling uncertainty is derived by comparing the fiducial region efficiencies for the signal Sherpa 2.2.11, aMC@NLO+Py8 (FxFx), and aMC@NLO+Py8 (NLO) $W + D^{(*)}$ simulations (aMC@NLO+Py8 (NLO) only for the $W + D_s$ measurement). In each differential bin or inclusively, the maximum difference between the nominal MC simulation (Sherpa) and either of the MadGraph5_aMC@NLO simulations is taken and a symmetric systematic uncertainty is applied in the two directions. The uncertainty is correlated between the differential bins and between W boson charges. It accounts for the fact that the choice of MC simulation for unfolding affects the unfolded values of the observables because of differences in the ME calculation, PS simulation, and heavy-flavor quark fragmentation and hadronization, all of which can change the efficiency and affect the bin-to-bin migration. The uncertainty ranges from 1% to 4%, depending on the bin, and is generally one of the largest uncertainties in the analysis. The relatively large difference in fiducial efficiency between Sherpa and MadGraph5_aMC@NLO simulations arises from the modeling of the correlation between W boson and $D^{(*)}$ meson kinematics when the $E_{\mathrm{T}}^{\mathrm{miss}}$ and m_{T} cuts are applied at the detector level. Including the same $E_{\mathrm{T}}^{\mathrm{miss}}$ and m_{T} cuts in the truth fiducial definition would reduce the uncertainty; however, it would give rise to a large background from signal $W + D^{(*)}$ events that fail the truth $E_{\mathrm{T}}^{\mathrm{miss}}$ and m_{T} selection, but pass the detector-level selection due to the poor $E_{\mathrm{T}}^{\mathrm{miss}}$ resolution, ultimately increasing the total uncertainty.

Additional uncertainties are considered by varying the QCD scales, the PDFs, α_{s}, and the virtual EW corrections in Sherpa 2.2.11. The PDF variations, α_{s} uncertainty, and EW corrections were found to have a negligible effect on the fiducial efficiency. The effect of QCD scale uncertainties is defined by the envelope of variations resulting from changing

the renormalization and factorization scales by factors of two with an additional constraint of $0.5 \leq \mu_r/\mu_f \leq 2$. In most differential bins the effect was found to be smaller than the corresponding difference between SHERPA and MADGRAPH5_AMC@NLO. Lastly, the uncertainties in the $D^+ \to K\pi\pi$ and $D^* \to D^0\pi \to K\pi\pi$ branching ratios [158] are applied as uncertainties of 1.7% and 1.1%, respectively, in the signal yield in the likelihood fit.

Background MC modeling: The implementation of the background modeling uncertainties varies between the backgrounds. For $W + c^{\text{matched}}$, $W + c^{\text{mis-matched}}$, and $W+$jets backgrounds, SHERPA 2.2.11 QCD scale, PDF, and α_s variations are used. Among the three, the QCD scale uncertainty generally has the largest effect and leads to a 10%–30% uncertainty in the yield of the corresponding background process, depending on the differential bin. The uncertainty is constrained in the likelihood fit by the small statistical uncertainties in the tails of the invariant mass distributions in the D^+, D^*, D_s channels, reducing its impact on the observables. As in the case of the signal process, these uncertainties are correlated between the differential bins. An additional modeling uncertainty is included by taking the full difference between SHERPA and MADGRAPH5_AMC@NLO predicted background yields. To be conservative, this uncertainty is taken to be uncorrelated between the differential bins. This avoids the assumption that either of the simulations have an a priori perfect description of the shape of the differential variable (i.e. $p_T(D^{(*)})$ or $|\eta(\ell)|$), and provides more flexibility in the likelihood fit.

Internal event weight variations in the MADGRAPH5_AMC@NLO 2.3.3 $t\bar{t}$ simulation are used to determine the effect of the PDF uncertainty on the top quark background. The uncertainty due to initial-state radiation is estimated by simultaneously varying the h_{damp} parameter and the μ_r and μ_f scales, and by choosing the VAR3C up and down variants of the A14 tune as described in [128]. The impact of final-state radiation is evaluated by halving and doubling the renormalization scale for emissions from the parton shower. Uncertainties in the $t\bar{t}$ ME calculation and PS are estimated by replacing the nominal $t\bar{t}$ prediction with two alternative simulations: POWHEG+HERWIG 7.04 and MADGRAPH5_AMC@NLO+PYTHIA 8 and taking the full difference as a systematic uncertainty. For other small backgrounds ($Z+$jets and diboson events) a conservative 20% uncertainty in their yields is used. Due to the high purity of the $W + D^{(*)}$ signal process in the $W + D^{(*)}$ SR selection, background modeling uncertainties are subdominant in the statistical analysis.

Charm Hadronization and Decay

The $W + c^{\text{matched}}$ and $W + c^{\text{mis-matched}}$ backgrounds in the D^+ channel have large contributions from weakly decaying charmed mesons incorrectly reconstructed as $D^+ \to K\pi\pi$ (e.g. $D_s \to \phi\pi \to (KK)\pi$ reconstructed as $D^+ \to K\pi\pi$). Two sources of associated systematic uncertainty are included: uncertainties in the charmed hadron production fractions and uncertainties in the charmed hadron branching ratios. Charmed hadron production fractions in the MC samples are reweighted to the world-average values as described in Section 8.2. Following the procedure in [87], three eigenvector variations of the event weights are derived to describe the correlated experimental systematic uncertainties associated with the measurements of the

charmed hadron production fractions. The uncertainty affects the relative background yield by up to 3% and also the shape of the background invariant mass distribution because the different charmed hadron species populate different ranges of the reconstructed D^+ invariant mass. The impact of the uncertainties in the charmed hadron branching ratios is estimated conservatively: by generating SPG D^+ samples with the signal branching ratios shifted, to cover the systematic uncertainties in charmed hadron decays reported in [158]. The relative change in the background yield and shape of the $W + c^{\text{matched}}$ background with respect to the nominal SPG configuration is propagated to the SHERPA MC sample and implemented in the statistical analysis. The size of the uncertainty is up to 5%. Both sources of charmed hadronization uncertainty related to background processes were found to have a negligible impact on all observables, since the size and shape of the background are highly constrained in the likelihood fit.

9.1.3 Other Systematic Uncertainties

In addition to the uncertainties discussed above, systematic uncertainties associated with the data-driven multijet estimation and with the finite size of the MC samples are included in the likelihood fit

Multijet Estimation

The multijet background and its uncertainties are estimated in the Fake CR, as described in Section 7, and the corresponding systematic uncertainties are implemented as nuisance parameters in the likelihood fit. Due to the difficulty of estimating the multijet background in the $W + D^{(*)}$ SR selection, the relative uncertainties are large (>50%). However, the multijet background is largely symmetric between OS and SS regions and its relative size is reduced in the OS–SS subtraction. Therefore, despite the large relative uncertainty in the multijet yield, the impact on the measured observables is negligible.

Finite Size of MC Samples

MC statistical uncertainties affect the measurement in several ways. The binomial uncertainties in the $W + D^{(*)}$ fiducial efficiencies calculated with the SHERPA MC samples are propagated into the likelihood fit via nuisance parameters affecting the yield of the signal sample. There is one parameter per nonzero element of the detector response matrix. The statistical uncertainty in the diagonal elements is less than 1%, while the uncertainty in the off-diagonal elements exceeds 10%. However, because the off-diagonal elements have small values compared to the diagonal ones, the corresponding statistical uncertainty has a negligible impact on the results. Furthermore, statistical uncertainties associated with the bins of the invariant mass distributions are implemented as constrained "γ" parameters in the likelihood fit as explained in Section 8. There is one such parameter per invariant mass bin and its impact on the observables is of the order of 1%.

9.2 Evaluation of the overall systematic uncertainty

The impact of each individual systematic uncertainty on the observables is calculated by performing two likelihood fits with the corresponding nuisance parameter (θ) fixed to its post-fit one-standard-deviation bounds. The changes in the values of the normalization factors associated with the observables, relative to the unconditional likelihood fit, are then taken as the impact of the given systematic uncertainty on the observables. Several nuisance parameters are grouped together by summing their impact on the observables in quadrature. A summary of the dominant systematic uncertainties is given in Table 9.1 for inclusive cross-sections and the cross-section ratio $R_c^{\pm}$. The table demonstrates that most of the systematic uncertainties are correlated between the positive and negative charge channels and therefore cancel out in the $R_c^{\pm}$ calculation. The dominant uncertainties in $R_c^{\pm}$ are the data and MC statistical uncertainties. Similarly to the $R_c^{\pm}$ calculation, uncertainties with no dependence on the differential variable cancel out in the normalized cross-section. For example, the SV reconstruction efficiency uncertainties almost completely cancel out in normalized $|\eta(\ell)|$ cross-sections because the $D^{(*)}$ SV reconstruction has no dependence on the lepton pseudorapidity. However, the same uncertainties do not cancel out in the $p_{\mathrm{T}}(D^{(*)})$ measurement because there is a strong dependence on $p_{\mathrm{T}}(D^{(*)})$.

Table 9.1: Summary of the main systematic uncertainties as percentages of the measured observable for $\sigma(W^-+D^{(*)})$, $\sigma(W^++D^{(*)})$, and $R_c^{\pm}$ in the D^+ and D^{*+} channels. The individual groups of uncertainties are defined in the text.

	D^+ channel			D^{*+} channel		
Uncertainty [%]	$\sigma(W^-+D^+)$	$\sigma(W^++D^-)$	$R_c^{\pm}(D^+)$	$\sigma(W^-+D^{*+})$	$\sigma(W^++D^{*-})$	$R_c^{\pm}(D^{*+})$
SV reconstruction	3.0	2.9	0.5	2.3	2.3	0.4
Jets and $E_{\mathrm{T}}^{\mathrm{miss}}$	1.7	1.9	0.2	1.5	1.5	0.4
Luminosity	0.8	0.8	0.0	0.8	0.8	0.0
Muon reconstruction	0.6	0.7	0.3	0.7	0.7	0.3
Electron reconstruction	0.2	0.2	0.0	0.2	0.2	0.0
Multijet background	0.2	0.2	0.1	0.1	0.1	0.1
Signal modeling	2.1	2.1	0.1	1.2	1.2	0.0
Signal branching ratio	1.6	1.6	0.0	1.1	1.1	0.0
Background modeling	1.1	1.2	0.3	1.3	1.3	0.5
Finite size of MC samples	1.2	1.2	1.1	1.4	1.4	1.3
Data statistical uncertainty	0.5	0.5	0.7	0.7	0.7	1.0
Total	4.6	4.6	1.4	3.7	3.7	1.7

The impact of systematic uncertainty categories in the $W + D_s$ inclusive cross section fit is shown in Table 9.2. The evaluations of the categories is calculated with the same strategy that is employed in the $W + D^{(*)}$ inclusive cross section fit. It can be seen in the table that for

$R_c^{\pm}$, most uncertainties that are correlated between the positive and negative channels cancel out, leading to a more precise measurement of $R_c^{\pm}$ than either of the inclusive cross sections individually. Similarly, R_{D^+/D_s} sees a reduction in most uncertainties that are correlated between the positive and negative channels, although to a lesser extent than $R_c^{\pm}$. This is due to the use of two cross section per charge that is used to extract R_{D^+/D_s}, see Eq. 8.8 for more details on the expression. Additionally, the uncertainty on the D meson branching ratios are different for each species, and thus these have a large impact on the ratio between D^+ and D_s. Similar to $R_c^{\pm}$, the MC statistics and data statics have a large impact on the measured R_{D^+/D_s}, because these are uncorrelated between the positive and negative channels.

Table 9.2: Summary of the main systematic uncertainties as percentages of the measured observable for $\sigma(W^-+D_s^+)$, $\sigma(W^++D_s^-)$, $R_c^{\pm}$, and R_{D^+/D_s} in the $W + D_s$ inclusive cross section. The individual groups of uncertainties are defined in the text.

	D_s channel			
Uncertainty [%]	$\sigma(W^-+D_s^+)$	$\sigma(W^++D_s^-)$	$R_c^{\pm}$	R_{D^+/D_s}
SV reconstruction	3.3	3.0	0.6	0.1
Jet and $E_{\mathrm{T}}^{\mathrm{miss}}$	1.6	2.4	1.7	0.7
Luminosity	0.8	0.9	0.1	0.1
Muon reconstruction	0.7	0.8	0.3	0.3
Electron reconstruction	0.1	0.1	0.2	0.1
Multijet background	0.3	0.6	0.7	0.6
Signal modeling	6.2	6.3	0.1	0.6
Signal branching ratio	2.3	2.4	0.1	3.8
Background modeling	4.3	3.7	4.5	5.9
Finite size of MC samples	4.3	4.7	5.8	8.6
Data statistical uncertainty	2.2	2.7	3.3	5.2
Total	9.6	9.6	7.3	11.2

Chapter 10

$W + D^{(*)}$ Differential Cross Section Results

This chapter describes the results from the differential $W+D^{(*)}$ analysis. These measurements include the following observables: the total cross sections, differential cross sections, $R_c^{\pm}$, and comparisons of the results to several modern PDF sets. The analysis results show a high degree of statistical precision, with uncertainties $< 5\%$ for the total cross sections and an uncertainty on $R_c^{\pm}$ of 1%.

10.1 Post-fit Yields and Cross Sections

The data and MC distributions, normalized to the fitted yields, are shown for the D^+ and D^{*+} channels in Figure 10.1. The distributions are separated for the W^- and W^+ channels. The data largely lies within 1σ systematic uncertainties as determined by the fit. The yields from the likelihood fit are shown in Tables 10.1 and 10.2. Yields are given for the differential fits in $p_{\mathrm{T}}(D^{(*)})$ and $|\eta(\ell)|$. The results from the fit are consistent between the D^+ and D^{*+} channels. The $p_{\mathrm{T}}(D^{(*)})$ fits results in slightly larger uncertainties, with respect to the $|\eta(\ell)|$ fits, due to the dependence of the largest systematic uncertainties depending more strongly on $p_{\mathrm{T}}(D^{(*)})$. This results in more constraints on the yields in the $p_{\mathrm{T}}(D^{(*)})$ fit.

The cross sections for $\sigma(W + D^{(*)})^{\text{OS-SS}} \times B(W \to \ell\nu)$ and $R_c^{\pm}$ from the likelihood fit are presented in Table 10.3. Note these results are extracted from the $p_{\mathrm{T}}(D^{(*)})$ fit, but all results are compatible for both differential variables. The cross sections ratios obtained by comparing the D^+ and D^{*+} channels are consistent with world-average production fractions results. In particular, the world average ratio of the two channels is measured to be $\sigma(W + D^*)/\sigma(W + D^+) = 1.01 \pm 0.034$, with uncertainties determined from the full correlation matrix from Ref. [86]. This is consistent with the ratio of cross sections measured by this analysis, $\sigma(W + D^*)/\sigma(W + D^+) = 1.02$. A combination measurement of the charge ratio, $R_c^{\pm}(D^{(*)})$, is derived from the two separate channels. For the measurements of $R_c^{\pm}$, the systematic uncertainties are are dominated by the MC statistical uncertainties that are largely

uncorrelated between the channels, as seen in Table 9.1. The results from this measurements are consistent with, but more precise than, the comparable CMS $W + D^*$ results [31], which were made with a smaller data set, after adjusting for differences between the chosen fiducial regions.

Table 10.1: Signal and background yields from the profile likelihood fit in the OS–SS $W + D^+$ SR extracted from the $p_{\mathrm{T}}(D^+)$ differential fit. The data statistical uncertainty is calculated as $\sqrt{N_{\mathrm{OS}} + N_{\mathrm{SS}}}$. Uncertainties in individual SM components are the full post-fit systematic uncertainties.

	OS–SS $W + D^+$ SR ($p_{\mathrm{T}}(D^+)$ fit)		OS–SS $W + D^+$ SR ($\lvert\eta(\ell)\rvert$ fit)	
Sample	W^-+D^+	W^++D^-	W^-+D^+	W^++D^-
$W^{\pm}+D^{\mp}$ (bin 1)	26 430 ± 510	26 180 ± 550	31 530 ± 530	30 920 ± 560
$W^{\pm}+D^{\mp}$ (bin 2)	39 090 ± 660	38 610 ± 660	30 560 ± 650	30 790 ± 620
$W^{\pm}+D^{\mp}$ (bin 3)	43 520 ± 660	41 510 ± 670	25 640 ± 470	24 940 ± 450
$W^{\pm}+D^{\mp}$ (bin 4)	15 330 ± 350	14 520 ± 350	23 890 ± 450	22 380 ± 500
$W^{\pm}+D^{\mp}$ (bin 5)	2740 ± 120	2346 ± 93	15 860 ± 480	14 630 ± 470
$W + c^{\mathrm{matched}}$	24 800 ± 2400	24 300 ± 2400	23 500 ± 2600	22 800 ± 2700
$W + c^{\mathrm{mis-matched}}$	34 300 ± 2500	29 700 ± 2400	33 900 ± 2500	29 200 ± 2500
W+jets	1300 ± 1400	1900 ± 1500	2200 ± 1500	2500 ± 1800
$t\bar{t}$ + single top	6500 ± 550	6220 ± 590	6520 ± 540	6160 ± 590
Other	1030 ± 430	1830 ± 460	1060 ± 450	1940 ± 470
Multijet	730 ± 410	1070 ± 450	1180 ± 640	1600 ± 690
Total SM	195 800 ± 1200	188 200 ± 1300	195 800 ± 1300	187 900 ± 1400
Data	195 800 ± 1100	188 200 ± 1100	195 800 ± 1100	188 200 ± 1100

10.2 Ranking of Systematic Uncertainties

The impact of the nuisance parameters on the fitted values of the absolute fiducial cross section in the differential $p_{\mathrm{T}}(D^{(*)})$ fits is shown as a "ranking plot" in Figure 10.2. The 20 nuisance parameters with the largest contribution are ordered by decreasing impact on the corresponding observable. The post-fit central values and uncertainties of the corresponding parameters are given in the same plots. The ranking plots demonstrate that most nuisance parameters with large impact on the integrated fiducial cross section do not deviate significantly from the initial values in the likelihood fit. The parameters associated with the signal mass-peak shape uncertainties have the most significant pulls in the fit, however, the impact of the corresponding systematic uncertainties on the observables is small (up to 1% for cross sections and negligible for $R_c^{\pm}$). These parameters are constrained by the observed width of the $D^{(*)}$ peaks in the data. The NP shifts depend on the charge of the $D^{(*)}$ meson and are

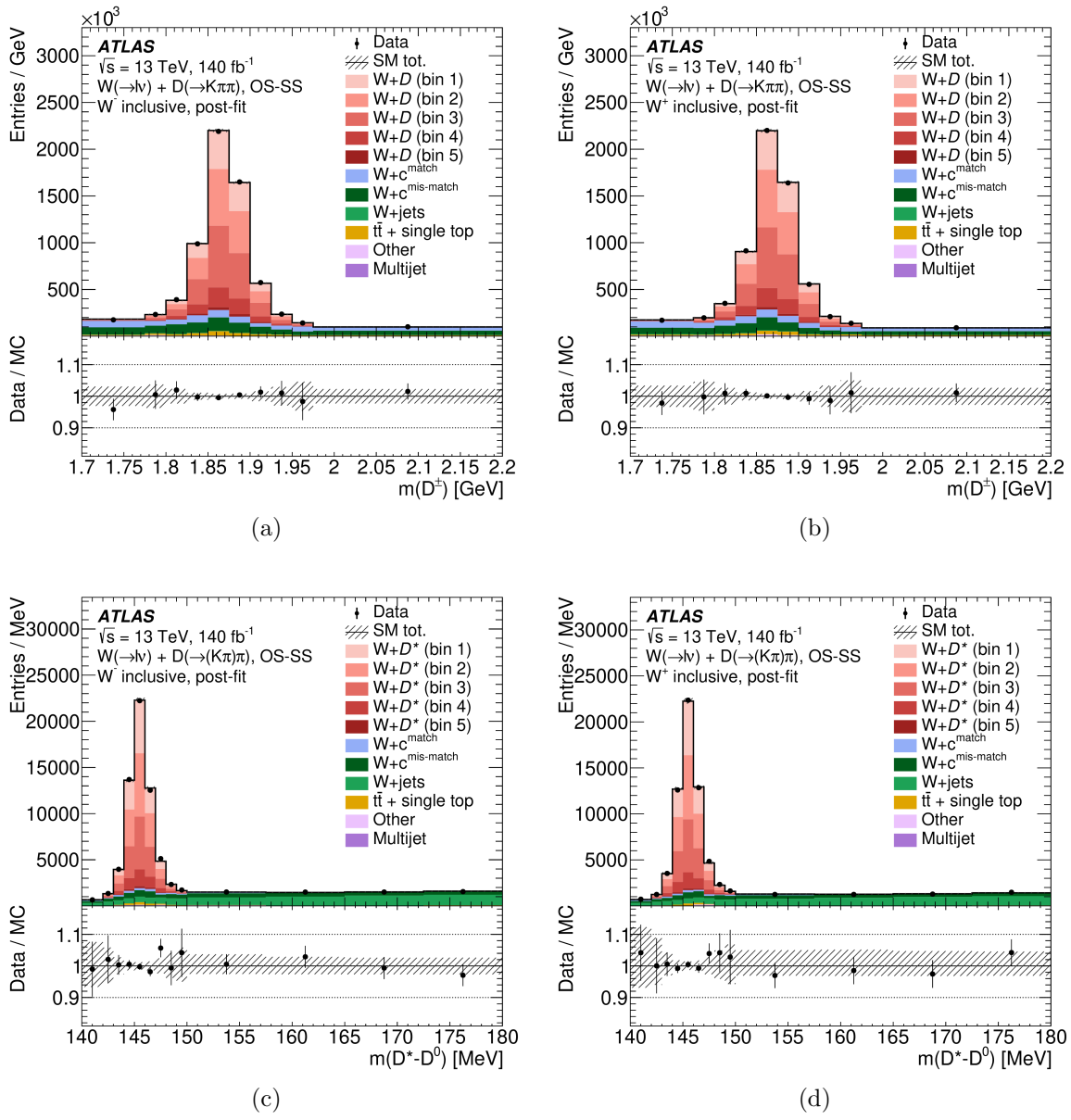

Figure 10.1: Post-fit OS–SS $W + D^{(*)}$ signal and background predictions compared with data: (a) W^-+D^+ channel, (b) W^++D^- channel, (c) W^-+D^{*+} channel, and (d) W^++D^{*-} channel. The "SM Tot." line represents the sum of all signal and background samples and the corresponding hatched band shows the full post-fit systematic uncertainty. The five bins associated with the signal samples are the truth bins of the $p_{\mathrm{T}}(D^{(*)})$ differential distribution.

Table 10.2: Post-fit yields in the OS–SS $W + D^*$ SR from the $p_{\mathrm{T}}(D^{*+})$ differential fit. The data statistical uncertainty is calculated as $\sqrt{N_{\mathrm{OS}} + N_{\mathrm{SS}}}$. Uncertainties in individual SM components are the full post-fit systematic uncertainties.

	OS–SS $W + D^*$ SR ($p_{\mathrm{T}}(D^{*+})$ fit)		OS–SS $W + D^*$ SR ($\lvert\eta(\ell)\rvert$ fit)	
Sample	W^-+D^{*+}	W^++D^{*-}	W^-+D^{*+}	W^++D^{*-}
$W^{\pm}$+$D^{*\mp}$ (bin 1)	13 670 ± 280	13 880 ± 260	12 640 ± 260	12 980 ± 230
$W^{\pm}$+$D^{*\mp}$ (bin 2)	17 210 ± 250	16 950 ± 280	12 470 ± 260	12 910 ± 280
$W^{\pm}$+$D^{*\mp}$ (bin 3)	15 000 ± 200	14 890 ± 200	10 370 ± 220	10 250 ± 200
$W^{\pm}$+$D^{*\mp}$ (bin 4)	5402 ± 89	5139 ± 95	9500 ± 230	9120 ± 240
$W^{\pm}$+$D^{*\mp}$ (bin 5)	822 ± 45	744 ± 41	6900 ± 290	6390 ± 290
$W + c^{\mathrm{matched}}$	2800 ± 530	2730 ± 530	3060 ± 450	2690 ± 480
$W + c^{\mathrm{mis-matched}}$	15 900 ± 1700	14 000 ± 1600	16 400 ± 1400	14 200 ± 1400
W+jets	35 600 ± 1800	32 000 ± 1700	35 600 ± 1800	31 900 ± 1700
$t\bar{t}$ + single top	1580 ± 200	1320 ± 180	1480 ± 180	1350 ± 160
Other	1710 ± 540	650 ± 480	1480 ± 480	510 ± 420
Multijet	−90 ± 190	−20 ± 200	−160 ± 220	−120 ± 240
Total SM	109 600 ± 1100	102 200 ± 1500	109 700 ± 1000	102 200 ± 1000
Data	109 690 ± 900	102 320 ± 970	109 690 ± 900	102 320 ± 970

Table 10.3: Measured fiducial cross sections times the single-lepton-flavor W boson branching ratio and the cross section ratios. $R_c^{\pm}(D^{(*)})$ is obtained by combining the individual measurements of $R_c^{\pm}(D^+)$ and $R_c^{\pm}(D^{*+})$, as explained in the text.

Channel	$\sigma(W + D^{(*)})^{\text{OS-SS}} \times B(W \to \ell\nu)$ [pb]
W^-+D^+	50.2 ± 0.2 (stat.) $^{+2.4}_{-2.3}$ (syst.)
W^++D^-	48.5 ± 0.2 (stat.) $^{+2.3}_{-2.2}$ (syst.)
W^-+D^{*+}	51.1 ± 0.4 (stat.) $^{+1.9}_{-1.8}$ (syst.)
W^++D^{*-}	50.0 ± 0.4 (stat.) $^{+1.9}_{-1.8}$ (syst.)
	$R_c^{\pm} = \sigma(W^+ + D^{(*)})/\sigma(W^- + D^{(*)})$
$R_c^{\pm}(D^+)$	0.965 ± 0.007 (stat.) ± 0.012 (syst.)
$R_c^{\pm}(D^{*+})$	0.980 ± 0.010 (stat.) ± 0.013 (syst.)
$R_c^{\pm}(D^{(*)})$	0.971 ± 0.006 (stat.) ± 0.011 (syst.)

therefore treated with independent parameters for each charge. They account for the small residual resolution degradation that is not accounted for in the MC simulation.

10.3 Cross Section Comparisons to PDFs

Theoretical predictions for the $W + D^{(*)}$ cross section for a variety of state-of-the-art PDF sets are obtained using the signal aMC@NLO+Py8 (NLO) samples with the configuration described in Section 4.2. A finite charm quark mass of $m_c = 1.55\,\text{GeV}$ is used to regularize the cross section and a full CKM matrix is used to calculate the hard-scattering amplitudes. For each PDF set, the uncertainty is obtained from the alternative generator weights using the LHAPDF prescription [150]. Uncertainties due to the choice of Pythia 8 tune are assessed by replacing the A14 tune with the Monash tune [159]. Uncertainties associated with the choice of parton shower model are estimated from a comparison of events generated with the baseline configuration and events generated with Herwig 7.2 [160] using its default tune. Differences between predictions associated with the choice of NLO matching algorithm are assessed by comparing the aMC@NLO+Py8 (NLO) cross sections with those obtained using the calculation described in Ref. [46]. This calculation is based on the Powhel event generator, which uses the Powheg Box v2 interface to implement Powheg NLO matching. A charm quark mass $m_c = 1.5\,\text{GeV}$ is used to regularize the cross section. Effects of nondiagonal CKM matrix elements and off-shell W boson decays, including spin correlations, are taken into account in both the aMC@NLO+Py8 (NLO) and Powhel calculations. For these comparisons, the renormalization and factorization scales are set to one half of the transverse mass calculated using all final-state partons and leptons, and the ABMP16_3_NLO PDF set with $\alpha_s = 0.118$ and Monash Pythia 8.2 tune are used for both samples. The uncertainty in the direct charm production fractions is assessed using the results from Ref. [86].

Figure 10.3 shows the measured fiducial cross sections for each of the four channels compared with the theoretical predictions obtained using different NNLO PDF sets, including a PDF set tailored to describe the strangeness of the proton – NNPDF3.1_strange [20]. Results for all four channels show a consistent pattern. The experimental precision is comparable to the PDF uncertainties and smaller than the total NLO theory uncertainty. All PDF sets are consistent with the measured cross sections once the combined theory and PDF set uncertainties are considered.

The two channel combination cross section ratio, $R_c^{\pm}(D^{(*)})$, is shown in Figure 10.4. This result agrees within uncertainties with all PDF sets, however the NNPDF4.0nnlo shows a slight tension with the measurement. The measurements of $R_c^{\pm}$ have comparable statistical and systematic uncertainties, as opposed to the total cross section measurement which is dominated by systematic uncertainties. The PDF set uncertainties fall into two broad categories, as they relate to $R_c^{\pm}$. One group of PDF sets require that the strange-sea be symmetric ($s = \bar{s}$), and these include CT18 and AMBP16. These PDFs have a smaller uncertainty on $R_c^{\pm}$ than those PDFs that do not require the s and $\bar{s}$ distributions to be equivalent, such as NNPDF or MSHT. For the Bjorken-x region probed by this

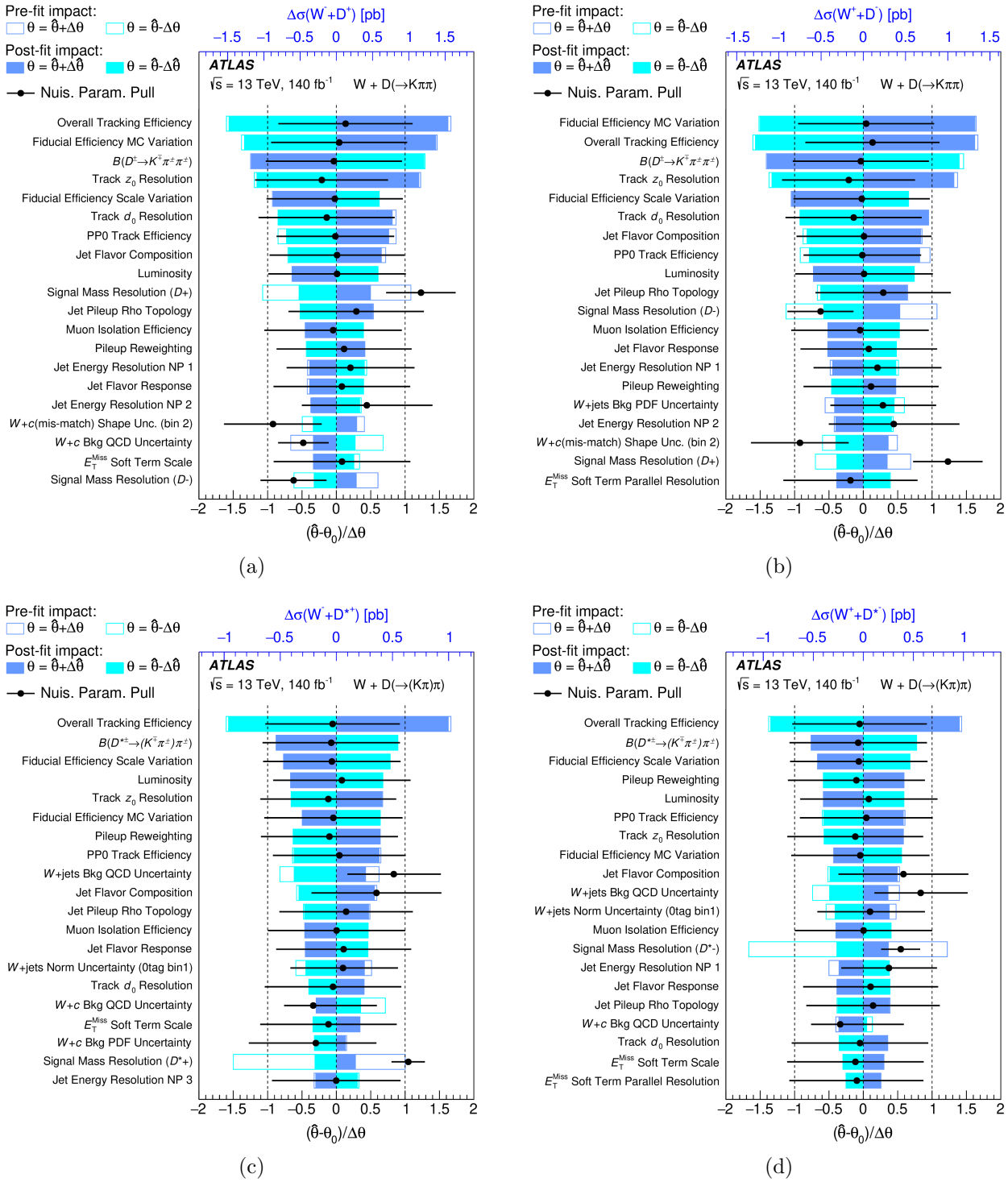

Figure 10.2: Impact of systematic uncertainties, for the 20 largest contributions, on the fitted cross section from the $p_{\mathrm{T}}(D^{(*)})$ fits, sorted in decreasing order. Impact on: (a) $\sigma(W^-+D^+)$, (b) $\sigma(W^++D^-)$, (c) $\sigma(W^-+D^{*+})$, and (d) $\sigma(W^++D^{*-})$. The impact of pre-fit (post-fit) nuisance parameters $\vec{\theta}$ on the signal strength are shown with empty (colored) boxes. The post-fit central value ($\hat{\theta}$) and uncertainty are shown for each parameter with black dots.

measurement, the measured $R_c^{\pm}$ value is consistent with those PDF sets that impose the symmetry requirement on the strange sea, suggesting that any s-$\bar{s}$ asymmetry is small in the Bjorken-x region probed by this measurement. Results from Ref. [42] provide a study of the NLO and NNLO fiducial cross sections for different charm-jet selections that can be compared to the results presented in this thesis. While the $\sigma(W + D^{(*)})^{\text{OS-SS}}$ results cannot be compared with the $W + c$-jet cross section calculations (since the calculations do not include the effects of charm quark fragmentation), the values of $R_c^{\pm}$ are comparable. For the $W + c$-jet $R_c^{\pm}$ NLO calculation, the value is consistent within statistical uncertainties with the results from the $W + D^{(*)}$ measurement, obtained using MadGraph5_aMC@NLO and an equivalent PDF set, (NNPDF3.1). A comparison of the NNLO+EW(NLO) value of $R_c^{\pm}$ for the $W + c$-jet calculation gives a number that is less than the NLO value by ∼1%. However, both the NLO and EW(NNLO) predictions are consistent with this measurement within the statistical uncertainty, which is on the order of 1%. NNLO impacts of the scale uncertainties on the computed $R_c^{\pm}$ are below 0.3%.

The differential cross sections for the D^+ channel, Figures 10.5 and , and the D^* channel,10.6, are presented below. The measured results are compared with cross sections predictions calculated with a variety of NNLO PDF sets. Both $D^{(*)}$ channels show consistent patterns in the measurement results for both differential variables, $D^{(*)}$ p_{T} and $|\eta(\ell)|$. The differential results are split by lepton charge and $D^{(*)}$ species, and further separated into three distributions, from top to bottom: a comparison of the absolute value of the cross section in each bin, compared to the prediction for that bin for each PDF set; the fraction of the total cross section that appears in each bin, compared to the predicted fraction of the cross section per bin for each PDF set; and the ratio of the prediction to the normalized cross section in each bin. The PDF sets that are compared are equivalent to those seen in Figure 10.3. Due to the correlation of systematic uncertainties between bins for the predicted values, the lower two panels more clearly highlight to compatibility between the PDF predictions and measured results.

Variations in the shape of the $p_{\text{T}}(D^{(*)})$ distribution depend only weakly on the choice of PDF. Experimental sensitivity to this dependence is reduced by the presence of p_{T}-dependent systematic uncertainties in the $D^{(*)}$ fiducial efficiency. Thus, while measurements of the cross section as a function of $p_{\text{T}}(D^{(*)})$ are an important test of the quality of MC modeling, they do not provide incisive constraints on PDFs. Systematic uncertainties for $|\eta(\ell)|$ are small and highly correlated among bins, providing good sensitivity to PDF variations. Measured differential cross sections have a broader $|\eta(\ell)|$ distribution than the central values of the predictions obtained with any of the PDF sets. The significance of the discrepancy is reduced if the PDF uncertainties are considered.

The compatibility of the measurements and predictions is tested with a χ^2 formula using experimental and theory covariance matrices,

$$\chi^2 = \sum_{i,j} (x_i - \mu_i) \left(C^{-1}\right)_{ij} (x_j - \mu_j), \tag{10.1}$$

where $\vec{x}$ are the measured differential cross sections in the 10 $|\eta(\ell)|$ bins, and $\vec{\mu}$ are

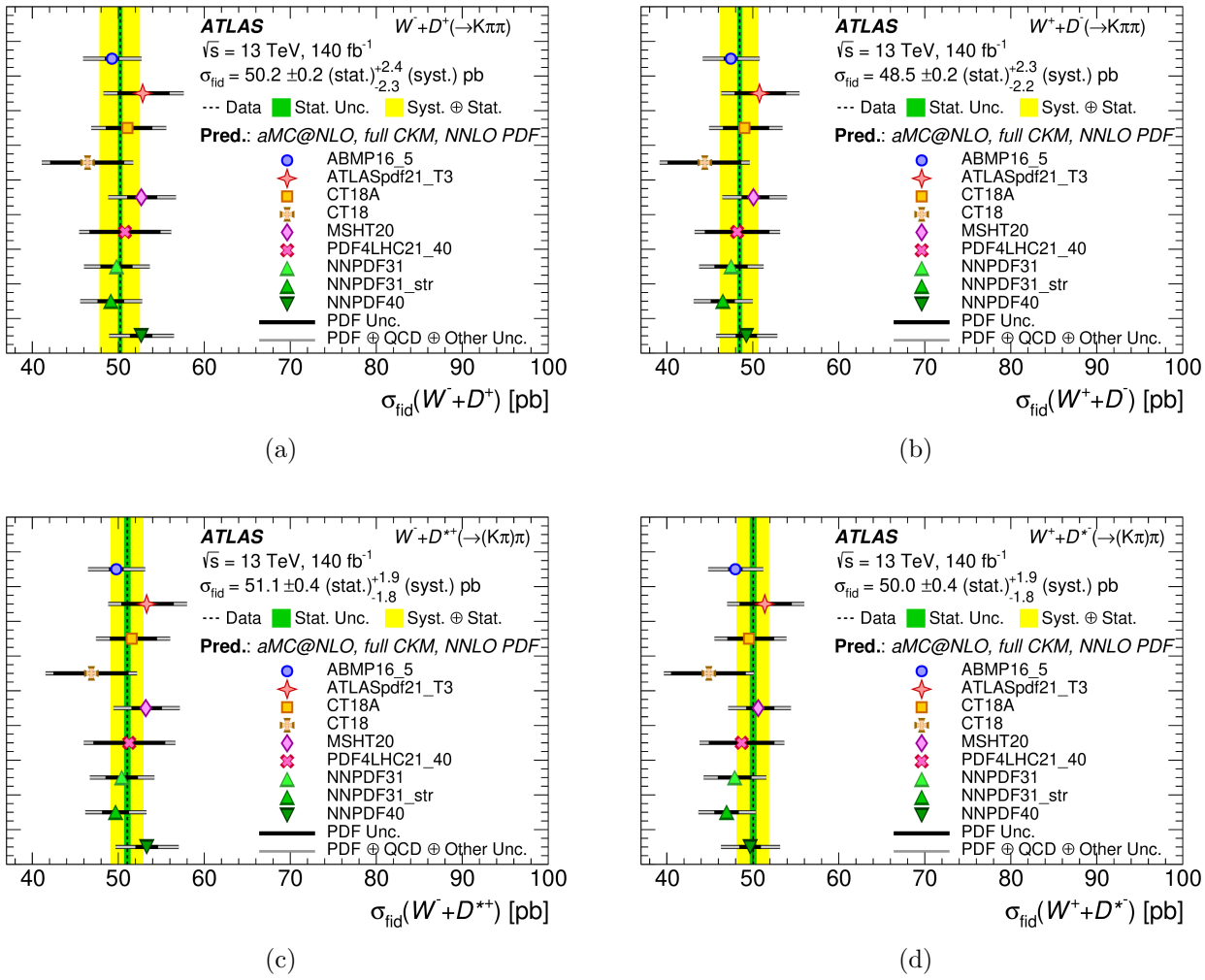

Figure 10.3: Measured fiducial cross section times the single-lepton-flavor W branching ratio compared with different NNLO PDF predictions for (a) W^-+D^+, (b) W^++D^-, (c) W^-+D^{*+}, and (d) W^++D^{*-}. The dotted vertical line shows the central value of the measurement, the green band shows the statistical uncertainty and the yellow band shows the combined statistical and systematic uncertainty. The PDF predictions are designated by markers. The inner error bars on the theoretical predictions show the 68% CL uncertainties obtained from the error sets provided with each PDF set, while the outer error bar represents the quadrature sum of the 68% CL PDF, scale, hadronization, and matching uncertainties. The PDF predictions are based on NLO calculations performed using aMC@NLO and a full CKM matrix: ABMP16_5 [161], ATLASpdf21_T3 [162], CT18A, CT18 [163], MSHT20 [164], PDF4LHC21_40 [165], NNPDF31 [166], NNPDF31_str [20], NNPDF40 [167]. ABMP16_5, ATLASpdf21_T3, CT18A, and CT18 impose symmetric strange-sea PDFs.

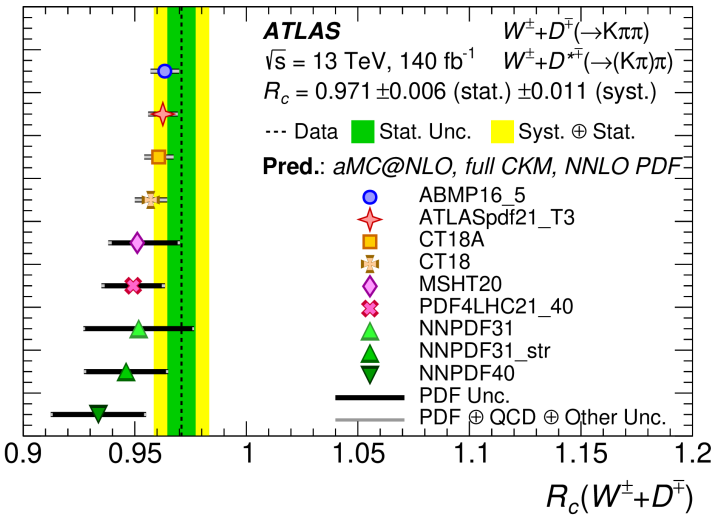

Figure 10.4: Measured fiducial cross section ratio, $R_c^{\pm}$, compared with different PDF predictions. The data are a combination of the separate $W + D^+$ and $W + D^*$ channel measurements. The dotted vertical line shows the central value of the measurement, the green band shows the statistical uncertainty and the yellow band shows the combined statistical and systematic uncertainty. The PDF predictions are designated by markers. The inner error bars on the theoretical predictions show the 68% CL uncertainties obtained from the error sets provided with each PDF set, while the outer error bar represents the quadrature sum of the 68% CL PDF, scale, hadronization, and matching uncertainties. The PDF predictions are based on NLO calculations performed using aMC@NLO and a full CKM matrix: ABMP16_5 [161], ATLASpdf21_T3 [162], CT18A, CT18 [163], MSHT20 [164], PDF4LHC21_40 [165], NNPDF31 [166], NNPDF31_str [20], NNPDF40 [167]. ABMP16_5, ATLASpdf21_T3, CT18A, and CT18 impose symmetric strange-sea PDFs.

the predicted cross sections in the same bin and depend on the choice of PDF set. The total covariance matrix C is the sum of the experimental covariance matrix, encoding the measurement error, and the theory covariance matrix describing the uncertainties in the theory predictions as described below. The χ^2 is then converted to a p-value assuming 10 degrees of freedom. The theory covariance matrix corresponding to the PDF uncertainty is calculated following the LHAPDF prescription [150]. Other theory uncertainties are assumed to be 100% correlated across differential bins.

The resulting p-values for the aMC@NLO predictions of the $|\eta(\ell)|$ differential cross sections with different PDF sets are given in Table 10.4 for the D^+ channel and in Table 10.5 for the D^{*+} channel. The p-values are calculated with progressively more systematic uncertainties included in the theory covariance matrix, ranging from an "Exp. Only" calculation, where no systematic uncertainties related to the theory predictions are included, to a calculation

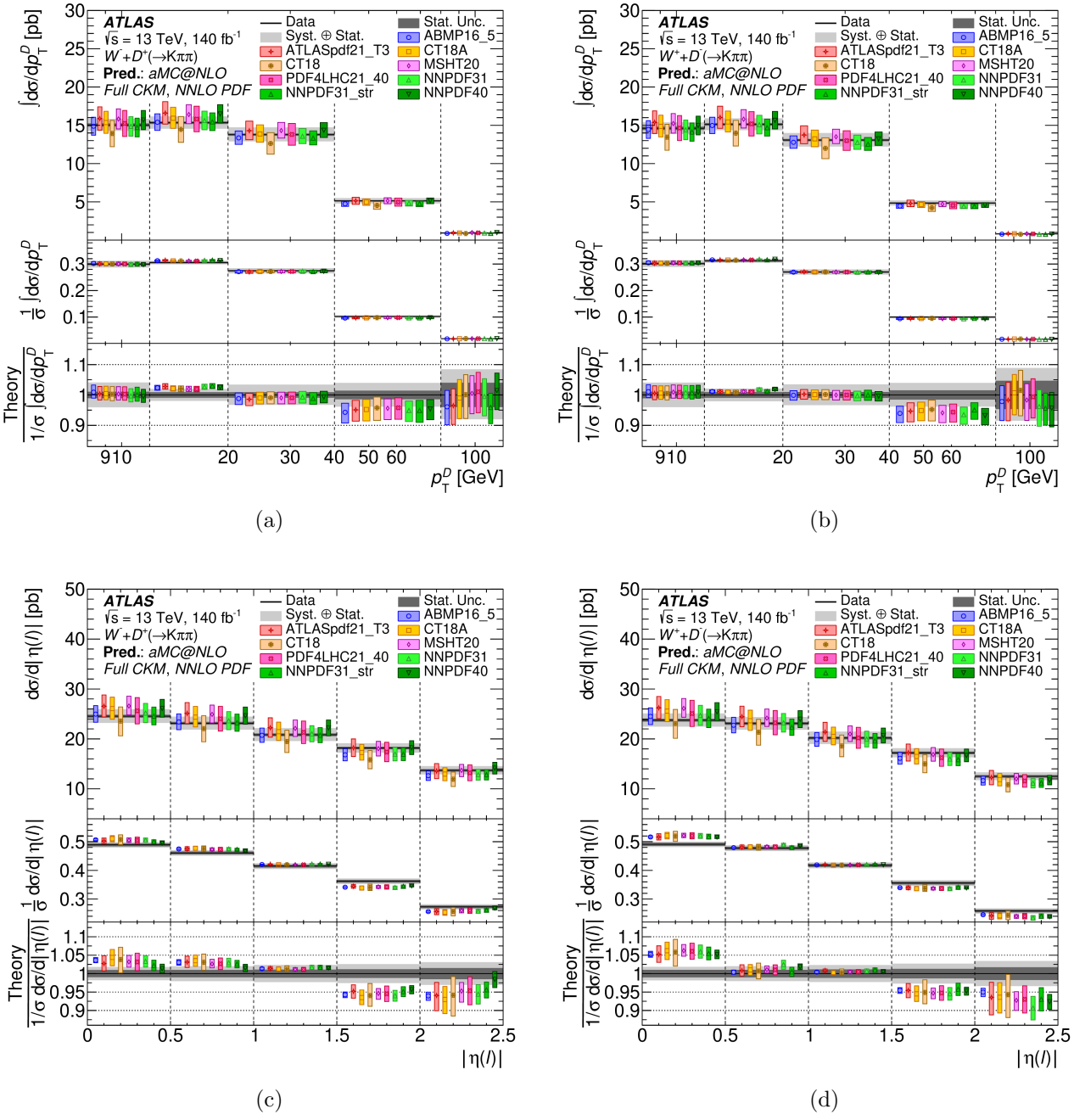

(a) (b) (c) (d)

Figure 10.5: Measured differential fiducial cross section times the single-lepton-flavor W branching ratio compared with different NNLO PDF predictions in the D^+ channel: (a) W^-+D^+ $p_{\mathrm{T}}(D^+)$, (b) W^++D^- $p_{\mathrm{T}}(D^+)$, (c) W^-+D^+ $|\eta(\ell)|$, and (d) W^++D^- $|\eta(\ell)|$. The displayed cross sections in p_{T} (D^+) plots are integrated over each bin. Error bars on the predictions are the quadrature sum of the QCD scale, PDF, hadronization, and matching uncertainties. The PDF predictions are based on NLO calculations performed using aMC@NLO and a full CKM matrix: ABMP16_5 [161], ATLASpdf21_T3 [162], CT18A, CT18 [163], MSHT20 [164], PDF4LHC21_40 [165], NNPDF31 [166], NNPDF31_str [20], NNPDF40 [167]. ABMP16_5, ATLASpdf21_T3, CT18A, and CT18 impose symmetric strange-sea PDFs.

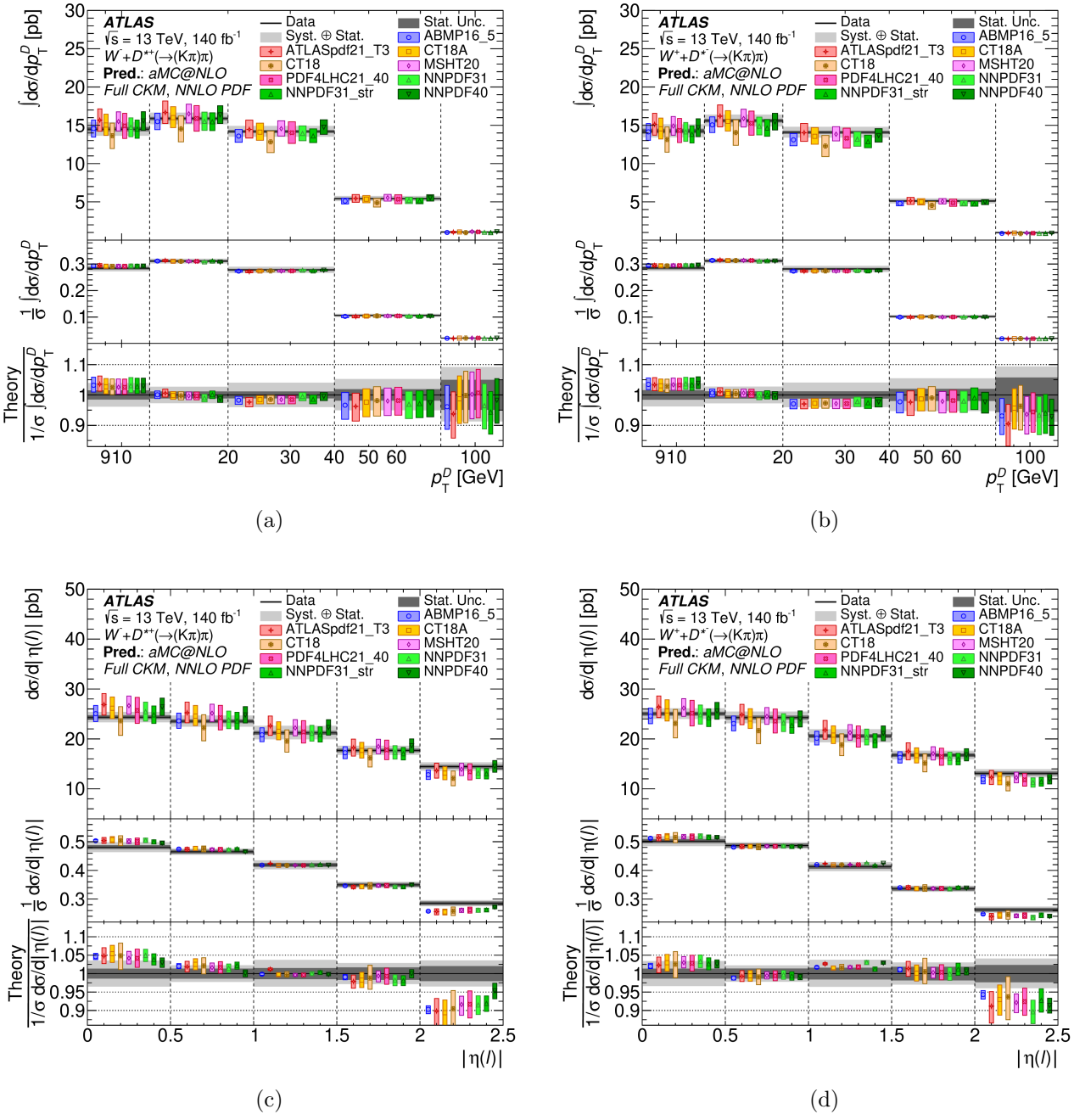

Figure 10.6: Measured differential fiducial cross section times the single-lepton-flavor W branching ratio compared with different PDF predictions in the D^{*+} channel: (a) W^-+D^{*+} $p_{\mathrm{T}}(D^{*+})$, (b) W^++D^{*-} $p_{\mathrm{T}}(D^{*+})$, (c) W^-+D^{*+} $|\eta(\ell)|$, and (d) W^++D^{*-} $|\eta(\ell)|$. The displayed cross sections in p_{T} (D^+) plots are integrated over each differential bin. Error bars on the MC predictions are the quadrature sum of the QCD scale uncertainty, PDF uncertainties, hadronization uncertainties, and matching uncertainty. The PDF predictions are based on NLO calculations performed using aMC@NLO and a full CKM matrix: ABMP16_5 [161], ATLASpdf21_T3 [162], CT18A, CT18 [163], MSHT20 [164], PDF4LHC21_40 [165], NNPDF31 [166], NNPDF31_str [20], NNPDF40 [167]. ABMP16_5, ATLASpdf21_T3, CT18A, and CT18 impose symmetric strange-sea PDFs.

including all theory uncertainties: QCD scale, "hadronization and matching", and PDF uncertainties. The hadronization and matching uncertainty is defined to be the quadrature sum of the uncertainty in the charm production fractions, two-point uncertainties associated with the choice of showering program (PYTHIA vs. HERWIG), the tune (A14 vs. Monash) and the matching algorithm (aMC@NLO vs. POWHEG). These uncertainties are treated as fully correlated between the $W^+ + D^-$ and $W^- + D^+$ channels. Without considering the theory uncertainties (i.e. just comparing the PDF central values with the experimental measurements) the p-values are below 10% for all PDFs in the D^+ channel and most of the PDFs in the D^{*+} channel. Adding hadronization and QCD scale uncertainties increases the probabilities to at most 15% in the D^+ channel and 24% in the D^{*+} channel. Although the QCD scale uncertainty is a large uncertainty in the absolute cross section, it does not change the p-values significantly because the uncertainty is 100% correlated between the $|\eta(\ell)|$ bins, and it does not have a large impact on the shape of the differential distribution. Adding the PDF uncertainties greatly increases the p-values; the PDF uncertainty has a significant effect on the shape of the differential $|\eta(\ell)|$ distribution. This suggests that including these measurements in a global PDF fit would provide useful constraints on the allowed PDF variations.

Table 10.4: The p-values for compatibility of the measurement and the predictions, calculated with the χ^2 formula (see Eq. 10.1) using experimental and theory covariance matrices. The first column shows the p-values for the $|\eta(\ell)|$ (D^+) differential cross section using only experimental uncertainties. The next columns show p-values when progressively more theory systematic uncertainties are included. The PDF predictions are based on NLO calculations performed using aMC@NLO and a full CKM matrix: ABMP16_5 [161], ATLASpdf21_T3 [162], CT18A, CT18 [163], MSHT20 [164], PDF4LHC21_40 [165], NNPDF31 [166], NNPDF31_str [20], NNPDF40 [167]. ABMP16_5, ATLASpdf21_T3, CT18A, and CT18 impose symmetric strange-sea PDFs.

Channel	D^+ $\|\eta(\ell)\|$			
p-value for PDF [%]	Exp. Only	$\oplus$ QCD Scale	$\oplus$ Had. and Matching	$\oplus$ PDF
ABMP16_5_nnlo	7.1	11.8	12.9	19.8
ATLASpdf21_T3	9.0	9.7	11.5	84.7
CT18ANNLO	0.7	1.0	1.1	76.0
CT18NNLO	1.4	6.1	6.3	87.6
MSHT20nnlo_as118	2.7	2.9	3.3	45.6
PDF4LHC21_40	3.9	5.3	5.6	75.8
NNPDF31_nnlo_as_0118_hessian	1.5	2.6	2.8	50.7
NNPDF31_nnlo_as_0118_strange	9.1	14.7	15.2	59.9
NNPDF40_nnlo_as_01180_hessian	9.9	10.2	10.2	43.7

Table 10.5: The p-values for compatibility of the measurement and the predictions, calculated with the χ^2 formula (see Eq. 10.1) using experimental and theory covariance matrices. The first column shows the p-values for the $|\eta(\ell)|$ (D^{*+}) differential cross section using only experimental uncertainties. The next columns show p-values when progressively more theory systematic uncertainties are included. The PDF predictions are based on NLO calculations performed using aMC@NLO and a full CKM matrix: ABMP16_5 [161], ATLASpdf21_T3 [162], CT18A, CT18 [163], MSHT20 [164], PDF4LHC21_40 [165], NNPDF31 [166], NNPDF31_str [20], NNPDF40 [167]. ABMP16_5, ATLASpdf21_T3, CT18A, and CT18 impose symmetric strange-sea PDFs.

Channel	D^{*+} $\|\eta(\ell)\|$			
p-value for PDF [%]	Exp. Only	$\oplus$ QCD Scale	$\oplus$ Had. and Matching	$\oplus$ PDF
ABMP16_5_nnlo	22.8	23.7	25.0	28.8
ATLASpdf21_T3	1.9	2.9	3.4	33.7
CT18ANNLO	6.5	6.9	7.8	47.3
CT18NNLO	9.4	19.2	19.7	52.8
MSHT20nnlo_as118	7.0	9.4	10.4	31.3
PDF4LHC21_40	14.2	14.2	15.2	51.4
NNPDF31_nnlo_as_0118_hessian	5.0	5.1	5.5	34.9
NNPDF31_nnlo_as_0118_strange	11.4	12.4	13.2	46.0
NNPDF40_nnlo_as_01180_hessian	4.5	6.1	6.4	36.0

Chapter 11

$W + D_s$ Total Cross Section Results

This chapter presents results from the $W + D_s$ inclusive cross section measurement. The measured observables are the cross sections of $W + D_s$ in both OS charge combinations, a measurement of $R_c^{\pm}$ (D_s), and a measurement of R_{D^+/D_s}. Due to limitations of the statistics in this measurement, as well as lower ratio of signal events to background events as compared to the $W + D^{(*)}$ differential cross section measurement, the uncertainties on the total cross section are $\approx$ 10% for the D_s channel, rather than the 5% obtained for the D^+ and D^* channels. The $R_c^{\pm}$ value which is extracted from both D_s and D^+ channels simultaneously, and is measured to 8% precision. R_{D^+/D_s} is measured to approximately 8% precision, with the ration reducing some systematic impacts with respect to the total cross section precision.

11.1 Post-fit Yields and Cross Sections

The mass distributions for the post-fit D_s and D^+ mass are shown in Figure 11.1 in OS-SS for the the W^+ and W^- channels separately. The data largely falls within the uncertainty band showing one standard deviation of statistical and systematic uncertainties. The post-fit yields in the $W + D^{(*)}$ SR extracted from the likelihood fit are shown in Table 11.1.

The cross section results for $\sigma(W + D_s)^{\text{OS-SS}} \times B(W \to \ell\nu)$, $R_c^{\pm}$ (D_s), and R_{D^+/D_s} are summarized in Table 11.2. The uncertainties on the inclusive cross section and measured value of $R_c^{\pm}$ for these results are larger than those in the $W + D^{(*)}$ differential analysis, as is discussed in the context of the impact of systematic uncertainties, in Section 11.2. $R_c^{\pm}$ is computed from the likelihood fit expression, and directly extracted as a fitted parameter for both the D_s and D^+ signals. The ratio of the $W + D^+$ cross section to the $W + D_s$ cross section is derived simultaneously for both charges, to enforce CP conservation which is not expected to be significant at the level of precision of this measurement. In addition to the large impact on the measurement from the MC statistical uncertainties, uncertainties that affect only the D^+ or D_s signals, in particularly the signal branching ratio uncertainties, have an effect on the uncertainty of the result that is extracted directly from the fit. Due to the large uncertainties from the D^+ cross section, the directly extracted value of R_{D^+/D_s} has a

12% relative uncertainty, $R_{D^+/D_s} = 3.32 \pm 0.17\,(\text{stat.})^{+0.34}_{-0.36}\,(\text{syst.})$. To overcome this statistical limitation, a second value of R_{D^+/D_s} is calculated in the same fiducial region by combining the D_s cross section from the simultaneous fit, and use the higher precision D^+ cross section from the differential $W + D^+$ fit, described in Section 10. As these two measurements are not performed simultaneously, their uncertainties must be combined following the procedure for correlated errors. A conservative approach is taken, assuming the only correlated uncertainties are those related to experimental calibrations — $E_{\text{T}}^{\text{miss}}$, photon, electron, muon, jet, tracking, and luminosity — and the correlation is assigned to be 100%. The ratio is computed with the combination of both the positive and negative W boson channels, to reduce the data statistical uncertainty and enforce the assumption that CP is conserved. This value of R_{D^+/D_s} is found to be $R_{D^+/D_s} = 2.93 \pm 0.06(\text{stat.}) \pm 0.24(\text{syst.})$, which is more precise than the simultaneous measurement, due to the greater data statistics for the $D^+ \to K\pi\pi$ decay relative to the $D^+ \to \phi\pi \to (KK)\pi$ mode. Both of the measured values of R_{D^+/D_s} are compatible within the measured uncertainties. The world average value of R_{D^+/D_s} [86] is measured to be $f(c \to D^+)/f(c \to D_s) = 2.998 \pm 0.185$, which is compatible with both results from this measurement, within the uncertainty.

The $R_c^{\pm}$ ratio in the $W + D_s$ measurement is found to differ from the measurement made in the differential $W + D^{(*)}$ analysis by approximately 1.5σ. The largest background contribution in the $W + D_s$ originates from the $W+$jets background category, which is sensitive to the MC modeling, and has large uncertainties that come from both the QCD scale, α_S, and PDF uncertainties, in addition to the two point variations substituting aMC@NLO+Py8 (FxFx) for the nominal MC simulation of Sherpa 2.2.11. Multiple iterations of the fit were attempted, specifically targeted towards charge correlated uncertainties that modify the background shape and yield of $W+$jets background. The impact of these changes modified the central value of $R_c^{\pm}$ by up to 2%, well within the uncertainty extracted by the fit itself, and thus the changes are assessed to be marginal. Ultimately, for the stability of the fit, the $W+$jets backgrounds originating from two point variation with the aMC@NLO+Py8 (FxFx) sample are decorrelated between charges. Due to the smaller systematic uncertainties, the $R_c^{\pm}$ measurement from the $W + D^{(*)}$ differential analysis are preferred.

11.2 Ranking of Systematic Uncertainties

The impact of the systematic uncertainties on the fitted values for the inclusive cross sections are shown as "ranking plots" in Figure 11.2, analogous to Section 10.2. The 15 nuisance parameters with the largest impact on the fit are shown in descending order. These ranking plots indicate that the modeling of signal yield, originating from fiducial efficiency variations and tracking uncertainties; background modeling including shape and normalization, originating from two point variations in the MC sample used for the background and changes to the QCD scale and α_S; and the statistical power of the MC samples, represented in the ranking plots as γ parameters in each bin. In contrast to the $W + D^{(*)}$ differential analysis, the presence of the γ parameters in the ranking indicates that the analysis is limited by the

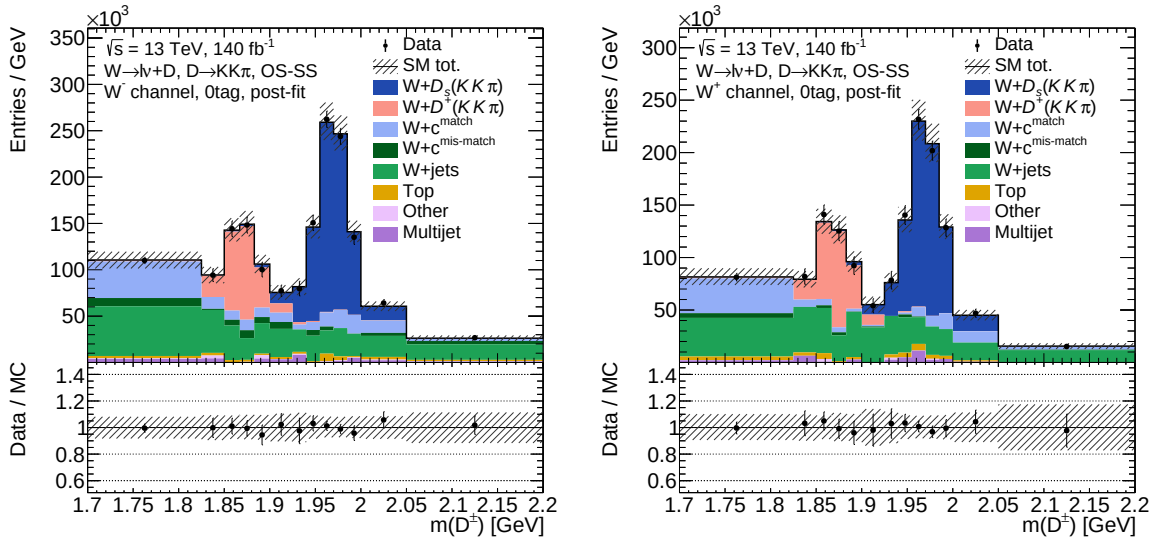

(a) (b)

Figure 11.1: Post-fit OS–SS $W + D^{(*)}$ signal and background predictions compared with data: (a) W^-+D_s^+channel, (b) W^++D_s^-channel, The "SM Tot." line represents the sum of all signal and background samples and the corresponding hatched band shows the full post-fit systematic uncertainty.

Table 11.1: Post-fit yields in the OS–SS $W + D_s$ and $W + D^+$ SR for the full ATLAS Run 2 from the inclusive simultaneous fit. The data statistical uncertainty is calculated as $\sqrt{N_{\mathrm{OS}} + N_{\mathrm{SS}}}$. Uncertainties in individual SM components are the full post-fit systematic uncertainties.

OS–SS $W + D_s$ SR fit)		
Sample	W^-+D_s^+	W^++D_s^-
$W^{\pm}$+$D_s^{\mp}$	10 675 ± 1037	9391 ± 1026
$W^{\pm}$+$D^{\mp}$	4872 ± 644	4317 ± 612
$W + c^{\mathrm{matched}}$	8128 ± 1258	6280 ± 1150
$W + c^{\mathrm{mis-matched}}$	2485 ± 2100	527 ± 703
W+jets	15 809 ± 1988	13 444 ± 1392
$t\bar{t}$ + single top	1247 ± 258	1318 ± 323
Other	494 ± 242	−92 ± 236
Multijet	1062 ± 190	589 ± 145
Total SM	44 773 ± 2908	35 775 ± 2381
Data	44 866 ± 696	35 874 ± 743

Table 11.2: Measured fiducial cross sections times the single-lepton-flavor W boson branching ratio and the cross section ratios for the simultaneous D_s and D^+ mass peak fits.

Channel	$\sigma(W + D^{(*)})^{\text{OS-SS}} \times B(W \to \ell\nu)$ [pb]
$W^-+D_s^+$	17.8 ± 0.4 (stat.) $^{+1.8}_{-1.6}$ (syst.)
$W^++D_s^-$	15.8 ± 0.4 (stat.) $^{+1.5}_{-1.4}$ (syst.)
	$R_c^{\pm} = \sigma(W^++D_s^-)/\sigma(W^-+D_s^+)$
$R_c^{\pm}$	0.884 ± 0.029 (stat.) $^{+0.059}_{-0.057}$ (syst.)
	$R_{D^+/D_s} = \sigma(W + D^+)/\sigma(W + D_s)$
R_{D^+/D_s}	2.93 ± 0.06 (stat.) ± 0.24 (syst.)

available MC simulation. The γ parameters are centered around 1 σ in the ranking plot, in contrast to other nuisance parameters which are centered near 0. For future analyses targeting this decay mode, it would be key amplify the statistical power of the background samples by both generating more simulated events, and developing additional strategies to reduce the statistical uncertainties on the templates.

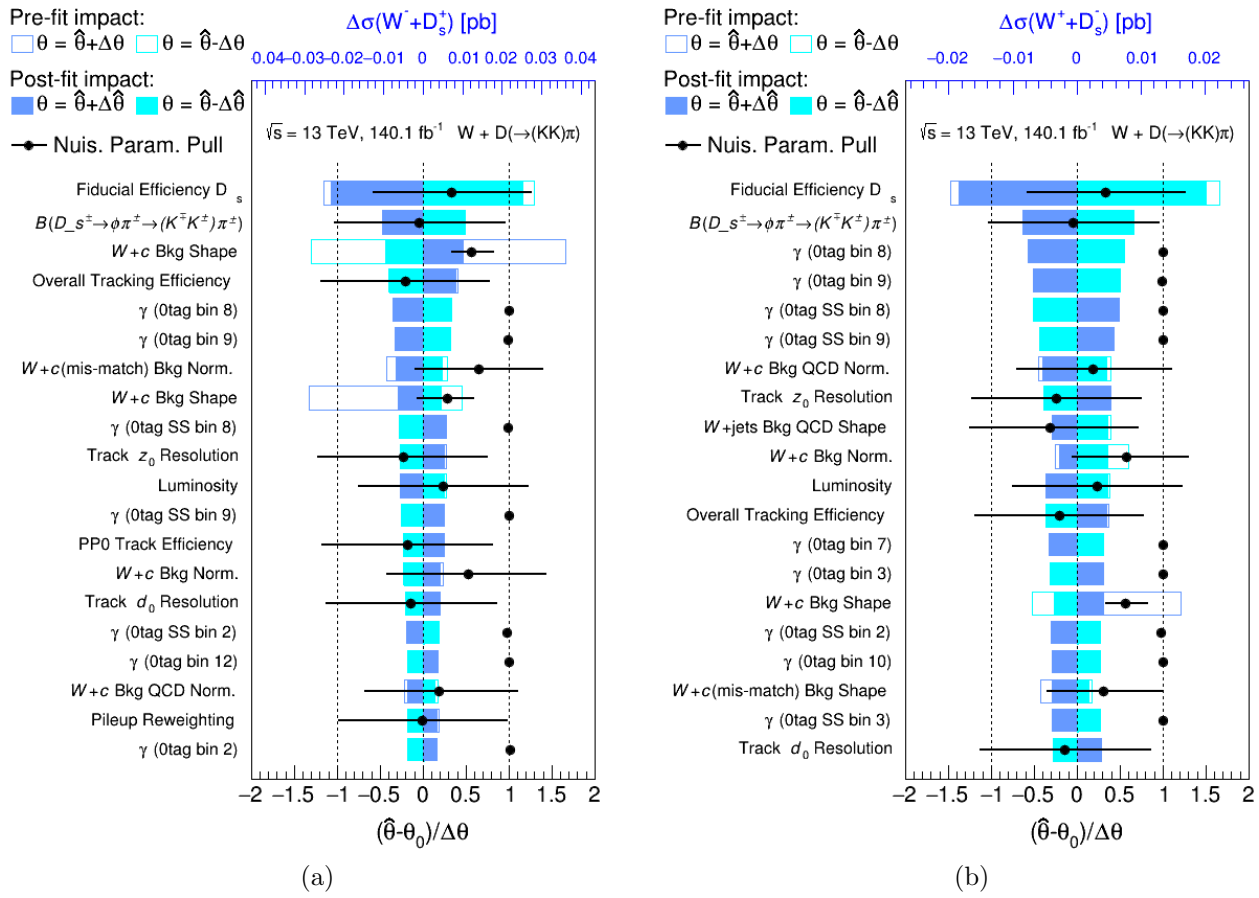

Figure 11.2: Impact of systematic uncertainties, for the 15 largest contributions, on the fitted cross section from the $p_{\mathrm{T}}(D^{(*)})$ fits, sorted in decreasing order. Impact on: (a) $\sigma(W^-+D^+)$, (b) $\sigma(W^++D^-)$. The impact of pre-fit (post-fit) nuisance parameters $\vec{\theta}$ on the signal strength are shown with empty (colored) boxes. The post-fit central value ($\hat{\theta}$) and uncertainty are shown for each parameter with black dots.

Chapter 12

Conclusions

Run 2 of the ATLAS experiment consisted of proton proton collisions at the the Large Hadron Collider at $\sqrt{s} = 13\,\text{TeV}$, and collected $140.1\,\text{fb}^{-1}$. This data set provides the opportunity to investigate physics process predicted by the Standard Model, as well as Beyond the Standard Model theories. The size of the data set allowed for unprecedented statistical precision for measurements of vector boson production, and $W + D$ production specifically.

By employing a direct reconstruction strategy on charm hadrons in the $W + D^{(*)}$ decay, the total fiducial cross sections for $W + D^+$ and $W + D^*$ production are measured for both charge combinations. The measured cross sections are:

- $\sigma(W^- + D^+) = 50.2 \pm 0.2(\text{stat.})\ ^{+2.4}_{-2.3}\ (\text{syst.})$
- $\sigma(W^+ + D^-) = 48.5 \pm 0.2(\text{stat.})\ ^{+2.3}_{-2.2}\ (\text{syst.})$
- $\sigma(W^- + D^{*+}) = 51.1 \pm 0.4(\text{stat.})\ ^{+1.9}_{-1.8}\ (\text{syst.})$
- $\sigma(W^+ + D^{*-}) = 50.0 \pm 0.4\ (\text{stat.})\ ^{+1.9}_{-1.8}\ (\text{syst.})$

These cross sections are precise to less than 5% total uncertainty. The ratios of the $W + D^+$ and $W + D^*$ cross sections for both charges are measured, as well as the combination of both $D^{(*)}$ species. These ratios are measured to $\approx 1\%$ precision, and are listed below for each channel and the combination:

- $R_c^{\pm}(D^+) = 0.965 \pm 0.007\ (\text{stat.})\ \pm 0.012\ (\text{syst.})$
- $R_c^{\pm}(D^{*+}) = 0.980 \pm 0.010\ (\text{stat.})\ \pm 0.013\ (\text{syst.})$
- $R_c^{\pm}(D^{(*)}) = 0.971 \pm 0.006\ (\text{stat.})\ \pm 0.011\ (\text{syst.})$

In addition to the total cross sections and ratios, the differential cross sections were measured in bins of $p_{\text{T}}(D^{(*)})$ and $\eta(l)$.

These results for $W + D^{(*)}$ cross sections and ratios are sensitive to the strange PDF of the proton. The high precision of these results, and the comparison of the results to a

variety of modern PDFs, indicates that inclusion of these cross sections would have an impact on measured values of protonic strangeness. The inclusion of these results in PDF fits is dependent on the development of a theory calculation at NNLO that incorporates the effects of the charm quark hadronization directly.

Beyond measuring the cross section of the $W + D$ production in the $D^+ \to K\pi\pi$ and $D^* \to D^0\pi \to K\pi\pi$ channels to high precision, the full weakly decaying spectrum of D meson decay modes has not been measured directly by the ATLAS experiment. Recent results from the ALICE experiment call into question whether the production fractions of the weakly decaying charm hadrons are universal between e^+e^-, ep, and pp collisions, particularly at lower charm hadron p_{T}. In an effort to measure these production fractions at ATLAS, additional charm decay modes are measured in the $W + D$ process, in particular the $D_s \to \phi\pi \to (KK)\pi$ and $D^+ \to \phi\pi \to (KK)\pi$ decay modes. The inclusive cross section of both of these processes is measured simultaneously as they both have the same final state. In addition to the cross section, the ratio of the charges, $R_c^{\pm}$, can be extracted, as well as a measurement of the ratio of production of D^+ to D_s, R_{D^+/D_s}. The measured values for the observables in ATLAS Run 2 are:

- $\sigma(W^+ + D_s^-) = 17.8 \pm 0.4\ (\mathrm{stat.})\ ^{+1.8}_{-1.6}\ (\mathrm{syst.})$
- $\sigma(W^- + D_s^+) = 15.8 \pm 0.4\ (\mathrm{stat.})\ ^{+1.5}_{-1.4}\ (\mathrm{syst.})$
- $R_c^{\pm} = 0.885 \pm 0.029\ (\mathrm{stat.})\ ^{+0.059}_{-0.057}\ (\mathrm{syst.})$
- $R_{D^+/D_s} = 2.93 \pm 0.06(\mathrm{stat.}) \pm 0.24(\mathrm{syst.})$

These measured values alone are insufficient to complete a measurement of the charm production fractions, due to the need of a measurement of the Λ_c cross section and statistical issues with the combination. The Λ_c channel has a higher signal to background ratio than other $D^{(*)}$ species, due to its shorter lifetime and the lack of a decay mode with distinctive kinematic features suitable for signal and background separation using the standard explicit charm decay techniques utilized in this thesis. Future work in ATLAS will target the Λ_c in the $W + \Lambda_c$ mode. When a sufficiently high precision measurement of $W + \Lambda_c$ is made, it will be possible to perform a statistical combination on all charm hadron species, which will enable the measurement of the charm hadron production fractions.

Beyond the $W + D$ measurements, explicit charm hadron reconstruction at ATLAS has the potential to be used in other Standard Model and Higgs measurements. In particular, a measurement of the $Z + D$ process can use both the charm reconstruction strategy employed in the $W + D$ analysis, as well as measurements of the gluon splitting background that the $W + D$ analysis can inform directly from data. Looking the HL-LHC, measuring Higgs boson production in association with a charm quark will become necessary to understand the Higgs coupling to the second generation of fermions. While the low statistics of Higgs plus charm quark production may limit precision of the measurement, improvements in the analysis techniques related to charm reconstruction may make the direct Higgs plus charm measurement possible.

Appendix A

ATLAS Upgrade ITk Strips Radiation Testing

The physics operation of the ATLAS experiment will continue beyond Run 2, results of which are the main topic of this thesis, into the ATLAS Run 3 and onto the High Luminosity LHC (HL LHC). The HL LHC will be marked by a significant increase in the instantaneous luminosity of the of the machine, delivering $5 \times 10^{34}\,\mathrm{cm}^{-}2\mathrm{s}^{-}1$, which is equivalent to an average of 200 collisions per bunch crossing [168]. The goal of the upgraded ATLAS experiment is to collect a total of $3000\,\mathrm{fb}^{-1}$ of integrated luminosity at 14 TeV. Due to the increased radiation environment of the HL-LHC, it will be necessary to ensure that all detector electronics perform within specification during the experimental operation. This appendix reports on studies of the performance of the new ATLAS inner tracker (ITk), in particular the performance of the set of chips responsible for powering and controlling the module units of the ITk strips detector.

A.1 ATLAS Upgrade and the ITk

The physics prospects of this future experiment lie in improved results in Standard Model, Higgs, and Beyond the Standard Model physics measurements and searches. Two results of relevance to this thesis is a measurement of the mass of the W boson [169].PDF uncertainties are a dominant source of error in the measurement of the W mass. With the assumption that the ATLAS upgrade from the HL LHC is implement as planned, and in the absence of additional DIS experiments to further measure PDFs directly, the PDF uncertainty on the W boson mass is approximately 5 to 8 MeV. Improvements only to the PDF set, including measurements like the $W + D^{(*)}$ differential cross section analysis described in this thesis, has the potential to reduce that PDF uncertainty to $\approx 4\,\mathrm{MeV}$.

The assumptions underlying the reduction in PDF uncertainties in the W mass measurement depend strongly on the development of the new ATLAS inner tracking detector (ITk) [170]. The ITk is a full silicon tracker that is composed of inner layers of high resolution

silicon pixels [171] and outer layers of silicon strips [172]. A schematic of the layout can be seen in Figure A.1. The key difference between the ITk and the current ATLAS ID is the coverage in η. The current ID is limited in its coverage to $|\eta| < 2.5$, see Section 3.2.1 for more discussion. The ITk by contrast will extend out to $|\eta| < 4.0$. The improved η coverage in particular is critical for improved W mass measurement. The additional extent of the detector is estimate to reduce the PDF uncertainties by approximately a factor of two.

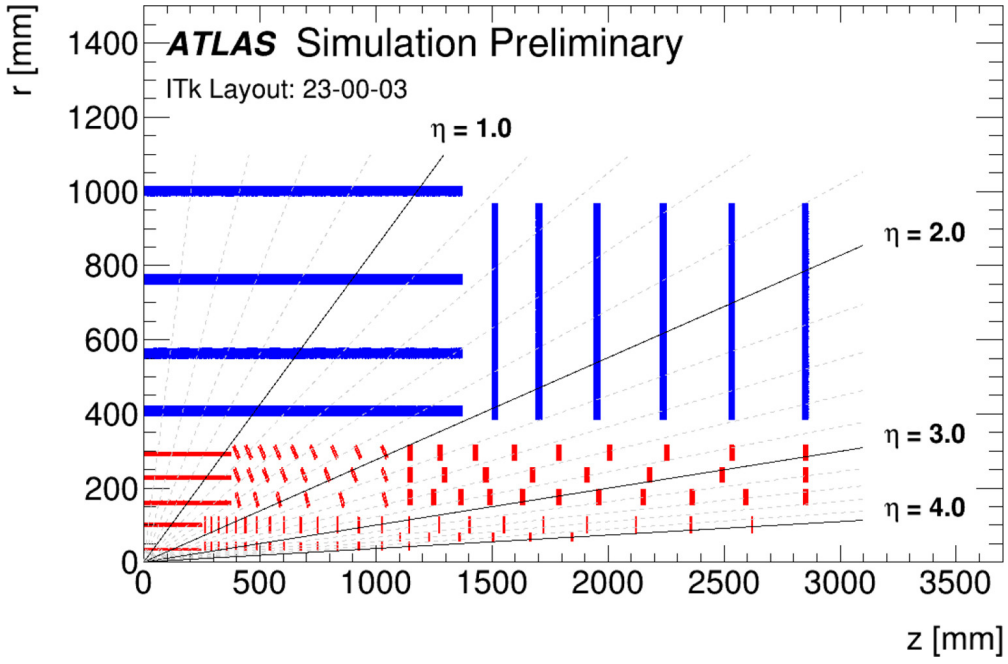

Figure A.1: A schematic diagram of the ATLAS ITk planned for the HL LHC upgrade. The pixel portion of the detector can be seen in red, and the strips layers can be seen in blue. The detector extends to 1000 mm in the radial direction and out to about 3000 mm in the longitudinal direction.

Beyond the η coverage of the ITk, there are other considerations related to the HL LHC environment that must be taken into account. In particular, the increased luminosity has two significant impacts on the ITk, reduced performance and increased radiation. The impact of the performance changes is due to the higher expected occupancy that comes from the increased number of collisions per bunch crossing. Even with the increased number of layers and resolution, the resolution of the ITk is reduced by up to 5% in the central η region. The change in the resolution can be seen in Figure A.2, for a simulated $t\bar{t}$ sample. Note that the p_{T} coverage of the new ITk extends down only to $p_{\mathrm{T}} > 1\,\mathrm{GeV}$, and so the comparison is made only for tracks exceeding that threshold.

The Strips subsystem comprises the outer layers of the ITk detector. The strips are broken into two regions, the barrel region which is centered along the beam axis, and two identical disks which are perpendicular to the beamline, known as the endcaps. The basic unit of the

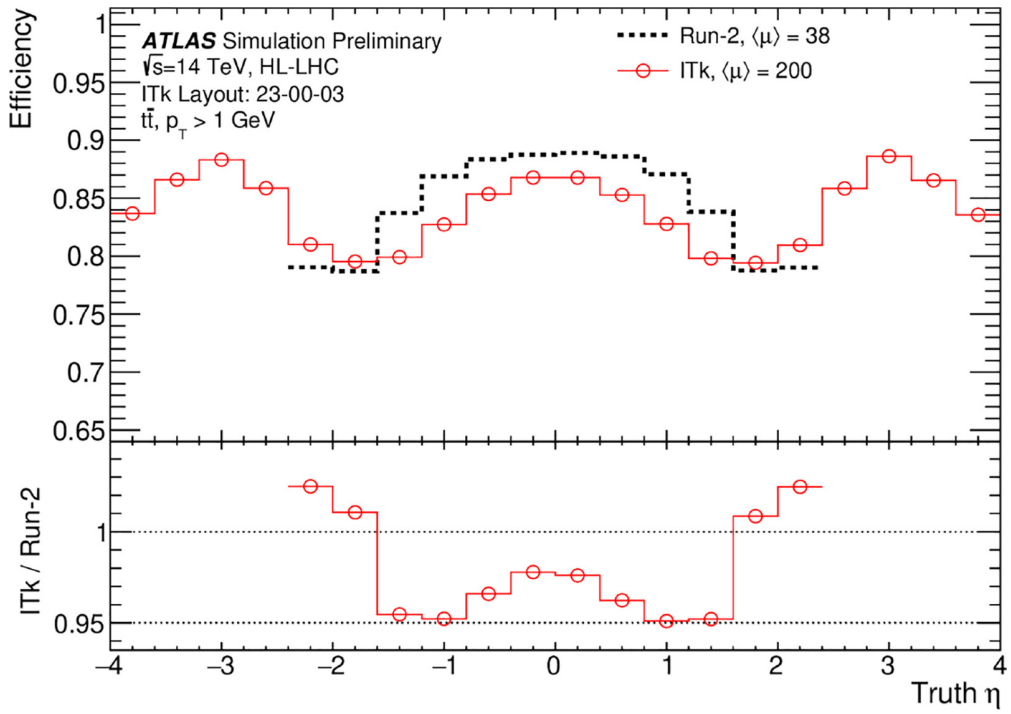

Figure A.2: A comparison of the performance of the current ATLAS ID tracking detector and the planned ITk tracker upgrade for the HL LHC [170]. The performance shows both the change in the η coverage and the change in performance.

strips detector is the module, which are mounted in pairs, facing opposite directions on a local support structure at a small stereo angle in order to provide a measurement of two coordinates. There are eight module configurations which account for difference in the shape of active sensor needed in the inner and outer barrel layers and the end cap modules. A photograph of a strip module is shown in Figure A.3.

The ASICs that will be utilized in the ITk strips are designed in $SI130nm$ CMOS technology. Each module contains up to two HCCStar controller ASICs and up to 12 ABCStar readout ASICs. The module is controlled, monitored, and powered by the power board. The power board provides the sensor bias, a DC-DC buck converter to power the the ASICs on the module, and the AMAC control chip to control other ASICs and monitor the system status.

A.2 Irradiation of the Strips Power Board

There are four ASICs that comprise the active components of the strips module's power board: the DC-DC buck converter, known as the BPol12V; the high voltage switching ASIC, known as the HV Mux; a linear regulator that powers the main control ASIC, known as

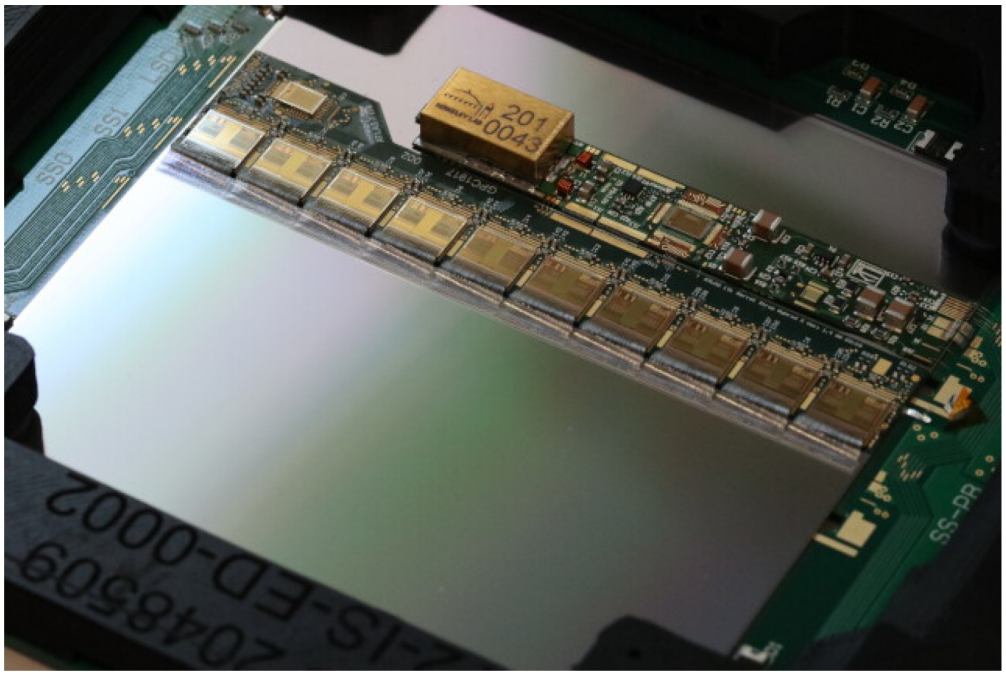

Figure A.3: A photograph of an ITk long strip module [170], which will is what will be used in the outer layers of the strips barrel detector. The active electronics can be seen laying flat across the active area of the sensor, including all electronics needed to operate the module.

the LinPol12V; and the control and monitoring chip, known as the AMAC. Each of these components will be exposed to ionizing radiation, characterized as Total Ionizing Dose (TID), and non ionizing energy loss (NEIL). Studies in this appendix focus on the damage to the strips power board ASICs due to TID.

The strips modules in the innermost layer of the detector are expected to be exposed to a TID of 33 Mrad over the lifetime of detector operation. To ensure that the detector electronics operate through the duration of the experiment, a safety factor of two is applied, and thus all detector components are desired to perform within specification up to at least 66 Mrad. In order to assess the damage from TID over the timescale of order days, it is necessary to expose the power board to ionizing radiation from an x-ray source.

Between September of 2018 and February of 2019, three fast x-ray irradiations were performed at the Rutherford Appelton Laboratory in Didcot, United Kingdom, and the setup can be seen in Figure A.4. These radiation tests had two main purposes, to verify expected behaviours are observed in the output current from the AMAC ASIC and to operate and test the electronics on the power board in continuous operation during the irradiation. One pronounced feature of TID on 130 nm CMOS technology in general and on the power board chip set specifically is the increase in output current at the scale of several hundred krad, which is well understood for this technology and described in Ref. [173]. Often referred to

informally at the "TID peak", this feature is expected to be observed in the output current of the AMAC. Results from the three irradiations can be seen in Figure A.5. In particular, the current rises until ≈ 1 Mrad, before returning to the level of normal operation. The presences of this TID peak, not only in the AMAC but in all the relevant strips module ASICs, motivates a production strategy known as preirradiation [174]. Preirradiation is the irradiation of the ASICs, still in wafers, prior to dicing. The preirradiated ASICs are then mounted as normal onto the modules. The three RAL irradiations show comparable behaviour, across approximately 10 Mrad. The outlier, labeled "November" in the figure, show a failure mode that was concluded to be independent of the irradiation.

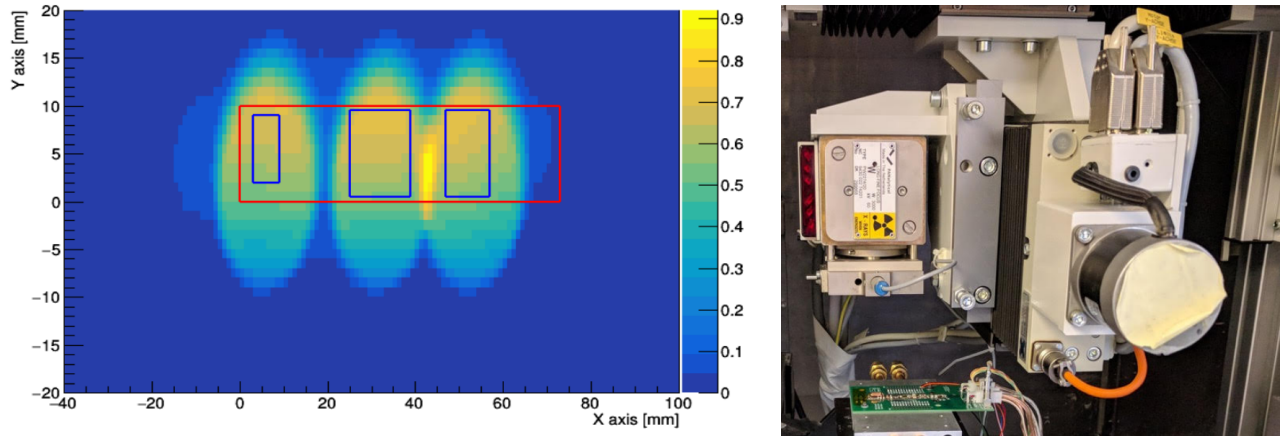

(a) (b)

Figure A.4: The experimental setup of the x-ray irradiations at RAL, which tested the performance of the ITk strips power board in isolation. (a) shows the dose map of x-rays from the machine. The general outline of the board (not to scale) can be seen in red, with the specific targets outlined in blue. From left to right, those targets are the DC-DC converter, linear regulator and AMAC, and the HV Mux. The same dose is accumulated on all targets, while they are cycled through on the order of minutes. (b) shows a picture of the setup at RAL, where the power board and associated test PCB can be seen in the bottom left corner.

The second main purpose of the irradiations on the strips power board was to ensure the operation of the ASICs beyond 66 Mrad of TID. Three outputs were monitored for the duration of the of the September and February irradiations, both exceeding the expected double the strips detector TID. These outputs were the efficiency of the power output from the DC-DC converter, the output voltage of the DC-DC converter, and the input voltage to the AMAC. The efficiency of the DC-DC converter is measured with an assumption that the output voltage is maintained at 1.5 V, and the input voltage is measured off of the AMAC monitoring channel directly, as seen in Figure A.6. The monitoring shows, beyond the 66 Mrad limit, that the efficiency stays above 70% which is the specified minimum level. The second output that was measured was the output voltage of the DC-DC converted as

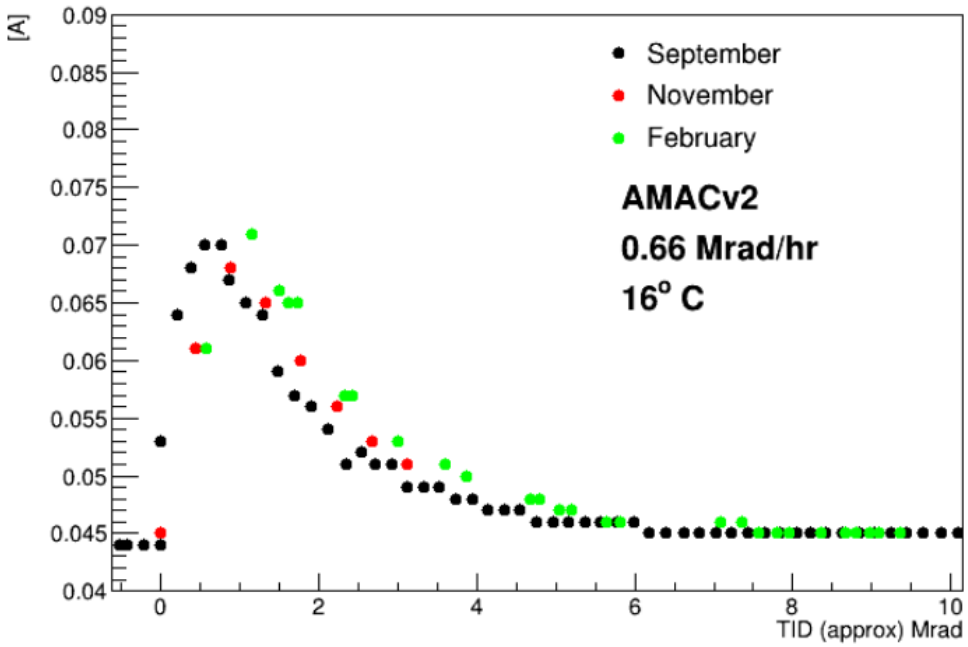

Figure A.5: Output current from the AMAC mounted on the strips power board v3 for a series of three irradiations taking place in September 2018, November 2018, and February 2019. All curves show the expected behaviour of the TID peak, increasing until about 1 MeV before returning to approximately the baseline level. The November curve experienced a failure mode, unrelated to the irradiation.

measured by the AMAC. The AMAC had a load of 2 A, which is expected to bring the performance below the expected 1.5 V output. The AMAC measured output voltage can be seen in Figure A.7, and is maintained between 1.42 to 1.44 V, for the duration of the irradiation. The final value is the AMAC's own input voltage, as measured by itself. Usefully, this value can measured externally, and the external measurement can be compared directly to the AMAC's monitoring output. Figure A.8 shows that 11 V input to the AMAC is well measured by the ASIC itself, deviating by less the 1.5% for the full irradiation up to 90 Mrad. The results of these tests indicate that the expected performace of the AMAC and the power board ASICs are performant to TID beyond what is needed for the HL LHC radiation environment.

The results of several fast x-ray irradiation on the strips power board indicate that designed chip set will perform beyond the specified TID expected in the HL LHC environment. These preliminary studies are complement by results in Ref. [175]. These update studies confirm what was observed in preliminary irradiations, both in the observation of the TID peak, as well as the performance of the ASICs for TID exceeding the requirements of the detector. Additionally, these updated studies are performed *in-situ* on a strips module, which provides

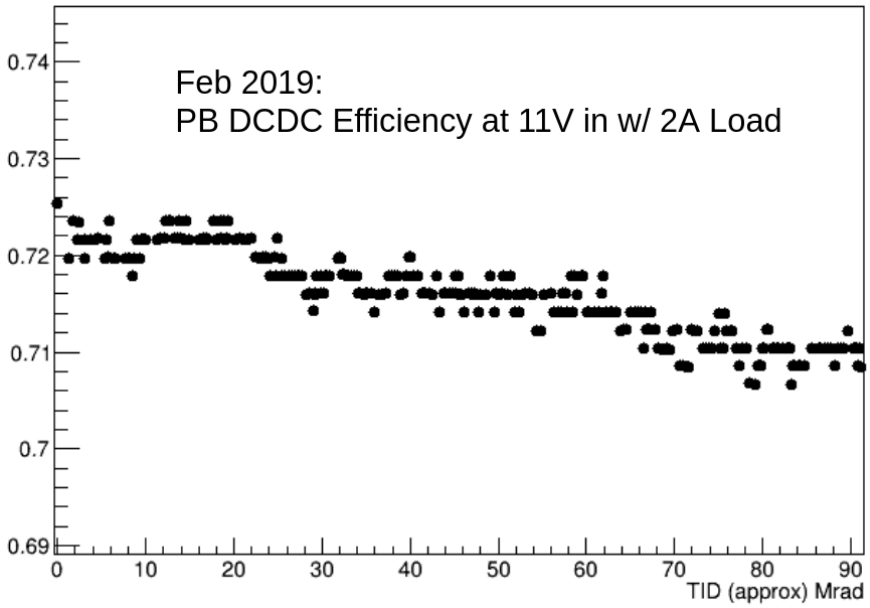

Figure A.6: The DC-DC converter efficiency (P_{out}/P_{in}) as measured by the AMAC. The input power is fully measured by the AMAC, and the output current is measured by the AMAC with the output voltage being assumed to be 1.5 V. The efficiency is required to remain above 70%, and it remains above that thresh hold for at least 90 Mrad.

additional confirmation of the radiation tolerance of the electronics that will enter into production for the full ITk.

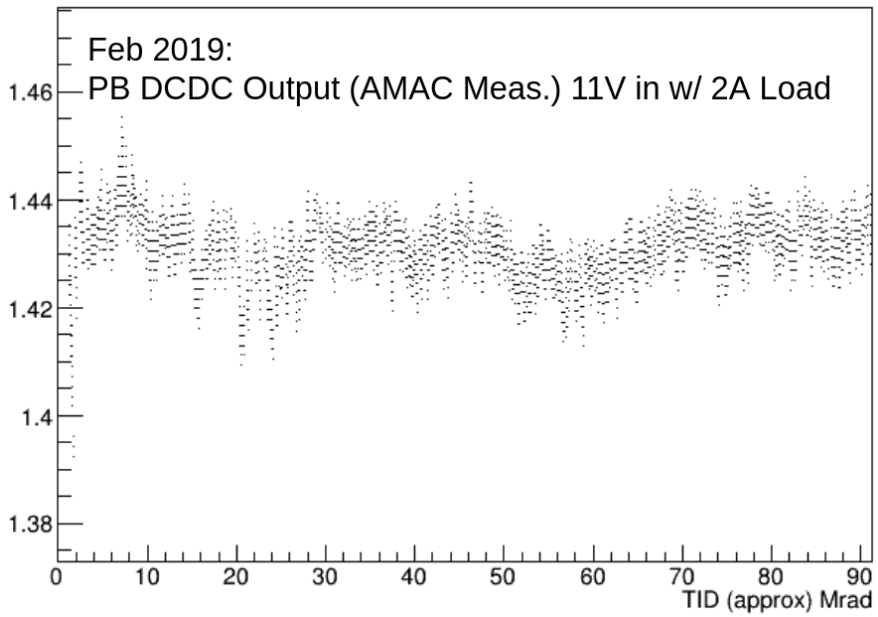

Figure A.7: The DC-DC converter output voltage as measured by the AMAC during the fast x-ray irradiation. The voltage is specified to be at 1.5 V, however the measured output is somewhat smaller. This discrepancy is likely due to the 2 A load and uncertainty on the relevant voltage divider inside of the AMAC. The measured output voltage is considered to be within specification for the duration of the 90 Mrad irradiation.

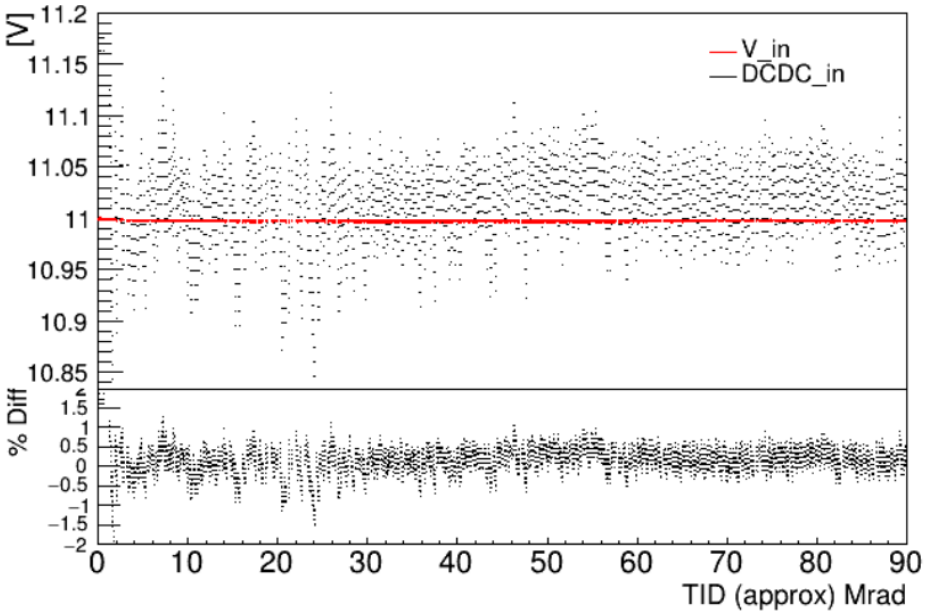

Figure A.8: The input voltage to the AMAC, as measured by the AMAC itself. This is compared to an external measurement of the AMAC input voltage and thus validate directly the AMAC measurement. Throughout the irradiation up to 90 Mrad, the input voltage is well measured, and the deviation of the measurement with respect to the external validation is less than 1.5%.

Bibliography

[1] M. Thomson, *Modern Particle Physics*, Cambridge University Press, 2013.

[2] URL: https://www.quantamagazine.org/what-no-new-particles-means-for-physics-20160809.

[3] S. L. Glashow, *Partial-symmetries of weak interactions*, Nuclear Physics **22** (1961) 579, ISSN: 0029-5582, URL: https://www.sciencedirect.com/science/article/pii/0029558261904692.

[4] S. Weinberg, *A Model of Leptons*, Phys. Rev. Lett. **19** (21 1967) 1264, URL: https://link.aps.org/doi/10.1103/PhysRevLett.19.1264.

[5] A. Salam, "Weak and electromagnetic interactions", *Selected Papers of Abdus Salam* 244, URL: https://www.worldscientific.com/doi/abs/10.1142/9789812795915_0034.

[6] D. J. Gross and F. Wilczek, *Ultraviolet Behavior of Non-Abelian Gauge Theories*, Phys. Rev. Lett. **30** (26 1973) 1343, URL: https://link.aps.org/doi/10.1103/PhysRevLett.30.1343.

[7] M. Banner et al., *Observation of single isolated electrons of high transverse momentum in events with missing transverse energy at the CERN pp collider*, Physics Letters B **122** (1983) 476, ISSN: 0370-2693, URL: https://www.sciencedirect.com/science/article/pii/0370269383916052.

[8] G. Arnison et al., *Experimental observation of isolated large transverse energy electrons with associated missing energy at s=540 GeV*, Physics Letters B **122** (1983) 103, ISSN: 0370-2693, URL: https://www.sciencedirect.com/science/article/pii/0370269383911772.

[9] C. Collaboration, *Observation of the Production of a W Boson in Association with a Single Charm Quark*, Physical Review Letters **110** (2013) 071801, ISSN: 0031-9007, 1079-7114.

[10] S. Abachi et al., *Observation of the top quark*, Phys. Rev. Lett. **74** (1995) 2632.

[11] S. Chatrchyan et al., *Observation of a new boson at a mass of 125 GeV with the CMS experiment at the LHC*, Physics Letters B **716** (2012) 30, ISSN: 0370-2693, URL: https://www.sciencedirect.com/science/article/pii/S0370269312008581.

[12] G. Aad et al., *Observation of a new particle in the search for the Standard Model Higgs boson with the ATLAS detector at the LHC*, Physics Letters B **716** (2012) 1, ISSN: 0370-2693, URL: https://www.sciencedirect.com/science/article/pii/S037026931200857X.

[13] *Standard Model Summary Plots February 2022*, tech. rep., All figures including auxiliary figures are available at https://atlas.web.cern.ch/Atlas/GROUPS/PHYSICS/PUBNOTES/ATL-PHYS-PUB-2022-009: CERN, 2022, URL: https://cds.cern.ch/record/2804061.

[14] P. D. Group and P. A. e. a. Zyla, *Review of Particle Physics*, Progress of Theoretical and Experimental Physics **2020** (2020), 083C01, ISSN: 2050-3911, URL: https://doi.org/10.1093/ptep/ptaa104.

[15] M. Breidenbach et al., *Observed Behavior of Highly Inelastic Electron-Proton Scattering*, Phys. Rev. Lett. **23** (16 1969) 935, URL: https://link.aps.org/doi/10.1103/PhysRevLett.23.935.

[16] A. Buckley et al., *LHAPDF6: parton density access in the LHC precision era*, The European Physical Journal C **75** (2015), URL: https://doi.org/10.1140%2Fepjc%2Fs10052-015-3318-8.

[17] S. Bailey et al., *Parton distributions from LHC, HERA, Tevatron and fixed target data: MSHT20 PDFs*, The European Physical Journal C **81** (2021), URL: https://doi.org/10.1140%2Fepjc%2Fs10052-021-09057-0.

[18] M. Schönherr, *Parton shower matching and merging*, 2018.

[19] B. Webber, *Fragmentation and Hadronization*, Int. J. Mod. Phys. AS **15S1** (2000) 577, URL: https://cds.cern.ch/record/419784.

[20] F. Faura et al., *The Strangest Proton?*, Eur. Phys. J. C **80** (2020) 1168.

[21] ATLAS Collaboration, *Precision measurement and interpretation of inclusive W^+, W^- and Z/γ^* production cross sections with the ATLAS detector*, Eur. Phys. J. C **77** (2017) 367.

[22] ATLAS Collaboration, *Determination of the parton distribution functions of the proton from ATLAS measurements of differential $W^{\pm}$ and Z boson production in association with jets*, JHEP **07** (2021) 223.

[23] G. Aad et al., *Determination of the parton distribution functions of the proton using diverse ATLAS data from pp collisions at $\sqrt{s} = 7$, 8 and 13 TeV.*, Eur. Phys. J. C **82** (2022) 438, 92 pages in total, author list starting page 77, 41 figures, 7 tables, published in EPJC. All figures including auxiliary figures are available at http://atlas.web.cern.ch/Atlas/GROUPS/PHYSICS/PAPERS/STDM-2020-32, URL: https://cds.cern.ch/record/2798650.

[24] A. Kayis-Topaksu et al.,
Leading order analysis of neutrino induced dimuon events in the CHORUS experiment,
Nuclear Physics B **798** (2008) 1,
URL: https://doi.org/10.1016%2Fj.nuclphysb.2008.02.013.

[25] N. Collaboration, *A Precision Measurement of Charm Dimuon Production in Neutrino Interactions from the NOMAD Experiment*, 2013.

[26] and A. O. Bazarko et al., *Determination of the strange quark content of the nucleon from a next-to-leading-order QCD analysis of neutrino charm production*,
Zeitschrift für Physik C Particles and Fields **65** (1995) 189,
URL: https://doi.org/10.1007%2Fbf01571875.

[27] D. Mason et al., *Measurement of the Nucleon Strange-Antistrange Asymmetry at Next-to-Leading Order in QCD from NuTeV Dimuon Data*,
Phys. Rev. Lett. **99** (19 2007) 192001,
URL: https://link.aps.org/doi/10.1103/PhysRevLett.99.192001.

[28] ATLAS Collaboration, *Measurement of the inclusive $W^{\pm}$ and Z/γ^{*} cross sections in the e and μ decay channels in pp collisions at $\sqrt{s} = 7$ TeV with the ATLAS detector*,
Phys. Rev. D **85** (2012) 072004.

[29] CMS Collaboration, *Measurement of the differential cross section and charge asymmetry for inclusive $pp \to W^{\pm} + X$ production at $\sqrt{s} = 8$ TeV*,
Eur. Phys. J. C **76** (2016) 469.

[30] ATLAS Collaboration, *Measurement of the production of a W boson in association with a charm quark in pp collisions at $\sqrt{s} = 7$ TeV with the ATLAS detector*,
JHEP **05** (2014) 068.

[31] CMS Collaboration, *Measurement of associated production of a W boson and a charm quark in proton–proton collisions at $\sqrt{s} = 13$ TeV*, Eur. Phys. J. C **79** (2019) 269.

[32] *Measurement of the production cross section for a W boson in association with a charm quark in proton-proton collisions at $\sqrt{s} = 13$ TeV*,
Submitted to the European Physical Journal C. All figures and tables can be found at http://cms-results.web.cern.ch/cms-results/public-results/publications/SMP-21-005 (CMS Public Pages), Geneva, 2023, URL: https://cds.cern.ch/record/2866842.

[33] M. Czakon et al., *NNLO QCD predictions for W + c-jet production at the LHC*,
Journal of High Energy Physics **2021** (2021),
URL: https://doi.org/10.1007%2Fjhep06%282021%29100.

[34] G. Aad et al.,
ATLAS flavour-tagging algorithms for the LHC Run 2 pp collision dataset,
Eur. Phys. J. C **83** (2023) 681.

[35] CMS Collaboration,
Measurement of associated W + charm production in pp collisions at $\sqrt{s} = 7$ TeV,
JHEP **02** (2014) 013.

[36] G. Aad et al., *Measurement of the production of a W boson in association with a charm quark in pp collisions at $\sqrt{s} = 7$ TeV with the ATLAS detector*, JHEP **05** (2014) 068.

[37] G. Aad et al., *Measurement of the production of a W boson in association with a charmed hadron in pp collisions at $\sqrt{s} = 13$ TeV with the ATLAS detector*, Phys. Rev. D **108** (2023) 032012, All figures including auxiliary figures are available at https://atlas.web.cern.ch/Atlas/GROUPS/PHYSICS/PAPERS/STDM-2019-22, URL: https://cds.cern.ch/record/2848047.

[38] ATLAS Collaboration, *Measurement of the W-boson mass in pp collisions at $\sqrt{s} = 7$ TeV with the ATLAS detector*, Eur. Phys. J. C **78** (2018) 110, Erratum: Eur. Phys. J. C **78** (2018) 898.

[39] ATLAS Collaboration, *Projections for measurements of Higgs boson cross sections, branching ratios, coupling parameters and mass with the ATLAS detector at the HL-LHC*, ATL-PHYS-PUB-2018-054, 2018, URL: https://cds.cern.ch/record/2652762.

[40] U. Baur et al., *The Charm Content of W+1 Jet Events as a Probe of the Strange Quark Distribution Function*, Physics Letters B **318** (1993) 544, ISSN: 03702693.

[41] W. T. Giele, S. Keller, and E. Laenen, *QCD Corrections to W Boson plus Heavy Quark Production at the Tevatron*, Physics Letters B **372** (1996) 141, ISSN: 03702693.

[42] M. Czakon et al., *NNLO QCD predictions for W + c-jet production at the LHC*, (2020).

[43] A. Banfi, G. P. Salam, and G. Zanderighi, *Infrared safe definition of jet flavor*, Eur. Phys. J. C **47** (2006) 113.

[44] M. L. Czakon et al., *B-hadron production in NNLO QCD: application to LHC $t\bar{t}$ events with leptonic decays*, JHEP **10** (2021) 216.

[45] J. Alwall et al., *The automated computation of tree-level and next-to-leading order differential cross sections, and their matching to parton shower simulations*, JHEP **07** (2014) 079.

[46] G. Bevilacqua et al., *W + charm production with massive c quarks in PowHel*, JHEP **04** (2022) 056.

[47] M. Lisovyi, A. Verbytskyi, and O. Zenaiev, *Combined analysis of charm-quark fragmentation-fraction measurements*, The European Physical Journal C **76** (2016), URL: https://doi.org/10.1140%2Fepjc%2Fs10052-016-4246-y.

[48] A. Collaboration, *Charm production and fragmentation fractions at midrapidity in pp collisions at $\sqrt{s} = 13$ TeV*, 2023.

[49] T. S. Pettersson and P. Lefèvre, *The Large Hadron Collider: conceptual design*, tech. rep., 1995, URL: https://cds.cern.ch/record/291782.

[50] O. S. Brüning et al., *LHC Design Report*, CERN Yellow Reports: Monographs, Geneva: CERN, 2004, URL: https://cds.cern.ch/record/782076.

[51] C. Lefèvre, "The CERN accelerator complex. Complexe des accélérateurs du CERN", 2008, URL: https://cds.cern.ch/record/1260465.

[52] W. Herr and B. Muratori, *Concept of luminosity*, (2006), URL: https://cds.cern.ch/record/941318.

[53] *Luminosity determination in pp collisions at* $\sqrt{s} = 13$ *TeV using the ATLAS detector at the LHC*, (2022).

[54] G. Avoni et al., *The new LUCID-2 detector for luminosity measurement and monitoring in ATLAS*, Journal of Instrumentation **13** (2018) P07017, URL: https://dx.doi.org/10.1088/1748-0221/13/07/P07017.

[55] J. Pequenao, "Computer generated image of the whole ATLAS detector", 2008, URL: https://cds.cern.ch/record/1095924.

[56] Mets501, "Different values of pseudorapidity shown against a polar grid", 2012, URL: https://commons.wikimedia.org/wiki/File:Pseudorapidity_plot.svg.

[57] ATLAS Collaboration, *The ATLAS Inner Detector commissioning and calibration*, Eur. Phys. J. C **70** (2010) 787.

[58] T. A. Collaboration et al., *The ATLAS Experiment at the CERN Large Hadron Collider*, Journal of Instrumentation **3** (2008) S08003, URL: https://dx.doi.org/10.1088/1748-0221/3/08/S08003.

[59] J. Pequenao, "Computer generated image of the ATLAS inner detector", 2008, URL: https://cds.cern.ch/record/1095926.

[60] B. Abbott et al., *Production and integration of the ATLAS Insertable B-Layer*, Journal of Instrumentation **13** (2018) T05008, URL: https://dx.doi.org/10.1088/1748-0221/13/05/T05008.

[61] Y. Rodina, *ATLAS b-tagging performance during LHC Run 2 with the new Insertable B-layer*, tech. rep., CERN, 2015, URL: https://cds.cern.ch/record/2112120.

[62] G. Aad et al., *ATLAS pixel detector electronics and sensors*, Journal of Instrumentation **3** (2008) P07007, URL: https://dx.doi.org/10.1088/1748-0221/3/07/P07007.

[63] A. Ahmad et al., *The silicon microstrip sensors of the ATLAS semiconductor tracker*, Nuclear Instruments and Methods in Physics Research Section A: Accelerators, Spectrometers, Detectors and Associated Equipment **578** (2007) 98, ISSN: 0168-9002, URL: https://www.sciencedirect.com/science/article/pii/S0168900207007644.

[64] T. Akesson et al., *Status of design and construction of the Transition Radiation Tracker (TRT) for the ATLAS experiment at the LHC*, Nuclear Instruments and Methods in Physics Research Section A: Accelerators, Spectrometers, Detectors and Associated Equipment **522** (2004) 131, TRDs for the Third Millenium. Proceedings of the 2nd Workshop on Advanced Transition Radiation Detectors for Accelerator and Space Applications, ISSN: 0168-9002, URL: https://www.sciencedirect.com/science/article/pii/S016890020400110X.

[65] *ATLAS tile calorimeter: Technical Design Report*, Technical design report. ATLAS, Geneva: CERN, 1996, URL: https://cds.cern.ch/record/331062.

[66] T. A. Collaboration et al., *Readiness of the ATLAS Tile Calorimeter for LHC collisions*, The European Physical Journal C **70** (2010) 1193.

[67] *ATLAS liquid-argon calorimeter: Technical Design Report*, Technical design report. ATLAS, Geneva: CERN, 1996, URL: http://cds.cern.ch/record/331061.

[68] T. A. Collaboration et al., *Readiness of the ATLAS liquid argon calorimeter for LHC collisions*, The European Physical Journal C **70** (2010) 723.

[69] J. Pequenao, "Computer Generated image of the ATLAS calorimeter", 2008, URL: https://cds.cern.ch/record/1095927.

[70] *ATLAS muon spectrometer: Technical Design Report*, Technical design report. ATLAS, Geneva: CERN, 1997, URL: https://cds.cern.ch/record/331068.

[71] G. Aad et al., *Commissioning of the ATLAS Muon Spectrometer with Cosmic Rays*, The European Physical Journal C **70** (2010) 875, ISSN: 1434-6052, URL: https://doi.org/10.1140/epjc/s10052-010-1415-2.

[72] J. Pequenao, "Computer generated image of the ATLAS Muons subsystem", 2008, URL: https://cds.cern.ch/record/1095929.

[73] T. A. collaboration, *Operation of the ATLAS trigger system in Run 2*, Journal of Instrumentation **15** (2020) P10004, URL: https://dx.doi.org/10.1088/1748-0221/15/10/P10004.

[74] A. Collaboration,
" Functional diagram of the ATLAS Trigger and Data Acquisition system in Run 2 showing expected peak rates and bandwidths through each component. ", 2018, URL: https://twiki.cern.ch/twiki/bin/view/AtlasPublic/ApprovedPlotsDAQ.

[75] M. Aaboud et al.,
Commissioning of the ATLAS Muon Spectrometer with Cosmic Rays,
Performance of the ATLAS Trigger System in 2015 **77** (2017).

[76] G. Avoni et al.,
The new LUCID-2 detector for luminosity measurement and monitoring in ATLAS,
JINST **13** (2018) P07017.

[77] *ATLAS Luminosity Public Results in Run 2*, https://twiki.cern.ch/twiki/bin/view/AtlasPublic/LuminosityPublicResultsRun2, Accessed: 2023-09-12.

[78] G. Aad et al.,
ATLAS data quality operations and performance for 2015–2018 data-taking,
Journal of Instrumentation **15** (2020) P04003,
URL: https://doi.org/10.1088%2F1748-0221%2F15%2F04%2Fp04003.

[79] *ATLAS Trigger*, https://twiki.cern.ch/twiki/bin/view/Atlas/AtlasTrigger, Accessed: 2021-07-05.

[80] ATLAS Collaboration, *The ATLAS Simulation Infrastructure*,
Eur. Phys. J. C **70** (2010) 823.

[81] GEANT4 Collaboration, S. Agostinelli, et al., GEANT4 – *a simulation toolkit*,
Nucl. Instrum. Meth. A **506** (2003) 250.

[82] T. Sjöstrand, S. Mrenna, and P. Skands, *A brief introduction to PYTHIA 8.1*,
Comput. Phys. Commun. **178** (2008) 852.

[83] R. D. Ball et al., *Parton distributions with LHC data*, Nucl. Phys. B **867** (2013) 244.

[84] ATLAS Collaboration, *The Pythia 8 A3 tune description of ATLAS minimum bias and inelastic measurements incorporating the Donnachie–Landshoff diffractive model*, ATL-PHYS-PUB-2016-017, 2016, URL: https://cds.cern.ch/record/2206965.

[85] ATLAS Collaboration, *Measurement of the Inelastic Proton–Proton Cross Section at* $\sqrt{s} = 13$ *TeV with the ATLAS Detector at the LHC*,
Phys. Rev. Lett. **117** (2016) 182002.

[86] M. Lisovyi, A. Verbytskyi, and O. Zenaiev,
Combined analysis of charm-quark fragmentation-fraction measurements,
Eur. Phys. J. C **76** (2016) 397.

[87] ATLAS Collaboration, *Reweighting heavy-flavor production fractions to reduce flavor modelling uncertainties for ATLAS*, ATL-PHYS-PUB-2022-035, 2022,
URL: https://cds.cern.ch/record/2816367.

[88] E. Bothmann et al., *Event generation with Sherpa 2.2*, SciPost Phys. **7** (2019) 034.

[89] T. Gleisberg and S. Höche, *Comix, a new matrix element generator*, JHEP **12** (2008) 039.

[90] F. Buccioni et al., *OpenLoops 2*, Eur. Phys. J. C **79** (2019) 866.

[91] F. Cascioli, P. Maierhöfer, and S. Pozzorini, *Scattering Amplitudes with Open Loops*, Phys. Rev. Lett. **108** (2012) 111601.

[92] A. Denner, S. Dittmaier, and L. Hofer, COLLIER*: A fortran-based complex one-loop library in extended regularizations*, Comput. Phys. Commun. **212** (2017) 220.

[93] R. D. Ball et al., *Parton distributions for the LHC run II*, JHEP **04** (2015) 040.

[94] S. Schumann and F. Krauss, *A parton shower algorithm based on Catani–Seymour dipole factorisation*, JHEP **03** (2008) 038.

[95] J.-C. Winter, F. Krauss, and G. Soff, *A modified cluster-hadronization model*, Eur. Phys. J. C **36** (2004) 381.

[96] S. Höche et al., *A critical appraisal of NLO+PS matching methods*, JHEP **09** (2012) 049.

[97] S. Catani et al., *QCD Matrix Elements + Parton Showers*, JHEP **11** (2001) 063.

[98] S. Höche et al., *QCD matrix elements and truncated showers*, JHEP **05** (2009) 053.

[99] S. Höche et al., *QCD matrix elements + parton showers. The NLO case*, JHEP **04** (2013) 027.

[100] E. Bothmann, M. Schönherr, and S. Schumann, *Reweighting QCD matrix-element and parton-shower calculations*, Eur. Phys. J. C **76** (2016) 590.

[101] ATLAS Collaboration, *Modelling and computational improvements to the simulation of single vector-boson plus jet processes for the ATLAS experiment*, (2021).

[102] L. Lönnblad, *Correcting the Colour-Dipole Cascade Model with Fixed Order Matrix Elements*, JHEP **05** (2002) 046.

[103] L. Lönnblad and S. Prestel, *Matching tree-level matrix elements with interleaved showers*, JHEP **03** (2012) 019.

[104] ATLAS Collaboration, *ATLAS Pythia 8 tunes to 7 TeV data*, ATL-PHYS-PUB-2014-021, 2014, URL: https://cds.cern.ch/record/1966419.

[105] D. J. Lange, *The EvtGen particle decay simulation package*, Nucl. Instrum. Meth. A **462** (2001) 152.

[106] R. Frederix and S. Frixione, *Merging meets matching in MC@NLO*, JHEP **12** (2012) 061.

[107] G. Bonvicini et al., *Dalitz plot analysis of the D+ —> K- pi+ pi+ decay*, Phys. Rev. D **78** (2008) 052001.

[108] S. Frixione, G. Ridolfi, and P. Nason, *A positive-weight next-to-leading-order Monte Carlo for heavy flavour hadroproduction*, JHEP **09** (2007) 126.

[109] P. Nason, *A new method for combining NLO QCD with shower Monte Carlo algorithms*, JHEP **11** (2004) 040.

[110] S. Frixione, P. Nason, and C. Oleari, *Matching NLO QCD computations with parton shower simulations: the POWHEG method*, JHEP **11** (2007) 070.

[111] S. Alioli et al., *A general framework for implementing NLO calculations in shower Monte Carlo programs: the POWHEG BOX*, JHEP **06** (2010) 043.

[112] ATLAS Collaboration, *Studies on top-quark Monte Carlo modelling for Top2016*, ATL-PHYS-PUB-2016-020, 2016, URL: https://cds.cern.ch/record/2216168.

[113] S. Frixione et al., *Angular correlations of lepton pairs from vector boson and top quark decays in Monte Carlo simulations*, JHEP **04** (2007) 081.

[114] P. Artoisenet et al., *Automatic spin-entangled decays of heavy resonances in Monte Carlo simulations*, JHEP **03** (2013) 015.

[115] M. Beneke et al., *Hadronic top-quark pair production with NNLL threshold resummation*, Nucl. Phys. B **855** (2012) 695.

[116] M. Cacciari et al., *Top-pair production at hadron colliders with next-to-next-to-leading logarithmic soft-gluon resummation*, Phys. Lett. B **710** (2012) 612.

[117] P. Bärnreuther, M. Czakon, and A. Mitov, *Percent-Level-Precision Physics at the Tevatron: Next-to-Next-to-Leading Order QCD Corrections to $q\bar{q} \to t\bar{t} + X$*, Phys. Rev. Lett. **109** (2012) 132001.

[118] M. Czakon and A. Mitov, *NNLO corrections to top-pair production at hadron colliders: the all-fermionic scattering channels*, JHEP **12** (2012) 054.

[119] M. Czakon and A. Mitov, *NNLO corrections to top pair production at hadron colliders: the quark-gluon reaction*, JHEP **01** (2013) 080.

[120] M. Czakon, P. Fiedler, and A. Mitov, *Total Top-Quark Pair-Production Cross Section at Hadron Colliders Through $O(\alpha_S^4)$*, Phys. Rev. Lett. **110** (2013) 252004.

[121] M. Czakon and A. Mitov,
Top++: A program for the calculation of the top-pair cross-section at hadron colliders,
Comput. Phys. Commun. **185** (2014) 2930.

[122] M. Bähr et al., *Herwig++ physics and manual*, Eur. Phys. J. C **58** (2008) 639.

[123] J. Bellm et al., *Herwig 7.0/Herwig++ 3.0 release note*,
Eur. Phys. J. C **76** (2016) 196.

[124] L. A. Harland-Lang et al., *Parton distributions in the LHC era: MMHT 2014 PDFs*,
Eur. Phys. J. C **75** (2015) 204.

[125] S. Frixione et al., *Single-top hadroproduction in association with a W boson*,
JHEP **07** (2008) 029.

[126] M. Aliev et al.,
HATHOR – HAdronic Top and Heavy quarks crOss section calculatoR,
Comput. Phys. Commun. **182** (2011) 1034.

[127] P. Kant et al., *HatHor for single top-quark production: Updated predictions and uncertainty estimates for single top-quark production in hadronic collisions*,
Comput. Phys. Commun. **191** (2015) 74.

[128] ATLAS Collaboration,
Studies on top-quark Monte Carlo modelling with Sherpa and MG5_aMC@NLO,
ATL-PHYS-PUB-2017-007, 2017, URL: https://cds.cern.ch/record/2261938.

[129] A. Denner et al., *Electroweak radiative corrections to e+ e- —> nu anti-nu H*,
Nucl. Phys. B **660** (2003) 289.

[130] J. Pequenao and P. Schaffner,
"How ATLAS detects particles: diagram of particle paths in the detector", 2013,
URL: https://cds.cern.ch/record/1505342.

[131] T. Cornelissen et al.,
Concepts, Design and Implementation of the ATLAS New Tracking (NEWT),
tech. rep., All figures including auxiliary figures are available at
https://atlas.web.cern.ch/Atlas/GROUPS/PHYSICS/PUBNOTES/ATL-SOFT-PUB-2007-007: CERN, 2007, URL: https://cds.cern.ch/record/1020106.

[132] H. Oide, *Improvements to ATLAS track reconstruction for Run-2*, tech. rep.,
CERN, 2015, URL: https://cds.cern.ch/record/2063753.

[133] A. Wharton, W. Yao, and R. Jansky,
ATLAS Inner Detector Track Quality Cuts for Run 2, tech. rep., CERN, 2014,
URL: https://cds.cern.ch/record/1752536.

[134] ATLAS Collaboration, *Electron and photon performance measurements with the ATLAS detector using the 2015–2017 LHC proton–proton collision data*,
JINST **14** (2019) P12006.

[135] ATLAS Collaboration,
Electron reconstruction and identification in the ATLAS experiment using the 2015 and 2016 LHC proton–proton collision data at $\sqrt{s} = 13$ *TeV*,
Eur. Phys. J. C **79** (2019) 639.

[136] ATLAS Collaboration, *Muon reconstruction performance of the ATLAS detector in proton–proton collision data at* $\sqrt{s} = 13$ *TeV*, Eur. Phys. J. C **76** (2016) 292.

[137] G. Aad et al., *Muon reconstruction and identification efficiency in ATLAS using the full Run 2 pp collision data set at* $\sqrt{s} = 13$ *TeV*, Eur. Phys. J. C **81** (2021) 578.

[138] ATLAS Collaboration,
Jet reconstruction and performance using particle flow with the ATLAS Detector,
Eur. Phys. J. C **77** (2017) 466.

[139] M. Cacciari, G. P. Salam, and G. Soyez, *The anti-*k_t *jet clustering algorithm*,
JHEP **04** (2008) 063.

[140] A. Collaboration, *Jet energy scale and resolution measured in proton-proton collisions at* $\sqrt{s} = 13$ *TeV with the ATLAS detector*, 2020.

[141] ATLAS Collaboration, *ATLAS b-jet identification performance and efficiency measurement with* $t\bar{t}$ *events in pp collisions at* $\sqrt{s} = 13$ *TeV*,
Eur. Phys. J. C **79** (2019) 970.

[142] ATLAS Collaboration, *Optimisation and performance studies of the ATLAS b-tagging algorithms for the 2017-18 LHC run*, ATL-PHYS-PUB-2017-013, 2017,
URL: https://cds.cern.ch/record/2273281.

[143] ATLAS Collaboration,
ATLAS flavour-tagging algorithms for the LHC Run 2 pp collision dataset, (2022).

[144] ATLAS Collaboration, *Performance of missing transverse momentum reconstruction with the ATLAS detector using proton–proton collisions at* $\sqrt{s} = 13$ *TeV*,
Eur. Phys. J. C **78** (2018) 903.

[145] V. Kostyukhin, *VKalVrt - package for vertex reconstruction in ATLAS.*,
tech. rep. ATL-PHYS-2003-031,
revised version number 1 submitted on 2003-09-24 11:10:53: CERN, 2003,
URL: https://cds.cern.ch/record/685551.

[146] J. Smith, W. L. van Neerven, and J. A. M. Vermaseren,
Transverse Mass and Width of the W Boson, Phys. Rev. Lett. **50** (22 1983) 1738,
URL: https://link.aps.org/doi/10.1103/PhysRevLett.50.1738.

[147] ATLAS Collaboration, *Performance of the ATLAS track reconstruction algorithms in dense environments in LHC Run 2*, Eur. Phys. J. C **77** (2017) 673.

[148] L. Moneta et al., *The RooStats Project*, (2011).

[149] W. Verkerke and D. Kirkby, *The RooFit toolkit for data modeling*, 2003.

[150] A. Buckley et al., *LHAPDF6: parton density access in the LHC precision era*, Eur. Phys. J. C **75** (2015) 132.

[151] ATLAS Collaboration, *Jet energy scale and resolution measured in proton–proton collisions at* $\sqrt{s} = 13$ *TeV with the ATLAS detector*, Eur. Phys. J. C **81** (2020) 689.

[152] ATLAS Collaboration, *E_T^{miss} performance in the ATLAS detector using 2015–2016 LHC pp collisions*, ATLAS-CONF-2018-023, 2018, URL: https://cds.cern.ch/record/2625233.

[153] ATLAS Collaboration, *Measurement of the c-jet mistagging efficiency in $t\bar{t}$ events using pp collision data at* $\sqrt{s} = 13$ *TeV collected with the ATLAS detector*, (2021).

[154] ATLAS Collaboration, *Calibration of the light-flavour jet mistagging efficiency of the b-tagging algorithms with Z+jets events using 139* fb^{-1} *of ATLAS proton-proton collision data at* $\sqrt{s} = 13$ *TeV*, (2023).

[155] ATLAS Collaboration, *Luminosity determination in pp collisions at* $\sqrt{s} = 13$ *TeV using the ATLAS detector at the LHC*, (2022).

[156] ATLAS Collaboration, *Early Inner Detector Tracking Performance in the 2015 Data at* $\sqrt{s} = 13$ *TeV*, ATL-PHYS-PUB-2015-051, 2015, URL: https://cds.cern.ch/record/2110140.

[157] ATLAS Collaboration, *Alignment of the ATLAS Inner Detector in Run-2*, Eur. Phys. J. C **80** (2020) 1194.

[158] Particle Data Group, R. L. Workman, et al., *Review of Particle Physics*, PTEP **2022** (2022) 083C01.

[159] P. Skands, S. Carrazza, and J. Rojo, *Tuning PYTHIA 8.1: the Monash 2013 Tune*, Eur. Phys. J. C **74** (2014) 3024.

[160] J. Bellm et al., *Herwig 7.2 release note*, Eur. Phys. J. C **80** (2020) 452.

[161] S. Alekhin et al., *Parton distribution functions, α_s, and heavy-quark masses for LHC Run II*, Phys. Rev. D **96** (2017) 014011.

[162] ATLAS Collaboration, *Determination of the parton distribution functions of the proton using diverse ATLAS data from pp collisions at* $\sqrt{s} = 7, 8$ *and* 13 *TeV*, (2021).

[163] T.-J. Hou et al., *New CTEQ global analysis of quantum chromodynamics with high-precision data from the LHC*, Phys. Rev. D **103** (2021) 014013.

[164] S. Bailey et al., *Parton distributions from LHC, HERA, Tevatron and fixed target data: MSHT20 PDFs*, Eur. Phys. J. C **81** (2021) 341.

[165] R. D. Ball et al., *The PDF4LHC21 combination of global PDF fits for the LHC Run III*, J. Phys. G **49** (2022) 080501.

[166] R. D. Ball et al., *Parton distributions from high-precision collider data*, Eur. Phys. J. C **77** (2017) 663.

[167] R. D. Ball et al., *The path to proton structure at 1% accuracy*, Eur. Phys. J. C **82** (2022) 428.

[168] *Addendum to the report on the physics at the HL-LHC, and perspectives for the HE-LHC: Collection of notes from ATLAS and CMS*, tech. rep., CERN, 2019, URL: https://cds.cern.ch/record/2651134.

[169] ATLAS Collaboration, *Prospects for the measurement of the W-boson mass at the HL- and HE-LHC*, ATL-PHYS-PUB-2018-026, 2018, URL: https://cds.cern.ch/record/2645431.

[170] L. Gonella, *The ATLAS ITk detector system for the Phase-II LHC upgrade*, Nuclear Instruments and Methods in Physics Research Section A: Accelerators, Spectrometers, Detectors and Associated Equipment **1045** (2023) 167597, ISSN: 0168-9002, URL: https://www.sciencedirect.com/science/article/pii/S0168900222008890.

[171] *Technical Design Report for the ATLAS Inner Tracker Pixel Detector*, tech. rep., CERN, 2017, URL: https://cds.cern.ch/record/2285585.

[172] *Technical Design Report for the ATLAS Inner Tracker Strip Detector*, tech. rep., CERN, 2017, URL: https://cds.cern.ch/record/2257755.

[173] F. Faccio and G. Cervelli, *Radiation-induced edge effects in deep submicron CMOS transistors*, IEEE Trans. Nucl. Sci. **52** (2005) 2413, URL: https://cds.cern.ch/record/1024467.

[174] F. Faccio, *ASIC survival in the radiation environment of the LHC experiments: 30 years of struggle and still tantalizing*, Nuclear Instruments and Methods in Physics Research Section A: Accelerators, Spectrometers, Detectors and Associated Equipment **1045** (2023) 167569, ISSN: 0168-9002, URL: https://www.sciencedirect.com/science/article/pii/S0168900222008610.

[175] L. F. Gutierrez Zagazeta et al., *Testing of the HCC and AMAC functionality and radiation tolerance for the HL-LHC ATLAS ITk Strip Detector*, tech. rep. 03, CERN, 2023, URL: https://cds.cern.ch/record/2837314.